FACHBEREICH PHYSIK
BERGISCHE UNIVERSITÄT
GESAMTHOCHSCHULE WUPPERTAL

A Detailed Study of Perturbative QCD Predictions in e^+e^- Annihilation and a Precise Determination of $\alpha_s(M_Z)$

(Consistent Measurements of α_s from Precise Oriented Event Shape Distributions)

Siegfried Hahn

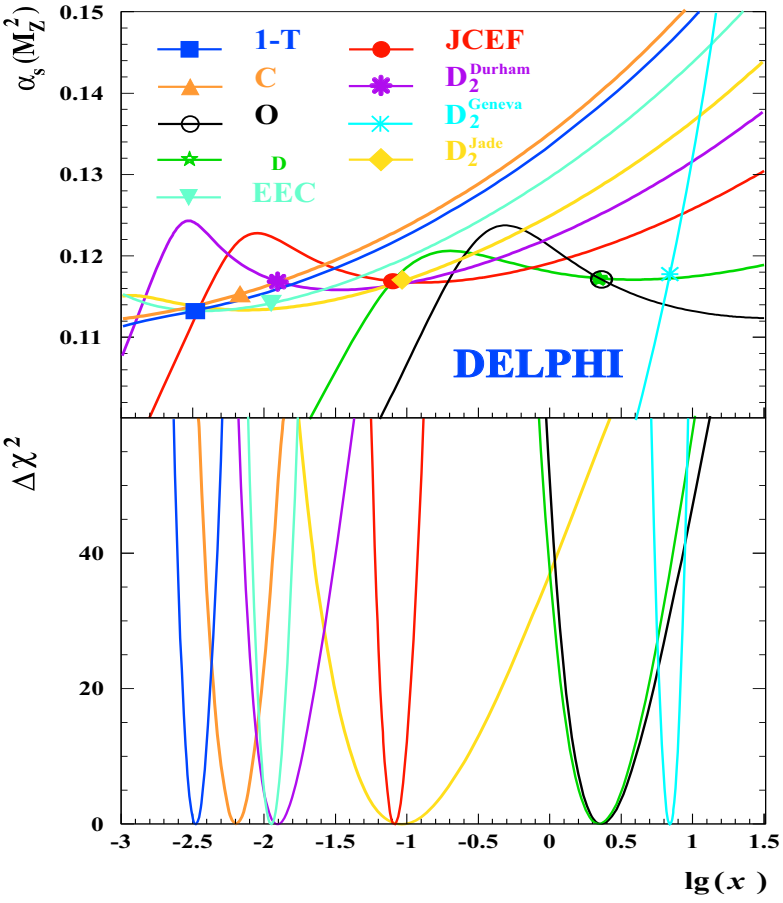

September 2000
WUB-DIS 2000-6

Abstract

An updated analysis using about 1.5 million events recorded at $\sqrt{s} = M_Z$ with the DELPHI detector in 1994 is presented. Eighteen infrared and collinear safe event shape observables are measured as a function of the polar angle of the thrust axis. The data are compared to theoretical calculations in $\mathcal{O}(\alpha_s^2)$ including the event orientation.

Detailed studies of the renormalization scale dependence of the $\mathcal{O}(\alpha_s^2)$ predictions have been performed, including fits applying experimentally optimized renormalization scale values as well as theoretically motivated scale setting prescriptions. It is found, that in general the predictions fail to describe the data if a renormalization scale value $\mu^2 = M_Z^2$ is applied. In this case, the slope of the observed distributions is badly described and the stability of $\alpha_s(M_z^2)$ with respect to a variation of the fit range is poor. These deviations with respect to the data propagate into the matched predictions of $\mathcal{O}(\alpha_s^2)$ and next-to-leading log approximation (NLLA), making them also inappropriate for an accurate description of the high precision data.

An excellent description of the 18 event shape distributions in $\mathcal{O}(\alpha_s^2)$ precision is obtained if the renormalization scale value is fitted to the individual data distributions. The stability of the fits with respect to a variation of the fit range is very good. The scale values obtained from the fits are found to be similar to those predicted by the effective charge method (ECH) and the principle of minimal sensitivity (PMS).

The influence of higher order contributions was also investigated by using the method of Padé approximants to obtain an estimate of the uncalculated $\mathcal{O}(\alpha_s^3)$ contribution as well as for the sum of the perturbative series. The renormalization scale dependence of the Padé predictions is found to be largely reduced with respect to the $\mathcal{O}(\alpha_s^2)$ predictions.

A combined fit of α_s and of the renormalization scale in $\mathcal{O}(\alpha_s^2)$ to the 18 oriented event shape distributions yields a perfectly consistent set of 18 measurements of the strong coupling. A weighted average from 18 observables yields $\alpha_s(M_Z^2) = 0.1174 \pm 0.0026$. This result accounts for heavy quark mass effects and considers correlations between the individual measurements.

The final result, derived from the jet cone energy fraction, the observable with the smallest theoretical and experimental uncertainty, is

$$\alpha_s(M_Z^2) = 0.1180 \pm 0.0006(exp.) \pm 0.0013(hadr.) \pm 0.0008(scale) \pm 0.0007(mass).$$

This value is in perfect agreement with recent α_s determinations from renormalization group improved predictions for the Bjorken sum rule and the hadronic decay of the τ lepton.

Contents

Chapter 1

Introduction

In the recent decades our understanding of the nature of elementary particles and fundamental forces has significantly improved. According to our present knowledge, the structure and the behaviour of matter is ruled by four fundamental forces: Gravitation, the electromagnetic, the weak and the strong nuclear force. The three latter ones are described within a common framework, the Standard Model of elementary particle physics. The Standard Model has been extraordinary successful in predicting properties of new particles and the structure of the interactions and has so far been able to describe all known experimental facts in particle physics. Numerous precision tests of Standard Model predictions have been performed at the Large Electron Positron Collider (LEP) at CERN, which is the world's largest particle accelerator to date. Several parameters of the Standard model have been determined with an extraordinary precision, for example the mass and the width of the Z^0 boson [1]:

$$\begin{aligned} M_Z &= 91186.7 \pm 2.1 \text{ MeV}, \\ \Gamma_Z &= 2493.9 \pm 2.4 \text{ MeV}. \end{aligned}$$

Standard Model predictions for physical observables are commonly expressed in terms of perturbative series, i.e. asymptotic expansions in powers of the relevant coupling for the process under consideration. These perturbative predictions are very successful in particular within the electroweak sector of the Standard Model which is related to the smallness of the electroweak coupling. For processes involving strong interactions the relevant coupling is much larger limiting the numerical precision of theoretical predictions. The convergence behavior of perturbative series is expected to be closely related to the renormalization scheme dependence of fixed order perturbative predictions [2].

The concept of renormalization is an essential feature for the success of the Standard Model. It provides a self consistent procedure for the removal of infinite quantities appearing within the calculation of higher order corrections to the basic interactions. Thus accurate numerical predictions for physical observables become possible. The price to pay however, is the dependence of the theoretical predictions on a number of arbitrary parameters which characterize the renormalization scheme and reflect the principal ambiguity introduced by the subtraction of the infinite expressions.

The scheme dependence problem is subject of an extensive literature. A number of proposals for controlling or avoiding this difficulty have been made [3, 4, 5, 6], but from a theoretical point of view, a definite answer to the solution of this problem is still missing. Within the theory of strong interactions, Quantum Chromo Dynamics (QCD), the dependence of finite order perturbative expansions on the choice of the renormalization scheme is however a very real phenomenological problem, which cannot be ignored. Numerous measurements of the strong coupling α_s have been published in the past, but so far 'consistency' between measurements of $\alpha_s(M_z^2)$ from a set of different observables has only been achieved by taking into account large renormalization scale uncertainties obtained by varying the renormalization scale value within a large and *ad hoc* range [6].

Although previous studies [7] indicated a better description of the experimental data and an improved consistency of the measurements of the strong coupling in combination with an optimization of the renormalization scale, definite answers about the qualification of the different approaches for the description of experimental observations have so far not been obtained. With the considerable and steady improvement of experimental data, the constraints implied on the theoretical predictions for the strong interaction are becoming more stringent and a judgement of the qualification of the different approaches becomes possible.

About 17 million hadronic events have been recorded by the four LEP experiments ALEPH , OPAL , DELPHI and L3 from the studies of electron positron annihilation around the Z^0 resonance. Owing to the large energy and the clean and well defined initial state of the process, the collected data provide an ideal testing field for the predictions of perturbative QCD.

The DELPHI data analyzed in this thesis are much improved in both their statistical and systematic precision compared with those of previous DELPHI publications [8, 9]. From the measured data, eighteen distributions of different infrared and collinear safe hadronic event observables are determined at various values of the polar angle ϑ_T of the thrust axis with respect to the e^+e^- beam direction. The ϑ_T dependence of all detector properties are taken into account, thus achieving an optimal experimental precision.

The data distributions are compared with next-to-leading order (NLO) QCD calculations for oriented event shapes. The renormalization scale dependence of the theoretical predictions has been studied in detail. Different prescriptions for obtaining an optimized scale value have been compared with the customary fixed scale approach and with methods for the estimate of higher order contributions by the means of Padé Approximation. Further studies cover all orders resummed predictions in next-to-leading-logarithmic approximation (NLLA).

It will be demonstrated that the precise experimental data are fully consistent with the expectation from second order QCD. A two parameter fit to each of the distributions results in experimentally optimized renormalization scale values and a consistent set of eighteen $\alpha_s(M_z^2)$ values. The renormalization scale values obtained are similar to those predicted by the Principle of Minimal Sensitivity (PMS) [3] and by the Effective Charge approach (ECH) [4]. Applying fixed renormalization scale values to the NLO predictions yields in general large deviations from the data distributions. The $\alpha_s(M_z^2)$ values obtained are unstable with respect to a variation of the fit range and the measurements from different observables are inconsistent. The deviations observed are propagating into the matched NLLA & NLO predictions.

This thesis is organized as follows: The next chapter contains a brief introduction to Quantum Chromo Dynamics and the Standard Model. The renormalization scheme dependence of perturbative predictions is discussed and methods for renormalization scheme optimization are introduced. Within Chapter 3 some theoretical aspects relevant for the determination of $\alpha_s(M_z^2)$ in e^+e^- annihilation are discussed in more detail and the eighteen collinear and infrared safe shape observables are defined. The LEP collider and the DELPHI experiment are introduced in Chapter 4. In the following chapter, the data analysis is presented and the obtained data distributions are compared to those obtained from other experiments. Chapter 6 contains the comparison of the measured distributions with the different theoretical predictions and a precision determination of $\alpha_s(M_z^2)$ taking into account leading order quark mass effects. The Jet Cone Energy Fraction (JCEF) is identified as the observable with the smallest theoretical and experimental uncertainties. The experimental results are summarized in Chapter 7. The last chapter contains a concluding discussion and suggestions which might be relevant for future QCD analyses and determinations of $\alpha_s(M_z^2)$.

Chapter 2

Quantum Chromo Dynamics and the Standard Model

Our present knowledge about the structure and the behaviour of matter is formulated by the Standard Model of elementary particle physics. After a brief introduction into some of its basic properties, some aspects relevant to this analysis will be discussed in more detail, in particular the renormalization scheme dependence problem of finite order perturbative predictions. The aim of this discussion is to enable an intuitive understanding of this problem, rather than a complete and mathematically exact derivation. For a general introduction the reader is referred to [10], an overview about the scheme dependence problem can be found e.g. in [6, 11] and the references given therein.

2.1 Introduction into the Standard Model

The development of the Standard Model of particles and their interactions started in the 1960's. It covers the electromagnetic, weak and the strong interactions, which are interpreted as an exchange of a gauge boson between fermions. Strong interactions are described by Quantum Chromo Dynamics (QCD), while the behaviour of electromagnetic and weak interactions is described by the Electroweak Theory (GWS[1]-model). The gravitation is described by general relativity. Although it is the most evident force in everyday life, it can be neglected in elementary particle physics, since it is by several orders of magnitude the weakest force. This is illustrated in Table 2.1.

[1] **Glashow Weinberg Salam**

	Interactions		
	strong	electroweak	gravity
Theory	QCD	GSW	general relativity
Symmetry Group	$SU(3)_C$	$SU(2)_L \times U(1)_Y$	-
Gauge Bosons	$g_1 \cdots g_8$	$\gamma, W^{\pm}, Z^0, H^0$	graviton
Charge	colour	weak isospin weak hypercharge	mass
Coupling	α_s	$\alpha, \sin^2 \Theta_W$	G
Strength	0.2	0.03	$< 10^{-30}$

Table 2.1: The fundamental forces.

Within the Standard Model, the basic constituents of matter, quarks and leptons, are considered to be fundamental fermions. They can be classified into three generations. The fermions of the second and third generation are identical copies of the fermions of the first generation, with the exception that they have larger masses. Table 2.2 gives an overview of the spectrum of elementary quarks and leptons. They appear in two different states of helicity, i.e. left- and right-handed states, which have different properties regarding the electroweak interaction. Right handed neutrinos have yet not been observed. Recently observed neutrino oscillations [12] however imply their existence. So far right handed neutrinos have not been incorporated in the Standard Model.

The basic theoretical framework used for the description of elementary particles and their interactions is Quantum Field Theory. The theories are constructed in terms of a Lagrangian, or an action, which is a well developed and known formalism of classical mechanics. The structure of the Lagrangian, i.e. its symmetries, already tell us something about the physics it is supposed to describe. For example, it can be elegantly deduced from the Lagrangian that the homogeneity of time, the homogeneity of space and the isotropy of space lead to the fundamental conservation laws of energy, momentum and angular momentum. The local gauge invariance of the Lagrangian induces forces and is necessary for realistic models of interactions, which are described by the exchange of gauge bosons. The introduction of a Higgs mechanism induces massive gauge bosons within a theory wich is still invariant under a local gauge transformation.

The prototype of local gauge theories is Quantum Electro Dynamics (QED). It describes the electromagnetic interaction between charged fermions by the exchange of a single massless gauge boson according to the gauge group $U(1)$, which characterizes the symmetry of the model. Here U stands for the unitary groups and the 1 reflects the dimension of the charge space. Due to the abelian character of the $U(1)$ group, the gauge boson carries no charge itself and can be identified with the well known photon.

The electromagnetic and the weak interaction, which has been introduced by Fermi [13] to describe the β-decay of the neutron, are nowadays described by a common gauge theory developed by Glashow, Salam and Weinberg [14] in the late 1960s. The underlying gauge symmetry of the electroweak theory is $U_Y(1) \times SU_L(2)$, where $SU(N)$ corresponds to the special unitary groups of dimension N. $SU(2)$ is a non-abelian gauge group, which implies that the corresponding gauge bosons are charged. $N = 2$ corresponds to a two dimensional charge which is usually expressed in terms

Fermions	Generations			Quantum Numbers		
	1.	2.	3.	Q/e	I_3	Y
Leptons	$\begin{pmatrix} \nu_e \\ e \end{pmatrix}_L$	$\begin{pmatrix} \nu_\mu \\ \mu \end{pmatrix}_L$	$\begin{pmatrix} \nu_\tau \\ \tau \end{pmatrix}_L$	0 -1	$1/2$ $-1/2$	-1 -1
	$(e)_R$	$(\mu)_R$	$(\tau)_R$	-1	0	-2
Quarks	$\begin{pmatrix} u \\ d' \end{pmatrix}_L$	$\begin{pmatrix} c \\ s' \end{pmatrix}_L$	$\begin{pmatrix} t \\ b' \end{pmatrix}_L$	$2/3$ $-1/3$	$1/2$ $-1/2$	$1/3$ $-1/3$
	$(u)_R$ $(d)_R$	$(c)_R$ $(s)_R$	$(t)_R$ $(b)_R$	$2/3$ $-1/3$	0 0	$4/3$ $-2/3$

Table 2.2: The fundamental particles and their electroweak quantum numbers. The neutrinos ν_e, ν_μ and ν_τ respectively belong to the electron (e), muon (μ) and tau (τ) leptons. The quarks, up (u), down (d), strange (s), charm (c), bottom (b) and top (t) also carry colour charge. The primes at the left handed quarks d', s' and b' indicate, that they are eigenstates of the electroweak interaction. These eigenstates are linear combinations of the mass eigenstates d, s and b and are determined by the so called Cabibbo-Kobayasshi-Maskawa (CKM) matrix.

of the weak hypercharge and the third component of the weak isospin I_3. They are related to the electrical charge Q by the Gell-Mann-Nishijima relation

$$Q = I_3 + \frac{Y}{2} \quad . \tag{2.1}$$

A special feature of the weak interaction is its parity violation. It has first been observed within the Wu-experiment [15], which has shown, that the electrons created within the β-decay are emitted with a preferred helicity, thus revealing that the weak interaction discriminates between left and right handed fermions. Within the GWS-model the left handed fermions belong to isospin doublets, whereas the right handed fermions are isospin singlets (see Table 2.2). The subscript L in $SU(2)_L$ indicates, that this gauge group is only relevant for the left handed fermions.

The fundamental gauge symmetry of the Standard model requires massless fermions and gauge bosons. In order to explain the physically observed massive particles, the gauge symmetry is considered to be spontaneously broken by the so-called Higgs mechanism. A direct consequence of this mechanism is the existence of a physical massive scalar particle, the Higgs boson H^0, which has not been observed yet. Its discovery is one of the major goals elementary particle physics is facing nowadays. If symmetry breaking of $U_Y(1) \times SU_L(2)$ is done by the simplest Higgs mechanism, it results in three massive vector bosons W^+, W^-, Z^0 and one massive, scalar Higgs boson H^0. The charged weak current is associated purely to $SU(2)$, while the neutral currents from $U(1)$ and $SU(2)$ undergo mixing, producing a massless γ and a massive Z^0 boson. The strength of this mixing is given by the Weinberg angle θ_W, thus relating the couplings belonging to $U(1)$ and $SU(2)$, which can be expressed for example in terms of the fine structure constant α and $sin^2\theta_W$. The values of the couplings cannot be determined from fundamental principles. They enter as free parameters into the theory and have to be measured by experiment. Due to the Higgs mechanism, two additional free parameters enter into the theory, which can be parameterized for example in terms of the masses of the Z^0 and the H^0. The masses of the $W^\pm$ bosons can then be related to the Z^0 mass via the Weinberg angle according to

$$sin^2\theta_W = 1 - \frac{M_W^2}{M_Z^2} \quad . \tag{2.2}$$

The masses of the fermions are also generated by the Higgs mechanism. Their masses are proportional to their coupling strength to the Higgs particle. To generate the fermion mass spectrum, for each particle an individual coupling is needed. These couplings cannot be derived from theoretical principles and also enter as free parameters

into the theory. Assuming massless neutrinos, in total nine free parameters have to be introduced to describe the fermion masses. The mass eigenstates of the quarks are however different to their interaction eigenstates. The electroweak eigenstates d', s', b' (see Table 2.2) are mixtures of the mass eigenstates d, s and b, thus allowing decays leading to transitions between the three generations. The electroweak eigenstates are related to the mass eigenstates by the Cabibbo-Kobayashi-Maskawa (CKM) matrix, which is a three dimensional unitary matrix. It can be parameterized by four independent numbers, for example three angles and one imaginary phase. Again these four parameters cannot be determined from fundamental considerations and their values have to be determined experimentally.

Since the discovery, that atomic nuclei consist of protons and neutrons, it is clear that a strong nuclear force must exist, which holds the protons and neutrons within the nuclei together. Otherwise, no nuclei with multiple protons could exist due to the coulomb rejection. Today we know that protons and neutrons are not elementary particles. They are build by three elementary constituents, which are called quarks. Quarks appear in six different flavours, $q = u, d, s, c, b, t$ and were proposed in 1964 by Gell-Mann [16] and Zweig [17] in order to describe the spectra of the large number of hadrons, which had been discovered at that time. This hadrons can be separated into two classes. The baryons, consisting of three quarks (qqq) or anti-quarks $(\bar{q}\bar{q}\bar{q})$ and the mesons, consisting of a quark and an anti-quark $(q\bar{q})$. In 1964, Gell-Mann and Zweig recognized, that all existing hadrons could be arranged into multiplets according to higher representations of a global $SU(3)_{flavour}$ symmetry, where the three corresponds to the three quark flavours (u,d,s) which were required to describe the hadron spectrum known in 1964.

The interaction between the hadrons is described by Quantum Chromo Dynamics (QCD) [18], a local gauge theory with a $SU(3)_C$ symmetry structure. The C indicates the charge of the strong interaction, which is called colour. According to the dimension three of the gauge group, colour appears in three different states called red (r), green (g), blue (b) and their anti-states. Each quark carries exactly one unit of colour. Free colour charges are not observed. The $SU(3)_C$ symmetry implies that the physically observed mesons $(q\bar{q})$ and baryons $(\bar{q}\bar{q}\bar{q})$ are colour-singlets, i.e. that the colour charges of constituent quarks combine to a colour-less (white) configuration.

The gauge bosons mediating the strong force are named gluons and carry one unit colour and one unit of anti-colour. There are eight different types of gluons representing an octet with respect to the $SU(3)_C$ gauge group. Since the gluons carry colour charge, they also interact among themselves. The strength of the quark gluon and the gluonic interaction is given in terms of a single universal coupling, the strong coupling α_s. As for the couplings of the electroweak interaction, α_s is a free parameter of the theory, which can only be determined by measurement.

2.2 The concept of a running coupling

Since the structure of the Standard Model lagrangian is rather complicated and involves non-liner interaction terms and an infinite number of degrees of freedom, the theory cannot be solved analytically. In order to derive measurable quantities from the Lagrangian, one has in general two choices to obtain them. Firstly one can try to solve the complicated expressions by numerical integration on fast computers. This is done by Lattice Gauge Theory (LGT). The main concern of this approach is the confinement region of QCD, where the physical coupling is strong.

The second approach is perturbation theory. Within QCD theory, it can be applied for interactions involving a large momentum transfer, where the physical coupling is small. According to perturbation theory, a specific process, i.e. a transition from a well defined initial state to a well defined final state, can be understood with the help of so-called Feynman Rules as an infinite sum over all possible virtual intermediate states which can contribute to the observed transition. These Feynman Rules are mathematical instructions to calculate the transition amplitudes involved. They can be visualized with the help of diagrams, thereby having the advantage of reflecting an intuitive picture of the physical processes. The basic diagrams of QCD are shown in Figure 2.1.

A coupling is associated to each vertex, and a propagator term describes the lines encapsulated by two vertices. Mathematically, the amplitude for a particular intermediate state, is proportional to a specific power of the strong coupling. The power is given by the number of vertices. In order to calculate transition probabilities, the

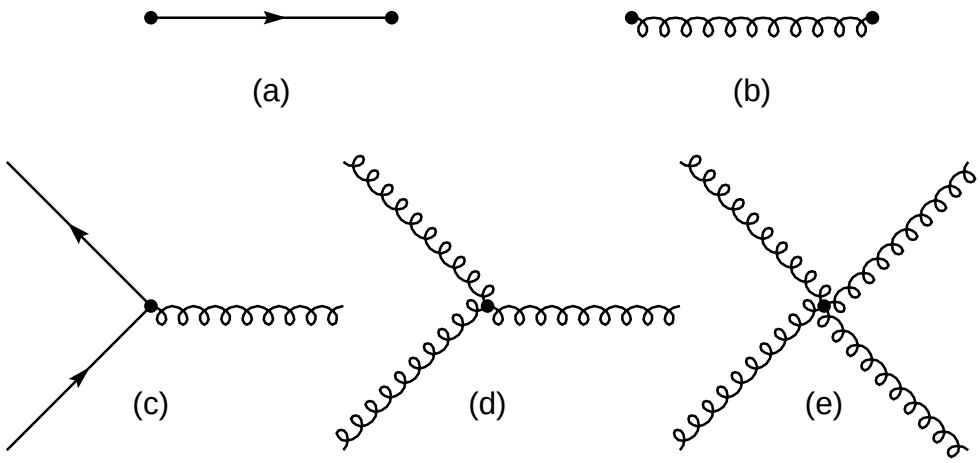

Figure 2.1: The fundamental QCD Feynman diagrams. (a) quark propagator, (b) gluon propagator, (c) quark-gluon vertex, (d) 3-gluon vertex and (e) 4-gluon vertex.

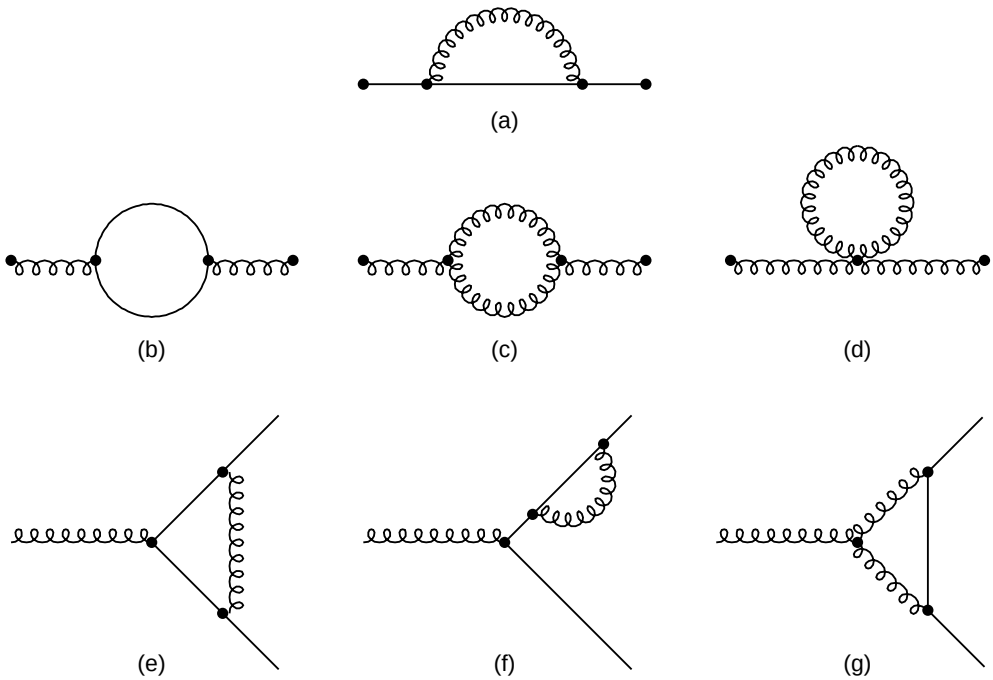

Figure 2.2: Some first order corrections to the basic QCD diagrams. (a) The first order correction to the fermion propagator called 'self' energy. (b) The vacuum polarization diagram, which also exists in QED. (c) The gluon self coupling diagram and the direct gluon self coupling diagram (d), which are absent in the abelian QED theory. (e-g) First order corrections to the quark gluon vertex.

sum over all amplitudes has to be squared. The resulting expression is a power series in powers of the coupling. Provided the involved coupling is small, the higher orders can be neglected and the concept of perturbation theory is applicable. The calculation of higher order corrections to QCD perturbative series are extremely difficult and cumbersome, thus for most observables only next-to-leading order calculations are available. Little is known about the higher order behaviour of the series and it is not proven that QCD perturbative expansions converge at all[2]. It is commonly assumed that the series of Feynman diagrams is an asymptotic series, i.e. that finite physical predictions can be derived by considering just the first N orders of the expansion, even though the whole series may diverge. For a detailed discussion about the convergence problem of perturbative QCD predictions and its relevance for different physical situations see for example reference [20].

[2]For the special case of perturbative expansions applying the so-called 't Hooft renormalization scheme, it can be shown, that the corresponding series are factorially divergent. It should however be noted, that the factorial growth of the coefficients has no scheme invariant meaning. Exploiting the freedom of choosing a renormalization scheme could result in not just summable but even convergent perturbative predictions [19].

2.2.1 Quantum Loops

At lowest order perturbation theory (tree-level), it is straightforward to compute all kind of scattering amplitudes. Since for example the QCD Lagrangian involves a single coupling $g_s = \sqrt{4\pi\alpha_s}$, all strong interacting phenomena should be described in terms of the single parameter g_s. Unfortunately, the tree-level diagrams itself do not help very much to understand the physically observed hadronic world. First, one observes hadrons instead of quarks and gluons. Second, one observes that the strength of the strong force changes with the energy scale. The strength is very strong (confining) at low energies, but quarks behave as nearly free particles at high energies. However, apart from the quark masses (which will be neglected in the following consideration), the QCD Lagrangian does not contain any energy scale at all, thus, there is no way to decide if the energy of a given process is large or small, because there is no reference scale to compare with. In order to understand the energy dependence of QCD, one has to calculate the perturbative corrections to the tree-level diagrams, which introduce a dynamical scale through quantum loop effects. Figure 2.2 shows some of the first order corrections to the basic QCD diagrams.

2.2.2 Regularization of loop integrals

The computation of perturbative corrections to the tree-level results involves divergent loop integrals. Therefore, it is necessary to find a way of getting finite results with physical meaning from the a priori meaningless divergent quantities. The technique achieving this is called regularization. Considering quantum loop effects introduces an energy scale, which can be illustrated by considering the vacuum polarization diagram as an example [21].

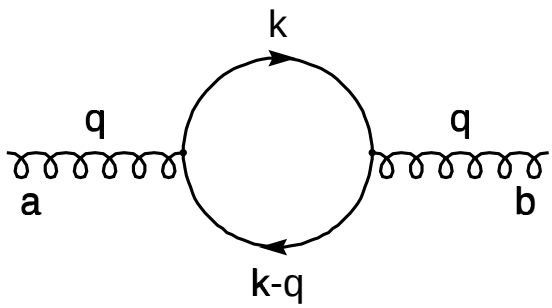

Figure 2.3: The QCD vacuum polarization diagram. k and q represent the four-momenta involved and $a, b = 1, \ldots, 8$ indicate the colour octet label of the incoming and outgoing gluon respectively.

The contribution of the vacuum polarization diagram as shown in Figure 2.3 can be obtained using standard Feynman rule techniques (for an introduction see e.g. [10]):

$$i\Pi_{ab}^{\mu\nu}(q) = -g_s^2 \delta_{ab} T_F \int \frac{d^4k}{(2\pi)^4} \frac{\mathrm{Tr}\left[\gamma^\mu(\gamma^\lambda k_\lambda)\gamma^\nu(\gamma^\sigma(q-k)_\sigma)\right]}{k^2\,(k-q)^2} \quad , \tag{2.3}$$

where μ, ν, etc. are Dirac-Indices and γ_μ are the Dirac-matrices. The contribution is proportional to g_s^2, because there are two $q\bar{q}g$ vertices, and there is a $SU(3)_C$ factor, $T_F = 1/2$. The problem arises with the integration over all internal momenta, which is logarithmically divergent in the ultraviolett region ($|k| \to \infty$). In principal, there are several methods to define the momentum integral, like e.g. introducing a momentum cut-off parameter. Conventionally the so-called dimensional regularization [22] is applied, which has several advantages because it conserves the gauge symmetry of the lagrangian. Within dimensional regularization the calculation is performed in $D = 4 + 2\epsilon$ dimensions. For $\epsilon \neq 0$ the resulting integral is well-defined:

$$\int \frac{d^Dk}{(2\pi)^D} \frac{k^\alpha (k-q)^\beta}{k^2(k-q)^2} = \frac{-i}{6(4\pi)^2} \left(\frac{-q^2}{4\pi}\right)^\epsilon \Gamma(-\epsilon) \left(1 - \frac{5}{3}\epsilon\right) \left\{\frac{q^2 g^{\alpha\beta}}{2(1+\epsilon)} + q^\alpha q^\beta\right\} \tag{2.4}$$

The ultraviolet divergence of the loop appears at $\epsilon = 0$, through the pole of the Gamma function,

$$\Gamma(-\epsilon) = -\frac{1}{\epsilon} - \gamma_E + \mathcal{O}(\epsilon^2) \quad , \tag{2.5}$$

where $\gamma_E = 0.577215\ldots$ is the Euler constant. Since the momentum-transfer q^2 has dimensions, it is useful to introduce an arbitrary energy scale μ and write

$$\begin{aligned} \left(\frac{-q^2}{4\pi}\right)^\epsilon \gamma(-\epsilon) &= \mu^{2\epsilon} \left(\frac{-q^2}{4\pi\mu^2}\right)^\epsilon \gamma(-\epsilon) \\ &= -\mu^{2\epsilon} \left\{\frac{1}{\epsilon} + \gamma_E - \ln 4\pi + \ln(-q^2/\mu^2) + \mathcal{O}(-\epsilon)\right\} \quad . \end{aligned} \tag{2.6}$$

Obviously, this expression does not depend on μ, but written in this form one has a dimensionless quantity $(-q^2/\mu^2)$ inside the logarithm. The contribution of the loop diagram in Figure 2.3 can finally be written as

$$\begin{aligned}\Pi_{ab}^{\mu\nu} &= \delta_{ab}\left(-q^2 g^{\mu\nu} + q^\mu q^\nu\right)\Pi(q^2) \\ \Pi(q^2) &= -\frac{4}{3}T_F\left(\frac{g_s\mu^\epsilon}{4\pi}\right)^2\left\{\frac{1}{\epsilon} + \gamma_E - \ln 4\pi + \ln(-q^2/\mu^2) - \frac{5}{3} + \mathcal{O}(-\epsilon)\right\} \quad (2.7)\end{aligned}$$

Owing to the ultraviolet divergence, Eq. 2.7 does not determine the wanted contribution from the vacuum polarization graph. However, it shows how this effect changes with the energy scale. If one could fix the value of $\Pi(q^2)$ at some reference momentum transfer q_0^2, the result would be known at any other scale:

$$\Pi(q^2) = \Pi(q_0^2) - \frac{4}{3}T_F\left(\frac{g_s}{4\pi}\right)^2 \ln(q^2/q_0^2) \quad . \qquad (2.8)$$

$\Pi(q^2)$ can be splitted into a meaningless divergent piece and a finite term, which includes the q^2 dependence.

$$\Pi(q^2) = \Delta\Pi_\epsilon(\mu^2) + \Pi_R(q^2/\mu^2) \quad . \qquad (2.9)$$

This separation is of course ambiguous, because the finite q^2 – independent contributions can be splitted in an infinite number of ways. A given choice defines a renormalization scheme (RS), some examples are given below:

$$\Delta\Pi_\epsilon = \begin{cases} -\frac{T_F}{3\pi}\frac{g_s^2}{4\pi}\mu^{2\epsilon}\left[\frac{1}{\epsilon} + \gamma_e - \ln 4\pi - \frac{5}{3}\right] & (\mu - \text{scheme}), \\ -\frac{T_F}{3\pi}\frac{g_s^2}{4\pi}\mu^{2\epsilon}\frac{1}{\epsilon} & (\text{MS} - \text{scheme}), \\ -\frac{T_F}{3\pi}\frac{g_s^2}{4\pi}\mu^{2\epsilon}\left[\frac{1}{\epsilon} + \gamma_e - \ln 4\pi\right] & (\overline{\text{MS}} - \text{scheme}), \end{cases} \qquad (2.10)$$

$$\Delta\Pi_R = \begin{cases} -\frac{T_F}{3\pi}\frac{g_s^2}{4\pi}\ln\left(-q^2/\mu^2\right) & (\mu - \text{scheme}), \\ -\frac{T_F}{3\pi}\frac{g_s^2}{4\pi}\left[(-q^2/\mu^2) + \gamma_E - \ln 4\pi - \frac{5}{3}\right] & (\text{MS} - \text{scheme}), \\ -\frac{T_F}{3\pi}\frac{g_s^2}{4\pi}\left[(-q^2/\mu^2) - \frac{5}{3}\right] & (\overline{\text{MS}} - \text{scheme}). \end{cases} \qquad (2.11)$$

In the μ – scheme, one uses the value of $\Pi(-\mu^2)$ to define the divergent part. MS and $\overline{\text{MS}}$ stand for minimal subtraction and modified minimal subtraction schemes, in the MS case, one subtracts only the divergent $1/\epsilon$ term, while in the $\overline{\text{MS}}$ scheme also the annoying $\gamma_E - \ln 4\pi$ term is put into the divergent part.

The idea of renormalization is to redefine the original fields and couplings (the so-called *bare* fields and couplings) through absorbing all ultraviolett divergences into them, thus yielding renormalized quantities. Theoretical predictions expressed in terms of the renormalized quantities yield finite results, which can be compared with experiment. Such a strategy is meaningful, provided that it can be done in a selfconsistent way, i.e. that all ultraviolett divergent contributions from all possible scattering amplitudes can be eliminated through the same redefinition of the couplings and fields. This is valid for the Standard Model but it is not a general feature of gauge theories.

The principle of this mechanism is shown in the following example. The scattering amplitude of the QED interaction between two electrons takes the form

$$T(q^2) \sim J^\mu J_\mu \frac{\alpha}{q^2} \left\{1 - \pi(q^2) + \ldots\right\} \quad , \tag{2.12}$$

with the coupling $\alpha = e^2/(4\pi)$ and J^μ denoting the electromagnetic current. The vacuum polarization contribution $\Pi(q^2)$ at one loop level is just given by Eq. 2.7 with the modifications $T_F \to 1$ and $g_s \to e$. The divergent correction is absorbed by a redefinition of the coupling;

$$\frac{\alpha_0}{q^2} \left\{1 - \Delta\Pi_\epsilon(\mu^2) - \Pi_R(q^2/\mu^2)\right\} = \frac{\alpha_R(\mu^2)}{q^2} \left\{1 - \Pi_R(q^2/\mu^2)\right\} \quad , \tag{2.13}$$

$$\alpha_R(\mu^2) = \alpha_0 \left\{1 + \frac{\alpha_0}{3\pi}\mu^{2\epsilon}\left[\frac{1}{\epsilon} + C_{\text{scheme}}\right] + \ldots\right\} \quad , \tag{2.14}$$

where $\alpha_0 = e_0^2/(4\pi)$ denotes the bare coupling. Bare quantities, like the bare coupling α_0 are not measurable at all. The goal of experimental measurements is the determination of the value of the renormalized coupling α_R. However, $\alpha_R(\mu^2)$ depends on the arbitrary renormalization scale μ and on the choice of the RS. C_{scheme} in Eq. 2.14 denotes the term coming from the splitting of the finite q^2 – independent contribution of $\Pi(q^2)$. This is not a principal problem, since the renormalized coupling itself is not a directly observable quantity. Observable quantities like the scattering amplitude $T(q)^2$ should of course be μ – independent:

$$T(q^2) \sim J^\mu J_\mu \frac{\alpha_R(\mu^2)}{q^2} \left\{1 + \frac{\alpha_R(\mu^2)}{3\pi}\left[\ln\left(-q^2/\mu^2\right) + C_{\text{scheme}}\right] + \ldots\right\}. \tag{2.15}$$

To leading order, the above expression is inescapable renormalization scale dependent and therefore completely arbitrary. The scale dependence is however cancelled to some extent due to the logarithmic term coming up in next to leading order. Completely $\mu-$independent expressions can only be achieved by a non-trivial cancellation of all scale dependent terms involving all orders perturbation theory, i.e. any prediction from a truncated perturbative expression comes with a residual renormalization scale dependence. Internal consistency of perturbation theory only guarantees that the residual scale dependence is of one order higher than the one considered.

2.2.3 The Renormalization Group Equation of QCD

As outlined in the previous subsection, renormalization scale independence of physical quantities is achieved through a non-trivial cancellation process involving all orders perturbation theory. Consider a generic dimensionless physical observable R, which depends on an energy scale Q^2 and can be calculated perturbatively within QCD, yielding a power series in terms of the renormalized coupling $\alpha_s = \alpha_s(\mu^2)$ of the following form:

$$R\left(\alpha_s, Q^2/\mu^2\right) = \alpha_s r_1(Q^2/\mu^2) + \alpha_s^2 r_2(Q^2/\mu^2) + \ldots = \sum_{i=1}^{\infty} \alpha_s^i r_i(Q^2/\mu^2) \quad . \tag{2.16}$$

R depends on μ explicitly via the functions $r_i(Q^2/\mu^2)$ and implicitly through α_s. Since R is an observable, it should be independent of μ, i.e. all implicit and explicit renormalization scale dependence should cancel if R is summed up to all orders. This condition is expressed by the so-called Renormalization Group Equation (RGE):

$$\mu^2 \frac{d}{d\mu^2} R\left(\alpha_s, \frac{Q^2}{\mu^2}\right) = \left[\mu^2 \frac{\partial}{\partial \mu^2} + \mu^2 \frac{\partial \alpha_s}{\partial \mu^2} \frac{\partial}{\partial \alpha_s}\right] R = 0 \quad . \tag{2.17}$$

A solution of this equation is found by introducing a new function, which describes the renormalization scale dependence of α_s:

$$\mu^2 \frac{\partial \alpha_s(\mu^2)}{\partial \mu^2} = \beta(\alpha_s) = -b_0 \alpha_s^2 - b_1 \alpha_s^3 - \ldots = \sum_{i=0}^{\infty} b_i \alpha_s^{i+2} \quad . \tag{2.18}$$

The right hand side of Eq. 2.18 is the so-called β – function, its coefficients b_i are calculated by considering loop diagrams as shown in Figure 2.2 up to the desired

order. The first two coefficients are universal, i.e. independent of the RS and have been computed to be

$$b_0 = \frac{33 - 2n_f}{12\pi} \quad , \tag{2.19}$$

$$b_1 = \frac{153 - 19n_f}{24\pi^2} \quad , \tag{2.20}$$

where n_f is the number of active quark flavours which contribute to quark loop corrections as shown in Figure 2.3, which has to be set to $n_f = 5$ at LEP energies.

The higher order coefficients $b_i, i \geq 2$ are RS dependent and therefore arbitrary parameters. The dependence of the coupling α_s on these parameters is determined by equations similar to Eq. 2.18 [3]:

$$\frac{\partial \alpha_s(b_i)}{\partial b_i} = \beta_i(\alpha_s) = \frac{1}{i-1}\left(\alpha_s^{i+1} + w_1^i \alpha_s^{i+2} + w_2^i \alpha_s^{i+3} + \ldots\right) \tag{2.21}$$

Within the $\overline{\rm MS}$ – scheme the coefficient b_2 has been computed to be

$$b_2^{\overline{\rm MS}} = \frac{1}{128\pi}\left(2857 - \frac{5033}{9}n_f - \frac{325}{27}n_f^2\right) \quad . \tag{2.22}$$

The relation of the coupling α_s at one scale μ^2 to that at another scale μ_0^2 is given by:

$$\begin{aligned} \alpha_s(\mu^2) &= \alpha_s(\mu_0^2) \Bigg/ \left\{1 + b_0 \ln\left(\frac{\mu^2}{\mu_0^2}\right)\alpha_s(\mu_0^2) + b_1 \ln\left(\frac{\mu^2}{\mu_0^2}\right)\alpha_s^2(\mu_0^2) + \ldots\right\} \\ &\simeq \alpha_s(\mu_0^2)\left\{1 - b_0 \ln\left(\frac{\mu^2}{\mu_0^2}\right)\alpha_s(\mu_0^2)\right. \\ &\quad \left. + \left[b_0^2 \ln^2\left(\frac{\mu^2}{\mu_0^2}\right) - b_1 \ln\left(\frac{\mu^2}{\mu_0^2}\right)\right]\alpha_s^2(\mu_0^2) + \ldots\right\} \quad . \end{aligned} \tag{2.23}$$

The coupling decreases at large scales, i.e.

$$\lim_{\mu^2 \to \infty} \alpha_s(\mu^2) = 0 \quad , \tag{2.24}$$

which is an important property of QCD and is called *asymptotic freedom*. The perturbative calculations tell us how the coupling evolves with the scale (which is called *running of the coupling*), but nothing about its absolute value. The latter has to be determined from experiment. Apart from the problem of assigning an appropriate RS, one could choose for example the value of α_s at a convenient reference scale, e.g. the mass of the Z^0 – boson M_Z as the fundamental parameter of the theory. Instead of this, it has become standard to introduce a dimensionful parameter directly into the definition of $\alpha_s(\mu^2)$. By convention this parameter is called Λ and is a constant of integration defined by

$$\ln\left(\frac{\mu^2}{\Lambda^2}\right) = -\int_{\alpha_s(\mu^2)}^{\infty} \frac{dx}{\beta(x)} = \int_{\alpha_s(\mu^2)}^{\infty} \frac{dx}{b_0 x^2 + b_1 x^3 + b^2 x^4 + \ldots} \tag{2.25}$$

Formally, Λ represents the scale at which $\alpha_s(\mu^2)$ diverges. The arbitrariness of the integration constant is reflected in the fact that the replacement $\Lambda \to c \cdot \Lambda$, $c =$ constant still gives a solution of Eq. 2.18.

Utilizing the definition of Λ according to Eq. 2.25, α_s can be written as an expansion in inverse powers of $\ln(\mu^2/\Lambda^2)$. The leading order (LO) expression is

$$\alpha_s(\mu^2) = \frac{1}{b_0 \ln\left(\mu^2/\Lambda^2\right)} \tag{2.26}$$

and the calculation in next-to-next-to-leading (NNLO) calculation yields [23]

$$\begin{aligned} \alpha_s(\mu^2) \;=\; & \frac{1}{b_0 \ln\left(\mu^2/\Lambda^2\right)} \left[1 - \frac{b_1}{b_0^2} \frac{\ln\left[\ln\left(\mu^2/\Lambda^2\right)\right]}{\ln\left(\mu^2/\Lambda^2\right)} + \frac{b_1^2}{b_0^4 \ln^2\left(\mu^2/\Lambda^2\right)} \right. \\ & \left. \times \left(\left[\ln\left[\ln\left(\mu^2/\Lambda^2\right)\right] - \frac{1}{2} \right]^2 + \frac{b_0 b_2}{b_1^2} - \frac{5}{4} \right) \right] \quad . \end{aligned} \tag{2.27}$$

The value of Λ, and hence the value of α_s, depends on the number of active quark flavours and on the RS employed. In order to distinguish different definitions of Λ, it is usual to label them $\Lambda_{RS}^{n_f}$, where n_f indicates the number of active quark flavours and RS the renormalization scheme employed. For example $\Lambda_{\overline{\rm MS}}^{5}$ stands for the definition within the $\overline{\rm MS}$ – scheme with 5 active quark flavours. In order to compare measurements from different experiments at different energies, it has

become conventional to give values for the strong coupling within the $\overline{\rm MS}$ – scheme and in terms of $\alpha_s(M_Z)$, i.e. the value of α_s at the Z^0 mass scale.

Invariance with respect to the renormalization group equation (RGE) (2.17) determines also the renormalization scale dependence of the functions r_i of the perturbative expansion (2.16). Up to $\mathcal{O}(\alpha_s^3)$ the μ – dependence is given by

$$R = \hat{r}_1\alpha_s + \Big(\hat{r}_2 + \hat{r}_1 b_0 \ln\left(\mu^2/Q^2\right)\Big)\alpha_s^2 + \Big[\hat{r}_3 + 2\hat{r}_2 b_0 \ln\left(\mu^2/Q^2\right) + \hat{r}_1\Big(b_1 \ln\left(\mu^2/Q^2\right) + b_0^2 \ln^2\left(\mu^2/Q^2\right)\Big)\Big]\alpha_s^3 \quad . \tag{2.28}$$

where $\hat{r}_i$ denote the coefficients evaluated from the Feynman diagrams in i – th order perturbation theory. The logarithmic terms appearing at higher orders in the perturbative expansion are determined in terms of lower order coefficients $\hat{r}_i$. It can be shown, that RGE invariance requires the presence of such logarithmic terms at all orders perturbation theory (see for example [24]), i.e.

$$r_i(\mu^2/Q^2) = \hat{r}_i \left[b_0 \ln\left(\frac{\mu^2}{Q^2}\right)\right]^i + \ldots \quad . \tag{2.29}$$

Thus, even for low order calculations like $\mathcal{O}(\alpha_s^2)$, an infinite subset of contributions from all orders perturbation theory is already known and the form of the higher order corrections is highly constrained. Obviously, the choice of the arbitrary renormalization scale μ is of major importance for the convergence behaviour of the perturbative expression. Since any value $\mu^2 > \Lambda^2$ is principally allowed, the size of the higher order contributions depend crucially on an appropriate choice. Within the $\overline{\rm MS}$ – scheme for example, the choice $\mu^2 = Q^2$ yields for many observables quite large second order contributions, which may be of the same size or even larger than the first order contribution. Clearly, such large higher order terms can hardly be interpreted as a 'perturbation' of the lower order expressions.

An often heard argument for the choice $\mu^2 = Q^2$ (see for example [24]), the so-called 'physical scale' originates from the expansion of the higher order logarithmic terms according to Eq. 2.29. For $\mu^2 = Q^2$ these logarithms are resummed automatically, e.g.

$$
\begin{aligned}
R &= \hat{r}_1 \alpha_s \left[1 + \alpha_s b_0 \ln\left(\mu^2/Q^2\right) + \left(\alpha_s b_0 \ln\left(\mu^2/Q^2\right) \right)^2 + \ldots \right] \\
&= \hat{r}_1 \frac{\alpha_s(\mu^2)}{1 + \alpha_s(\mu^2) b_0 \ln(Q^2/\mu^2)} \\
&= \hat{r}_1 \frac{1}{b_0 \ln\left(\mu^2/\Lambda^2\right) + b_0 \ln(Q^2/\mu^2)} \\
&= \hat{r}_1 \frac{1}{b_0 \ln(Q^2/\Lambda^2)} = \hat{r}_1 \alpha_s(Q^2) \quad . \qquad (2.30)
\end{aligned}
$$

Thereby $\overline{\text{MS}}$ is implicitly assumed to be an appropriate RS and the scheme dependence problem is ignored.

In order to investigate this argument further, it is quite instructive to study the RS dependence problem in more detail. Stevenson [3] has shown, that one can parameterize the RS dependence of the perturbative expansion (2.16) up to $\mathcal{O}(\alpha_s^n)$ by a set of $n-1$ parameters. In NLO the full scheme dependence may be parameterized by the integration constant (2.25) $\tau = b_0 \ln(\mu^2/\Lambda^2)$. Equivalently, one can choose $\Lambda = \Lambda_{RS}$ as a fundamental constant, and parameterize the RS dependence by the renormalization scale parameter μ^2. This connection may easily be understood by comparing Eq. 2.9 with Eq. 2.10. In higher order perturbation theory, additional RS dependence enters through the scheme dependent parameters b_i, $i \geq 1$, of the β – function (2.21). Thus RS = RS$(\mu^2, b_2, \ldots, b^{n-1})$ is a complete parameterization of the scheme dependence problem in $\mathcal{O}(\alpha_s^n)$.

Since μ^2 serves to label the NLO scale dependence, the above argument for the choice $\mu^2_{\text{RS}} = Q^2$ is not of too much relevance. In fact, for any choice $\mu^2 \neq Q^2$ within a specific RS, an alternative scheme $\overline{\text{RS}}$ can be specified, where $\mu^2_{\overline{\text{RS}}} = Q^2$ is satisfied, and the resummation of the logarithmic terms in Eq. 2.30 is again performed automatically. Moreover, the implicit change of the scheme in conjunction with the choice $\mu^2 \neq Q^2$ is completely equivalent with the explicit change to the corresponding scheme with $\mu^2 = Q^2$. Thus, within any RS, i.e. for any choice of the renormalization scale μ^2, the renormalization group predictable logarithms are resummed to all orders. Therefore, the principle of resumming all renormalization group predictable terms does not fix the renormalization scale (i.e. renormalization scheme) problem.

Supposing however, that an optimal RS can be specified and assuming that the resummation of the higher order logarithmic terms within this optimal scheme is performed correctly, the choice of an unsuitable scheme corresponds to a truncation of the optimal resummation series [25]. If for example the effective charge scheme

(ECH) [4] is considered to be such an optimal RS, it can be shown [25], that for typical observables in e^+e^- annihilation the measurement of $\alpha_s(M_z^2)$ within the $\overline{\rm MS}$ – scheme will lead to a sizeable overestimate of the true value of the coupling in combination with a large scatter of the $\alpha_s(M_z^2)$ values measured from different observables [6]. Both features have indeed been observed within this analysis.

2.3 Renormalization scheme optimization

Obviously, the RS dependence of finite order perturbative predictions plays in important role in experimental QCD analysis, which cannot be ignored. Without any assumption about the values allowed for the parameters μ^2 and b_i, $i > 1$, any result for the strong coupling can be obtained. Since QCD theory however gives no principal answer on the choice of these parameters, any choice involves some additional assumptions beyond the scope of fundamental theory. Several proposals have been made for the choice of an 'optimal' RS, and so far no one has been able to command universal support [6]. Within this analysis, several optimization methods have been examined with respect to their applicability for the measurement of the strong coupling from hadronic Z^0 – events. They will be briefly introduced in the following.

2.3.1 The Principle of Minimal Sensitivity (PMS)

In this approach, suggested in Ref. [3], the RS is fixed by demanding that

$$\left.\frac{\partial R^{(N)}}{\partial \mu}\right|_{\mu=\mu^{PMS}} = \left.\frac{\partial R^{(N)}}{\partial b_2}\right|_{b_2=b_2^{PMS}} = \ldots = \left.\frac{\partial R^{(N)}}{\partial b_{N-1}}\right|_{b_{N-1}=b_{N-1}^{PMS}} = 0 \quad , \tag{2.31}$$

i.e. the N – th order approximant $R^{(N)}$ of the expansion (2.16) has locally the property that the full expansion must satisfy globally. At NLO, the PMS criterion (2.31) reduces to the choice of the renormalization scale in such a way, that it is least sensitive with respect to its variation. Note that, contrary to fixed RS approaches, the PMS choice selects an RS which depends on the observable under study. The same is true also for the methods introduced in the following subsections.

2.3.2 The method of Effective Charges (ECH)

By dividing the expansion (2.16) by the RS independent tree level coefficient r_1, Eq. 2.16 may be rewritten without loss of generality as

$$\tilde{R}\left(\alpha_s, Q^2\right) = \alpha_s + \tilde{r}_1\alpha_s^2 + \tilde{r}_2\alpha_s^3 + \ldots \quad . \tag{2.32}$$

where the lowest order approximant is the coupling itself. The basic idea of the ECH approach [4] is, to choose the RS in such a way, that the relation between the physical quantity and the coupling is the simplest possible one:

$$\tilde{R}\left(\alpha_s, Q^2\right) = \alpha_s^{ECH} \quad , \tag{2.33}$$

i.e. all higher order coefficients $\tilde{r}_i$ vanish, and hence $\tilde{R}^{(N)} = \alpha_s^{(N)}$ is called an effective charge. The RS parameters μ and b_i, $i \geq 2$ have to be chosen in such a way, that Eq. 2.33 holds. At NLO, this corresponds to the choice of the renormalization scale in such a way, that the NLO coefficient vanishes. Since all higher order coefficients vanish, this method has also become known as method of fastest apparent convergence (FAC). It might appear, that there is no convergence problem at all applying this method, however the problem reappears with the expansion of the corresponding β – function [11].

It should be noted, that the PMS and the ECH renormalization scheme optimization introduced above are closely related with renormalization scheme invariant quantities derived from the renormalization group equation. For the demonstration of these relations it is convenient to introduce a more compact notification for the renormalization group, as it can be found in many theoretical discussions. Using this notation the perturbative expansion of a generic dimensionless observable reads

$$R\left(Q^2\right) = \alpha\left(1 + r_1\alpha + r_2\alpha^2 + \ldots\right) \tag{2.34}$$

and the β–function, which specifies the strong coupling $\alpha = \alpha_s/\pi$, is written in the following form

$$\frac{d\alpha}{d\tau} = -\beta(\alpha) = -\alpha^2\left(1 + c\alpha + c_2\alpha^2 + \ldots\right) \quad , \tag{2.35}$$

where $\tau = b \ln(\mu/\tilde{\Lambda})$ with μ denoting the renormalization scale and $\tilde{\Lambda}$ the fundamental QCD parameter differing from the traditional definition by a factor $(2c/b)^{-c/b}$ [6]. The renormalization scheme invariant coefficients b and c are linear combinations of the coefficients b_1 and b_2 of Eq. 2.18. τ and the higher order coefficients $c_2, c_3, \ldots$ are used to parameterize the renormalization scheme dependence in NLO and higher orders respectively. By iterating the consistency conditions on the finite order coefficients r_i of expansion (2.34)

$$\frac{dr_N}{d\tau} = \mathcal{O}(\alpha^{N+1}) \quad , \quad \frac{dr_N}{dc_i} = \mathcal{O}(\alpha^{N+1}) \quad , \tag{2.36}$$

the renormalization scheme invariant quantities ρ_i can be identified order by order. In NLO one finds

$$\rho_1 = \tau - r_1(\tau) \tag{2.37}$$

and in NNLO

$$\rho_2 = c_2 + r_2(\tau, c_2) - c r_1(\tau) - r_1^2(\tau) \quad , \tag{2.38}$$

which allows to calculate $r_1(\tau)$ and $r_2(\tau, c_2)$ from any r_1 and r_2 obtained in an initial scheme specified by the parameters τ and c_2. The renormalization scheme invariance of the quantities ρ_i implies that all scheme dependence cancels order by order between the scheme dependent terms on the right hand side of Eq. 2.37 and Eq. 2.38. The first invariant ρ_1 is a function of the scheme invariant combination $\mu/\tilde{\Lambda}$, whereas the higher order invariants $\rho_i, i = 2, 3, \ldots$ are pure numbers. The observable $R(Q)$ depends on a single dimensionful scale Q, which suggests the following identification:

$$\rho_1(Q) = \tau - r_1(\tau) \equiv b \ln \frac{Q}{\overline{\Lambda}} \quad , \tag{2.39}$$

with $\rho_1(Q)$ and $\overline{\Lambda}$ being renormalization scheme invariants and $\overline{\Lambda}$ depending on the particular observable $R(Q)$. According to [6] the quantities $\rho_1(Q)$ and $\overline{\Lambda}$ should have more physical significance than RS dependent quantities such as $\alpha(\tau)$ and $r_1(\tau)$.

The ECH renormalization scheme is fixed by the requirement, that all higher order coefficients r_i vanish, i.e.

$$\tau^{ECH} = \rho_1 \quad , \quad c_2^{ECH} = \rho_2 \tag{2.40}$$

and similarly for still higher orders. Thus the ECH scheme is entirely formulated in terms of the renormalization group invariants ρ_i. It should however be noted, that the ECH approach does not represent a unique solution for defining a scheme in terms of renormalization group invariants. An investigation of the PMS approach shows [6] for example, that in NLO the PMS scheme corresponds with τ being approximately

$$\tau^{ECH} \simeq \rho_1 - c/2 \tag{2.41}$$

which suggests, that in principle any combination of renormalization scheme invariant expressions can be considered for the definition of such a scheme. In section 6.4.6 it will however be shown, that the results obtained by applying the PMS and ECH renormalization schemes are almost identical.

2.3.3 The method of Brodsky, Lepage and MacKenzie (BLM)

This method [5] borrows its basic idea from QED, where the renormalized electric charge is fully given by the vacuum polarization due to charged fermion-antifermion pairs. In QCD, the authors of this method suggest, that all effects of quark-antiquark pairs should be absorbed in the definition of the renormalized coupling itself, leaving no residual dependence in the expansion coefficients. At NLO, this corresponds to a choice of the renormalization scale in such a way, that the n_f dependence vanishes. Since the higher order coefficients $\hat{r}_i$, $i \geq 2$ can be split into a n_f dependent and an n_f independent part, e.g.

$$\hat{r}_1 = \hat{r}_{10} + n_f \hat{r}_{11} \quad , \tag{2.42}$$

the above condition can be satisfied at NLO by a choice of $\mu = \mu^{BLM}$ which compensates for the n_f dependent part of Eq. 2.42. A basic problem of the BLM method is, that the splitting above (2.42) is RS dependent [26]. Contrary to the PMS and ECH method, the BLM scheme prescription is not unique and depends on the initial

scheme, in which the splitting (2.42) is performed. In [27] it has been shown, that this ambiguity is completely equivalent to the original scheme ambiguity for any fixed RS.

2.3.4 Experimentally optimized Renormalization Scheme

The aim of the theoretically motivated RS optimization approaches is, to find a scheme, which minimizes the difference between the exact and RS-independent all order prediction for an observable R (2.16) and their fixed order approximation R^n. Obviously an all order prediction is unknown and might even not exist at all. Therefore, a rigorous proof, that the methods described above serve with the desired qualities, is impossible. Although the concept of renormalization group invariants may turn out to be an important ingredient for obtaining an optimized prediction, the differences in the results obtained from the PMS and ECH prescriptions demonstrate that it does not allow the construction of a uniquely determined series.

Since the RS dependence of perturbative predictions cannot be uniquely fixed by theoretical means, the scheme parameters may be allowed to vary freely in fits to experimental data and their optimal values may be determined by the constraints from the shape of the data distributions. In Chapter 6 will be demonstrated that in NLO this method yields a superior description of the data distributions and perfectly consistent $\alpha_s(M_z^2)$ values from a large set of data distributions. The renormalization scale values obtained will turn out to be strongly correlated with those obtained from the PMS and ECH methods.

The success of this strategy may be understood by considering that additional information about the behavior of higher order contributions is required in order to determine an optimized renormalization scheme. In the ECH approach, the higher order corrections are assumed to be small and set to zero. In the PMS approach the information is utilized, that an all order prediction R does not depend on the choice of the RS. In fits to the experimental data however, the information about the higher order behavior is provided by the data distributions themselves. Provided QCD is the correct theory, the all order prediction for an observable R should be identical (apart from additional non-perturbative contributions) with the experimentally observed value R_{exp}. Thus the experimental data R_{exp} provide the maximum knowledge which can be obtained about the missing all order prediction. Thereby it is required, that R_{exp} is not just a pure number from an inclusive measurement, since one has to determine the coupling itself in combination with $N-1$ scheme parameters. Fortunately, most QCD observables are differential distributions in terms of a kinematical variable. The observables studied within this analysis are even double differential distributions with respect to a kinematical variable and to the event orientation.

All observables studied are known in NLO, where the RS determination is equivalent to the determination of the renormalization scale value μ. Practically, a simultaneous fit of the coupling and the renormalization scale to the data distributions is performed. Therefore, the renormalization scales determined by a fit to the measured data have become known as experimentally optimized renormalization scales. It should however be emphasized, that 'scale' optimization has to be understood in terms of *scheme* optimization, i.e. RS $\equiv$ RS(μ) is supposed. As outlined before, this is indeed true for a fixed order perturbative expansion in NLO, but not however for example for the popular all orders next-to-leading-logarithmic (NLLA) resummation, where a parameterization of the RS dependence is still unknown and cannot be obtained easily (see e.g. [6]).

Chapter 3

Perturbative QCD in Electron-Positron-Annihilation

The e^+e^- annihilation into a quark-antiquark pair at large centre-of-mass energies $\sqrt{s}$, in particular at $\sqrt{s} = M_z$, is an ideal process for studies of perturbative QCD. It provides the most simple initial state for strong interaction studies, where apart from initial and final state photon radiation, the energy of the process is well known. Owing to the Z^0 resonance, the cross section at $Q = M_Z$ is much larger than at any other energy scale within the perturbative region. A very large statistics of several million hadronic events per LEP experiment has been collected in the past, allowing a careful analysis and minimization of experimental uncertainties. Additionally background processes, in particular from initial state radiation, are largely suppressed at the Z^0 resonance. Due to asymptotic freedom, the value of α_s at $Q = M_Z$ is roughly three times smaller than the value at $Q = m_\tau$, which is relevant for the decay of the τ lepton, where the convergence behaviour of the perturbative series is expected to be more relevant [30].

The quarks and gluons produced by strong interaction are however not directly observable. QCD confinement enforces a transition of these colour charged objects into colourless hadrons. The final state hadrons appear as bundles of particles, the so called hadron-jets. At large energies these jets are strongly collimated and the jet directions closely correspond to the directions of the initial partons. The effects of hadronization cannot be described perturbatively. They are expected to decrease proportional $1/Q$ for most of the observables studied in e^+e^- annihilation [29], thus becoming less important with increasing centre-of-mass energies.

Within this chapter, an overview of some theoretical aspects concerning the determination of the strong coupling in e^+e^- annihilation is given. After a brief discussion of the structure of a multihadronic hadronic event in e^+e^- annihilation, a set of

collinear and infrared save event shape observables is introduced which are used for the determination of the strong coupling. Different theoretical approaches to obtain predictions for these observables will be discussed, in particular with respect to the event orientation. Also a brief overview is given about Monte Carlo generators in e^+e^- annihilation. These programs combine perturbative QCD predictions with phenomenological models for the hadronization process in order to simulate the complete annihilation process on an event-by-event basis and are used in order to study the influence of hadronization effects on the perturbative predictions.

3.1 The Hadronic Decay of the Z^0

The structure of a typical multihadronic event in e^+e^- annihilation is shown in Fig. 3.1. The process from the annihilation of the initial electron and positron to the formation of the finally observed hadrons can be divided into four phases.

In the first stage, an electron and a positron annihilate into a quark-antiquark pair by the exchange of a virtual γ or a Z^0 boson. This process is described by the GWS model and can be calculated perturbatively. For precise quantitative studies, it has to be considered, that the electron and or the positron can radiate a photon before annihilation takes place, which reduces the energy available for the subsequent processes. At the Z^0 resonance however, this initial state radiation (ISR) is strongly suppressed.

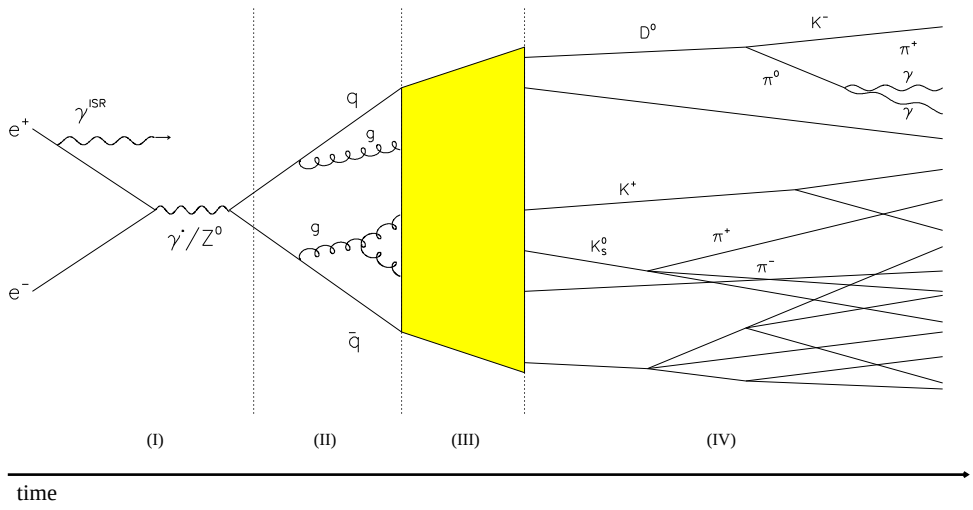

Figure 3.1: A schematic view of the process $e^+e^- \to \gamma^*/Z^0 \to$ hadrons.

The second stage is the phase of strong interaction in combination with large momentum transfers. The primary quarks radiate gluons which themselves can decay into further quarks or gluons, thus producing multi-parton cascades or showers. This phase can be described by perturbative QCD.

With subsequent branching of the partons, the momentum transfer decreases in combination with an increase of the strength of the strong interaction and the transition of quarks and gluons into colourless hadrons takes place. Since this phase cannot be described perturbatively, one has to rely on phenomenological models, which are implemented within so called Monte-Carlo-Generators such as JETSET (string fragmentation) and HERWIG (cluster fragmentation).

During the last phase, the primary hadrons decay into stable particles. It can be adequately described by the particles' lifetimes and branching ratios determined from experimental measurements.

3.2 Event Shape Observables

In order to characterize the structure of the multihadronic final states in e^+e^- annihilation a large number of observables have been developed, which describe the global properties of the final state, like the number of jets or the topology of an event. For a measurement of the strong coupling one has to choose observables, which are both sensitive to α_s and which can be calculated in at least next-to-leading order perturbation theory. For the calculability of observables in perturbation theory at least two conditions have to be satisfied. The observable must be infrared save, i.e. insensitive with respect to the radiation of gluons with infinitesimal momenta. Additionally, the observable must be collinear safe, i.e. they it be insensitive with respect to a splitting of particles into two parallel moving particles with equal momentum (see also Section 3.3).

Due to the RS dependence of perturbative predictions, one is principally faced with an infinite number of a priori valid renormalization schemes in combination with an infinite range of possible α_s values. Hadronization corrections and their uncertainties as well experimental systematic uncertainties are of different size and structure for individual event shape observables. The relevance of an α_s determination can therefore hardly be judged by a single measurement from a single observable. In order to study the reliability of the different approaches for the determination of α_s suggested in literature, a large number of observables with different higher order and hadronization corrections and different experimental systematics should be taken into account. Conclusions may then be drawn from the consistence of the α_s measurements from the different approaches for the different observables.

Within this analysis, eighteen event shape observables have been considered, which represents the most complete list of commonly studied observables for the determination of α_s in e^+e^- annihilation so far. The definition of these observables is presented in the following.

3.2.1 Definition of the Observables

Thrust T is defined by [31] :

$$T = \max_{\vec{n}_T} \frac{\sum_i |\vec{p}_i \cdot \vec{n}_T|}{\sum_i |\vec{p}_i|} \quad , \tag{3.1}$$

where $\vec{p}_i$ is the momentum vector of particle i, and $\vec{n}_T$ is the thrust axis to be determined.

Major M and Minor m are defined similarly, replacing $\vec{n}_T$ in the expression above by the Major axis $\vec{n}_{Maj}$, which maximizes the momentum sum transverse to $\vec{n}_T$ or the Minor axis $\vec{n}_{Min} = \vec{n}_{Maj} \times \vec{n}_T$ respectively.

The oblateness O is then defined by [32]:

$$O = M - m \quad . \tag{3.2}$$

The C-parameter C is derived from the eigenvalues λ of the infrared-safe linear momentum tensor $\Theta^{i,j}$ [33]:

$$\Theta^{i,j} = \frac{1}{\sum_k |\vec{p}_k|} \cdot \sum_k \frac{p_k^i p_k^j}{|\vec{p}_k|} \tag{3.3}$$

$$C = 3 \cdot (\lambda_1\lambda_2 + \lambda_2\lambda_3 + \lambda_3\lambda_1) \quad . \tag{3.4}$$

Here p_k^i denotes the i-component of $\vec{p}_k$.

Events can be divided into two hemispheres, a and b, by a plane perpendicular to the thrust axis $\vec{n}_T$. With M_a and M_b denoting the invariant masses of the two hemispheres, the normalized heavy jet mass ρ_{H}, light jet mass ρ_{L}, the sum of the jet masses ρ_{S} and their difference ρ_{D} can be defined as

$$\rho_H = \frac{\max(M_a^2, M_b^2)}{E_{vis}^2} \tag{3.5}$$

$$\rho_L = \frac{\min(M_a^2, M_b^2)}{E_{vis}^2} \tag{3.6}$$

$$\rho_S = \rho_H + \rho_L \tag{3.7}$$

$$\rho_D = \rho_H - \rho_L \tag{3.8}$$

where

$$E_{vis} = \sum_i E_i \tag{3.9}$$

and the energy of the particles i has been calculated assuming pion mass for charged and zero mass for neutral particles.

Jet broadening measures have been proposed in [34]. In both hemispheres a and b the transverse momenta of the particles are summed thus:

$$B_{a,b} = \frac{\sum_{i \in a,b} |\vec{p}_i \times \vec{n}_T|}{2 \sum_i |\vec{p}_i|} \quad . \tag{3.10}$$

The wide jet broadening $\mathrm{B_{max}}$, the narrow jet broadening $\mathrm{B_{min}}$, and the total jet broadening $\mathrm{B_{sum}}$ are then defined by

$$B_{max} = \max(B_a, B_b) \tag{3.11}$$

$$B_{min} = \min(B_a, B_b) \tag{3.12}$$

$$B_{sum} = B_{max} + B_{min} \quad . \tag{3.13}$$

The first order prediction in perturbative QCD vanishes for both ρ_{L} and $\mathrm{B_{min}}$. Therefore these observables cannot be used for the determination of α_{s} in $\mathcal{O}(\alpha_s^2)$.

Jet rates are commonly obtained using iterative clustering algorithms [35] in which a distance criterion or a metric y_{ij}, such as the scaled invariant mass, is computed for all pairs of particles i and j. The pair with the smallest y_{ij} is combined into a pseudoparticle (cluster) according to one of several recombination schemes. The clustering procedure is repeated until all of the y_{ij} are greater than a given threshold, the jet resolution parameter y_{cut}. The jet multiplicity of the event is defined as the number of clusters remaining; the n-jet rate $R_n(y_{cut})$ is the fraction of events classified as n-jet, and the differential two-jet rate is defined as

$$D_2(y_{cut}) = \frac{R_2(y_{cut}) - R_2(y_{cut} - \Delta y_{cut})}{\Delta y_{cut}} \quad . \tag{3.14}$$

Several algorithms have been proposed differing from each other in their definition of y_{ij} and their recombination procedure. We apply the E0, P, P0, JADE [36], Durham [37], Geneva [35] and the Cambridge algorithms [38]. The definitions of the metrics y_{ij} and the recombination schemes for the different algorithms are given below.

In the E0 algorithm y_{ij} is defined as the square of the scaled invariant mass of the pair of particles i and j:

$$y_{ij} = \frac{(p_i + p_j)^2}{E_{vis}^2} \quad . \tag{3.15}$$

The recombination is defined by:

$$E_k = E_i + E_j \ , \ \vec{p}_k = \frac{E_k}{|\vec{p}_i + \vec{p}_j|}(\vec{p}_i + \vec{p}_j) \quad , \tag{3.16}$$

where E_i and E_j are the energies and $\vec{p}_i$ and $\vec{p}_j$ are the momenta of the particles.

In the P algorithm y_{ij} is defined by Eq. (3.15), and the recombination is defined by

$$\vec{p}_k = \vec{p}_i + \vec{p}_j \ , \ E_k = |\vec{p}_k| \quad . \tag{3.17}$$

The P0 algorithm is defined similarly to the P algorithm, however the total energy E_{vis} (Eq. 3.9) is recalculated at each iteration for the remaining pseudoparticles.

In the JADE algorithm, the definition of y_{ij} is

$$y_{ij} = \frac{2E_iE_j(1-\cos\theta_{ij})}{E_{vis}^2} \quad , \tag{3.18}$$

where θ_{ij} is the angle between the pair of particles i and j.

For the Durham algorithm y_{ij} is given by

$$y_{ij} = \frac{2\min(E_i^2, E_j^2)(1-\cos\theta_{ij})}{E_{vis}^2} \tag{3.19}$$

and for the Geneva algorithm by

$$y_{ij} = \frac{8E_iE_j(1-\cos\theta_{ij})}{9(E_i+E_j)^2} \quad . \tag{3.20}$$

For the algorithms given by Equations (3.18), (3.19) and (3.20) the recombination is done by adding the particles four-momenta.

The Cambridge algorithm [38] introduces an ordering of the particles i and j according to their opening angle, using the ordering variable

$$\nu_{ij} = 2(1-\cos\theta_{ij}) \tag{3.21}$$

and y_{ij} is defined by Eq. (3.19). The algorithm starts clustering from a table of N_{obj} primary objects, which are the particles' four-momenta, and proceeds as follows:

1. If only one object remains, store this as a jet and stop.
2. Select the pair of objects i and j that have the minimal value of the ordering variable ν_{ij} and calculate y_{ij} for that pair.

3. If $y_{ij} < y_{cut}$ then remove the objects i and j from the table and add the combined object with four-momentum $p_i + p_j$. If $y_{ij} \geq y_{cut}$ then store the object i or j with the smaller energy as a separated jet and remove it from the table. The higher energy object remains in the table.

4. go to 1.

The energy-energy correlation EEC [39] is defined in terms of the angle χ_{ij} between two particles i and j in an hadronic event:

$$EEC(\chi) = \frac{1}{N}\frac{1}{\Delta\chi}\sum_{N}\sum_{i,j}\frac{E_i E_j}{E_{vis}^2}\int_{\chi-\frac{\Delta\chi}{2}}^{\chi+\frac{\Delta\chi}{2}}\delta(\chi'-\chi_{ij})d\chi' \quad , \tag{3.22}$$

where N is the total number of events, $\Delta\chi$ is the angular bin width and the angle χ is taken from $\chi = 0°$ to $\chi = 180°$.

The asymmetry of the energy-energy correlation AEEC is defined as

$$AEEC(\chi) = EEC(180° - \chi) - EEC(\chi) \quad . \tag{3.23}$$

The jet cone energy fraction JCEF [40] integrates the energy within a conical shell of an opening angle χ about the thrust axis. It is defined as

$$JCEF(\chi) = \frac{1}{N}\frac{1}{\Delta\chi}\sum_{N}\sum_{i}\frac{E_i}{E_{vis}}\int_{\chi-\frac{\Delta\chi}{2}}^{\chi+\frac{\Delta\chi}{2}}\delta(\chi'-\chi_i)d\chi' \quad , \tag{3.24}$$

where χ_i is the opening angle between a particle and the thrust axis vector $\vec{n}_T$, whose direction is defined here to point from the heavy jet mass hemisphere to the light jet mass hemisphere. Although the JCEF is a particularly simple and excellent observable for the determination of α_s , it has been rarely used until now in experimental measurements. Within an $\mathcal{O}(\alpha_s^2)$ analysis, the region $90° < \chi \leq 180°$, corresponding to the heavy jet mass hemisphere, can be used for the measurement of α_s . Hadronization corrections and detector corrections as well as the next-to-leading order perturbative corrections are small. This allows a specially wide fit range to be used.

3.3 Perturbative QCD Predictions in Next-To-Leading Order

In Born approximation the cross section for the process $e^+e^- \to q\bar{q}$ is given by the GWS model. For an exact calculation of the QCD effects contributing to the process above, all QCD matrix elements up to the desired order perturbation theory have to be considered. Practically, the full perturbative calculation becomes extremely difficult to perform. Today, a complete calculation of the fully differential matrix elements exists only up to $\mathcal{O}(\alpha_s^2)$, which corresponds to a maximum number of four partons in the final state (four quarks or two quarks and two gluons).

Fig. 3.2(a) shows the Feynman diagrams contributing up to $\mathcal{O}(\alpha_s)$. Within this order, up to three partons can appear in the final state. Neglecting quark masses, the differential cross section for the production of three partons is given by [41]

$$\frac{1}{\sigma_0}\frac{d^2\sigma^{(3)}}{dx_1 dx_2} = C_F\bar{\alpha}_s\frac{x_1^2+x_2^2}{(1-x_1)(1-x_2)} \quad , \tag{3.25}$$

where σ_0 is the Born cross section, $\bar{\alpha}_s = \alpha_s/2\pi$, $C_F = 4/3$ is a $SU(3)_C$ factor and

$$x_i = \frac{2E_i}{E_{cm}} \quad i = 1,2,3 \quad . \tag{3.26}$$

E_i are the energies of the three decay particles (i = 1: quark, 2: anti-quark, 3: gluon), E_{cm} is the centre-of-mass energy and from energy conservation it follows that $x_1 + x_2 + x_3 = 2$.

The differential cross section (3.26) diverges for $x_1 \to 1$ or $x_2 \to 1$. There are two distinct kinematical configurations leading to this divergence. The first type of singularity is called *collinear divergence* and appears if the gluon is radiated collinear to the quark or the anti-quark. The second type is called *infrared divergence*, coming from the radiation of a gluon with vanishing energy, i.e. $x_1, x_2 \to 1$, $x_3 \to 0$. Virtual corrections to the production of 2 parton states however contain the same kind of divergence with opposite sign. They cancel with the singularities above in such a way that well defined inclusive quantities, like the the total hadronic cross section, are finite. Also less inclusive observables like the shape distributions introduced in Section 3.2 are finite, provided they are defined collinear and infrared safe (see Section 3.2). Similar infrared and collinear divergences appear also for the matrix elements in higher order perturbation theory. It has been shown that a cancellation of divergent terms from real matrix elements with those from virtual corrections occurs

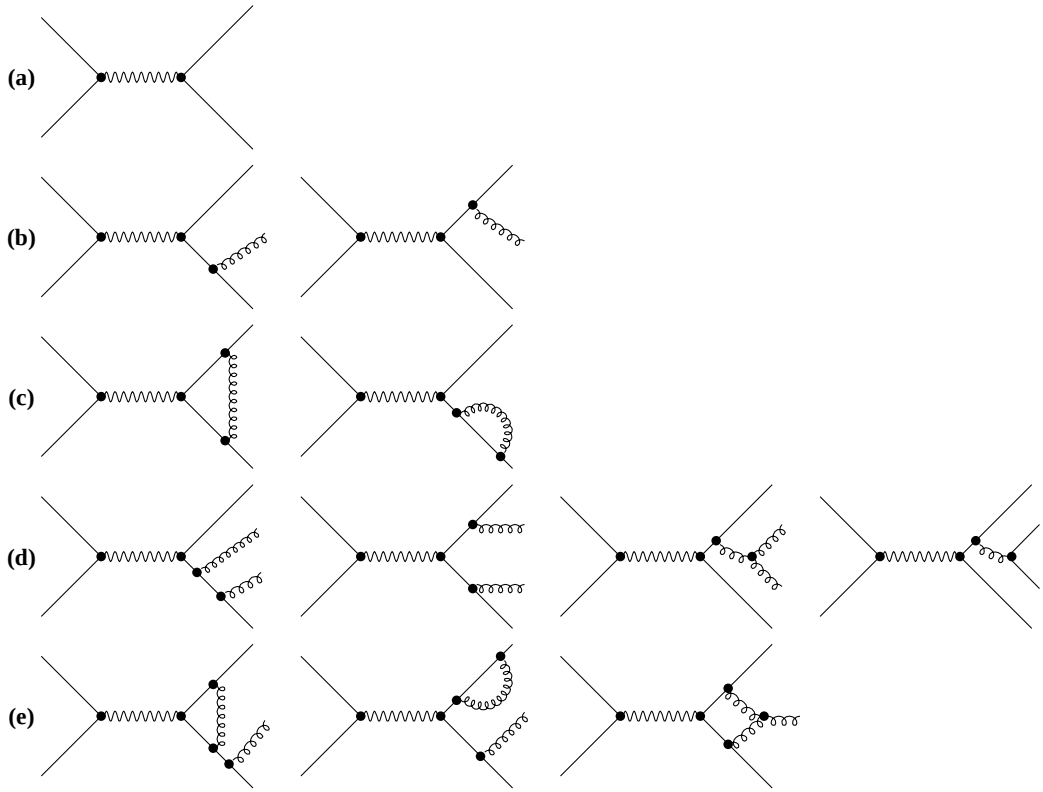

Figure 3.2: Feynman Diagram for the process $e^+e^- \to q\bar{q}$ in Born approximation and some QCD corrections up to $\mathcal{O}(\alpha_s^2)$.
(a) Feynman Diagram for the process $e^+e^- \to q\bar{q}$ in Born approximation.
(b) Feynman diagrams contributing to the 3-jet production in $\mathcal{O}(\alpha_s)$.
(c) Some virtual corrections contributing to the 2-jet production in $\mathcal{O}(\alpha_s)$.
(d) Some diagrams contributing to the the 4-jet production in $\mathcal{O}(\alpha_s^2)$.
(e) Some virtual corrections contributing to the 3-jet production in $\mathcal{O}(\alpha_s^2)$.
(Diagrams not shown are symmetrically.)

in every order α_s [42], which guarantees infrared and collinear safe predictions order by order perturbation theory.

The $\mathcal{O}(\alpha_s^2)$ matrix elements have been calculated by several groups. The calculation of the Leiden group [43] has some advantages over the calculation in [44], which has been considered as standard calculation for many years. In [44], the matrix elements have been summed over permutations of the outgoing partons, which means that quarks and gluons cannot be distinguished in the final state. Also they consider only the decay of a virtual photon, thus they can only predict quantities averaged over orientations of hadronic events, loosing all information on their lab-frame directions and lepton-hadron correlations [45].

The integration of these matrix elements over the phase space is rather complicated and cannot be solved analytically. Several programs for the numerical integration by Monte Carlo techniques have been developed. The most recent one, EVENT2 [46], is based on the so-called *Dipole Formalism* introduced in [47] and implements the matrix elements of the Leiden group.

With EVENT2 , weighted cross sections for any infrared and collinear safe observable Y in e^+e^- annihilation can be calculated within the $\overline{\text{MS}}$ renormalization scheme prescription:

$$\frac{1}{\sigma_0} W(Y) \frac{d\sigma}{dY} = \bar{\alpha}_s \cdot A(Y) + \bar{\alpha}_s^2 \cdot B(Y) \quad , \tag{3.27}$$

where $\bar{\alpha}_s = \alpha_s/2\pi$ and σ_0 is the total cross section in Born approximation. The weight of the cross sections $W(Y)$ will be discussed below. $A(Y)$ denotes the $\mathcal{O}(\alpha_s)$ QCD coefficient and $B(Y)$ the $\mathcal{O}(\alpha_s^2)$ QCD coefficient within the $\overline{\text{MS}}$ scheme, which can be decomposed into three parts proportional to different $SU(3)_C$ factors:

$$B(Y) = C_F \cdot \Big(C_F \cdot B_{C_F}(Y) + C_A \cdot B_{C_A}(Y) + T_R \cdot B_{T_R}(Y) \Big) \tag{3.28}$$

with the $SU(3)_C$ factors $C_F = 4/3$, $C_A = 3$ and the n_f dependent factor $T_R = n_f T_F$ with $T_F = 1/2$. The consideration of the n_f dependence of the coefficients $B(Y)$ becomes important for the optimization of the renormalization scale according to the BLM approach.

Although the integration over the phase space yields in principle infrared finite results, some care has to be taken with respect to the numerical stability of the Monte Carlo integration and the number of calculations required for numerical convergence. It is for example important to introduce a weight $W(Y)$ to damp the sharp rise of the cross sections at the phase space boundaries. The weights appropriate for the observables studied within this analysis are

$$W(Y) = \begin{cases} \sin^2(\chi/2) & \text{for EEC, AEEC and JCEF,} \\ Y & \text{otherwise.} \end{cases} \tag{3.29}$$

Since the cancellation of the collinear and infrared divergences occurs only for the coherent sum of real and virtual partonic configurations, i.e. by taking the difference between two very large contributions, the exact treatment of the infrared region would require an infinite numerical accuracy. Thus, an infrared cut-off on the phase

space has to be applied. If any pair of partons i, j has an invariant mass $m_{ij}^2 < Q_{\text{cutoff}}^2$, the whole configuration is thrown away. The number of iterations needed for numerical convergence of the integration depends crucially on the accuracy of the integration i.e. on the choice of Q_{cutoff}^2. For the cross sections calculated within this analysis the integration has been performed in quadruple precision with $Q_{\text{cutoff}}^2 = 10^{-13}$.

Figure 3.3 shows the A and B coefficients for the Thrust distribution together with the contributions B_{C_F}, B_{C_A} and B_{T_F} to the second order coefficient according to Eq. 3.28. Whereas the LO coefficients are positive definite, one can observe, that the NLO coefficients for the Thrust distribution take largely negative values in the extreme two-jet region $(1 - T) \to 0$. Figure 3.4 shows the same for the Oblateness distribution. Here, the next-to-leading order coefficients are negative for almost the whole kinematical range.

In order to compare the theoretical predictions with experimentally measured quantities, one has to consider also QCD corrections to the total hadronic cross section up to the desired order

$$\frac{\sigma_0}{\sigma_{tot}} = 1 + 2 \cdot \bar{\alpha}_s(\mu^2) + K \cdot \bar{\alpha}_s^2(\mu^2) + \cdots \tag{3.30}$$

with the $\mathcal{O}(\alpha_s^2)$ coefficient given in the $\overline{\text{MS}}$ scheme [48]:

$$K = \frac{365}{6} - \frac{11}{3} n_f - 8\beta_0 \zeta(3) \tag{3.31}$$

with $\beta_0 = (33 - 2n_f)/6$ and $\zeta(3) = \sum_{n=1}^{\infty}(1/n^3) = 1.2021\ldots$.

Considering also the scale dependence of the theoretical predictions, the weighted cross section for an infrared and collinear safe observable Y in $\mathcal{O}(\alpha_s^2)$ can finally be written as

$$\frac{1}{\sigma_{tot}} W(Y) \frac{d\sigma}{dY} = \bar{\alpha}_s(\mu^2) \cdot A(Y) + \bar{\alpha}_s^2(\mu^2) \cdot \left[B(Y) + \Big(2\pi b_0 \ln(x_\mu) - 2 \Big) A(y) \right] \tag{3.32}$$

with the renormalization scale parameter $x_\mu = \mu^2 / E_{CM}^2$. The ordinary cross section can be obtained by dividing prediction (3.32) by the mean weight $\langle W(Y) \rangle$ in each Y bin.

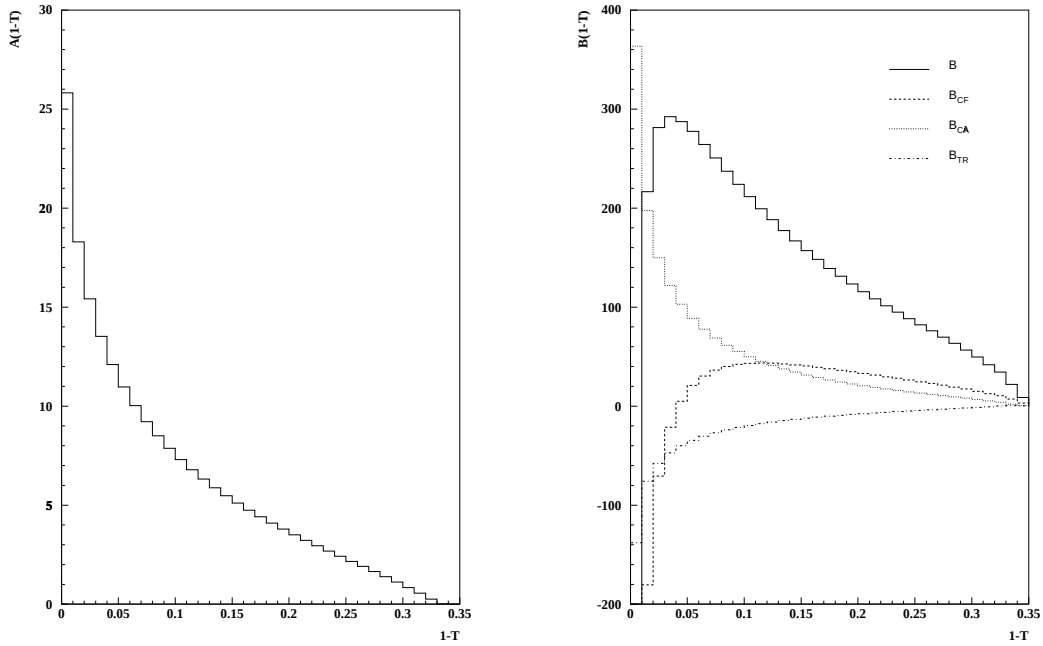

Figure 3.3: QCD coefficients for the Thrust distribution $(1-T)$. (*left side*) A coefficients proportional to $\mathcal{O}(\alpha_s)$. (*right side*) B coefficients proportional to $\mathcal{O}(\alpha_s^2)$ and the contributions B_{C_F}, B_{C_A} and B_{T_R} according to Eq. 3.28.

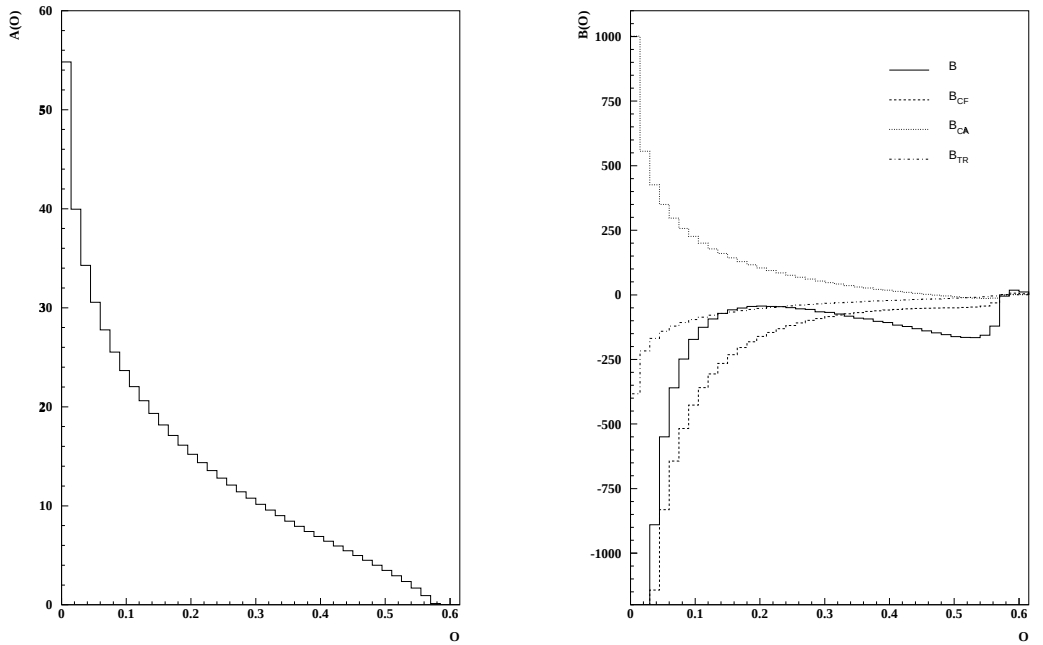

Figure 3.4: The same as Fig. 3.3 but for the Oblateness distribution (O).

3.3.1 QCD dependence on the Event Orientation

Additional information on the strong coupling is given by the angular dependence of hadronic events. It can be exploited by using the matrix element calculations of the Leiden group [43].

At the Born level, the Z^0 with spin 1 will decay into a quark and an antiquark with spin 1/2, with an angular distribution proportional to $1 + \cos^2\vartheta$ and an additional parity violating term proportional to $\cos\vartheta$, where ϑ is the angle between the quark and the e^- beam. The angular distribution is however modified due to gluon radiation. Instead of the primary quark direction, which is not directly observable, the event orientation is usually specified by the polar angle ϑ_T of the thrust axis with respect to the e^+e^- beam direction. The general form of the angular distribution can be expressed as

$$\frac{d\sigma}{d\cos\vartheta_T} = \frac{3}{8}\left(1 + \cos^2\vartheta_T\right) \cdot \sigma_T + \frac{3}{4} sin^2\vartheta_T \cdot \sigma_L \tag{3.33}$$

where the parity violating term is absent, which reflects that the sense of the thrust axis is arbitrary. The terms σ_L and σ_T are called longitudinal and transverse cross section respectively, with the total cross section given by $\sigma_{tot} = \sigma_L + \sigma_T$. The terminology originates from the circumstance, that a longitudinally polarized Z^0, i.e. having spin component zero along the e^+e^- direction, would yield a $\sin^2\vartheta_T$ dependence in its decay into fermions, though however this component of the angular distribution is entirely generated by final state QCD effects. At $\mathcal{O}(\alpha_s^2)$, the longitudinal cross section is given by [49]

$$\frac{\sigma_L}{\sigma_0} = -2\left(8\ln\frac{2}{3} + 3\right)C_F\frac{\alpha_s}{2\pi}\left(1 + l\frac{\alpha_s}{2\pi}\right) \quad , \tag{3.34}$$

where the $\mathcal{O}(\alpha_s^2)$ coefficient l can be obtained by numerical integration of the Leiden Group matrix elements. The QCD prediction for the longitudinal cross section can be used to determine $\alpha_s(M_z^2)$. This analysis has been done by ALEPH [50] with the result $\alpha_s(M_Z^2) = 0.121 \pm 0.022(stat.) \pm 0.011(sys)$. The relatively large statistical error stems from the fact that the overall effect of gluon radiation on the $\cos\vartheta$ distribution is small. The effect is however enhanced in the region of hard gluon radiation, thus one can combine the information from the α_s dependence of the angular distribution with the information of event shape observables sensitive to the kinematics of an event in order to enhance the sensitivity to the strong coupling for the combined prediction, which has been done in the present analysis.

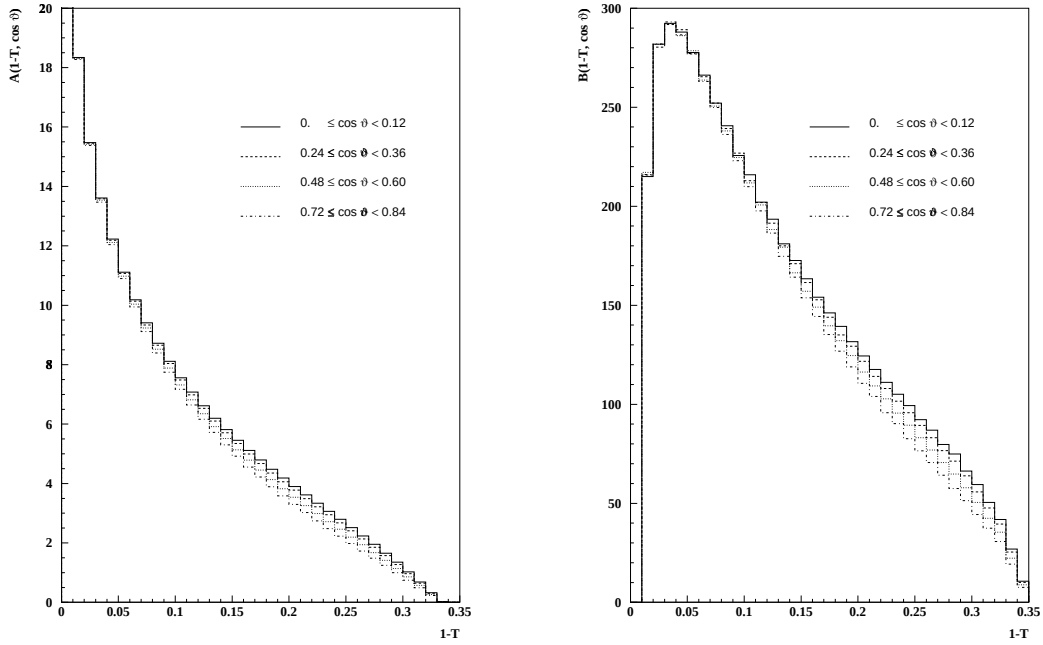

Figure 3.5: Angular dependent QCD coefficients for the Thrust distribution $1 - T$, in four different intervals of $\cos \vartheta_T$.

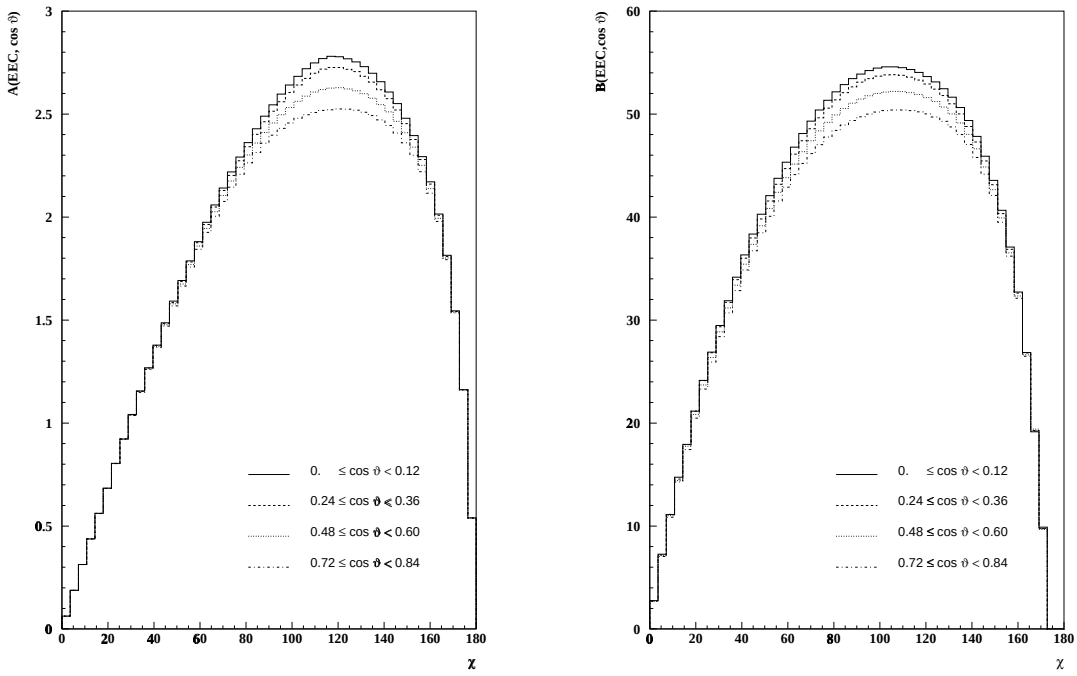

Figure 3.6: The same as Figure 3.5 but for the Energy Energy Correlation EEC.

Within this study, the α_s dependence of the combined information of the collinear and infrared save event shape observables introduced in the previous section and of the angular dependence has been parameterized in the following way:

$$\left(\frac{d\sigma_0}{d\cos\vartheta_T}\right)^{-1} W(Y)\frac{d^2\sigma(Y,\cos\vartheta_T)}{dY d\vartheta_T} = \bar{\alpha}_s \cdot A(Y,\vartheta_T) + \bar{\alpha}_s^2 \cdot B(Y,\vartheta_T) \quad . \tag{3.35}$$

The double differential cross section (3.35) has been normalized to the $\cos\vartheta_T$ dependence of the Born cross section $d\sigma_0/d\cos\vartheta_T$. Both, A and B coefficients depend on the event orientation. Numerical calculations have been done for eight equidistant intervals of $\cos\vartheta_T$ between 0.0 and 0.96. Figure 3.5 shows the angular dependence of the $\mathcal{O}(\alpha_s)$ and $\mathcal{O}(\alpha_s^2)$ coefficients for the Thrust distribution. Figure 3.6 shows the same for the distribution of the Energy Energy Correlation EEC.

For the comparison with measured cross sections, the unweighted form of expression 3.35 has to considered and the Born cross section has to be corrected for QCD effects according to Eq. 3.30, thus yielding an expression of the following form:

$$R(Y,\vartheta_T) = \left(\frac{d\sigma_{tot}}{d\cos\vartheta_T}\right)^{-1} \frac{d^2\sigma(Y,\cos\vartheta_T)}{dY d\vartheta_T} \tag{3.36}$$

where σ_{tot} corresponds to the one-loop corrected cross section for an α_s determination in $\mathcal{O}(\alpha_s^2)$ and the two-loop corrected cross section for the estimated $\mathcal{O}(\alpha_s^3)$ predictions by the means of Padé approximants.

3.4 Predictions in Next-To-Leading Logarithmic Approximation

An alternative theoretical prediction can be applied for a limited number of so-called exponentiating [51] observables. Here, the leading and next-to-leading logarithmic terms of the perturbative expansion can be resummed to all orders perturbation theory. These expressions can be applied in a limited kinematical region close to the infrared limit (the *semi-inclusive* region) where these contributions dominate the theoretical predictions.

Within the framework of next-to-leading logarithmic approximation (NLLA), theoretical predictions are calculated for the cumulative cross-sections defined by:

$$R(Y,\alpha_s) = \frac{1}{\sigma}\int_0^Y \frac{d\sigma}{dY'}dY' \quad . \tag{3.37}$$

They can be expanded in the form

$$R(Y,\alpha_s) = C(\alpha_s)\exp\Sigma(\alpha_s,L) + F(\alpha_s,Y) \ , \tag{3.38}$$

where $L \equiv \ln(1/Y)$ and

$$C(\alpha_s) = 1 + \sum_{i=1}^{\infty} C_i \bar{\alpha}_s^i \tag{3.39}$$

$$\Sigma(\alpha_s,L) = \sum_{i=1}^{\infty} \bar{\alpha}_s^i \sum_{j=1}^{i+1} G_{ij} L^j \tag{3.40}$$

$$F(\alpha_s,Y) = \sum_{i=1}^{\infty} F_i(Y)\bar{\alpha}_s^i \ . \tag{3.41}$$

The constants C_i and the functions $F_i(Y)$ can be calculated perturbatively by comparing the NLLA predictions for $\exp\Sigma(\alpha_s,L)$ order by order with the corresponding fixed order expression.

Eq. 3.40 can be written in the form:

$$\Sigma(\alpha_s,L) = Lf_{LL}(\alpha_s L) + f_{NLL}(\alpha_s L) + \text{subleading terms} \tag{3.42}$$

where

$$Lf_{LL}(\alpha_s L) = \sum_{i=1}^{\infty} \bar{\alpha}_s^i G_{i,i+1} L^{i+1} \tag{3.43}$$

represent the leading and

$$f_{NLL}(\alpha_s L) = \sum_{i=1}^{\infty} \bar{\alpha}_s^i G_{i,i} L^i \tag{3.44}$$

the next-to-leading logarithms. They have been calculated for a number of observables, including $1-T$ [52], C [53], B_{max} [54], B_{sum}[54], ρ_H [55] and D_2^{Durham} [56], where the NLLA predictions for B_{max} and B_{sum} entering into this analysis are the recently improved calculations by Yu. L. Dokshitzer et al. [57].

The $F_i(Y)$ vanish in the infrared limit $Y \to 0$ and are neglected within *pure* NLLA predictions:

$$R_{NLLA}(Y, \alpha_s) = \left(1 + C_1 \bar{\alpha}_s + C_2 \bar{\alpha}_s^2\right) \exp\Big[L f_{LL}(\alpha_s L) + f_{NLL}(\alpha_s L)\Big] \quad . \tag{3.45}$$

All calculations above have been done within the $\overline{\text{MS}}$ – scheme at the renormalization scale $Q^2 \equiv s$. Whereas the expression for the leading logarithms f_{LL} is renormalization scheme invariant, the expressions for the non leading terms are scheme dependent. The renormalization scale dependence of f_{NLL} is given by:

$$f_{NLL}(\alpha_s L, \mu^2) = f_{NLL}(\alpha_s L, Q^2) + b_0 (\alpha_s L)^2 f'_{LL}(\alpha_s L) \ln(x_\mu) \quad , \tag{3.46}$$

where f'_{LL} is the derivative of f_{LL}. Unlike the $\mathcal{O}(\alpha_s^2)$ case, where x_μ parameterizes the complete renormalization scheme dependence, such a parameterization is not known for the predictions in NLLA.

3.4.1 Combining NLLA with fixed order predictions

Pure NLLA calculations can be used to measure $\alpha_s(M_z^2)$ in a limited kinematic region close to the infrared limit, where L becomes large. In order to achieve a prediction where the kinematical range can be extended towards the 3 jet region, several procedures have been suggested [58] to match the NLLA calculations with the calculations in $\mathcal{O}(\alpha_s^2)$.

The $\mathcal{O}(\alpha_s^2)$ QCD formula can be written in the integrated form:

$$R_{\mathcal{O}(\alpha_s^2)}(Y, \alpha_s) = 1 + \mathcal{A}(Y) \bar{\alpha}_s + \mathcal{B}(Y) \bar{\alpha}_s^2 \ , \tag{3.47}$$

where $\mathcal{A}\ (Y)$ and $\mathcal{B}\ (Y)$ are the cumulative forms of the fixed order coefficients $A(Y, \cos\vartheta_T)$ and $B(Y, \cos\vartheta_T)$, integrated over ϑ_T. Together with the first and second order terms of the NLLA prediction:

$$g_1(L) = G_{12}L^2 + G_{11}L \quad , \tag{3.48}$$

$$g_2(L) = G_{23}L^3 + G_{22}L^2 \tag{3.49}$$

the $\ln R$ matching scheme can be defined as:

$$\ln R(Y, \alpha_s) = Lf_{LL}(\alpha_s L) + f_{NLL}(\alpha_s L) + H_1(Y)\bar{\alpha}_s + H_2(Y)\bar{\alpha}_s^2 \tag{3.50}$$

with

$$H_1(Y) = \mathcal{A}(Y) - g_1(L) \quad , \tag{3.51}$$

$$H_2(Y) = \mathcal{B}(Y) - \frac{1}{2}\mathcal{A}^2(Y) - g_2(L) \quad . \tag{3.52}$$

Within the $\ln R$ matching scheme, all logarithmic and non-logarithmic terms are exponentiated. Several other matching schemes can be defined which differ only in the treatment of the subleading terms, thus introducing a principal ambiguity in the matching procedure. Within the R matching scheme, only the leading and next-to-leading logarithmic terms are exponentiated:

$$\begin{aligned} R(Y, \alpha_s) \;\; = \;\; & \left(1 + C_1\bar{\alpha}_s + C_2\bar{\alpha}_s^2\right) \exp\Big[Lf_{LL}(\alpha_s L) + f_{NLL}(\alpha_s L)\Big] \\ & + F_1(Y)\bar{\alpha}_s + F_2(Y)\bar{\alpha}_s^2 \end{aligned} \tag{3.53}$$

with

$$F_1(Y) = \mathcal{A}(Y) - g_1(L) - C_1 \quad , \tag{3.54}$$

$$F_1(Y) = \mathcal{B}(Y) - \frac{1}{2}g_1^2(L) - g_2(L) - C_1 g_1(L) - C_2 \quad . \tag{3.55}$$

Within the $R-G_{21}$ matching scheme, additionally the analytically known subleading logarithm G_{21} proportional to $\mathcal{O}(\alpha_s^2)$ is exponentiated:

$$\begin{aligned} R(Y,\alpha_s) &= \left(1+C_1\bar{\alpha}_s+C_2\bar{\alpha}_s^2\right)\exp\left[Lf_{LL}(\alpha_s L)+f_{NLL}(\alpha_s L)+G_{21}L\bar{\alpha}_s^2\right] \\ &\quad +F_1(Y)\bar{\alpha}_s+F_2(Y)\bar{\alpha}_s^2-G_{21}L\bar{\alpha}_s^2 \quad . \end{aligned} \tag{3.56}$$

When combining $\mathcal{O}(\alpha_s^2)$ predictions with NLLA calculations one has to take into account that the resummed terms do not vanish at the upper kinematic limit Y_{max} of the event shape distributions. In order to correct for this, the resummed logarithms are redefined [59] by:

$$L = \ln(1/Y - 1/Y_{max} + 1). \tag{3.57}$$

The $\ln R$ matching scheme has become the preferred one, because it includes the C_2 and the G_{21} coefficients implicitly and uses only those NLLA terms which are known analytically. It yields the best description of the data in terms of χ^2/n_{df} in most cases [9]. Therefore, it has been chosen as the standard matching procedure within this analysis and the R and $R-G_{21}$ matching schemes have been used for the estimation of the uncertainty due to the matching ambiguity.

3.5 From Quarks to Hadrons

The formation of quarks and gluons, i.e. the hard process, can be understood within the framework of perturbative QCD. The transition into the final state hadrons observed in experiment however occurs at small momentum scales, where the perturbative predictions are no longer valid. In order to account for these *hadronization effects*, phenomenological models have to be employed. These models are in general implemented within Monte Carlo Generators, which simulate the complete process $e^+e^- \rightarrow$ *hadrons* according to the four phases shown in Fig. 3.1 on an event-by-event basis. For each event simulated, the complete kinematical information is available for the final state hadrons as well as for the initial quarks and gluons, thus allowing to evaluate the hadronization corrections for any collinear and infrared safe shape observable.

3.5.1 Simulation of the Perturbative Phase

Historically the first approach for the simulation of the initial parton state was based on the $\mathcal{O}(\alpha_s^2)$ matrix element calculations and is implemented for example as 'matrix element' option within the JETSET Monte Carlo generator [60]. This matrix element approach works reasonably well but yields a poor description of the data in comparison with models based on the *parton shower* approach [61].

A fundamental problem of the matrix element approach has been found in [62] and arises due to the renormalization scale dependence of the $\mathcal{O}(\alpha_s^2)$ predictions. Since the second order QCD coefficients can be negative over a large kinematical range (see for example Figures 3.3 and 3.4) also the corresponding differential cross sections can be negative for certain choices of the renormalization scale. This suggests, that a the three-jet cross section may be negative over a large fraction of the phase space. For small renormalization scale values of $x_\mu \approx 0.002$ which are required in order to describe the measured data [61], the fraction with negative three-jet cross section covers about 15 % of the phase space [62]. The Monte Carlo prediction however is unreliable if the three-jet cross section is negative, because it is interpreted as probability for the event generation. Within the JETSET matrix element Monte Carlo, the contribution from the region with negative cross section is ignored. The contribution from the region with positive cross section is then rescaled by a constant factor in order to conserve the overall three-jet rate.

Today, the simulation of the perturbative phase within event generators is most commonly based on the parton shower approach. It is derived within the framework of the renormalization scheme invariant leading logarithmic approximation LLA. There are several Monte Carlo Generators with different implementations of the basic approach. The algorithms are based on the iterative use of the basic branchings $q \to qg$, $g \to q\bar{q}$ and $g \to gg$. The Altarelli-Parisi equations [63]:

$$\frac{\mathcal{P}_{a\to bc}}{dt} = \int dz \frac{\alpha_s(\mu^2)}{2\pi} P_{a\to bc}(z) \tag{3.58}$$

give the probability $\mathcal{P}$ of the branching $a \to bc$ during a change dt of the evolution parameter $t = \ln(Q^2_{evol}/\Lambda^2)$. The $P_{a\to bc}(z)$ are the Altarelli-Parisi splitting kernels given by

$$P_{q\to qg}(z) = C_F \frac{1+z^2}{1-z} \quad , \tag{3.59}$$

$$P_{g\to gg}(z) = N_C \frac{(1-z(1-z))^2}{z(1-z)} \quad , \tag{3.60}$$

$$P_{g\to q\bar{q}}(z) = T_R(z^2 + (1-z)^2) \tag{3.61}$$

where z and $1-z$ are the four-momenta fractions assigned to the daughter particles b and c respectively.

Within the JETSET parton shower (PS) generator the first branch of a quark into a quark and a gluon is done according to the leading order matrix element prediction. All subsequent branches are done according to the partonshower approach (Eq. 3.58). Interference effects between the radiated gluons are taken into account via angular ordering. This means that the angle between the radiated partons must decrease with every subsequent branch. The strong coupling α_s applied for the shower development corresponds to the leading order solution (Eq. 2.26) where the QCD scale is chosen to be proportional to the transverse momentum of the branching parton, i.e. $\mu^2 = p_\perp^2$. The evolution scale Q^2_{evol} corresponds to be the effective mass or the virtuality of the branching parton a, i.e. $Q^2_{evol} = m_a^2 = E_a^2 - p_a^2$. The virtuality is decreasing in subsequent branches down to a cutoff scale Q_0^2 of $\mathcal{O}(1GeV)$, where the parton shower is terminated.

The HERWIG parton shower [64] is quite similar to the Jetset parton shower. The HERWIG choice of the evolution scale $Q^2_{evol} \simeq m_a^2/(2z(1-z))$ guarantees angular ordering automatically, whereas the angular ordering in JETSET is achieved by additional kinematical constrains. The main difference between the HERWIG and the JETSET Monte Carlo generator is the treatment of the non-perturbative phase, which is described below.

The successive splitting into quarks and gluons within the ARIADNE Monte Carlo generator [65] is based on the colour dipole model, which is somewhat different from the commonly used parton shower approach. Here the gluon emission is treated as a radiation from a colour dipole spanning between pairs of partons. As in HERWIG and JETSET , the QCD scale is taken to be the transverse momentum of the radiating partons and the choice of the evolution scale $Q^2_{evol} = p_\perp^2$ guarantees angular ordering by a decrease of the transverse momentum for subsequent branches. The shower development is stopped when the transverse momenta are below a given cut-off value.

3.5.2 Hadronization Models

The simulation of the non-perturbative phase, i.e. the transition from the initial quarks and gluons to the observed final state hadrons is based on QCD inspired, phenomenological models. The most successful of these models is the Lund *string fragmentation model* [66], which is applied within the Monte Carlo Generators JETSET and ARIADNE . Within this model, a colour string, i.e. a colour flux tube is stretched between between quarks and antiquarks via the gluon colour charges. The string has a linearly rising potential $V(r) = \kappa r$ with a *string tension* $\kappa \simeq 1\text{GeV}$, wich is supported by lattice calculations and provides a natural explanation for QCD confinement. With increasing distance between the quark anti-quark pair, the energy contained within the string allows the production of a new quark anti-quark pair by breaking the string into two independent pieces. The breakup mechanism is interpreted as a tunneling phenomenon according to the probability

$$\exp\left(\frac{(-m_q^2 - p_\perp^2)\pi}{\kappa}\right) \quad . \tag{3.62}$$

The consideration of quark masses m_q leads to a suppression of heavy quark pair production, which is a consequence of the larger tunneling distance required for picking up enough string energy in order to materialize heavy quarks. Baryon production takes place due to the direct production of di-quark anti-di-quark pairs analogously to quark anti-quark pairs. The iterative production mechanism continues until all remaining hadrons are *on-shell*, i.e. that their virtuality vanishes.

An alternative model for the hadronization phase is the *cluster model* [67]. It is implemented within the HERWIG Monte Carlo generator. Here the gluons at the end of the perturbative phase are split into quark anti-quark pairs. Colour-neutral pairs of quarks nearby in phase space are then recombined into massive clusters. Hadronization takes place mainly by isotropic two body decays of the individual clusters.

Chapter 4

The DELPHI Experiment

The DELPHI experiment is one of the four large high energy physics experiments, which are operating at the Large Electron Positron Collider LEP at the European Laboratory for Particle Physics CERN in Geneva, Switzerland. The experiment is operated by a collaboration of about 600 physicists from 56 institutes worldwide. During the first operation period (LEP 1) from 1989 to 1995, e^+e^- annihilation has been studied at centre-of-mass energies around the Z^0 resonance. Several million of hadronic Z^0 decays have been recorded, allowing extensive tests of the standard model and a high precision determination of its parameters.

Within this chapter an overview is given of the LEP collider, the DELPHI detector and its components and of the data analysis software. Detailed information about the detector and its performance can be found in [68, 69].

4.1 The LEP collider

With a circumference of 26.7 km the LEP collider is the worlds largest particle accelerator to date. The accelerator ring is situated about 100 m below ground at the French-Swiss border near Geneva, Switzerland (see Fig. 4.1). It has the shape of an octagon with rounded corners, i.e. eight straight sections and eight arcs alternating around the circumference. There are altogether eight interaction regions at the center of the straight sections, four of them equipped with sophisticated general purpose detectors (ALEPH [70], DELPHI [68], L3 [71] and OPAL [72]) for the study of the complete spectrum of e^+e^- annihilation physics at LEP.

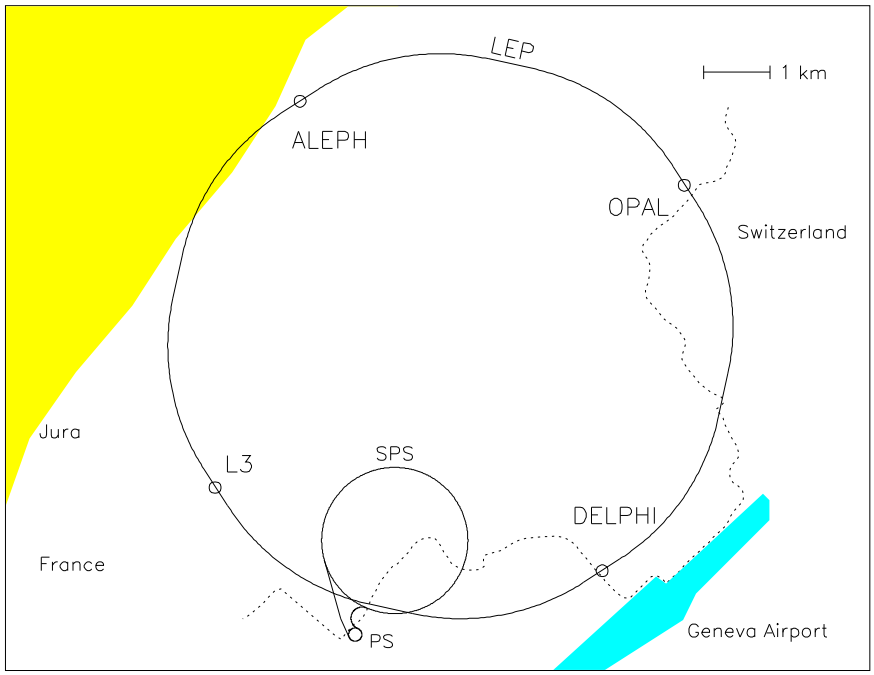

Figure 4.1: Map of the area around the LEP collider.

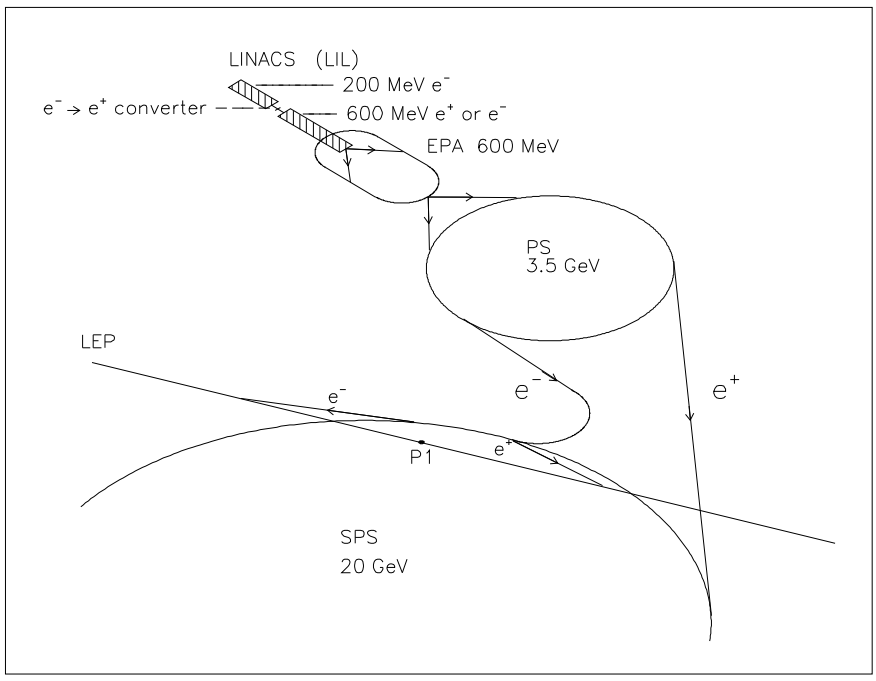

Figure 4.2: Schematic Map of the LEP injection system, including the two stage LEP Injector Linacs (LIL), the Electron Positron Accumulator (EPA), the Proton Synchrotron (PS) and the Super Proton Synchrotron (SPS).

Two beams consisting of bunches of electrons and positrons, respectively, circulate in opposite directions within one beam pipe, which is kept at ultra high vacuum with a residual pressure of about 10^{-12} bar. The electrons and positrons are injected into the LEP collider with an energy of about 20 GeV after being accelerated by a series of other accelerators as illustrated in Fig. 4.2.

The LEP ring accelerates the beams from 20 GeV to the desired energy between about 45 GeV and 100 GeV. This acceleration is done by the means of radio frequency (RF) cavities which are installed in the straight sections of the LEP tunnel. The electrons and positrons are maintained on a circular orbit by dipole magnets installed in the curved sections of the tunnel. The particle beams are focussed by the means of quadrupole and sextupole magnets, which are located close to the interaction points, where the electron and positron bunches are made to collide. A detailed description of the LEP collider can be found in the design reports [73].

4.2 The DELPHI Detector

The DELPHI detector (DEtector with Lepton, Photon and Hadron Identification) is one of the four big particle detectors installed at the LEP collider. It covers as much as possible of the solid angle around the interaction point and is forward backward and azimutally symmetric, reflecting that the outgoing particles are essentially symetrically emitted in the laboratory frame. It is designed with special emphasis on particle identification and on precise vertex determination. Most of the detector components provide three-dimensional information of high granularity.

The DELPHI detector consists of a cylindrical section, the so-called barrel, and two end-caps. The detector is about 10 m long and 9 m in diameter and its weight is about 3500 tons. Fig. 4.3 shows the layout of the barrel region and of one endcap. Cartesian as well as cylindric coordinate systems are applied for the description of the detector elements. Their origin is at the nominal interaction point. The z axis is defined along the direction of the electron beam, the x axis pointing towards the center of LEP and the y axis pointing vertically upwards. The polar angle θ is defined with respect to the z axis and the azimuthal angle ϕ and the radius r are defined in the xy plane.

The various sub-detectors of DELPHI can be divided into several groups. The first group consist of tracking detectors, which are used to measure the positions and trajectories of charged particles by the means of the ionisation produced in a medium by their passage. The presence of a magnetic field allows the determination of their momenta and electric charges.

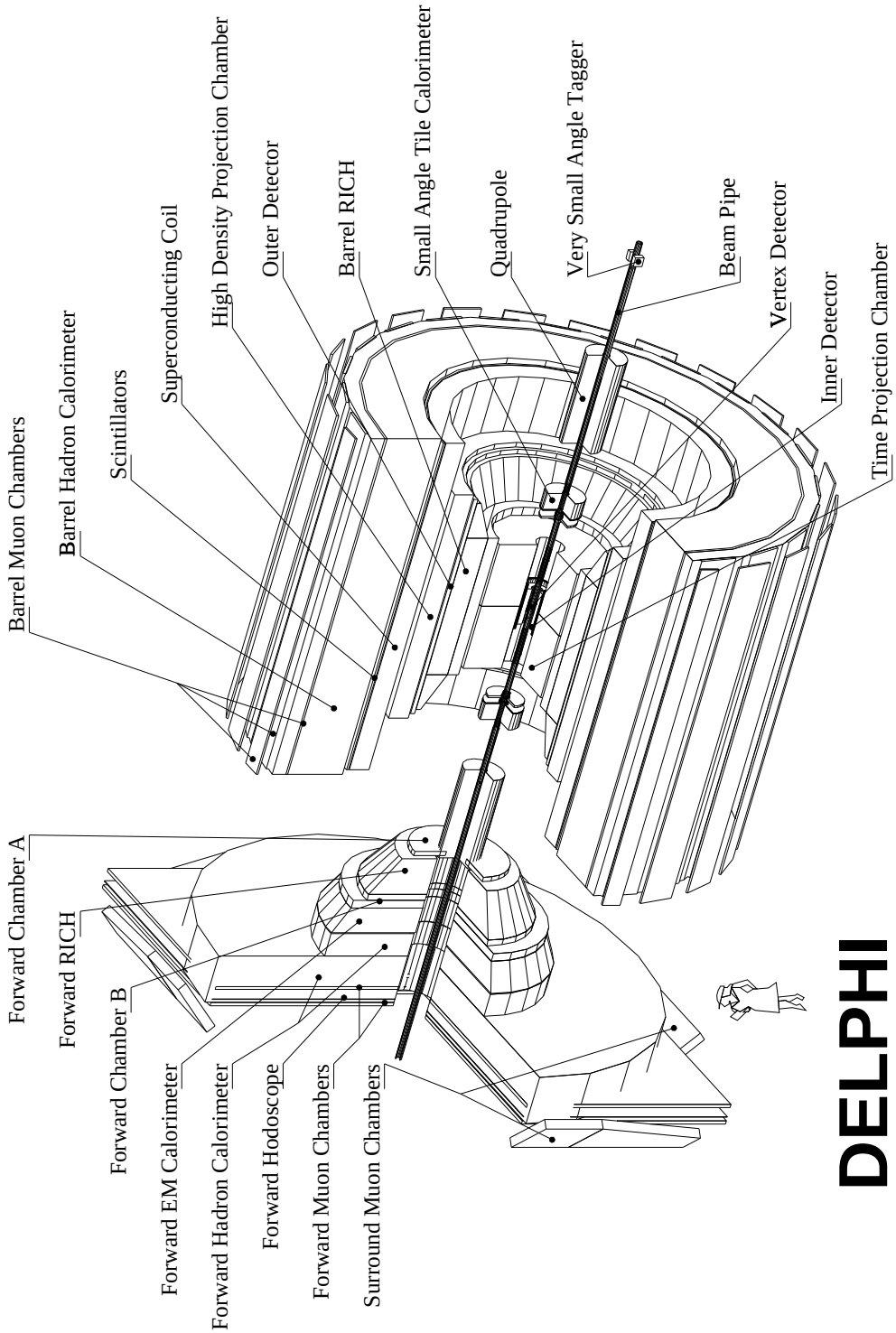

Figure 4.3: A perspective view of the DELPHI detector, showing the layout of the barrel region and of one endcap.

The second group of detectors, the calorimeters, measure the energy of charged and neutral particles. This measurement requires the deposition of essentially all the particles energy, whereas the energy loss in a tracking detector should be minimal. Calorimeters contain therefore a large amount of high density material, where the particles loose their energy by producing showers of secondary particles. Within sampling calorimeters, the passive high density material is layered with active materials in order to reconstruct the position and energy of the original particle from the showers of secondary particles produced. Within homogeneous calorimeters, the high density and the active materials are identical.

RICH detectors (Ring Imaging CHerenkow detectors) are located both in the barrel and in the forward region of DELPHI . They use the Cherenkow radiation emitted by a charged particle traversing a medium with a velocity which exceeds the velocity of light within this medium to measure the particles' velocity. This allows to determine the particles' mass, i.e. the identification of a particle by combining the results of the velocity and the momentum measurement. A detailed description can be found in reference [68].

Scintillation counters are installed in the barrel region (Time of Flight Counter TOF) and in the forward region (Forward Scintillator Hodoscope HOF). Both systems are used for increasing the muon trigger efficiency and to reject cosmic background.

4.2.1 The Super Conducting Solenoid

The barrel section contains a super conducting solenoid of 7.2 m length and an inner diameter of 5.2 m. It is made of a Nb-Ti alloy, which is cooled with liquid helium to a temperature of 4.5 K. The solenoid provides a homogeneous magnetic field of 1.2 T parallel to the z direction, which is the basis of an accurate momentum determination of charged particles from their curved trajectory with an average momentum resolution of $\sigma_p/p \simeq 0.0008 \cdot p$ GeV/c.

4.2.2 The Tracking Detectors

The Vertex Detector

The Vertex Detector (VD) directly surrounds the beam pipe and consists of three concentric layers of silicon micro-strips at at radii of 6.3, 9 and 11 cm. The individual layers cover polar angles θ between 25° and 155°. Within a polar angle range between 44° and 136°, a particle crosses all three layers of the VD. For the 1994 LEP running

period, the most inner and the most outer layer have been equipped with double sided micro-strips, allowing measurements both in $r\phi$ and z direction. The intrinsic resolution is 7.6 μm in $r\phi$ and 9 μm in z. The detector provides precise extrapolation of the tracks back towards the interaction point and allows a precise reconstruction of both the primary vertex and of secondary vertices due to the decay of short living particles.

The Inner Detector

The Inner Detector (ID) immediately surrounds the VD and extends from an inner radius of 12.0 cm to an outer radius of 28.0 cm. It covers polar angles θ from 25° to 155° and provides an accurate track measurement both in $r\phi$ and z direction. Additionally, the ID information is used for fast trigger information. The ID consists of two components, the Jet Chamber and the Trigger Layers.

The Jet chamber is located at the most inner side and extends to a radius of 22 cm. It is a drift chamber, segmented into 24 azimuthal sectors of 15° in ϕ. Each sector contains 24 anode wires stretched in radial direction, thus providing a maximum of 24 $r\phi$ measurements for each traversing particle with a typical resolution of about 90 μm. The Jet Chamber is surrounded by the Trigger Layers at radii between 23 cm and 28 cm. These are five cylindrical layers of Multi Wire Proportional Chambers (MWPC), each layer consisting of 192 signal wires for the $r\phi$ measurement and 192 circular cathode strips for the z measurement.

The Time Projection Chamber

The Time Projection Chamber (TPC) is the principal tracking device in DELPHI . The pattern recognition of DELPHI starts in general with the information provided by the TPC, which is located around the ID at radii between 35 cm and 111 cm and covers a polar angle region θ between 44° and 136°.

In the middle of the detector, at $z = 0$, the TPC is divided by a high voltage plane into two drift volumes, both are 130 cm long and filled with an a mixture of argon (80%) and methane (20%) at a pressure of 1 atm. The read out chambers and its electronics are mounted on each end plate. Charged particles will ionize the gas on their way through the TPC and the resulting electrons will drift with an velocity of $v_D = 6.7\mathrm{cm}\mu\mathrm{s}$ towards the end plates in the homogeneous electrical field, whose direction is parallel to the beam axis. The transverse diffusion of the drifting electrons is suppressed by the parallel and homogeneous magnetic field of the super conducting solenoid. Both end caps are segmented into six azimuthal sectors ϕ of

60°, each of which containing a MWPC with 192 anode wires and 16 concentric cathode pad-rows. The z coordinate is measured by the drift time. The analysis of the height of the read out signal allows the measurement of the energy loss dE/dx of the particles along the track direction, which can be used for particle identification. The spatial resolution is about 250 μm in $r\phi$ and about 880 μm in z direction.

The Outer Detector

An additional track measurement behind the Barrel RICH detector is provided by the Outer Detector (OD). Located at radii between 198 cm and 206 cm, it is the tracking detector with the largest distance to the interaction point. Thus the OD significantly improves the momentum resolution of the high energetic particles with small curvature of the corresponding tracks. Additionally, the OD is important in providing fast trigger information in both $r\phi$ and z direction. The OD covers an polar angle between 43° and 137°. It has 24 modules, each consisting of 145 drift tubes disposed in five layers. The resolution in $r\phi$ is 110 μm. The z information is obtained with a resolution of 3.5 cm from the difference of the drift time to both ends of the tubes.

The Forward Chambers

Two sets of planar drift chambers, the Forward Chambers A (FCA) and the Forward Chambers B (FCB) are installed within the two end caps of the DELPHI detector.

The FCA is located on both sides behind the TPC at a distance of $|z| = 160cm$ from the interaction point and covers polar angles from 11° to 32° and from 148° to 169°. Each side of the FCA consists of three modules, each of which having two staggered layers with 64 wires. To obtain an optimal track reconstruction and good resolution, the modules are rotated by 120° with respect to each other. The reconstructed track elements have a precision of $\sigma(x) = 290$ μm, $\sigma(y) = 240$ μm, $\sigma(\theta) = 8.5$ mrad and $\sigma(\phi) = 24$ mrad (averaged over θ).

The FCB is a drift chamber located in each of the end caps behind the Forward RICH detector at a distance of of $|z| = 275cm$ from the interaction point. It covers polar angles from 11° to 36° and from 144° to 169°. The chamber consists of 12 wire planes, which are divided into 3 groups of 4 planes. Similar to the FCA case, these groups are rotated by 120° with respect to each other. The precision achieved on the parameters of reconstructed track elements are $\sigma(x, y) = 150$ μm, $\sigma(\theta) = 3.5$ mrad and $\sigma(\phi) = 4$ mrad.

The Muon Chambers

The Muon Chambers (MUC) are a set of drift chambers placed in the outermost part of DELPHI. They are crucial for Muon Identification, since muons are essentially the only particles which can traverse the lead and iron of the electromagnetic and the hadron calorimeters. They are separated into three components: The barrel region (MUB), covering polar angles from 53.0° to 88.5° and from 91.5° to 127°, the forward region (MUF) with an polar angle coverage between 20° and 42° and between 138° and 160° and the Surround Muon Chambers (SMC), which have been installed in 1994 to fill the gap between the barrel and forward regions.

4.2.3 The Calorimeters

The High Density Projection Chamber

The High Density Projection Chamber (HPC) is the DELPHI electromagnetic calorimeter in the barrel region. It is located between the OD and the superconducting solenoid at radii between 206 cm and 260 cm. It consists of 144 independent modules, arranged into six concentric rings around z, each ring consisting of 24 modules and covers a polar angle from 43° to 137°.

Each HPC module consists of 40 planes of lead with a thickness of about 3 mm, corresponding to 18 radiation length altogether. The 8 mm gaps between the lead planes are filled with an argon-methane (80%/20%) gas mixture. Traversing particles shower in the lead converter and deposit electrical charge in the gas. As in the TPC, the electrons drift in a homogeneous electrical field ($v_D = 5.5$ cm/μs) towards the end of a module where they are detected by a MWPC. The MWPCs consist of 39 sense wires and 128 pads arranged in nine rows, which provide the $r\phi$ measurement. The z coordinate is measured by the drift time, thus allowing a three dimensional shower reconstruction with an angular resolution of $\sigma(\theta) = 1.0$ mrad and $\sigma(\phi) = 3.1$ mrad. The relative precision of the energy measurement can be parameterized as $\sigma(E)/E = 32\%/\sqrt{E} + 4.3\%$ (E in GeV).

The Forward Electromagnetic Calorimeter

The Forward Electromagnetic Calorimeter (FEMC) is a homogeneous calorimeter installed in each end cap behind the FCB at a distance of $|z| = 284$ cm. It covers the polar angle regions from 10° to 36.5° and from 143.5° to 170°.

The FEMC consists of two times 4532 blocks of lead-glass with a shape of truncated pyramids disposed in two layers, corresponding to 20 radiation length. The Cherenkow light emitted by the charged particles of the electromagnetic shower is read out by photomultipliers. For neutral showers of energy larger than 2 GeV, the average precision on the reconstructed hit position in x and y projected to $|z| = 284$ cm is about 0.5 cm. The relative precision on the measured energy can be parameterized as $\sigma(E)/E = 11\%/E + 12\%/\sqrt{E} + 3.\%$ (E in GeV).

The Hadron Calorimeters

The Hadron Calorimeter (HAC) is a sampling gas detector incorporated in the magnet yoke. The barrel part (HAB) covers polar angles from 42.6° to 137.4° and the forward part (HAF) from 11.2° to 48.5° and from 131.5° to 168.8°.

The HAC consists of successive layers of 5 cm iron and 2 cm wire chambers, 20 layers in the barrel and 19 layers in the forward region. For hadronic Z^0 events in the barrel region, the relative precision on the measured energy has been found to $\sigma(E)/E = 112\%/\sqrt{E} + 21\%$ (E in GeV).

The Luminosity Monitoring Detectors

Two additional calorimeters are installed in the very forward region to measure the luminosity of the beam by using the well known Bhabha cross section under small angles. The Small Angle Tile Calorimeter (STIC) is a lead scintillator sampling calorimeter and covers polar angles between 1.7° and 10.6°. Even smaller polar angles between 0.29° and 0.4° are covered by the Very Small Angle Tagger (VSAT), which consists of 4 calorimeter modules, each of which composed of 12 silicon diodes.

Hermeticity of the Electromagnetic Calorimeters

The DELPHI detector covers about 90% of the solid angle. There are however some weak points in particular with respect to the homogeneity of electromagnetic calorimetery in DELPHI . Around $\theta \simeq 90° \pm 1.5°$ there is an uncovered region due to the passage of the supports for the super conducting solenoid. Another gap exists between the HPC and the FEMC at $\theta \simeq 40°$, providing a passage for cables of various detector components. Additionally there are ϕ cracks in the HPC coverage between the 24 HPC modules.

The reconstruction of neutral tracks in the forward region is hampered due to multiple scattering processes induced by the large amount of material placed in front of the FEMC, which corresponds to about 2 radiation length.

4.2.4 Trigger and Data Acquisition

The time between two Beam Cross Overs (BCO) at LEP is 22 μs (11 μs in 8 bunch mode). Only for a small fraction of these BCOs ($\mathcal{O}(10^{-5})$) an e^+e^- annihilation event occurs. The goal of the trigger system is to select those events with high efficiency, thereby reducing the flux of data and the dead time of the detector and readout system. The DELPHI trigger system is composed of four successive levels (T1, T2, T3 and T4) of increasing selectivity. The T1 decision is made after 3.9 μs and incorporates fast tracking detectors (ID, OD, FCA, FCB) and scintillator arrays in the HPC. The T1 rate is about 400 Hz. After a positive outcome of the T1 decision, the T2 decision is taken within 39 μs after the BCO, incorporating the information from slow drift detectors (TPC,HPC) and combinations of signals from different sub-detectors. The T2 rate is typically about 4 Hz. With a positive T2 decision the data from all detector components are read out and stored into local event buffers. The complete read out process requires about 3 ms.

The trigger levels T3 and T4 are software filters and based on pattern recognition algorithms for specific detectors. They are performed asynchronously with respect to the BCO. If an event passes the T3 decision, the data are transferred from the local memories to the central Data Acquisition System (DAS). The T4 level decides if the data is stored for physics analysis and provides the information for the online Quality Checking (QC). With the complete four level trigger system the event rate is reduced to less than 2 Hz with an efficiency for multihadronic events of about 99.9%.

4.2.5 The Data Analysis Chain

Before the recorded raw data can be used for physics analysis, they undergo a chain of central processings including calibration and alignment of detector components, reconstruction of tracks and particle identification. An overview over the offline analysis chain is shown in Fig. 4.4. It basically consists of three software packages. The event reconstruction program DELANA, the detector simulation program DELSIM and the graphics package DELGRA.

The DELGRA software offers a three dimensional colour display of an event, visualizing the contributions obtained from different detector components. It is useful for

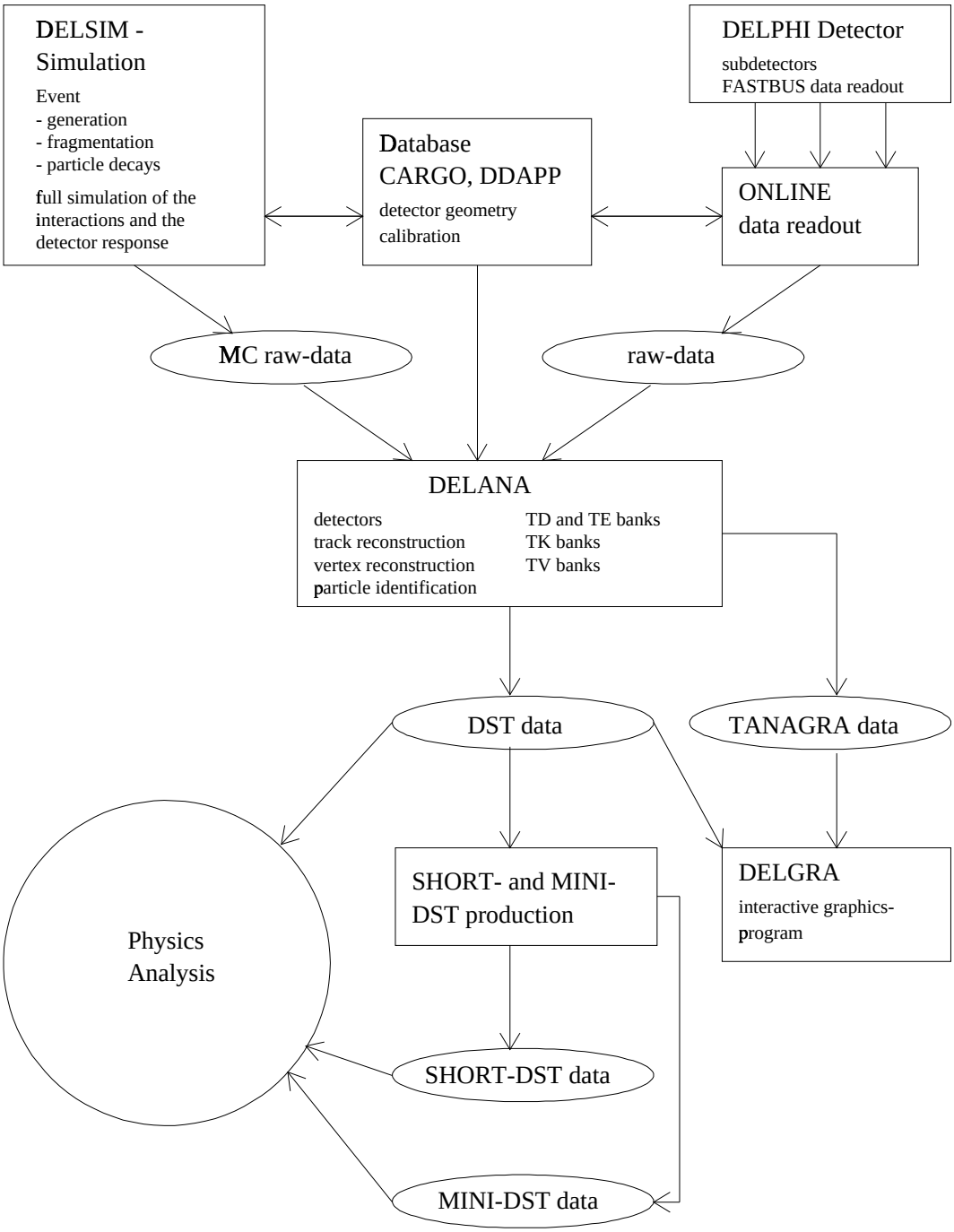

Figure 4.4: The DELPHI offline analysis chain.

investigation of the detector performance and for visualizing the results of the event reconstruction software. An example of a three jet event presented by DELGRA is shown in Fig. 4.5.

Event Reconstruction and DST production

The recorded raw data are further processed by the event reconstruction program DELANA [74]. It uses the information from the DELPHI database to perform the calibration and alignment of the raw data for each sub detector.

The event reconstruction proceeds in several steps. It begins with the reconstruction of the local information of each sub detector by pattern recognition algorithms, which try to combine the separated space points into local track elements. In a second step the track elements from all components are combined into track candidates. For each candidate, a trajectory fit is performed. After resolving ambiguities, the fitted tracks are extrapolated in order to obtain an estimate of the particles trajectory through the detector. Then the local pattern recognition is repeated in order to improve the trajectories by incorporating additional information from the sub detectors which could not have been exploited in the first pattern recognition step. Now the charged tracks are extrapolated to the calorimeters. Calorimeter hits, which are consistent with this extrapolation, are associated with the trajectories. The remaining energy depositions are interpreted as neutral tracks. In a final step, all reconstructed tracks are combined for fit of the primary vertex. The output of DELANA is written on Data Summary Tapes (DST), which is a tree structure of banks containing all information needed for further analyses. The size of a multihadronic event on DST is about 80 Kbyte. At this stage all measured track elements are stored with errors and selected technical data.

In order to reduce the amount of data to be processed within the most common physics analyses, a condensed version of the DST, the so-called Short DST is produced. Eventually remaining calibration and alignment corrections are hereby applied in combination with an improvement of the track and vertex fits and detector specific data are removed. Additionally, some basic physics analyses are performed, for example the identification of electrons, photons and muons, the reconstruction of decayed particles and the tagging of $b-$events. The short DST contains the most relevant information within a volume of about 50% of the initial DST size. For many physics analyses, the amount of information provided by Short DST is still too extensive and can be further reduced by applying even more condensed data formats like Mini DST or the Wuppertal Mini format, which allows to store the most relevant information of a hadronic event within about 6 Kbyte.

Detector Simulation

The physical interpretation of measured data requires a precise knowledge of detector resolution and acceptance effects. These studies are most commonly done by applying detector simulation programs, where the output of physics event generators serves as input for the simulation of the particles interactions with the detector material and the signal response of the individual detector components.

The Monte Carlo simulation program of the DELPHI detector is called DELSIM[75]. The event generator is be chosen according to the process under consideration, usually the JETSET 7.3 PS generator for the simulation of hadronic Z^0 events. Within DELSIM, the generated tracks are traced on their passage through the detector, thereby considering secondary interactions like compton scattering, pair production, bremsstrahlung, positron annihilation, δ-ray emission, photon conversion, multiple scattering, nuclear interactions and absorptions and the decay of short-living particles. The simulation of the signal response like signal height, noise and treshold depends on the individual detector components and their operating conditions. These informations are obtained from the DELPHI database.

The output of the DELSIM simulation is stored in the same format as the raw data and undergoes the same treatment as discussed above. Additional banks are included in the resulting DST and Short DST, which provide the information from the initial Monte Carlo generators.

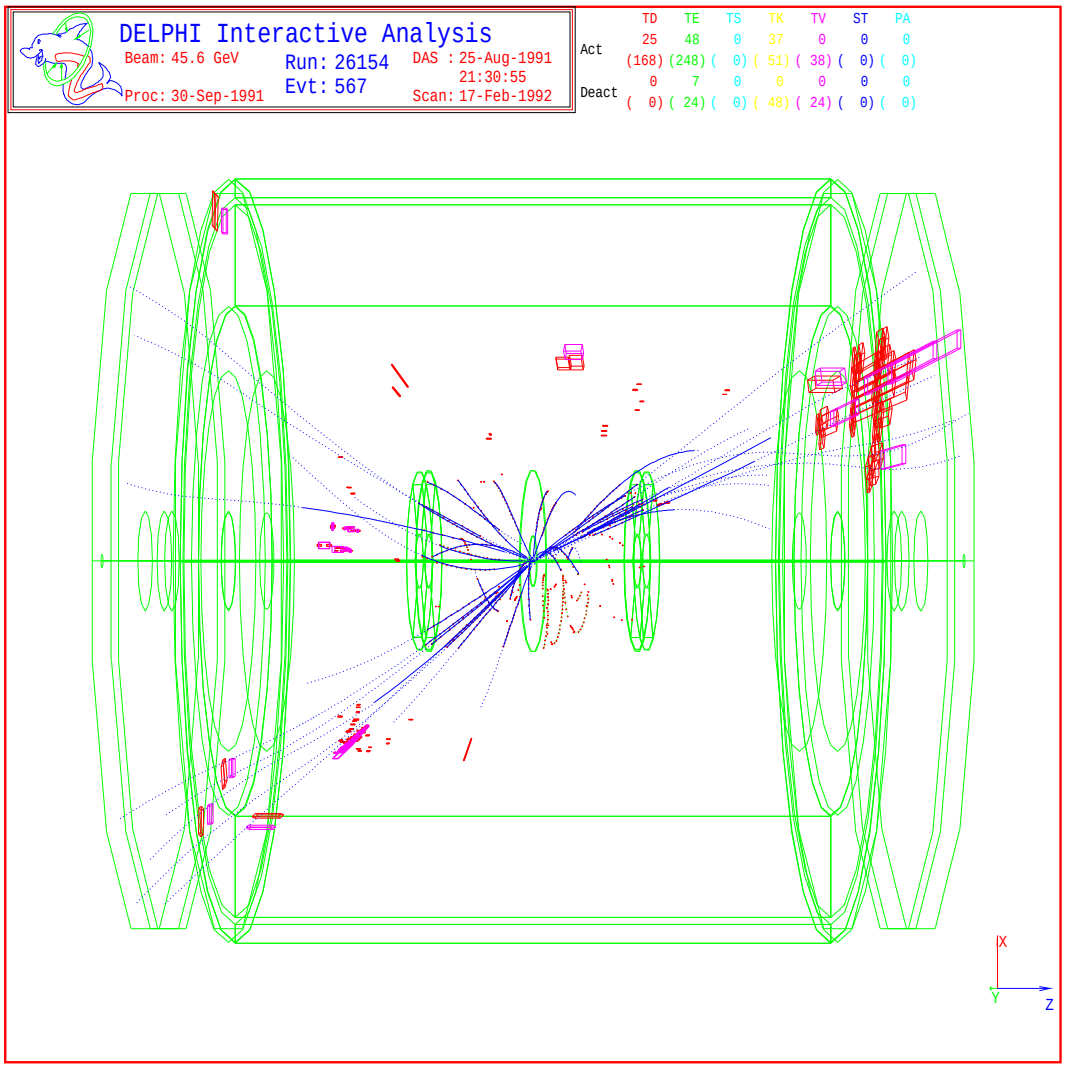

Figure 4.5: Hadronic event recorded with the DELPHI detector and presented with the DELGRA event display package. Charged tracks are shown as lines and the hits in the calorimeters as boxes. A three jet structure can be clearly observed. The jet in forward direction deposits a large amount of energy in the FEMC and the HAF.

Chapter 5

Data Analysis

Within the present study, the final data measured with the DELPHI detector in 1994 at a centre-of-mass energy of $\sqrt{s} = M_{\mathrm{Z}}$ are used. The statistics of about 1.5 million hadronic events from the 1994 data suffices for precise measurements of oriented event shape distributions and accurate QCD studies. The data have been largely improved in both their statistical and systematic precision compared with those of previous DELPHI publications [8, 9]. Furthermore, the ϑ_T dependence of all detector properties has been taken into account in order to achieve the best possible experimental precision.

The following chapter describes the selection criteria applied to the data, the subtraction of background processes, the corrections for detector acceptance and efficiency and for initial state photon radiation followed by an estimate of systematic effects due to the selection procedure and due to the corrections applied. Finally the measured data distributions are compared to the distributions published by other experiments.

5.1 Data Selection

In order to separate hadronic events from background events and to obtain a high quality data sample with small detector corrections and precisely measured tracks, several selection criteria have to be applied on the quality of individual tracks as well as on global properties of the events.

5.1.1 Run Selection

The data acquisition is separated into individual runs. Since the TPC is the main tracking device, only those runs have been accepted, where the TPC was at operational to at least 99%.

5.1.2 Track Selection

Only the charged particles in hadronic events were used for the central analysis. They were required to pass the following selection criteria:

- momentum, p, greater than 0.4 GeV/c,
- relative momentum uncertainty, $\Delta p/p$, less than 100%,
- measured track length greater than 30 cm,
- track polar angle between 16° and 164°,
- impact parameter with respect to the nominal interaction point within 4 cm perpendicular to and 10 cm along the beam.

The energy of the charged tracks has been recalculated from the measured momenta assuming the pion mass of $m_\pi = 0.1396$GeV.

The selection criteria listed above are applied in order to provide tracks of defined quality. Within the forward region however, the momentum resolution is reduced due to the reduced curvature of the charged tracks. The impact parameter cuts are applied in order to suppress the tracks originating from the decays of long lived particles and from secondary interactions with the detector material.

For a high precision measurement of oriented event shape distributions, the inclusion of neutral tracks is not appropriate due to the inhomogeneities in the DELPHI electromagnetic calorimetry, which would cause rather large acceptance corrections. For the study of systematic uncertainties however, the neutral tracks have been considered. They are assumed to be massless and have been selected if the measured energy deposition within the electromagnetic calorimeters was in the range between 0.5 GeV and 100.0 GeV, and within a range of 1.0 GeV and 100.0 GeV for a measurement with the hadron calorimeters.

5.1.3 Selection of Hadronic Events

Based on the track cuts listed above, hadronic events were selected by requiring:

- at least 5 charged particles,
- the total energy of charged particles greater than 12% of $\sqrt{s}$,
- the charged energy in each hemisphere of the detector, defined by the plane perpendicular to the beam, E_{hemis}, greater than 3% of $\sqrt{s}$,
- the polar angle of the thrust axis ϑ_T, between 90.0° and 16.3°.

The cut on the total energy in combination with the cut on the charged energy in each hemisphere is applied in order to suppress two photon events and beam-gas interactions which are mostly boosted in one direction. The requirement of at least five charged particles suppresses leptonic events $e^+e^- \to e^+e^-$, $\mu^+\mu^-$, $\tau^+\tau^-$. Significant background contribution arises only due to τ events because of the hadronic decay of the τ lepton. The contamination of beam-gas events, two photon events and leptonic events other than $\tau^+\tau^-$ is expected to be altogether about 0.01% and can be neglected.

In total about 1.4 million events satisfy the cuts listed above. Hadronic events are selected with an efficiency of $\epsilon_{hadr.} = 92,81\% \pm 0.06\%$, the selection efficiency for the τ background is $\epsilon_\tau = 8,92\% \pm 0.05\%$. The expected τ background is

$$\frac{\epsilon_\tau \Gamma_\tau}{\epsilon_{hadr.}\Gamma_{hadr.} + \epsilon_\tau \Gamma_\tau} = 0.46\% \pm 0.03\% \quad . \tag{5.1}$$

5.2 Event Orientation

Since the thrust axis does not distinguish between forward and backward directions, its orientation is chosen such that $\cos\vartheta_T \geq 0$. ϑ_T is called the event orientation. The data are binned according to the event orientation into eight equidistant bins of $\cos\vartheta_T$ between 0.0 and 0.96. With the exception of the eighth bin, the thrust axis is well contained within the detector acceptance. The correction of the data for background processes and acceptance corrections described below are considered for each angular interval individually.

For the comparison of event shape observables with QCD predictions in all orders resummed next-to-leading-log approximation, the distributions have been integrated over ϑ_T. Differing from the event selection criteria listed above, the hadronic events were selected if the polar angle of the thrust axis satisfied $40.0° < \vartheta_T < 90.0°$ for these angular integrated distributions. This cut corresponds to the requirement, that the events are well contained inside the barrel region of the detector, leading to a significant reduction of detector acceptance corrections in particular for small values of y_{cut}.

5.3 Data Corrections

5.3.1 Subtraction of the τ Background

The selection efficiencies for hadronic and for τ events given above have been determined with the DELSIM Monte Carlo including the full simulation of the DELPHI detector and by applying the same selection criteria than for real data. The underlying event generator for the hadronic Monte Carlo production has been JETSET 7.3 PS and the τ events have been simulated with the KORALZ [76] generator.

Fig. 5.1 shows the uncorrected data distributions integrated over $\cos\vartheta_T$ for some typical event shape observables together with the expectation from the hadron and the τ Monte Carlo. Due to the pronounced two jet topology of the $\tau^+\tau^-$ events their background contribution is limited to the extreme two jet region of the shape distributions. The τ background contribution is typically between 3% and 8% in the first bin of the distributions and about a few per mille in the next few following bins. The τ background as predicted by Monte Carlo has been subtracted from the measured data according to its relative proportion of $0.46\% \pm 0.03\%$.

5.3.2 Correction for Detector Effects

After subtraction of the τ background, the data distributions have to be corrected for detector acceptance and resolution effects. The size of the acceptance effects depends on the efficiency and the geometry of the detector. The event acceptance is always less than 100% and can lead to a preferred selection of particular event topologies. Detector resolution effects, track reconstruction problems, track losses and secondary interactions with the detector material result in smearing effects and a systematical deviation of the measured quantities.

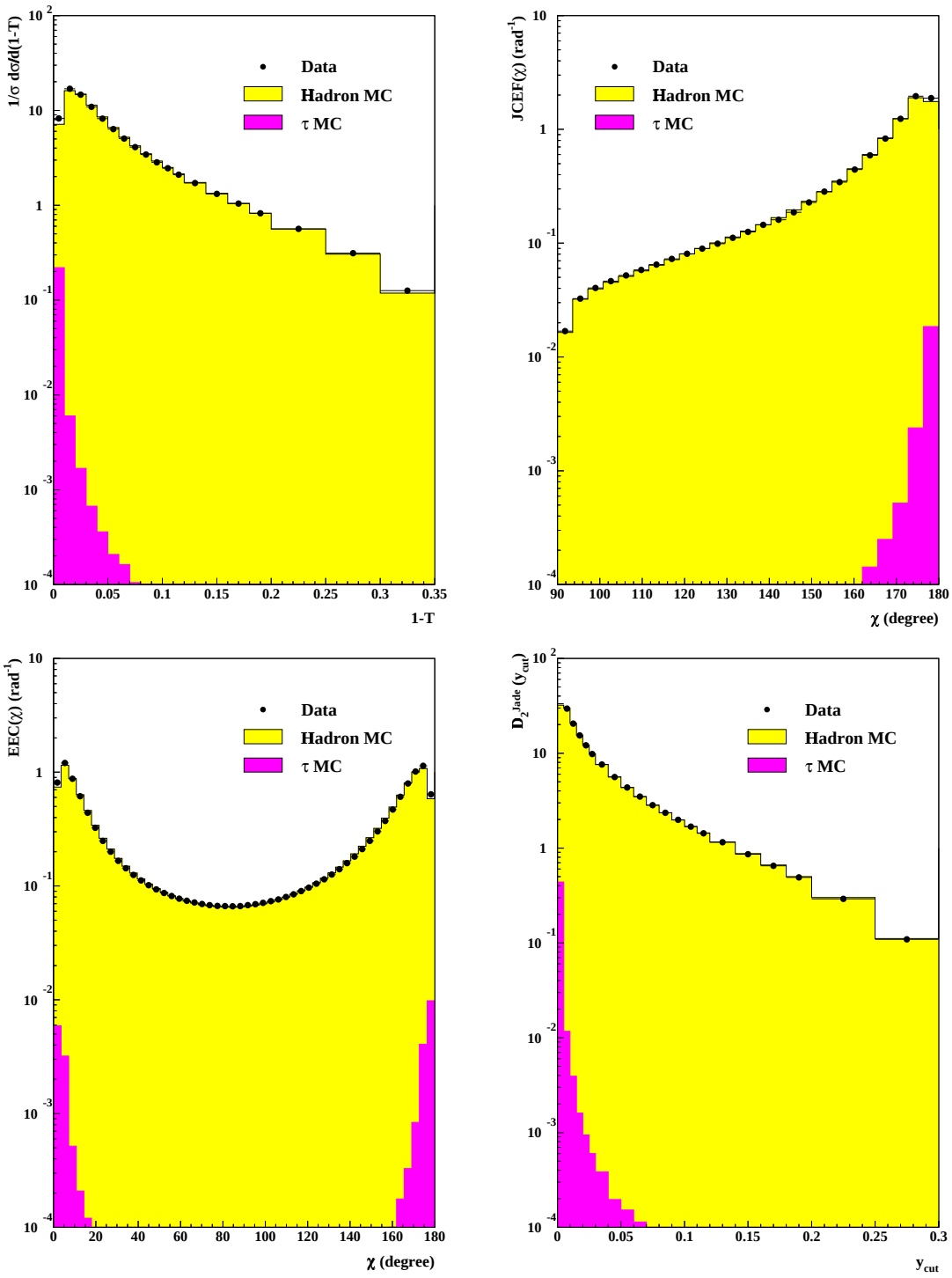

Figure 5.1: τ background in the uncorrected data distributions of the event shape observables $1-T$, $JCEF$, EEC and D_2^{Jade}. The distributions shown are integrated over the event orientation. The shaded areas show the expectation from the Hadron and the τ Monte Carlo, respectively. The Monte Carlo distributions have been calculated with the DELSIM generator by including the detector simulation and by applying the same selection criteria than for real data.

Detector effects and the corrections to be applied were determined by the means of Monte Carlo simulation. Several procedures have been suggested to obtain corrected, i.e. unfolded data distributions [77, 78]. Provided, the binning of the data distributions is large with respect to the detector resolution, a linear bin-by-bin correction can be applied. For most of the observables presented within this analysis, the validity of this assumption has been explicitly checked in [79]. For each observable Y introduced in section 3.2 a bin-by-bin correction factor $C(Y, \cos\vartheta_T)$ has been calculated:

$$C_{Det.Cor.}(Y, \cos\vartheta_T) = \frac{\left(\frac{1}{\sigma}\frac{d^2\sigma}{dY\,d\cos\vartheta_T}\right)^{DELSIM}_{generated}}{\left(\frac{1}{\sigma}\frac{d^2\sigma}{dY\,d\cos\vartheta_T}\right)^{DELSIM}_{reconstructed}} \tag{5.2}$$

where the subscript *reconstructed* refers to the Monte Carlo on reconstruction level, i.e. including full detector simulation and application of selection criteria, and the subscript *generated* denotes the same Monte Carlo on generator level, i.e. as from the simulation of the initial event generator. Particles with a lifetime larger than 1 ns were considered as stable in the generated distributions.

Figure 5.2 shows the detector correction for the $JCEF$ distribution in the eight different $\cos\vartheta_T$ intervals. The detector correction for all intervals of $\cos\vartheta_T$ is large at $\chi \backsimeq 90°$, i.e. for the cones adjoining the plane perpendicular to the thrust axis, i.e. a region with very soft particle emission. The size of the detector corrections in the other kinematical regions of the $JCEF$ distribution strongly depends on the event orientation within the detector. In the region $0. \leq \cos\vartheta_T < 0.12$, where the thrust axis is almost perpendicular to the beam axis, the detector correction is large around $\chi \simeq 100°$. For these particles emitted with large transverse momenta into the very forward direction, there is a large probability of not being detected at all. In the region of $0.84 \leq \cos\vartheta_T < 0.96$, where the thrust axis itself points into the very forward region, this large detector corrections occur around $\chi \simeq 160°$, again with a large probability for the emitted particles of not being detected. For $\cos\vartheta_T$ in between the two regions discussed above, the hump of large detector corrections is moving continuously through the kinematical range of the distribution. On the other hand, for each $\cos\vartheta_T$ a particular kinematical region of the $JCEF$ distribution can be found, where the detector correction and hence the corresponding systematic uncertainty is very small, in particular smaller than for an averaged detector correction not considering the event orientation. Thus, from an experimental point of view, the angular dependent detector corrections are important for obtaining precise data distributions.

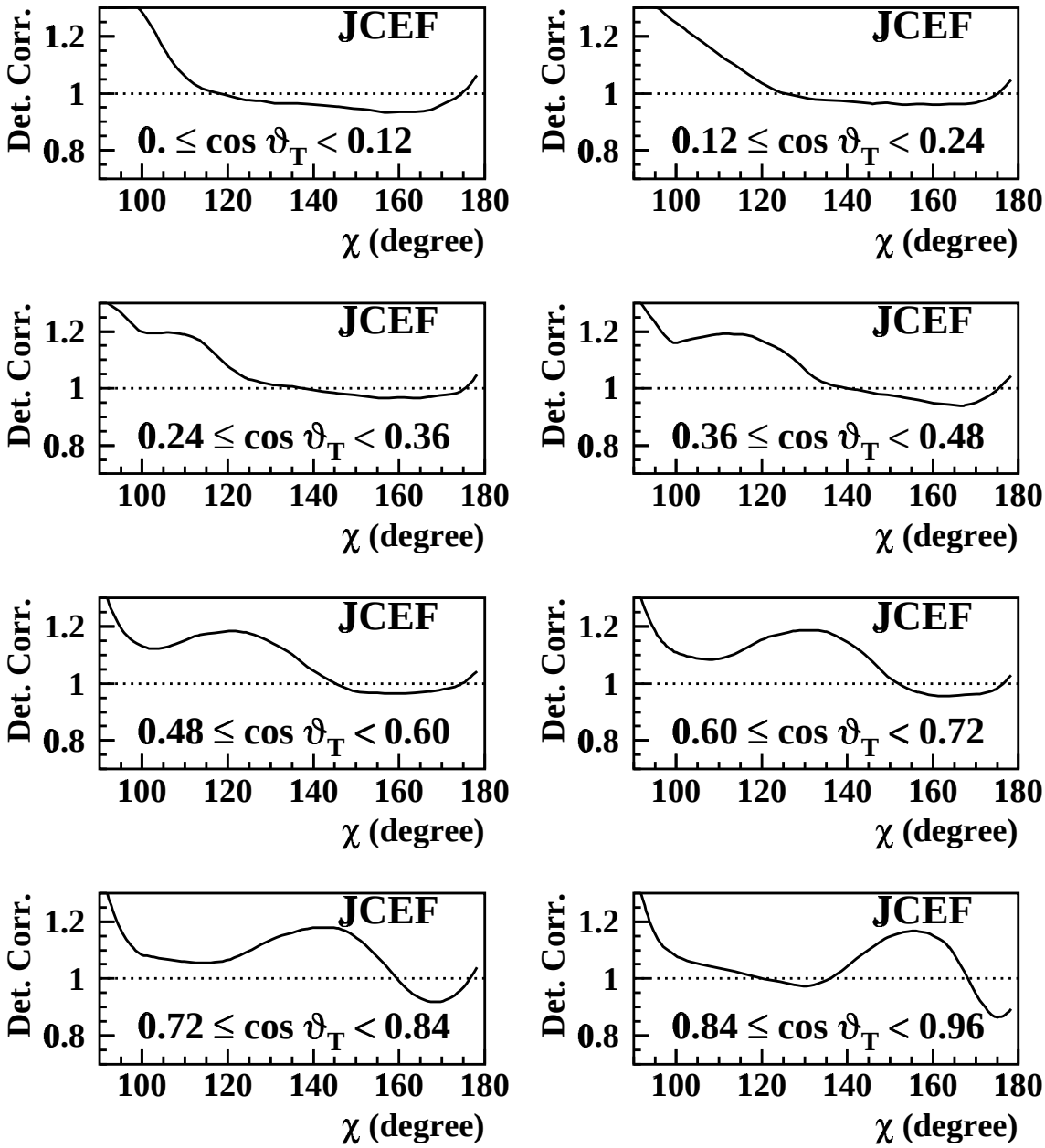

Figure 5.2: Detector correction for the JCEF distribution in dependence on the event orientation Shown are the detector corrections for the eight different bins in $\cos\vartheta_T$.

5.3.3 Correction for Initial State Photon Radiation

Initial state photon radiation (ISR) causes a reduction of the centre-of-mass energy available for the annihilation process resulting in a boost of the event and a corresponding modification of the event topology. ISR is in particular important at energies above the Z^0 resonance where radiative returns are possible, i.e. hard ISR due to the creation of a nearly on-shell Z^0 boson. At the Z^0 resonance itself, ISR is strongly suppressed and its influence on the event shape distributions is small (about 0.2%).

ISR corrections to the shape observables have been determined using events generated by JETSET 7.3 PS [60] with and without initial state photon radiation as predicted by DYMU3 [80]. For any given observable Y a bin-by-bin correction factor $C(Y, \cos\vartheta_T)$ is calculated as:

$$C_{ISR}(Y, \cos\vartheta_T) = \frac{\left(\frac{1}{\sigma}\frac{d^2\sigma}{dY\,d\cos\vartheta_T}\right)^{noISR}}{\left(\frac{1}{\sigma}\frac{d^2\sigma}{dY\,d\cos\vartheta_T}\right)^{ISR}} \quad . \tag{5.3}$$

5.4 Systematic Uncertainties

For the evaluation of systematic uncertainties due to the hadronic event selection, the data analysis has been repeated several times, whereas for each analysis one of the track and event selection criteria has been varied over a wide range:

- The measured track length has been demanded to be greater than 50 cm.
- The measured momentum of charged tracks has been demanded to be in the range between 1.0 GeV and 50 GeV. For the analysis including neutral tracks, the measured energy deposition within the hadronic and the electromagnetic calorimeters has been demanded to be within a range between 1.0 GeV and 50.0 GeV
- Hadronic events have been accepted if least 7 charged particles were selected.
- An additional criterion for the event selection has been applied by requiring the momentum imbalance

$$\delta p = \sqrt{\left(\sum_i^{N_{track}} \vec{p_i}\right)^2} \tag{5.4}$$

to be less than 15% of the centre-of-mass energy.

Additionally, a variation of the tracking efficiency has been considered by discarding 2% of the accepted tracks at random.

The influence of uncertainties in the momentum resolution has been estimated by applying an additional 10% Gaussian smearing of the inverse momenta of the simulated tracks.

From the stability of the measured distributions a systematic uncertainty has been computed as the variance with respect to the central value.

As the systematic error is expected to grow proportional to the deviation of the overall correction factor from unity, an additional relative systematic uncertainty of 10% of this deviation has been added quadratically to the above value. The resulting overall systematic uncertainty has been smoothed for each distribution individually.

Complete tables of the considered oriented and angular integrated shape distributions including statistical and systematic uncertainties can be found in Appendix B.

5.5 Comparison with Other Experiments

Oriented event shape distributions have so far not been published by other experiments. In order to compare the data measured by DELPHI with those from other experiments, the angular integrated distributions are considered. Moreover, the data distributions published by most experiments are derived from charged and neutral tracks and thus not directly comparable to the distributions used for the central part of this analysis. Therefore, the comparison with the data from these experiments can only be done with distributions derived from the analysis including charged and neutral tracks. In a second step, the distributions from the analysis including only charged tracks are compared with data distributions published by ALEPH .

Figures 5.3 and 5.4 show a comparison of the shape observables $1-T$, O, ρ_H and $JCEF$ with the measured distributions from ALEPH , L3, OPAL and SLD . The data have been published in references [81, 82, 83, 84]. For each observable, the distributions itself are shown in the upper part, whereas in the lower part the relative difference of the data distributions from the different experiments with respect to the DELPHI measurement is shown. The dark shaded band indicates the quadratic sum of the statistical and the systematic uncertainty of the DELPHI data distributions. It should be noted, that the data previously published by other experiments are

based on a much smaller statistics than those of the present analysis. Therefore, the light shaded band indicates the uncertainty of the ALEPH distributions as a representative example for the uncertainties of the lower statistics data published by the other experiments. For the $JCEF$ distribution, which has previously only been published by SLD , the light shaded band indicates the total uncertainty as determined by SLD . The relevance of the comparison between DELPHI and L3 is reduced due to the very different binning of the L3 distributions compared with the binning of the other experiments. All DELPHI distributions agree very well with those from the other experiments. Observed differences can be satisfactorily explained by statistic fluctuations.

Figures 5.5 and 5.6 show a comparison of event shape distributions derived from the analysis including only charged tracks with those from ALEPH . Shown are the observables D_2^{Jade}, ρ_D, C and ρ_H. The ALEPH distributions for D_2^{Jade} and ρ_D have been published in reference [81], whereas the distributions for C and ρ_H origin from an analysis with improved statistics and have been published in reference [50]. For large values of ρ_H, the ALEPH distribution is somewhat below the DELPHI disribution. However, all the DELPHI distributions derived from charged tracks only agree very well with those from ALEPH within the statistical and systematic uncertainty.

The statistical and systematic uncertainty of the DELPHI distributions is largely reduced in comparison of the published data of most other experiments. The uncertainty of the ALEPH distributions published in reference [50] is however comparable to those of the angular integrated DELPHI distributions. It should be noted, that α_s measurements from these ALEPH distributions with improved statistics have so far only been published for analyses in matched NLLA precision and not for pure $\mathcal{O}(\alpha_s^2)$ predictions which will be the preferred approach within this analysis.

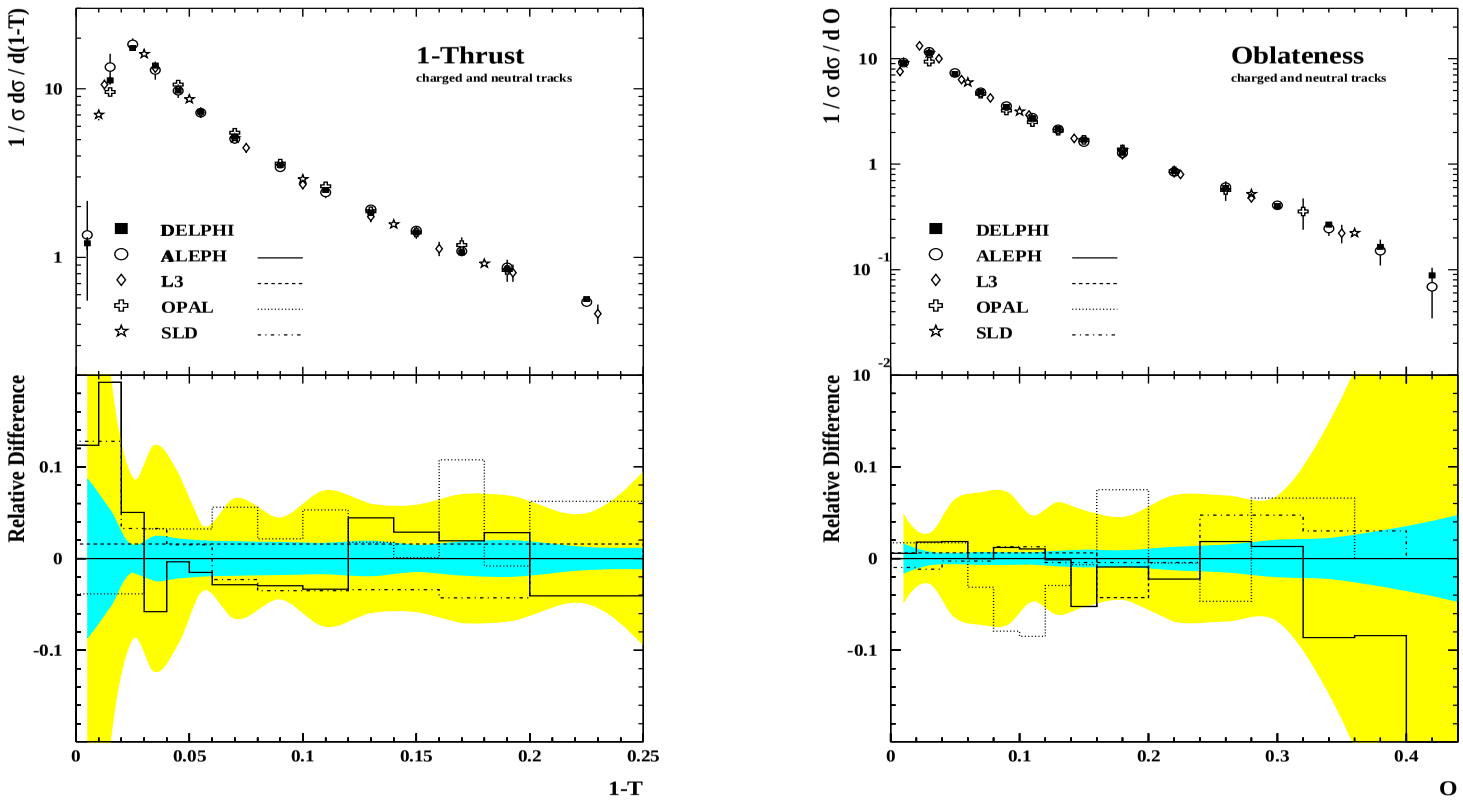

Figure 5.3: Comparison of the measured distributions with data from other experiments. Shown are the angular integrated distributions derived from the analysis including charged and neutral tracks for the shape observables $1 - T$ and O in comparison with the distributions from ALEPH , L3, OPAL and SLD . The lower part shows for each observable the relative difference of the data from the different experiments with respect to the DELPHI measurement. For comparison, the binning of the distributions from the different experiments has been readjusted. The dark shaded band indicates the quadratic sum of the statistical and the systematical uncertainty of the DELPHI data distributions. The light shaded band shows this uncertainty for the distributions of ALEPH as a representative example for the uncertainties of the lower statistics data published by the other experiments.

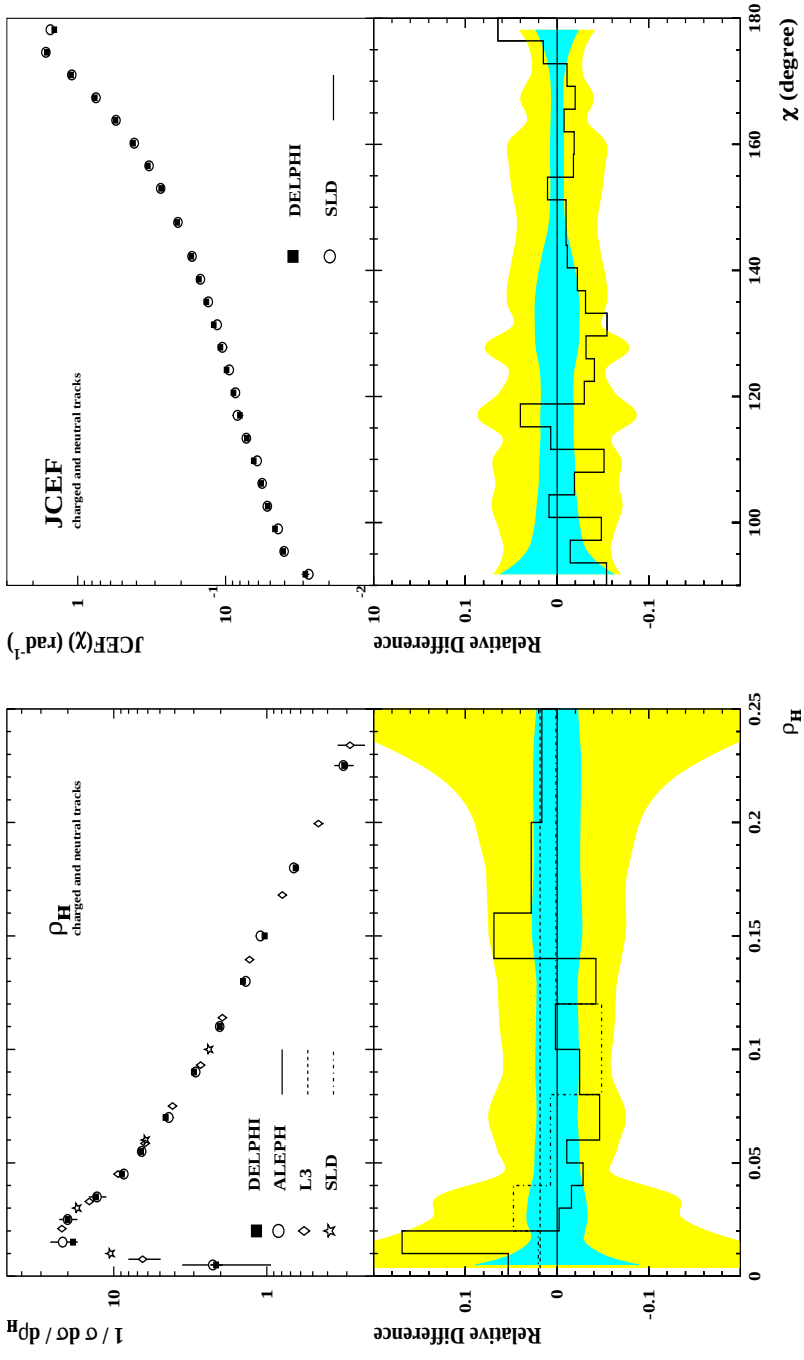

Figure 5.4: The same as in Figure 5.3 but for the distributions of ρ_H and $JCEF$. In the case of $JCEF$, which has previously only been published by SLD , the light shaded band indicates the total uncertainty as determined by SLD .

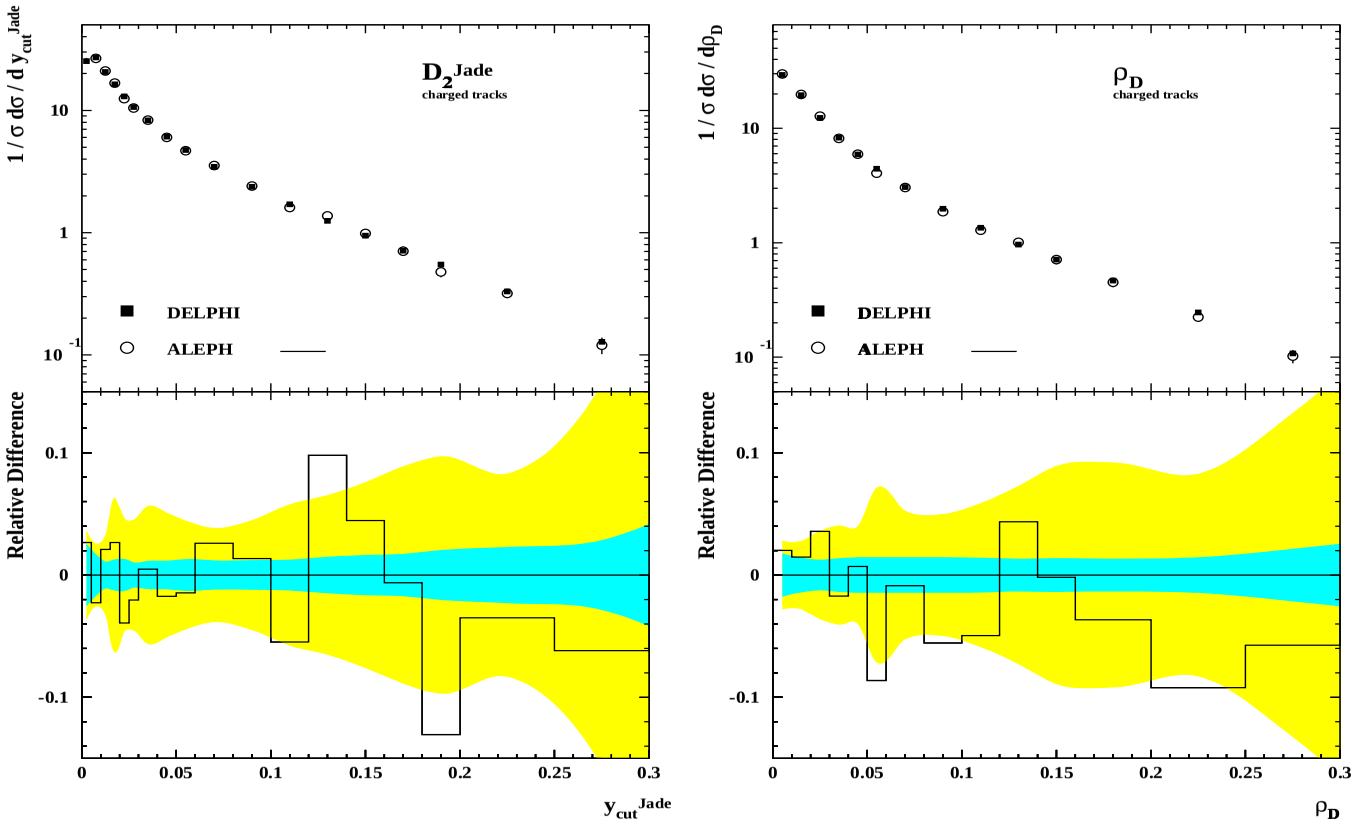

Figure 5.5: Comparison of the measured distributions with data from other experiments. Shown are the angular integrated distributions derived from the analysis including only charged tracks for the observables D_2^{Jade} and ρ_D in comparison with ALEPH distributions. The lower part shows for each observable the relative difference of the data from ALEPH with respect to the DELPHI measurement. For comparison, the binning of the distributions from DELPHI and ALEPH has been readjusted. The dark shaded band indicates the quadratic sum of the statistical and the systematical uncertainty of the DELPHI data distributions. The light shaded band shows the same for the ALEPH distributions.

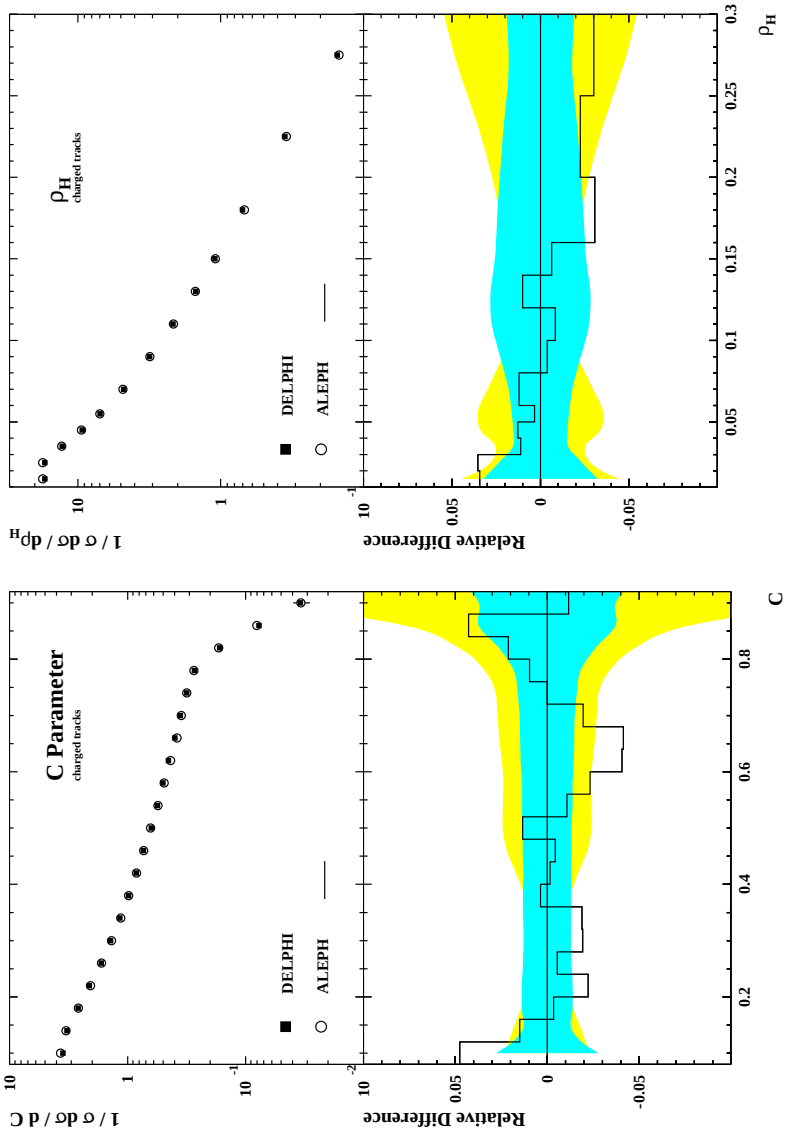

Figure 5.6: The same as in Figure 5.5 but for the distributions of C and ρ_H.

Chapter 6

Determination of the Strong Coupling

Numerous measurements of $\alpha_s(M_z^2)$ from event shape observables in e^+e^- annihilation have been published in the past, incorporating different theoretical approaches like fixed order perturbative perturbative expansion, all orders resummed predictions and several schemes for the matching of fixed order and resummed predictions. For an extensive overview of measurements from Z^0 data see for example [95]. A major problem arising from the comparison of measurements from various shape observables is that 'consistency' of the results can only be achieved by taking into account the large renormalization scale uncertainties obtained by varying the renormalization scale value within a large and *ad hoc* chosen range [6].

Some of the earlier studies in $\mathcal{O}(\alpha_s^2)$ including renormalization scheme optimization observed an improved consistency of the measurements including an experimental optimization of the renormalization scale value [7], the interpretation of these results was however hampered due to the very flat distribution of the χ^2 values of the fits in dependence of the renormalization scale, in particular with respect to large scale values (see for example [85, 84]). Thus, no decisive conclusion about the reliability of the different approaches has been taken so far. Predictions in matched NLLA and $\mathcal{O}(\alpha_s^2)$ precision have been considered to be more reliable by theoretical arguments [58], within experimental analyses however, they do not solve the problem of the consistency of individual measurements from different observables as well as fixed order predictions.

With the precise data of eighteen oriented event shape distributions determined from about 1.5 million hadronic events the significance of the results obtained from different approaches for the determination of $\alpha_s(M_z^2)$ is expected to increase. The number of shape observables studied within this analysis is the largest considered

so far within an experimental analysis of $\alpha_s(M_z^2)$ and covers practically all observables considered to be useful for the determination of $\alpha_s(M_z^2)$ in $\mathcal{O}(\alpha_s^2)$ perturbation theory. Thus, definite conclusions about the degree of consistency of individual measurements turned out to be possible.

This chapter is organized as follows: In the first section, the determination of the hadronization corrections is described and the data are compared with the predictions from various Monte Carlo generators. Section 6.2 covers a description of the fitting procedure and the criteria applied for the determination of the fit range applied. Section 6.3 contains a discussion of experimental and theoretical uncertainties. In Section 6.4 the results from the fits in $\mathcal{O}(\alpha_s^2)$ are presented. Measurements with experimentally optimized renormalization scale values are compared with fixed scale measurements as well as to measurements covering theoretical approaches for an optimized renormalization scheme. The problem of deriving a weighted average from correlated observables is discussed and a weighted average is given by estimating a common overall correlation factor. In the next section the Padé Approximants are used for the estimate of higher order corrections to the perturbative series and the results from fits in $\mathcal{O}(\alpha_s^3)$ Padé Approximation and Padé Sum Approximation are presented. Section 6.6 describes the results from fits in NLLA and matched NLLA and $\mathcal{O}(\alpha_s^2)$ precision and Section 6.7 describes the correction of the $\mathcal{O}(\alpha_s^2)$ measurements for effects from heavy quark masses. Finally, the results obtained from the determination of $\alpha_s(M_z^2)$ from the Jet Cone Energy Fraction are summarized and discussed in Section 6.8.

6.1 Hadronization Corrections

QCD based hadronization models have been introduced in Chapter 3.5. The parton shower models are known to describe well the distributions of event shape observables in the hadronic final state of e^+e^- annihilation and are commonly used for modelling the transition from the primary quarks to the hadronic final state. Perturbative QCD can describe only a part of this transition, the radiation of hard gluons and the evolution of a parton shower. For a comparison with perturbative QCD predictions and for the determination of the strong coupling α_s one has to take account of the so-called fragmentation or hadronization process, which is characterized by a small momentum transfer and hence a breakdown of perturbation theory.

Several parton shower Monte Carlo generators have been used to estimate the size of the hadronization effects and the corresponding uncertainty. All generators considered are described in Chapter 3.5 and are most frequently used within QCD analyses, namely JETSET 7.3 PS [60], ARIADNE 4.06 [65] and HERWIG 5.8c [64]. The models

have been extensively studied and tuned to DELPHI data and to identified particle spectra from all LEP experiments in reference [61]. As discussed in detail in [61] all models describe the data well.

As the central generator for the evaluation of hadronization effects the JETSET 7.3 Parton Shower (PS) Generator has been chosen. The DELPHI version of this program has been modified with respect to the heavy particle decays to obtain a better description of the heavy particle branching fraction. This modified version is denoted by JETSET 7.3 PS D in the following. The tuned parameters have been taken from [61], where the updated tuning procedure is described in detail.

In order to compare the measured data with the theoretical expressions describing the parton distributions, corrections have to be made for hadronization effects, i.e. effects resulting from the transition of the parton state into the observed hadronic state. For the global event shape observables this transition is performed by a matrix P, where P_{ij} is the probability that an event contributing to the bin j of the partonic distribution will contribute to the bin i in the hadronic distribution and is computed from a Monte Carlo model. This probability matrix has been applied to the distributions from $\mathcal{O}(\alpha_s^2)$ perturbative theory $D_{pert.}(Y, \cos\vartheta_T)$ to obtain the distributions for the predictions of the observed final state $D_{hadr.}(Y, \cos\vartheta_T)$:

$$D_{hadr.}(Y, \cos\vartheta_T)_i = \sum_j P_{ij}(Y, \cos\vartheta_T) D_{pert.}(Y, \cos\vartheta_T)_j \quad . \tag{6.1}$$

In the case of the JCEF, EEC and AEEC, which are defined in terms of single particles and pairs of particles, respectively, bin-by-bin correction factors $C_{Hadr.}$ similar to that described above for the detector effects have been computed such as:

$$D_{hadr.}(Y, \cos\vartheta_T)_i = C_{Hadr.}(Y, \cos\vartheta_T)_i D_{pert.}(Y, \cos\vartheta_T)_i \quad . \tag{6.2}$$

Comparison of the Data with Monte Carlo predictions

Fig. 6.1 shows a comparison of the angular integrated data distributions for the observables $1 - T$ and $JCEF$ with the predictions from the different Monte Carlo generators described in Section 3.5.1. Additionally shown are the detector corrections including effects due to initial state radiation, the size of the hadronization corrections and the fit ranges applied for the QCD fits in $\mathcal{O}(\alpha_s^2)$.

Figures for all shape observables considered can be found in the appendix. The agreement of the data distributions with the predictions from the Monte Carlo

generators is reasonable. Within the fit ranges applied for the QCD studies, the deviation between data and Monte Carlo predictions is in general less than 5%.

Fig. 6.2 shows the $1-T$ and the $JCEF$ distribution for two different intervals of ϑ_T in the forward and the barrel region, respectively. For these figures, the distributions for each angular interval have been normalized to the total hadronic cross section σ_{tot}. The ϑ_T dependence of the detector corrections is shown as well as the difference of the hadronization corrections for the individual ϑ_T interval with respect to the average hadronization correction. The angular dependence of the hadronization corrections is of the order 1% and thus quite small with respect to the angular dependence of the detector corrections.

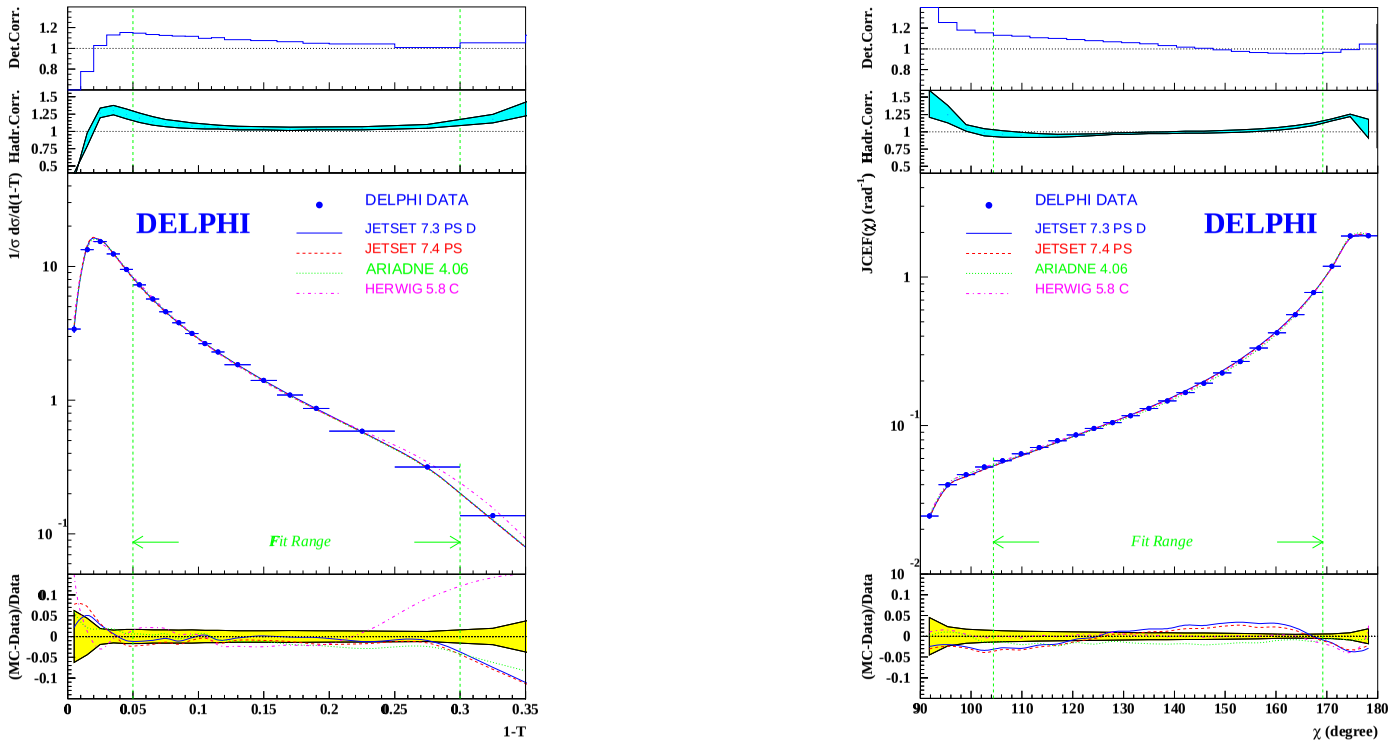

Figure 6.1: *left part:* Measured 1-T distribution integrated over $\cos\vartheta_{\mathrm{T}}$. The upper part shows the detector correction including effects due to initial state radiation. The part below shows the size of the hadronization correction. The width of the band indicates the uncertainty of the correction. In the central part the measured 1-T distribution is compared to the expectation from four hadronization generators, JETSET 7.3 PS D with DELPHI modification of heavy particle decays, JETSET 7.4 PS, ARIADNE 4.06 and HERWIG 5.8c. Also shown is the 1-T range used in the QCD fit. The lower part shows the ratio (Monte Carlo simulation-data)/data for the four hadronization generators. The width of the band indicates the size of the experimental errors. *right part:* Same curves as shown in the left part but for JCEF integrated over $\cos\vartheta_{\mathrm{T}}$.

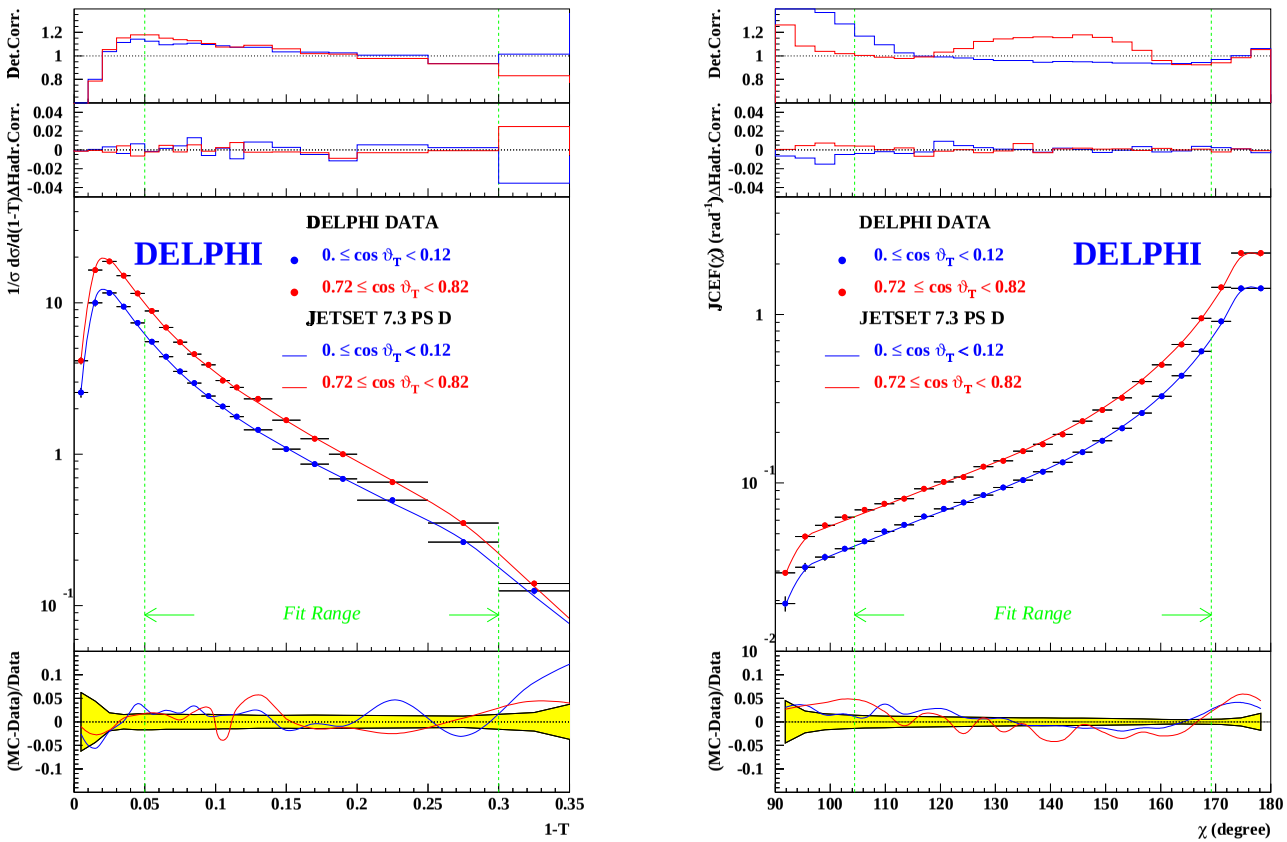

Figure 6.2: *left part:* Measured 1-T distribution in two bins of $\cos\vartheta_T$. The upper part shows the detector corrections in the two $\cos\vartheta_T$ bins. The part below shows the size of the relative hadronization correction in the two $\cos\vartheta_T$ bins with respect to the correction obtained for the distributions integrated over the full angular range. In the central part the measured 1-T distributions are compared to JETSET 7.3 PS D. The lower part shows the ratio (Monte Carlo simulation-data)/data for the two $\cos\vartheta_T$ bins. *right part:* Same curves as shown in the left part but for JCEF in two bins of $\cos\vartheta_T$.

6.2 The Fitting Procedure

The traditional experimental approach to account for the renormalization scheme problem of perturbative QCD predictions has been to measure all observables applying the same fixed renormalization scale value, the so-called physical scale $x_\mu = 1$ or equivalently $\mu^2 = \mathrm{Q}^2$. The scale dependence has been taken into account by varying μ over some wide ad hoc range, quoting the resulting change in the QCD predictions as theoretical uncertainty. It should be noted, that for the physical scale approach, the ratio of the $\mathcal{O}(\alpha_s)$ and the $\mathcal{O}(\alpha_s^2)$ contributions to the cross-section, defined as

$$r_{NLO}(Y, x_\mu) = \frac{\alpha_s(x_\mu)\Big[B(Y) + A(Y)(2\pi\beta_0 \ln(x_\mu) - 2)\Big]}{A(Y)} \quad , \tag{6.3}$$

is quite large for many of the observables studied within this analysis. In some cases this ratio can have a magnitude approaching unity, indicating a poor convergence behavior of the $\mathcal{O}(\alpha_s^2)$ predictions in the $\overline{\mathrm{MS}}$ scheme. This circumcstance could quite naturally result in a wide spread of the measured α_s values, which has indeed been observed in previous analyses using $\mathcal{O}(\alpha_s^2)$ QCD [8, 84, 85, 86].

The principal approach for the determination of α_s within the present analysis the experimentally optimized renormalization scale method has been chosen. Applying the measured scale values, the ratio $r_{NLO}(Y, x_\mu)$ is significantly reduced for many of the observables studied. In the past this strategy suffered from a poor sensitivity of the fit with respect to x_μ for most of the observables. Due to the high statistics and high precision data now available, an improved sensitivity for this parameter is expected.

In practice, $\alpha_s(M_Z^2)$ and the renormalization scale factor x_μ are determined simultaneously by comparing the corrected distributions for each observable Y with the perturbative QCD calculations corrected for hadronization effects as described above. The theoretical predictions have been fitted to the measured distributions $R(Y, \cos\vartheta_T)$ (Eq. 3.36) by minimizing χ^2, defined by using the sum of the squares of the statistical and systematic experimental errors, with respect to the variation of $\Lambda_{\overline{MS}}$ and x_μ.

The fit range for the central analysis, i.e. including the experimental optimization of x_μ, has been chosen according to the following criteria:

- Requiring a detector acceptance larger than 80%, the last bin in $\cos\vartheta_\mathrm{T}$ has been excluded in general, i.e. the fit range has been restricted to the interval

$0 \leq \cos\vartheta_{\mathrm{T}} < 0.84$ which corresponds to the polar angle interval $32.9° < \vartheta_{\mathrm{T}} \leq 90.0°$.

- Acceptance corrections have been required to be below about 25% and the hadronization corrections to be below $\sim$ 40%.
- The contribution of the absolute value of the second order term $r_{NLO}(Y)$ as defined in Eq. (6.3) has been required to be less than one over the whole fit range.
- The requirement that the data can be well described by the theoretical prediction, i.e. χ^2/n_{df} is approximately 1 and stable over the fit range.
- Stability of the α_{s} - measurement with respect to the variation of the fit range.

The requirement, that the contribution of the absolute value of the second order term is less than one over the whole fit range, restricts the fit interval only for the total jet broadening observable B_{sum}, which yields rather large $\mathcal{O}(\alpha_s^2)$ contributions for any choice of the renormalization scale value.

For the analysis with a fixed renormalization scale value $x_\mu = 1$, the requirement that χ^2/n_{df} is approximately one, can in general not be applied, since it would cause an unreasonably large reduction of the fit range for many observables. The thrust distribution for example could then be fitted only over a range of at most three bins. A detailed description of this problem can be found in the results section 6.4.1. The fit ranges for this analysis as well as for the analyses applying theoretically motivated scale setting methods have therefore been chosen identical to the analysis with experimentally optimized scale values, regardless of the χ^2 values of the fits.

6.3 Systematic and Statistical Uncertainties

For each observable the uncertainties from the fit of $\alpha_s(M_Z^2)$ and of x_μ have been determined by changing the parameters corresponding to a unit increase of χ^2. In the case of asymmetric errors the higher value has been taken.

Systematic Uncertainties

The systematic experimental uncertainty has been estimated by repeating the analysis with the distributions derived with the alternative data selection criteria and

the modified prescriptions for the calculation of the acceptance corrections as described in Section 5.4. Additionally, an analysis has been performed including neutral clusters measured with the hadronic and electromagnetic calorimeters. The overall uncertainty has been taken as the variance of the individual $\alpha_s(M_Z^2)$ measurements.

An additional source of experimental uncertainty arises from the determination of the fit range, which has been estimated by varying the lower and the upper edge of the fit range by ± 1 bin, respectively, while the other edge is kept fixed. Half of the maximum deviation in $\alpha_s(M_Z^2)$ has been taken as the error due to the variation of the fit range and has been added in quadrature. Whereas the fits applying $\mathcal{O}(\alpha_s^2)$ perturbative predictions are in general very stable with respect to the variation of the fit range, a significant contribution due to this uncertainty arises in particular for QCD fits applying pure NLLA predictions within a limited kinematical range.

Hadronization Uncertainties

In order to estimate the systematic error of the hadronization correction, the analysis is repeated using alternative Monte Carlo generators with different hadronization models. In addition, the parameters for the JETSET PS have been varied.

The alternative models used are ARIADNE 4.06, HERWIG 5.8c as well as version 7.4 JETSET PS [60]. All these models have been tuned to DELPHI data [61].

Additionally, an alternative tuning of the central hadronization generator to the DELPHI data has been applied, where Bose-Einstein Correlations (BEC) have been considered wich are not not included in the reference tuning.

Whereas the number of hard gluons predicted by second order QCD matrix elements is simulated by the hadronization models [87], additional soft gluons are produced within the parton shower cascade, controlled by the JETSET PS parameter Q_0, which describes the parton virtuality at which the parton shower is stopped. To account for the sensitivity of the shape observables with respect to the additional soft gluons, Q_0 has been varied from 0.5 GeV to 4.0 GeV.

The systematic error of α_s originating from hadronization corrections is then estimated as the variance of the fitted α_s values obtained by using all the hadronization corrections mentioned above.

Further studies have been made to investigate the influence of the main fragmentation parameters of the JETSET PS model by varying them within their experimental uncertainty. It has been found that this contribution to the uncertainty of α_s in general is less than one per mille, and has been neglected.

The total uncertainty on $\alpha_s(M_Z^2)$ is determined from the sum of the squares of the errors listed above.

Uncertainties due to Missing Higher Order Calculations

An additional source of theoretical uncertainty arises due to the missing higher order calculations of perturbative QCD. It is commonly assumed, that the size of these uncertainties can be estimated by varying the renormalization scale value applied for the determination of $\alpha_s(M_z^2)$ within some 'reasonable' range [88]. The choice of a 'reasonable' range involves subjective judgement and so far no common agreement about the size of this range has been achieved. Furthermore, this commonly used approach has been criticized in the literature [6]. According to [6] any artificial increase of the uncertainty of $\alpha_s(M_z^2)$ due to a large variation of the renormalization scale should be avoided so that the degree of precision to which QCD can be tested remains transparent. It should be pointed out that no such additional uncertainty is required to understand the scatter of the measurements from a large number of observables if experimentally optimized renormalization scale values are applied. This will be demonstrated in the results section. Other procedures for estimating uncertainties due to missing higher order corrections have been suggested, in particular the comparison of $\alpha_s(M_z^2)$ values obtained by applying different reasonable renormalization schemes or by replacing the missing higher order terms by their Padé Approximants [88]. Both strategies have been studied. By comparing the size of the uncertainties derived applying these methods (see e.g. Table 6.8 on page 139), a variation of x_μ between $0.5 \cdot x_\mu^{exp}$ and $2 \cdot x_\mu^{exp}$ seems justified to obtain an estimate of these uncertainties. Similar or identical ranges have for example also been chosen in [9, 89].

6.4 Comparison of the Data with Angular Dependent Second Order QCD

6.4.1 QCD Fits with Experimentally Optimized Renormalization Scales

The fit ranges for the 18 oriented event shape distributions and the results of the QCD fits applying experimentally optimized scales are summarized in tables 6.1 and 6.2. For a graphical view of the results obtained for $\alpha_s(M_z^2)$ see also Fig. 6.12 on page 108.

Figures 6.3 to 6.6 (pages 92 - 95) show a direct comparison of the measured oriented shape distributions for $1-T$, $JCEF$, EEC and D_2^{Jade} for various bins in $\cos\vartheta_T$ with the results of the QCD fits with experimentally optimized renormalization scales. The theoretical predictions describe the measured data distributions exactly over a large range of values. The measured dependence on both $\cos\vartheta_T$ and the studied observable are precisely reproduced by the fits. For all shape observables studied, the χ^2/n_{df} is about one for a typically large number of degrees of freedom ($n_{df} = 16-236$, see also Table 6.1).

The individual sources of errors contributing to the total error on the value of α_s are listed in Table 6.2. Typically the experimental uncertainty yields the smallest and the hadronization uncertainty yields the largest overall contribution. Among the observables considered, the $JCEF$ yields the most precise result. For a more complete discussion of the results of the $\alpha_s(M_z^2)$ determination from the $JCEF$ distribution see section 6.8.

More details concerning the renormalization scale dependence of the $\mathcal{O}(\alpha_s^2)$ QCD predictions are presented in Fig. 6.7 (page 96). Shown are the values of $\alpha_s(M_z^2)$ and the corresponding values of $\Delta\chi^2$, i.e. the change of χ^2 with respect to the optimal value, for the fits as a function of the scale $\lg(\mathrm{x}_\mu)$ for some of the investigated observables.

The optimized renormalization scale values vary over several orders of magnitude for the different observables. For the distributions of O, ρ_D and D_2^{Geneva}, the scale values are significantly larger than $x_\mu = 1.0$, which makes it difficult to understand these values in terms of any 'physical' scale of the underlying process. The shape of the $\Delta\chi^2$ curves indicates that for most distributions the renormalization scale is bound to a rather narrow range of values in order to be consistent with the data. For most of the observables the renormalization scale dependence of $\alpha_s(M_z^2)$ is significantly smaller in the region of the optimized scale value than in the region around $x_\mu = 1$.

Observable	Fit Range	$\cos\vartheta_T$ Range	x_μ	χ^2/n_{df}	n_{df}
EEC	$28.8° - 151.2°$	0.0 - 0.84	0.0112 ± 0.0006	1.02	236
AEEC	$25.2° - 64.8°$	0.0 - 0.84	0.0066 ± 0.0018	0.98	75
JCEF	$104.4° - 169.2°$	0.0 - 0.84	0.0820 ± 0.0046	1.05	124
$1 - T$	0.05 - 0.30	0.0 - 0.84	0.0033 ± 0.0002	1.24	89
O	0.24 - 0.44	0.0 - 0.84	2.30 ± 0.40	0.90	33
C	0.24 - 0.72	0.0 - 0.84	0.0068 ± 0.0006	1.02	82
B_{Max}	0.10 - 0.24	0.0 - 0.84	0.0204 ± 0.0090	0.89	47
B_{Sum}	0.12 - 0.24	0.0 - 0.84	0.0092 ± 0.0022	1.19	40
ρ_H	0.03 - 0.14	0.0 - 0.84	0.0036 ± 0.0004	0.63	54
ρ_S	0.10 - 0.30	0.0 - 0.36	0.0027 ± 0.0019	0.82	16
ρ_D	0.05 - 0.30	0.0 - 0.84	2.21 ± 0.38	1.02	68
D_2^{E0}	0.07 - 0.25	0.0 - 0.84	0.048 ± 0.020	0.85	68
D_2^{P0}	0.05 - 0.18	0.0 - 0.84	0.112 ± 0.048	1.02	68
D_2^{P}	0.10 - 0.25	0.0 - 0.84	0.0044 ± 0.0004	1.00	47
D_2^{Jade}	0.06 - 0.25	0.0 - 0.84	0.126 ± 0.049	1.05	75
D_2^{Durham}	0.015 - 0.16	0.0 - 0.84	0.0126 ± 0.0015	0.92	96
D_2^{Geneva}	0.015 - 0.03	0.0 - 0.84	7.10 ± 0.28	0.84	19
$D_2^{Cambridge}$	0.011 - 0.18	0.0 - 0.84	0.066 ± 0.019	0.98	145

Table 6.1: Observables used in the $\mathcal{O}(\alpha_s^2)$ QCD fits. For each of the observables the fit range, the range in $\cos\vartheta_T$, the measured renormalization scale factor x_μ together with the uncertainty as determined from the fit, the χ^2/n_{df} and the number of degrees of freedom n_{df} are shown. In the case of asymmetric errors the higher value is given.

Observable	$\alpha_s(M_z^2)$	$\Delta\alpha_s$ (Exp.)	$\Delta\alpha_s$ (Hadr.)	$\Delta\alpha_s$ (Scale.)	$\Delta\alpha_s$ (Tot.)
EEC	0.1142	$\pm$ 0.0007	$\pm$ 0.0023	$\pm$ 0.0014	$\pm$ 0.0028
AEEC	0.1150	$\pm$ 0.0037	$\pm$ 0.0029	$\pm$ 0.0100	$\pm$ 0.0111
JCEF	0.1169	$\pm$ 0.0006	$\pm$ 0.0013	$\pm$ 0.0008	$\pm$ 0.0017
$1-\mathrm{T}$	0.1132	$\pm$ 0.0009	$\pm$ 0.0026	$\pm$ 0.0023	$\pm$ 0.0036
O	0.1171	$\pm$ 0.0028	$\pm$ 0.0030	$\pm$ 0.0038	$\pm$ 0.0056
C	0.1153	$\pm$ 0.0021	$\pm$ 0.0023	$\pm$ 0.0017	$\pm$ 0.0036
$\mathrm{B_{Max}}$	0.1215	$\pm$ 0.0022	$\pm$ 0.0031	$\pm$ 0.0013	$\pm$ 0.0041
$\mathrm{B_{Sum}}$	0.1138	$\pm$ 0.0030	$\pm$ 0.0032	$\pm$ 0.0030	$\pm$ 0.0053
ρ_{H}	0.1215	$\pm$ 0.0014	$\pm$ 0.0029	$\pm$ 0.0050	$\pm$ 0.0060
ρ_{S}	0.1161	$\pm$ 0.0014	$\pm$ 0.0018	$\pm$ 0.0016	$\pm$ 0.0033
ρ_{D}	0.1172	$\pm$ 0.0013	$\pm$ 0.0034	$\pm$ 0.0007	$\pm$ 0.0038
$\mathrm{D_2^{E0}}$	0.1165	$\pm$ 0.0027	$\pm$ 0.0029	$\pm$ 0.0017	$\pm$ 0.0044
$\mathrm{D_2^{P0}}$	0.1210	$\pm$ 0.0018	$\pm$ 0.0026	$\pm$ 0.0009	$\pm$ 0.0033
$\mathrm{D_2^{P}}$	0.1187	$\pm$ 0.0019	$\pm$ 0.0021	$\pm$ 0.0036	$\pm$ 0.0046
$\mathrm{D_2^{Jade}}$	0.1169	$\pm$ 0.0011	$\pm$ 0.0020	$\pm$ 0.0028	$\pm$ 0.0040
$\mathrm{D_2^{Durham}}$	0.1169	$\pm$ 0.0013	$\pm$ 0.0016	$\pm$ 0.0015	$\pm$ 0.0026
$\mathrm{D_2^{Geneva}}$	0.1178	$\pm$ 0.0052	$\pm$ 0.0075	$\pm$ 0.0295	$\pm$ 0.0309
$\mathrm{D_2^{Cambridge}}$	0.1164	$\pm$ 0.0008	$\pm$ 0.0023	$\pm$ 0.0004	$\pm$ 0.0025

Table 6.2: Individual sources of errors of the $\alpha_s(M_z^2)$ measurement. For each observable, the value of $\alpha_s(M_z^2)$, the experimental uncertainty (statistical and systematic), the uncertainty resulting from hadronization corrections, the theoretical uncertainty due to scale variation around the central value x_μ^{exp} in the range $0.5 \cdot x_\mu^{exp} \leq x_\mu \leq 2 \cdot x_\mu^{exp}$ and the total uncertainty are shown.

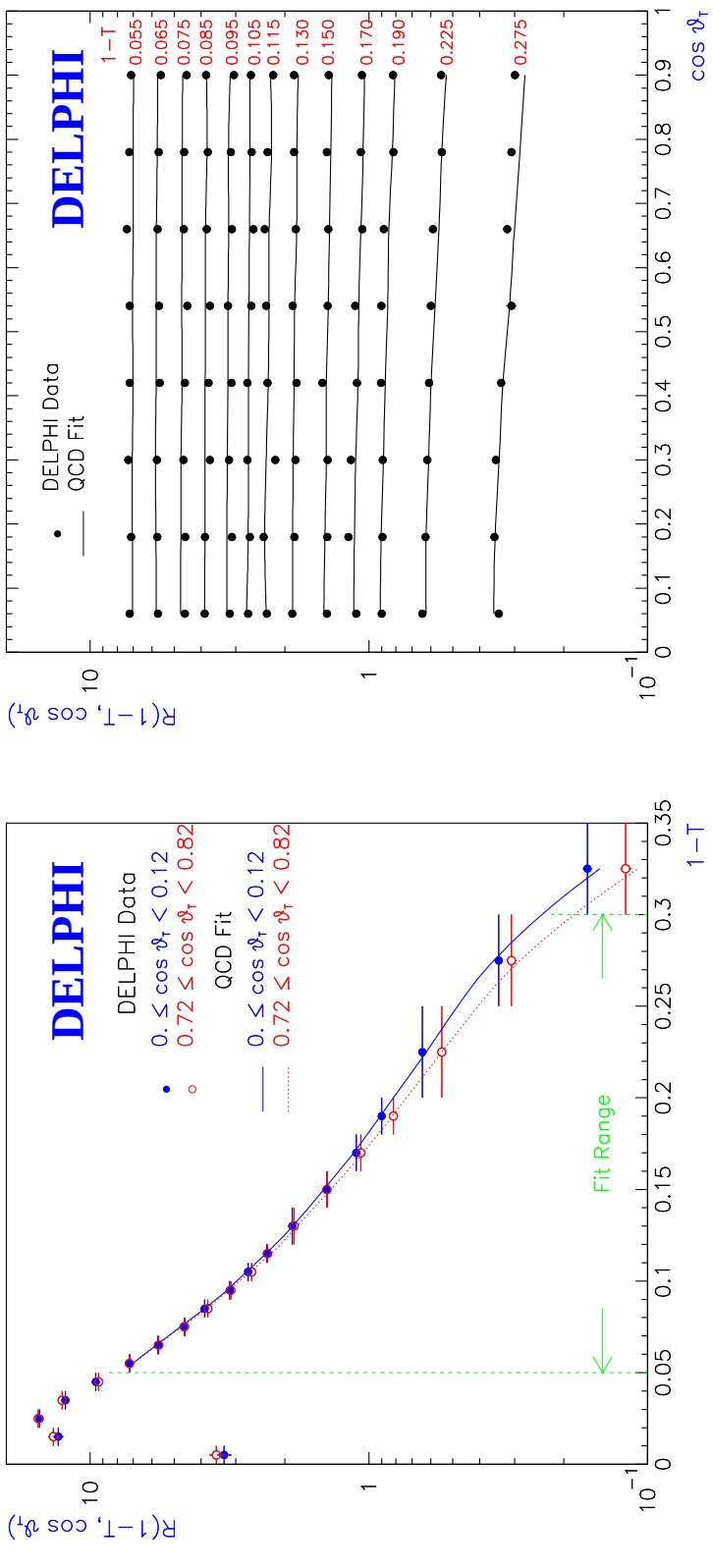

Figure 6.3: (*left side*) QCD fits to the measured thrust distribution for two bins in $\cos\vartheta_{\mathrm{T}}$. (*right side*) Measured thrust distribution at various fixed values of $1 - \mathrm{T}$ as a function of $\cos\vartheta_{\mathrm{T}}$. The solid lines represent the QCD fit.

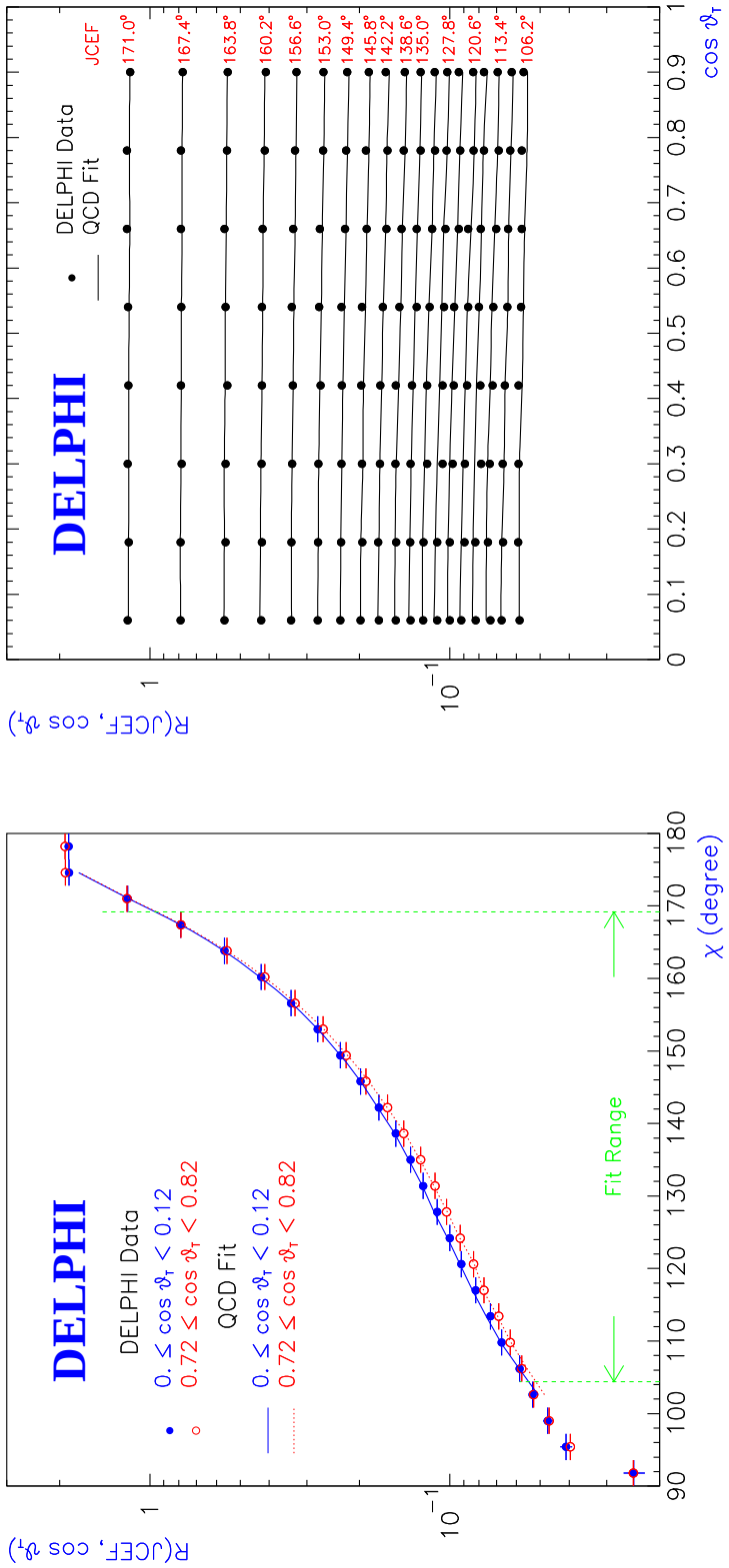

Figure 6.4: Same as Figure 6.3 but for the jet cone energy fraction JCEF

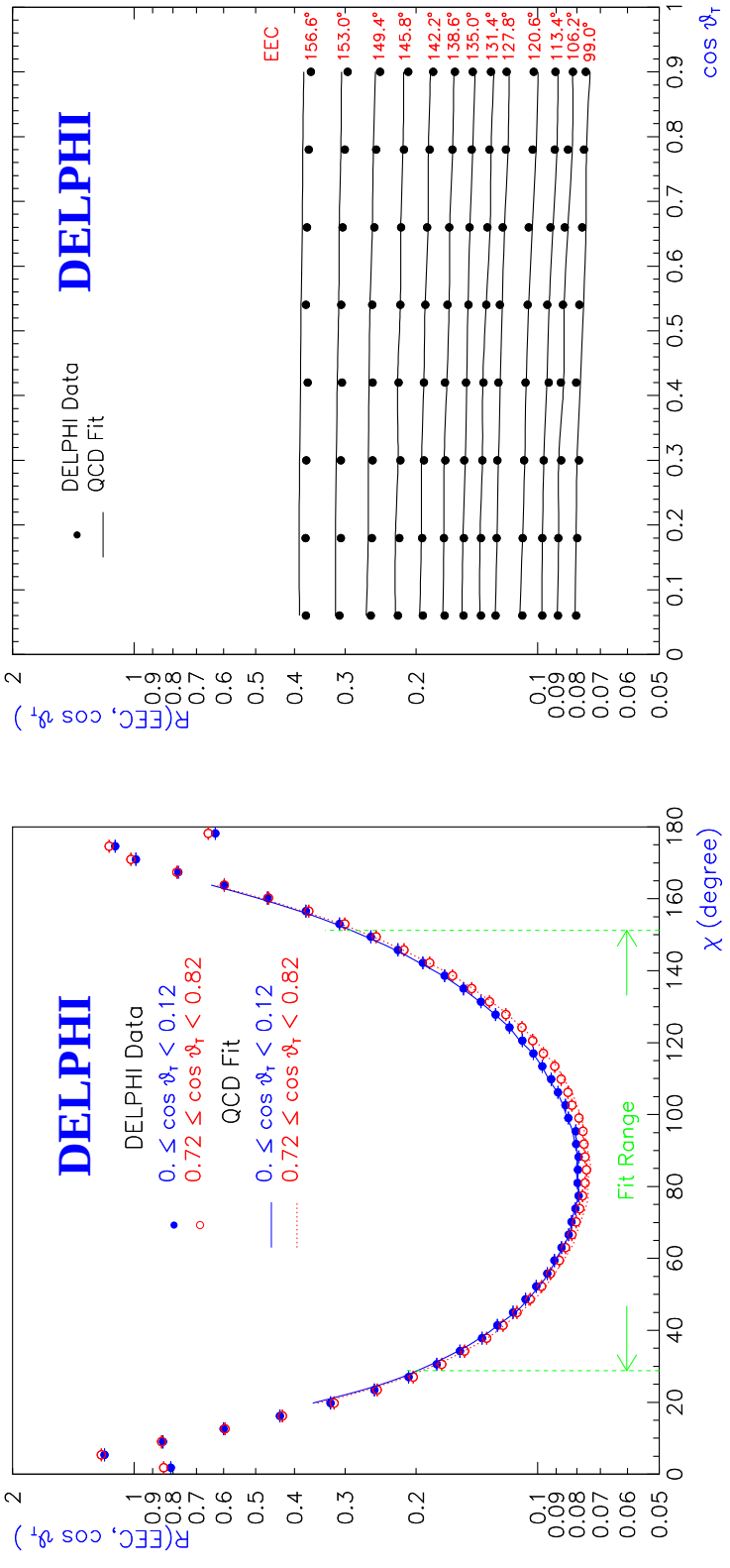

Figure 6.5: Same as Figure 6.3 but for the energy energy correlation EEC.

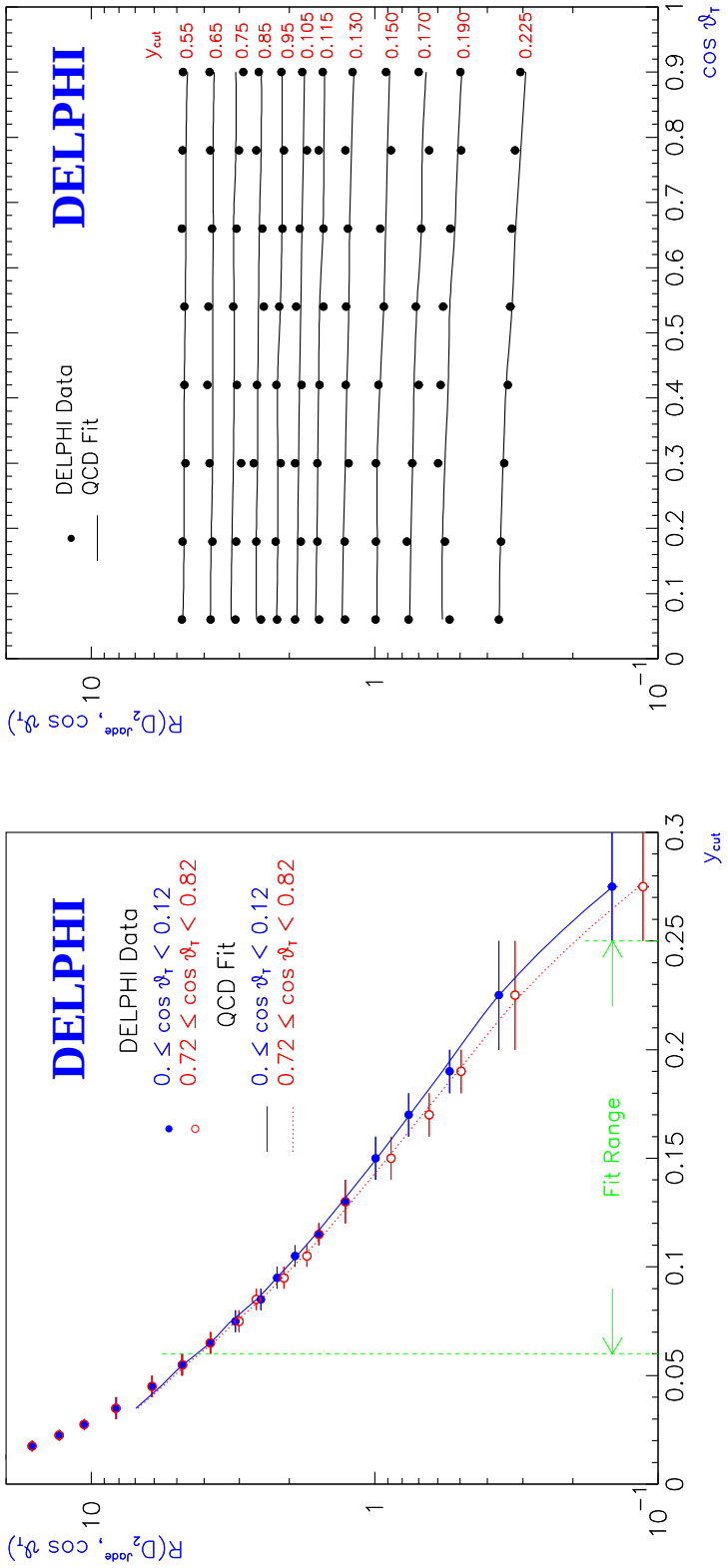

Figure 6.6: Same as Figure 6.3 but for the differential two jet rate with the Jade Algorithm D_2^{Jade}.

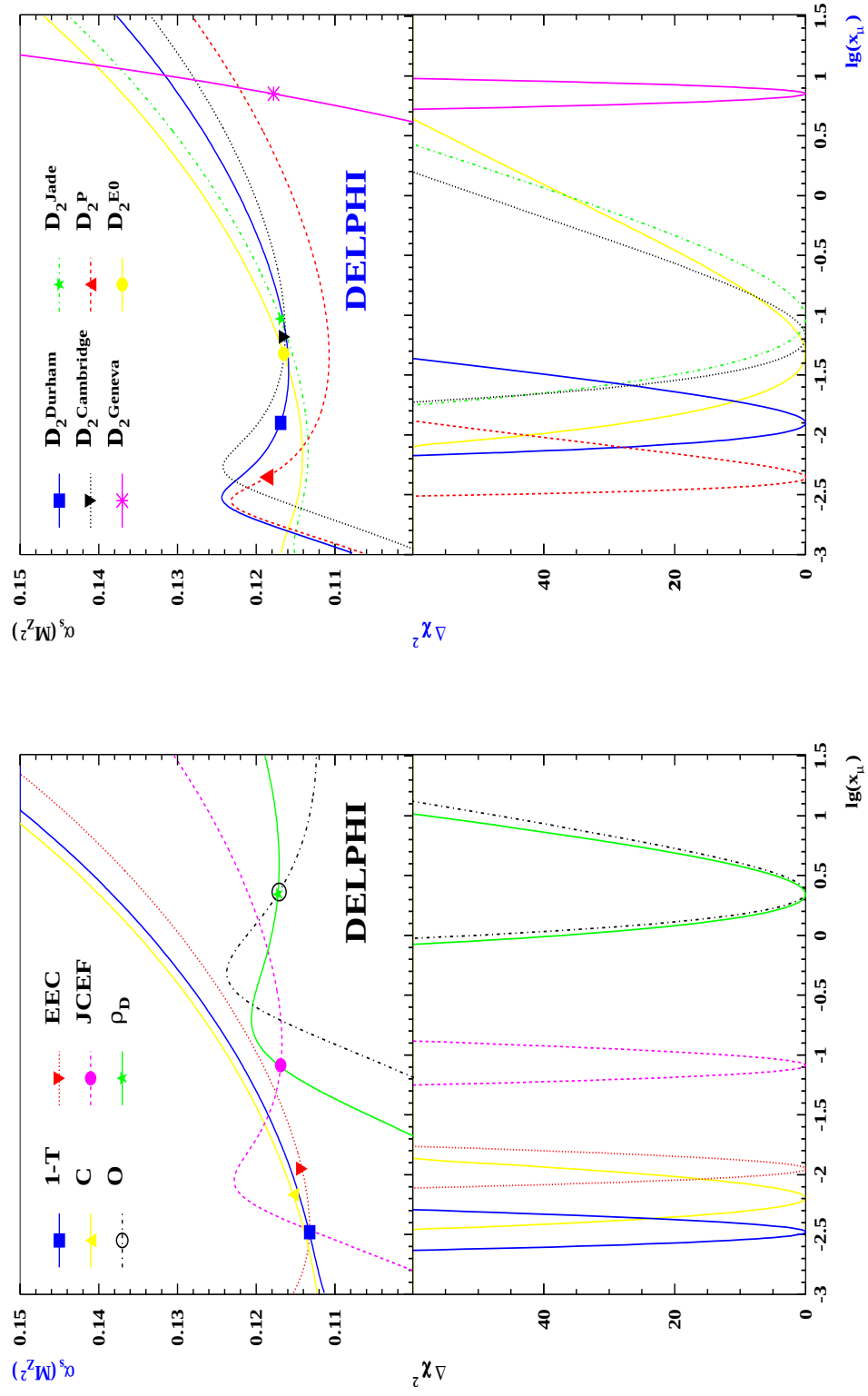

Figure 6.7: (*left side*) $\alpha_s(M_z^2)$ and $\Delta\chi^2 = \chi^2 - \chi^2_{\min}$ from $\mathcal{O}(\alpha_s^2)$ fits to the double differential distributions in $\cos\vartheta_T$ and $1-T$, C, O, EEC, JCEF, ρ_D as a function of the renormalization scale value. Additionally, the χ^2 minima are indicated in the $\alpha_s(M_z^2)$ curves. (*right side*) The same for the double differential distributions in $\cos\vartheta_T$ and the differential 2-jet rate applying the Durham, Cambridge, Geneva, Jade, P and E0 jet algorithm.

It should however be noted, that even for observables exhibiting a strong scale dependence of $\alpha_s(M_z^2)$, e.g. D_2^{Geneva}, the $\alpha_s(M_z^2)$ value for the experimentally optimized scale value is perfectly consistent with the average value.

Combining the 18 individual results from the $\alpha_s(M_z^2)$ measurements applying experimentally optimized renormalization scale values by using an unweighted average yields

$$\alpha_s(M_z^2) = 0.1170 \pm 0.0025$$

whereas the corresponding average for the measurements using the fixed scales $x_\mu = 1$ is $\alpha_s(M_z^2) = 0.1234 \pm 0.0154$ (see Section 6.4.2). For the experimentally optimized scales the scatter of the individual measurements is significantly reduced.

In order to verify the consistency of the $\alpha_s(M_z^2)$ values from individual measurements with experimentally optimized scales, a χ^2 has been computed on the basis of the experimental and the hadronization uncertainties, which have been added quadratically. No additional renormalization scale uncertainty has been considered here. The resulting value is $\chi^2/n_{df} = 9.6/17$, i.e. the individual measurements are clearly consistent and the measured values can be understood without assuming any additional theoretical uncertainty due to the renormalization scale dependence of the theoretical predictions.

The idea behind the common analysis of such a large number of observables is to optimize the use of the information contained in the complex structure of multi-hadron events. Errors due to the corrections for hadronization effects may be expected to cancel to some extent in the averaging procedure. To test this expectation the analysis of each of the individual 18 observables is repeated by performing hadronization corrections with the different hadronization models and different settings for the model parameters as described in Section 6.3. This results in 7 times 18 individual α_s values. As a first test for each of the 18 observables the unweighted average value of α_s from the seven models is evaluated. The average value of the 18 α_s values is $\alpha_s(M_z^2) = 0.1177 \pm 0.0029$. In a second step for each of the 7 hadronization models an unweighted average of the corresponding 18 α_s values is calculated. Finally an unweighted average of the 7 average values for the different hadronization models is computed resulting in $\alpha_s(M_z^2) = 0.1177 \pm 0.0016$. The result confirms that the scatter of the average values due to different assumptions for hadronization corrections is significantly smaller than the uncertainty of ± 0.0025 of the mean value from 18 individual observables.

6.4.2 QCD Fits with a fixed Renormalization Scale Value

For comparison, the data have also been fitted in $\mathcal{O}(\alpha_s^2)$ applying the conventional, so-called 'physical' scale approach of choosing a fixed renormalization scale value $x_\mu = 1$.

The choice of an appropriate fit range for the $\alpha_s(M_z^2)$ measurement turns out to be problematic. As illustrated in Fig. 6.7 the range of renormalization scale values required for a consistent description of the data varies within several orders of magnitude for the individual observables. If the fit range is chosen to be identical to the range for experimentally optimized scales, the resulting perturbative prediction yields only a poor description of the data, which makes it difficult to interpret the significance of the measured $\alpha_s(M_z^2)$ values. It may be argued, that the fit range applied for experimentally optimized scales may not be appropriate for the choice $x_\mu = 1$, since it is known that the theoretical description for $x_\mu = 1$ is worse in particular in the 2-jet region [90].

Figure 6.8 shows a comparison of the QCD fits to the data with experimentally optimized and with fixed renormalization scale values $x_\mu = 1$ for the observables $1 - T$, ρ_H and D_2^P. For the fixed scale predictions, the deviations with respect to the data are not at all limited to the 2-jet region but can be observed also within the 3-jet region. In particular the slope of the experimental distributions cannot be described and a good description can in general only be achieved within the small kinematical region where the fit curve intersects with the data. Similar deviations can be observed for some other observables studied within this analysis.

The requirement that χ^2/n_{df} is approximately 1 can in general not be applied for the fixed scale measurements, since it would cause an unreasonably large reduction of the fit range for many observables. The oriented thrust distribution for example could be fitted only over a range of at most three bins in $1 - T$. Two different choices of fit ranges for the thrust distribution would then be possible. The first one corresponds to $1 - T$ values between 0.08 and 0.11 with $\alpha_s(M_z^2) = 0.1343$ and $\chi^2/n_{df} = 0.97$. The second one corresponds to $1 - T$ values between 0.14 and 0.20 with $\alpha_s(M_z^2) = 0.1442$ and $\chi^2/n_{df} = 1.23$. If these two fit ranges are now combined, i.e. $0.08 < 1 - T \leq 0.20$ the result is $\alpha_s(M_z^2) = 0.1391$ with $\chi^2/n_{df} = 219 \,/\, 55 = 3.38$ and a probability of $p = 2 \cdot 10^{-21}$. The description of B_{sum} is even worse for $x_\mu = 1$. Here the oriented distribution can for example only be described within one single interval of two bins in B_{sum} ranging from 0.16 to 0.20.

Another problem arises due to the poor stability of the $\alpha_s(M_z^2)$ values with respect to the variation of the fit range. Fig. 6.9 on page 101 shows for example the $\alpha_s(M_z^2)$ values derived from the B_{sum} distribution within different ranges of three bin inter-

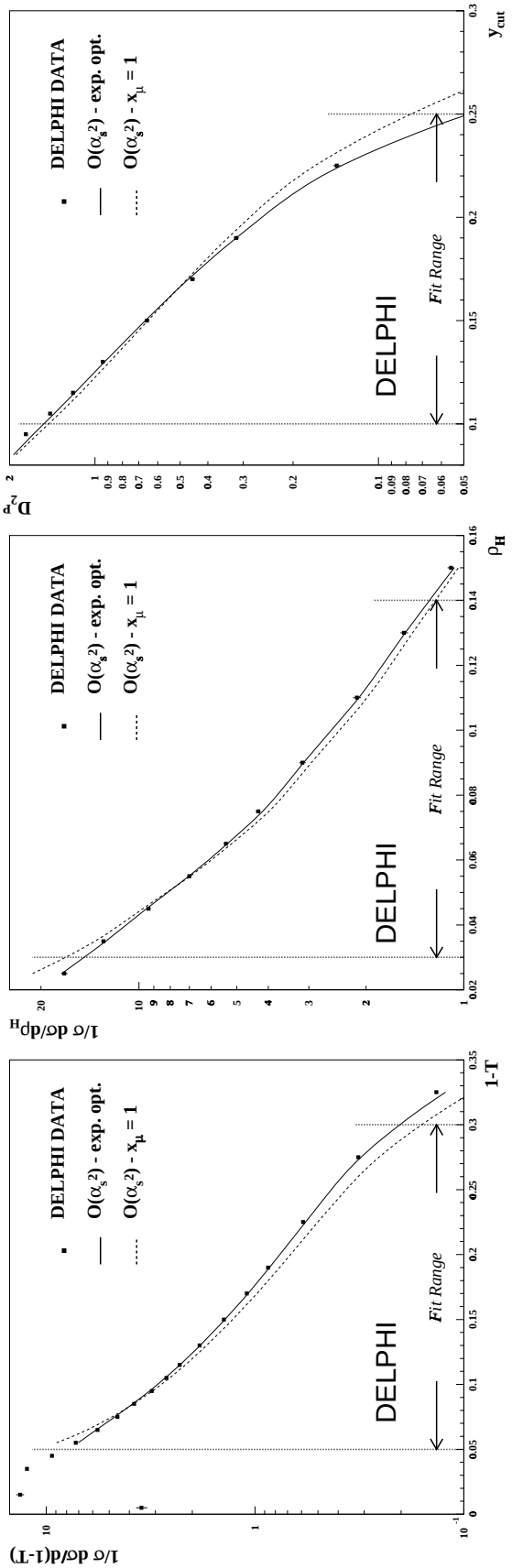

Figure 6.8: Comparison between $\mathcal{O}(\alpha_s^2)$ QCD fits with $x_\mu = 1$ and experimentally optimized renormalization scales for the observables $1-T$, ρ_H and D_2^P. DELPHI data and theoretical predictions are shown averaged over $\cos\vartheta_T$. The full (dotted) line correspond to fits with experimentally optimized renormalization scale values x_μ^{exp} ($x_\mu = 1$), respectively. The theoretical prediction is averaged over the bin width and drawn through the bin center.

vals. Stability of the $\alpha_s(M_z^2)$ values with respect to the fit range cannot be obtained if $x_\mu = 1.0$ is applied.

It should be noted, that B_{sum} is the observable with the largest corrections from the second order contribution of the perturbative expression (Eq. 6.3). Within the fit range applied, this contribution varies within $r_{NLO} = 0.74 - 0.98$ if $x_\mu = 1.0$ is applied. For the experimentally optimized scale value of $x_\mu = 0.0092$ the contribution from the second order term is still large and varies between $r_{NLO} = 0.40 - 0.82$. Applying this scale value for the determination of $\alpha_s(M_z^2)$ within the three bin fit intervals as described above, the measured $\alpha_s(M_z^2)$ values are extraordinary stable and well within the estimated uncertainty due to the variation of the renormalization scale.

In Figure 6.10 (page 102), the results from fits to the three bin fit intervals described above are shown for the thrust distribution. Again no stability of the $\alpha_s(M_z^2)$ values with respect to the variation of the fit range is achieved for measurements with $x_\mu = 1.0$. If however the scale value of $x_\mu = 0.0033$ from the fit including an experimental optimization is applied, the measured $\alpha_s(M_z^2)$ values are again very stable with respect to a variation of the fit range. The three bin intervals of the event shape distributions do not provide enough information to allow a combined fit of $\alpha_s(M_z^2)$ and the renormalization scale value. If however the fit range of the thrust distribution is separated into two almost disjunct fit intervals, and the renormalization scale value is optimized for both intervals individually, the $\alpha_s(M_z^2)$ values derived from both intervals are almost identical (see Figure 6.10 and also Table 6.6 in Section 6.4.5 for details).

The slope of the measured $\alpha_s(M_z^2)$ values of the thrust distribution for measurements with $x_\mu = 1.0$ offers a simple explanation for the wide spread of the published $\alpha_s(M_z^2)$ values for this observable. Table 6.3 shows a summary of $\alpha_s(M_z^2)$ values determined from the thrust distribution with a fixed renormalization scale value $x_\mu = 1$.

Due to the large statistics within the 2-jet region, the measured α_s values depend strongly on the lower limit of the fit interval. The $\alpha_s(M_z^2)$ values from the measurements listed in Table 6.3 increase almost monotonously with the lower limit of the fit interval from $\alpha_s(M_z^2) = 0.118 \pm 0.009$ for $1 - T \leq 0.$ to $\alpha_s(M_z^2) = 0.145 \pm 0.015$ for $1 - T \leq 0.10$. The $\alpha_s(M_z^2)$ value from the OPAL Collaboration [85] is larger than one would expect naively from the consideration of the lower fit interval. The $\alpha_s(M_z^2)$ determination has however been made from the weighted thrust distribution $(1-T) \cdot 1/\sigma_{tot}\ d\sigma/dT$. The weighting by (1-T) prefers however the 3-jet region of large (1-T) values, with the consequence of an increased α_s value. The slightly larger value of the present analysis with respect to the SLD measurement can be understood due to the enhanced precision of the data within the 3-jet region (see e.g. Fig. 5.3 on page 75).

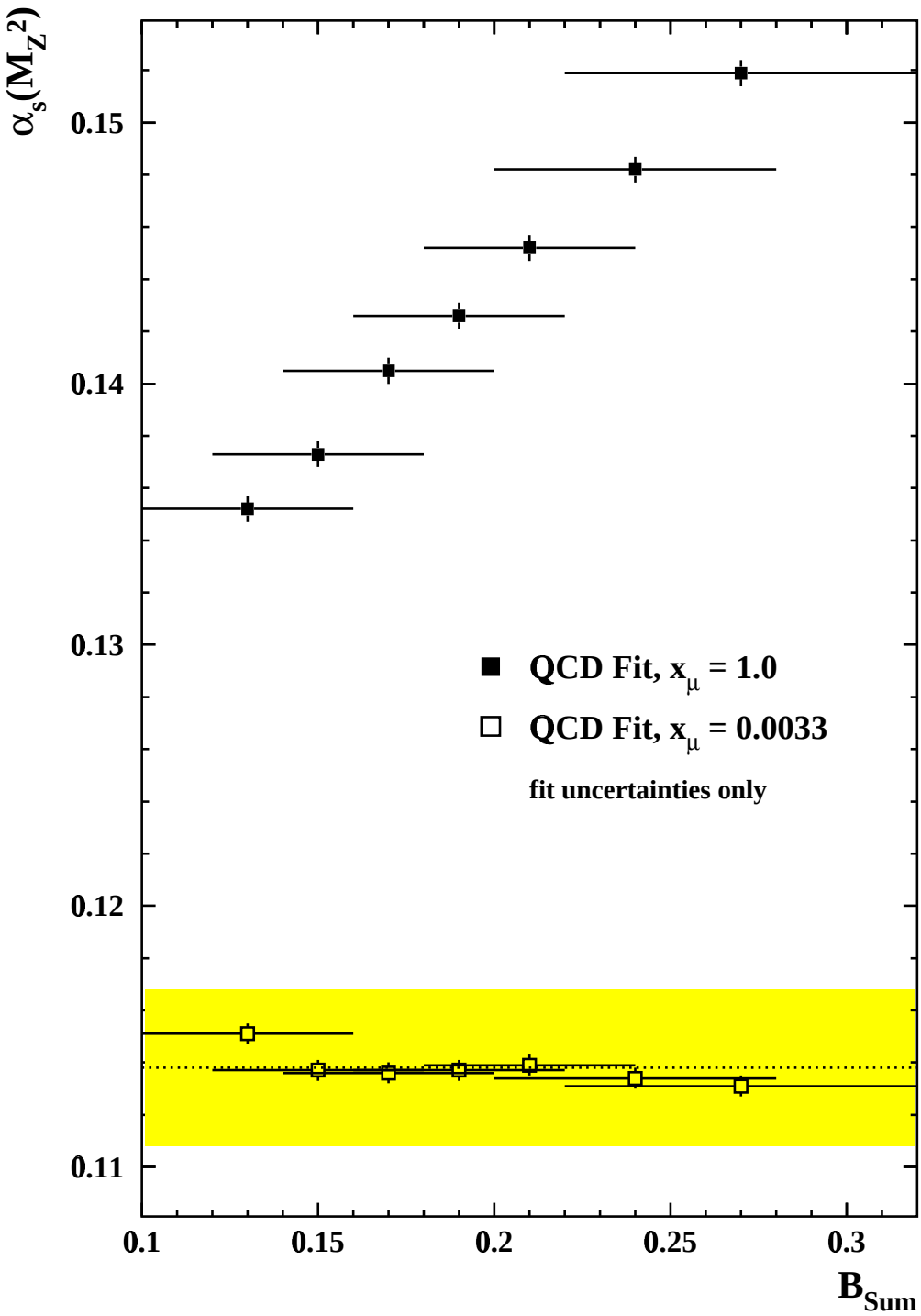

Figure 6.9: $\alpha_s(M_z^2)$ for the oriented B_{Sum} distribution in dependence on the fit range. $\mathcal{O}(\alpha_s^2)$ fits have been performed for all three bin intervals of the B_{Sum} distribution. The full symbols show the results for the fits with a renormalization scale value $x_\mu = 1.0$, the open dots indicate the results for fits with $x_\mu = 0.0033$, i.e. the experimentally optimized value obtained from the fit covering the full fit range as listed in Table 6.1. The horizontal bars indicate the fit ranges and the vertical bars represent the the uncertainties from the fits. The $\alpha_s(M_z^2)$ value derived from the fit to the complete fit range is indicated by the dotted line. The shaded band indicates the corresponding renormalization scale uncertainty as listed in Table 6.2.

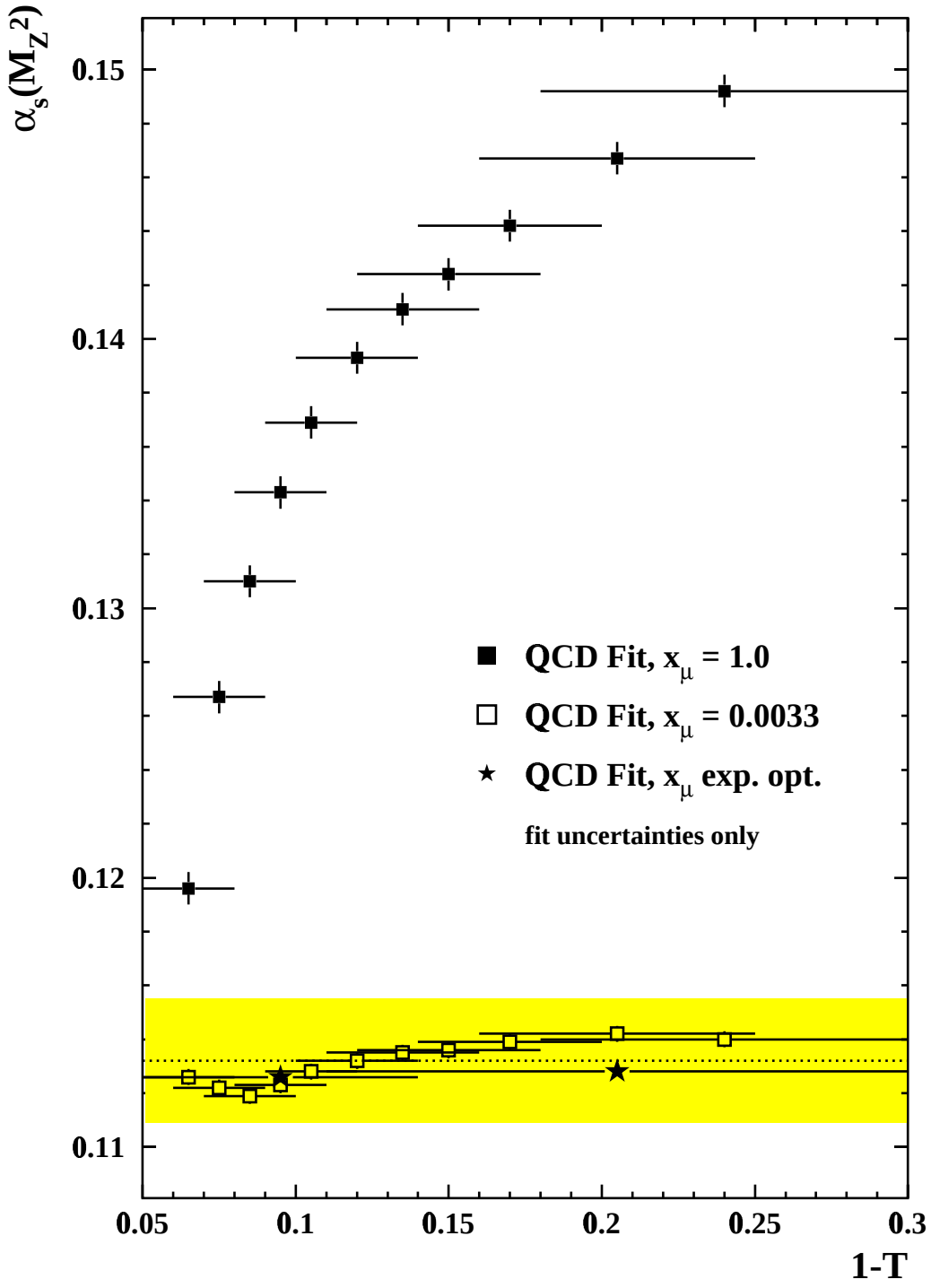

Figure 6.10: Same as Figure 6.9 but for the oriented thrust distribution. The star symbols represent the results from two additional fits, where the full fit range of the thrust distribution has been separated into two almost disjunct fit intervals and where the renormalization scale value has been optimized for both intervals individually (see also Section 6.4.5 for details).

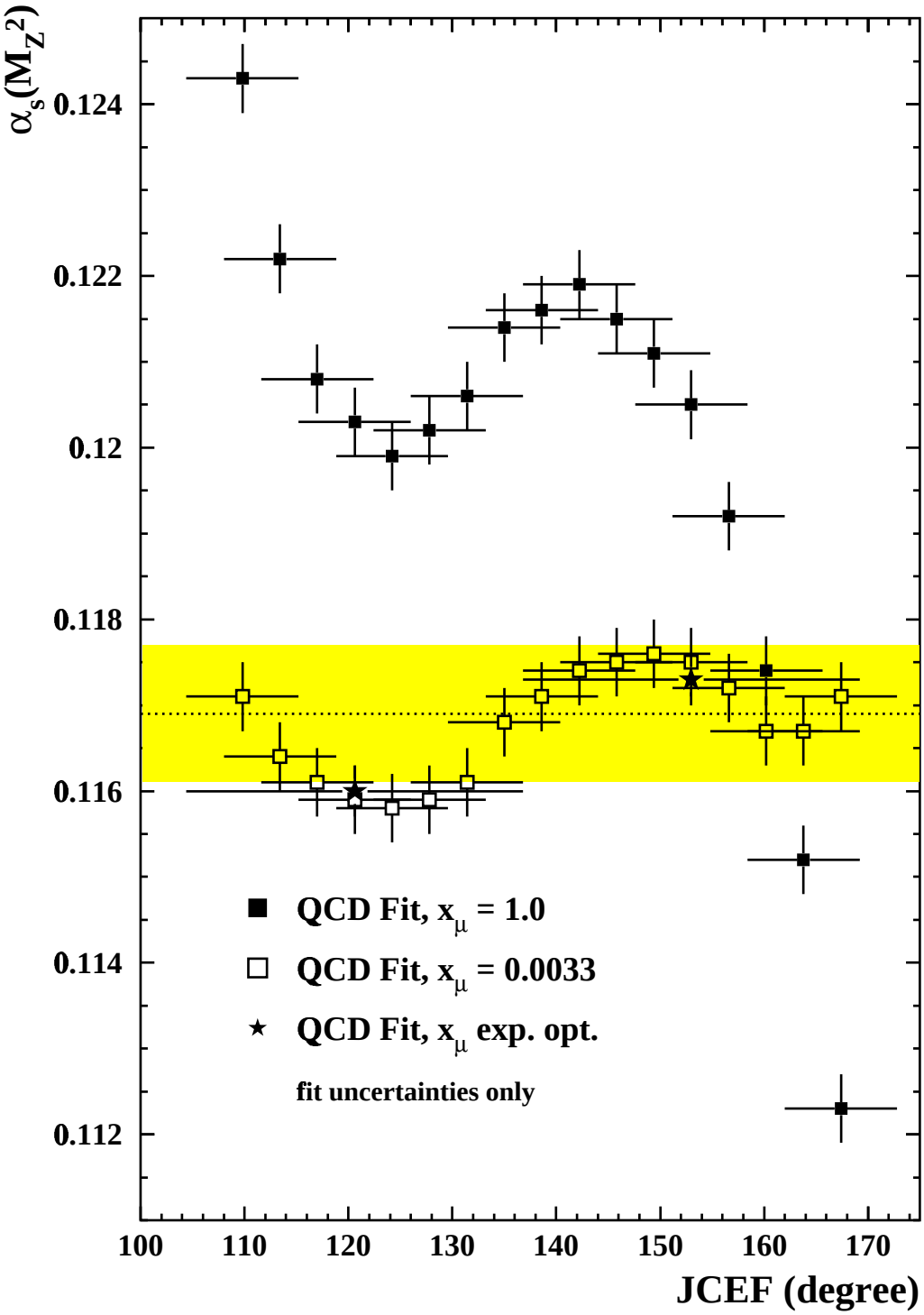

Figure 6.11: Same as Figure 6.10 but for the oriented $JCEF$ distribution.

Measurement	Reference	Fit Range (1-T)	$\alpha_s(M_z^2) \pm \Delta\alpha_s$ (tot.)
L3	[91]	0.00 - 0.29	0.118 ± 0.009
SLD	[84]	0.06 - 0.32	0.125 ± 0.020
DELPHI	[92]	0.09 - 0.30	0.140 ± 0.003
ALEPH	[93]	0.10 - 0.30	0.145 ± 0.015
this analysis		0.05 - 0.30	0.133 ± 0.006
OPAL	[85]	0.085 - 0.285	0.145 ± 0.001

Table 6.3: $\alpha_s(M_z^2)$ values determined from the Thrust Distribution by applying a fixed renormalization scale value $x_\mu = 1$. The error of the OPAL and the DELPHI measurement from reference [92] covers only the statistical uncertainty. The ALEPH measurement has been done by applying a renormalization scale value $x_\mu = 0.5$. For this comparison it has been recalculated by using the renormalization scale uncertainty given in reference [93]. The OPAL value originates from a fit to the weighted thrust distribution, where the 3-jet region of the distribution is statistically preferred.

Figure 6.11 (page 103) shows the results from $\alpha_s(M_z^2)$ fits to three bin intervals of the $JCEF$ distribution. The stability of the fits with $x_\mu = 1.0$ with respect to a variation of the fit range is partially increased. For $JCEF$ values between about 110° and 150° the variation in $\alpha_s(M_z^2)$ is of about 2%. If the fits are however compared with the corresponding fits applying the experimentally optimized scale value of $x_\mu = 0.0820$, the differences with respect to a variation of the fit range are remarkable.

The somewhat better behaviour of the $JCEF$ distribution may be understood due to the smaller deviation of the experimentally optimized renormalization scale value from $x_\mu = 1.0$. Also the contribution of the second order term is quite small for $JCEF$. Within the fit range applied, the average ratio of the second with respect to the first order contribution is $\langle r_{NLO} \rangle \sim 25\%$ if $x_\mu = 1$ is applied and only $\langle r_{NLO} \rangle \sim 6\%$ for the experimentally optimized renormalization scale value of $x_\mu = 0.0820$.

Due to the problems associated with the choice of the fit range as explained above, the fit ranges for the analysis with a fixed renormalization scale value as well as for the analyses applying theoretically motivated scale setting methods have therefore been chosen identical to the analysis with experimentally optimized scale values, regardless of the χ^2 values of the fits.

The results of the fits with a fixed renormalization scale value $x_\mu = 1$ are summarized in Table 6.4 and the $\alpha_s(M_z^2)$ values obtained are shown in Figure 6.13 on page 109. As can be seen from the χ^2/n_{df} values of the fits, the choice of $x_\mu = 1$ yields only a poor description of the data for most of the observables, for many observables

the description is even unacceptable. Combining the 18 individual $\alpha_s(M_z^2)$ measurements by using an unweighted average yields $\alpha_s(M_z^2) = 0.1234 \pm 0.0154$. Computing a χ^2 value on the basis of the total uncertainty but without considering any renormalization scale uncertainty analogously to the average value from experimentally optimized scale values, the resulting value is $\chi^2/n_{df} = 168/17$, thus in this case the individual measurements are clearly inconsistent with each other.

Observable	$\alpha_s(M_z^2)$	$\Delta\alpha_s$ (Scale)	$\Delta\alpha_s$ (Tot.)	χ^2/n_{df}
EEC	0.1297	$\pm$ 0.0037	$\pm$ 0.0042	10.7
AEEC	0.1088	$\pm$ 0.0015	$\pm$ 0.0050	2.04
JCEF	0.1191	$\pm$ 0.0012	$\pm$ 0.0024	7.7
1 – T	0.1334	$\pm$ 0.0042	$\pm$ 0.0051	25.9
O	0.1211	$\pm$ 0.0065	$\pm$ 0.0077	2.38
C	0.1352	$\pm$ 0.0043	$\pm$ 0.0053	12.0
B_{Max}	0.1311	$\pm$ 0.0073	$\pm$ 0.0083	1.67
B_{Sum}	0.1403	$\pm$ 0.0056	$\pm$ 0.0071	8.1
ρ_H	0.1325	$\pm$ 0.0036	$\pm$ 0.0049	5.1
ρ_S	0.1441	$\pm$ 0.0055	$\pm$ 0.0062	2.16
ρ_D	0.1181	$\pm$ 0.0012	$\pm$ 0.0039	1.54
D_2^{E0}	0.1267	$\pm$ 0.0033	$\pm$ 0.0052	1.35
D_2^{P0}	0.1265	$\pm$ 0.0026	$\pm$ 0.0041	1.31
D_2^{P}	0.1154	$\pm$ 0.0019	$\pm$ 0.0036	5.35
D_2^{Jade}	0.1249	$\pm$ 0.0030	$\pm$ 0.0042	1.53
D_2^{Durham}	0.1222	$\pm$ 0.0034	$\pm$ 0.0046	3.47
D_2^{Geneva}	0.0735	$\pm$ 0.0071	$\pm$ 0.0116	120.
$D_2^{Cambridge}$	0.1202	$\pm$ 0.0021	$\pm$ 0.0033	1.32

Table 6.4: Results of the $\alpha_s(M_z^2)$ measurements using a fixed renormalization scale $x_\mu = 1$. For each observable, the value of $\alpha_s(M_z^2)$, the uncertainty from the variation of the scale between $0.5 \leq x_\mu \leq 2$, the total uncertainty and the χ^2/n_{df} of the fit are shown.

6.4.3 Calculation of a Weighted Average

When trying to average the results of the $\alpha_s(M_z^2)$ measurements from the individual observables, one is confronted with the problem, that the individual results are correlated due to common uncertainties.

For gaussian distributed errors and provided the correlations between the individual measurements are described correctly by a covariance matrix C, a weighted average $\overline{x}$ can be calculated by minimizing the the χ^2 function

$$\chi^2 = \sum_{i,j}(x_i - \overline{x})(x_j - \overline{x})(C^{-1})_{ij} \tag{6.4}$$

with respect to $\overline{x}$. This procedure requires however a precise knowledge of the covariance matrix. Owing to the dominance of theoretical uncertainties of the measurements of $\alpha_s(M_z^2)$ the correlation pattern is unknown.

One possible solution to this problem is to reject the calculation of a weighted average at all and to quote the individual measurement with the smallest theoretical uncertainty as the final result. This is motivated by the point of view, that additional measurements involving large theoretical uncertainties cannot improve a precise measurement based on small theoretical uncertainties. This argumentation is followed in Section 6.8 after considering the additional studies described in the following section.

On the other hand the strategies applied for the estimation of the systematic and theoretical uncertainties may result in too optimistic values for particular observables. Additional and unknown sources of theoretical and systematic uncertainties may affect individual measurements or may even lead to an increase of the total error for all observables considered. Even if the correlations between the measurements would be known exactly, the weighted average calculated with the mathematical standard procedure will be pulled to the single most optimistic result.

This problem can be avoided completely by the calculation of a simple mean value in combination with a simple rms as it has been done in the previous sections. The simple rms indicates the scatter of all measurements around their common mean and does not depend on the individual errors quoted for each measurement. All measurements are treated on equal footing and the overall uncertainty is dominated by those measurements which are strongly deviating from the common mean, i.e. in general by the measurements with larger uncertainties.

A method for the calculation of a weighted average in case of unknown correlations between the measurements has been proposed in [94]. Here the effective size of the correlations is estimated from the data itself. The method has been applied for example for the calculation of a world average of the strong coupling [95, 96, 97] and a detailed discussion and comparison with other suggested methods can be found in reference [97]. In absence of a detailed knowledge of the covariance matrix it is assumed that the different measurements i and j are correlated with a fixed fraction ρ_{eff} of the maximum possible correlation $\mathrm{C_{ij}^{max}}$:

$$C_{ij} = \rho_{\mathrm{eff}} C_{ij}^{max} \quad i \neq j, \quad \text{with} \quad C_{ij}^{max} = \sigma_i \sigma_j \quad . \tag{6.5}$$

For $\rho_{\mathrm{eff}} = 0$ the measurements are treated as uncorrelated, for $\rho_{\mathrm{eff}} = 1$ as 100% correlated entities. The quality of the weighted average $\overline{x}$ can be judged by means of the corresponding χ^2 value (Eq. 6.4). For uncorrelated data one expects χ^2 to be equal to the number of degrees of freedom n_{df}. If the χ^2 is significantly smaller than its expectation value, the measurement uncertainties are either overestimated or positively correlated. When positive correlations are known to be present, then the χ^2 can be used to estimate the size of the effective correlation ρ_{eff} by adjusting its value such that $\chi^2(\rho_{\mathrm{eff}})$ is equal to n_{df}.

A χ^2 larger than n_{df} indicates that the errors of the individual measurements are underestimated. In this case an estimate of the size of the correlations is not possible. Within this analysis this case occurs for example for the $\alpha_s(M_z^2)$ measurements with a fixed renormalization scale value. For the calculation of a weighted average the value of ρ_{eff} is assumed to be identical with the one determined from the measurements with experimentally optimized scales and the errors of the individual measurements are scaled by a common factor until $\chi^2 = n_{df}$ is satisfied.

Applying this method to the 18 observables studied, the weighted average from the α_s measurements applying experimentally optimized renormalization scale values (see Fig. 6.12) yields:

$$\alpha_s(M_z^2) = 0.1168 \pm 0.0026$$

with ρ_{eff} being 0.635. Both the central value and its uncertainty are almost identical to the unweighted average and the rms quoted above, clearly indicating the robustness of the error estimate.

The corresponding average for the fixed scale measurements yields $\alpha_s(M_z^2) = 0.1232 \pm 0.0116$ (see Fig. 6.13). Here, the uncertainty of the average is largely increased with respect to the result from applying experimentally optimized scale values.

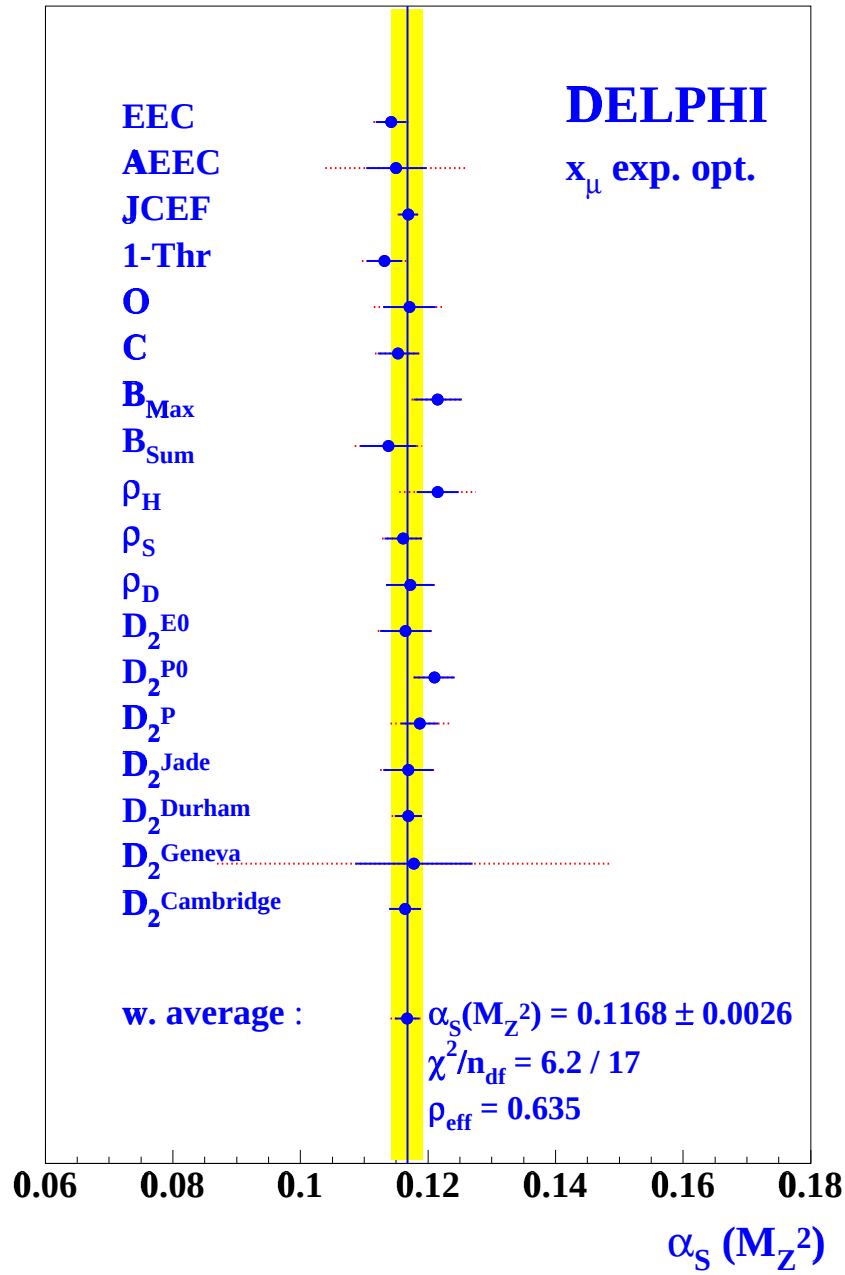

Figure 6.12: Results of the QCD fits applying experimentally optimized scales for 18 oriented event shape distributions. The error bars indicated by the solid lines are the quadratic sum of the experimental and the hadronization uncertainty. The error bars indicated by the dotted lines include also the additional uncertainty due to the variation of the renormalization scale due to scale variation around the central value x_μ^{exp} in the range $0.5 \cdot x_\mu^{exp} \leq x_\mu \leq 2 \cdot x_\mu^{exp}$. Also shown is the correlated weighted average (see text). The χ^2-value is given before readjusting according to Eq. 6.4.

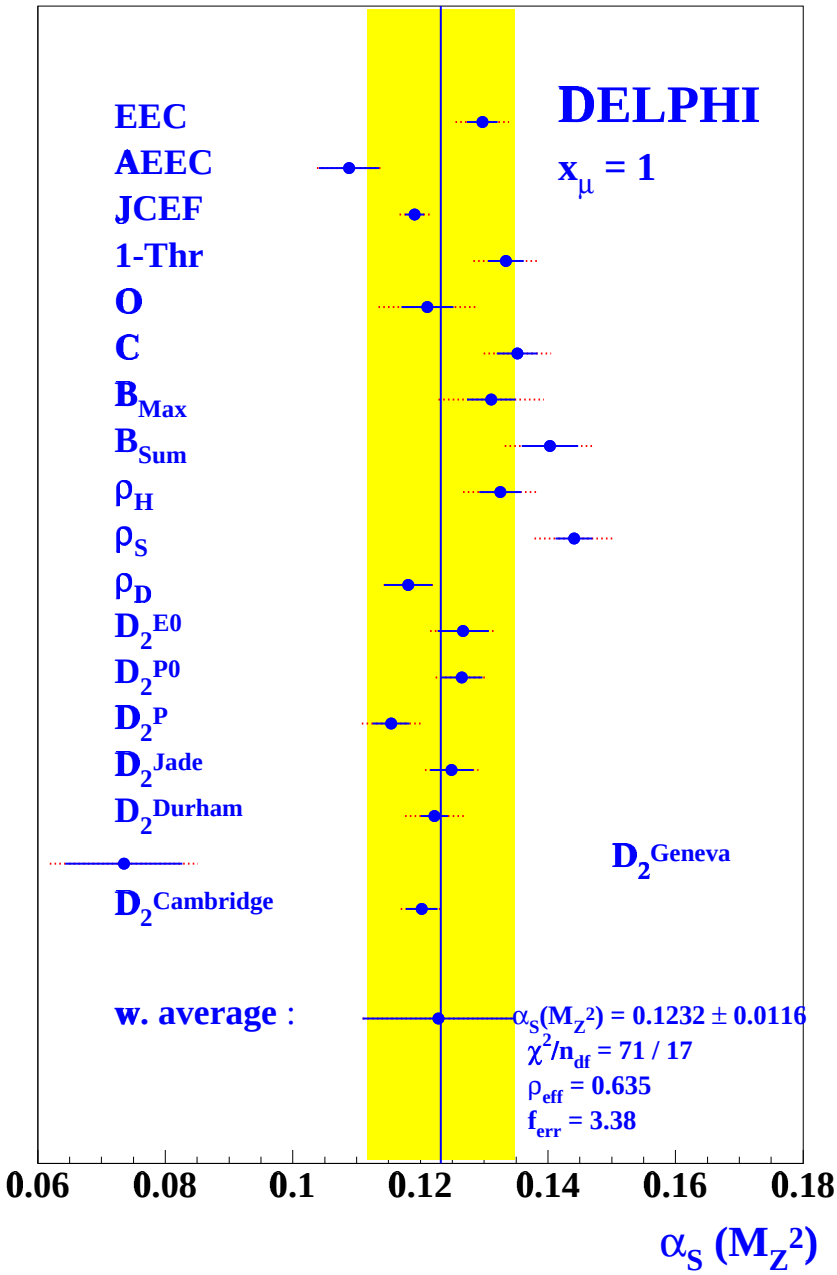

Figure 6.13: Results of the QCD fits applying a fixed renormalization scale $x_\mu = 1$. The error bars indicated by the solid lines are the quadratic sum of the experimental and the hadronization uncertainty. The error bars indicated by the dotted lines include also the additional uncertainty due to the variation of the renormalization scale around the central value from $0.5 \leq x_\mu \leq 2$. Also shown is the correlated weighted average. It has been calculated assuming the same effective correlation $\rho_{\text{eff}} = 0.635$ as for the fit results applying experimentally optimized scales. The χ^2/n_{df} for the weighted average is 71/17, where the χ^2 given corresponds to the value before adjusting ρ_{eff}. In order to yield $\chi^2/n_{df} = 1$, the errors have to be scaled by a factor $f_{\text{err}} = 3.38$.

The χ^2/n_{df} for this average yields 71/17 before adjusting ρ_{eff}. The χ^2 is largely reduced with respect to the χ^2 for the unweighted average due to the consideration of the renormalization scale uncertainties as given in table 6.4, but the individual measurements are still inconsistent in this case. Considering an effective correlation ρ_{eff} of 0.635 like for the measurements with experimentally optimized scales, the errors have additionally to be scaled by a common factor $f_{\text{err}} = 3.38$ in order to obtain $\chi^2/n_{df} = 1$.

According to reference [97], the method for calculating the weighted average introduced above is closest to a mathematically appropriate treatment of the correlated errors, however the χ^2 and the uncertainties derived do not have the same mathematical and probabilistic interpretation than the standard procedure. In particular the weighted average does not necessarily lead to the smallest possible error. In [97] it is shown for example, that the error of the weighted average is increased if less significant measurements are included. Within this analysis however, the α_s measurements from all individual observables have been considered, regardless of their significance. This is motivated by the fact that the errors of the α_s measurements quoted in Table 6.2 and in the following subsections contain all uncertainties which can be evaluated from a careful experimental analysis. The spread of the α_s measurements may however not be explainable by the individual uncertainties alone, there may be additional uncertainties, which cannot be derived from a single observable. Therefore the above averaging procedure has been applied and robustness of the error estimate has been preferred instead of minimizing the error.

Obviously the error estimate cannot cover a possible common shift of all measured $\alpha_s(M_z^2)$ values with respect to the true value. From an experimental point of view, such a shift could only be inferred by comparing with different types of theoretical calculations, like all orders resummed predictions or Padé approximation, which are studied in the following sections.

6.4.4 Discussion of Systematic and Theoretical Uncertainties

In order to investigate the contribution of individual sources of systematic and theoretical uncertainties to the weighted average, the $\alpha_s(M_z^2)$ measurements have been repeated for all observables by applying different track and event selection criteria, hadronization models and model parameters and by varying the optimized renormalization scale values as described in detail in Section 6.3. For each of the modified strategies for the determination of $\alpha_s(M_z^2)$, a weighted average has been computed from the results of the α_s measurements for all eighteen observables. These results are listed in Table 6.5.

$\alpha_s(M_Z)$ measurement	$\alpha_s(M_Z)$ average	$\alpha_s(M_Z)$ shift
standard procedure	0.1168 ± 0.0026	
systematic uncertainties (see also pages 72 and 86)		
modified track selection criteria	0.1168 ± 0.0026	± 0.0000
modified event selection criteria	0.1169 ± 0.0026	$+0.0001$
additional cut on momentum imbalance	0.1168 ± 0.0030	± 0.0000
modified tracking efficiency	0.1174 ± 0.0027	$+0.0006$
modified momentum resolution	0.1171 ± 0.0026	$+0.0003$
analysis including neutral tracks	0.1154 ± 0.0032	-0.0014
enlarged lower bound of fit range	0.1178 ± 0.0035	$+0.0010$
reduced lower bound of fit range	0.1166 ± 0.0030	-0.0002
enlarged upper bound of fit range	0.1166 ± 0.0026	-0.0002
reduced upper bound of fit range	0.1169 ± 0.0028	$+ 0.0001$
hadronization uncertainties (see also page 87)		
JETSET 7.4 PS	0.1172 ± 0.0030	$+0.0004$
ARIADNE 4.06c	0.1167 ± 0.0026	-0.0001
HERWIG 5.8 c	0.1170 ± 0.0050	$+0.0002$
JETSET 7.3 PS D + BEC	0.1192 ± 0.0038	$+0.0024$
JETSET 7.3 PS D, $Q_0 = 0.5$ GeV	0.1161 ± 0.0026	-0.0007
JETSET 7.3 PS D, $Q_0 = 4.0$ GeV	0.1184 ± 0.0046	$+0.0016$
renormalization scale uncertainty (see also page 88)		
$x_\mu^{exp} \rightarrow 0.5 \cdot x_\mu^{exp}$	0.1169 ± 0.0038	$+0.0001$
$x_\mu^{exp} \rightarrow 2.0 \cdot x_\mu^{exp}$	0.1174 ± 0.0029	$+0.0006$

Table 6.5: Individual sources of experimental and theoretical uncertainties contributing to the weighted average of $\alpha_s(M_z^2)$: Shown are the weighted averages of $\alpha_s(M_z^2)$ determined from the analyses of 18 observables by applying modified selection criteria, modified fit ranges, different hadronization models and model parameters and by varying the experimentally optimized renormalization scale values as described in Section 6.3. Also given is the corresponding shift of the average $\alpha_s(M_z^2)$ values with respect to the standard procedure.

The main systematic uncertainty comes from the inclusion of neutral tracks in the analysis. For α_s measurements from data distributions including charged and neutral tracks, the weighted average of $\alpha_s(M_z^2)$ is shifted to a lower value by about 1.2% with respect to the analysis using charged tracks only. However, also the error of the average value is about 20% larger. This can be understood due to the inhomogeneities in the DELPHI calorimetry (see also discussion in Section 4.2.3) in combination with increased systematic uncertainties of the corresponding data distributions.

The uncertainty of the weighted average derived from the variation of the experimentally optimized renormalization scale value x_μ^{exp} for each observable between $0.5 \cdot x_\mu^{exp}$ and $2.0 \cdot x_\mu^{exp}$ is small ($\sim 0.5\%$). This can be explained by the fact, that for most observables the experimentally optimized renormalization scale value is close to the scale value, where the strong coupling is least sensitive with respect to its variation (see Figure 6.14 on page 118 and discussion in Section 6.4.6).

The largest theoretical uncertainty is estimated by considering Bose-Einstein Correlations (BEC) for the hadronization corrections calculated with JETSET 7.3 PS. Here, the weighted average is shifted to a larger value by about 2%. Again the error of the average value of $\alpha_s(M_z^2)$ is larger ($\sim 50\%$) than for the standard analysis. It should be noted, that only a crude estimate of BEC effects on the determination of $\alpha_s(M_z^2)$ is possible since the JETSET algorithm for modelling BEC is known to violate energy momentum conservation [60, 98]. This is restored only by an additional Lorentz boost.

A larger uncertainty arises also from the variation of the Parton Shower parameter Q_0 to 4.0 GeV for the calculation of the hadronization corrections. Here the weighted average is shifted to a larger value by about 1.4%. The uncertainty of the average is about 80% larger than for the standard analysis. It should be noted, that by applying such a large value for Q_0 the Monte Carlo model is unable to describe the measured data [61], it has however been considered in order to simulate the smaller number of up to 4 partons, which are produced by second order QCD Matrix Elements.

6.4.5 Stability of the Renormalization Scale Value with respect to the Variation of the Fit Range

An underlying assumption for the $\mathcal{O}(\alpha_s^2)$ QCD fits to the shape observables is that the value of α_s is approximately independent of a variation of the renormalization scale within the fit range. To check this assumption, a cross check for the differential two jet rate observables has been performed following a suggestion in [99]. For these observables the QCD fits have been repeated, allowing the renormalization scale

to vary proportionally to y_{cut}, i.e. $\mu^2 = x_\mu y_{cut}\sqrt{s}$. The differences in the $\alpha_s(M_z^2)$ determination have been found to be of the order of a few per mille for the individual jet rate observables and to be less than two per mille for the average of these observables.

A further investigation has been performed for all observables of Table 6.1. The fit range listed in Table 6.1 has been divided into two separate regions, allowing a maximum overlap of one bin. $\alpha_s(M_z^2)$ has been determined applying experimentally optimized scales for both regions independently. The fits were successful for all observables except D_2^{Geneva}, where the resulting fit ranges were too small to allow the fits to converge. The results of these fits are shown in Table 6.6.

It is well known from previous analyses incorporating an experimentally optimization of the renormalization scale, that the sensitivity for the renormalization scale value can be increased by extending the fit range with respect to the 2-jet region. One reason for the reduced sensitivity within the 3-jet region are the larger uncertainties of the data due to the reduced statistics. Another theoretical argument arises from the smaller variation of the perturbative coefficients of the shape distributions within the 3-jet region [6].

For most of the observables listed in Table 6.6 the measurement uncertainties are significantly larger if the fit range is restricted with respect to the 2-jet region. However, for some observables a surprisingly accurate determination of both $\alpha_s(M_z^2)$ and x_μ can be obtained for both fit intervals, in particular for $JCEF$, $1-T$, C and $D_2^{P_0}$. For these observables, the renormalization scale values for both intervals agree within a factor two or even better. No systematic trend of the two values of the renormalization scale for the two fit ranges (dominated by two respectively three jet events) is observed. For many of the observables, the agreement between the two α_s values measured is very good.

In a further step, the two $\alpha_s(M_z^2)$ values have been combined for each observable according to their statistical weight (see Table 6.6). These α_s values have been combined by calculating a weighted average as described in Section 6.4.3. The resulting average value of $\alpha_s(M_Z^2) = 0.1168 \pm 0.0025$ is identical to the value determined from the standard procedure.

Observable	Fit Range	$\alpha_s(M_z^2) \pm \Delta\alpha_s$(Fit)	$x_\mu \pm \Delta x_\mu$(Fit)	$\overline{\alpha_s}(M_z^2)$
EEC	28.8°-90.0°	0.1194 ± 0.0011	0.0568 ± 0.0181	0.1151 ± 0.0003
	90.0°-151.2°	0.1148 ± 0.0003	0.0037 ± 0.0005	
AEEC	25.2°-46.8°	0.1148 ± 0.0040	0.0067 ± 0.0029	0.1145 ± 0.0031
	43.2°-64.8°	0.1141 ± 0.0048	0.0069 ± 0.0037	
JCEF	104.4°-136.8°	0.1160 ± 0.0003	0.0385 ± 0.0094	0.1167 ± 0.0003
	136.8°-169.2°	0.1173 ± 0.0003	0.0740 ± 0.0048	
$1-T$	0.05 - 0.12	0.1126 ± 0.0003	0.0042 ± 0.0004	0.1126 ± 0.0003
	0.11 - 0.30	0.1128 ± 0.0007	0.0023 ± 0.0006	
O	0.24 - 0.36	0.1218 ± 0.0022	0.93 ± 0.31	0.1168 ± 0.0017
	0.32 - 0.44	0.1097 ± 0.0026	4.25 ± 2.01	
C	0.24 - 0.48	0.1150 ± 0.0003	0.0079 ± 0.0010	0.1150 ± 0.0003
	0.48 - 0.72	0.1162 ± 0.0021	0.0076 ± 0.0053	
B_{Max}	0.10 - 0.18	0.1229 ± 0.0036	0.0072 ± 0.0290	0.1210 ± 0.0006
	0.16 - 0.24	0.1209 ± 0.0006	0.0292 ± 0.0204	
B_{Sum}	0.12 - 0.18	0.1145 ± 0.0017	0.0113 ± 0.0061	0.1133 ± 0.0015
	0.18 - 0.24	0.1088 ± 0.0033	0.0030 ± 0.0030	
ρ_H	0.03 - 0.06	0.1192 ± 0.0011	0.0055 ± 0.0022	0.1194 ± 0.0011
	0.06 - 0.14	0.1213 ± 0.0036	0.0066 ± 0.0431	
ρ_S	0.10 - 0.16	0.1221 ± 0.0228	0.032 ± 0.827	0.1145 ± 0.0013
	0.14 - 0.30	0.1145 ± 0.0013	0.0004 ± 0.0004	
ρ_D	0.05 - 0.10	0.1212 ± 0.0013	1.18 ± 0.24	0.1208 ± 0.0012
	0.08 - 0.30	0.1195 ± 0.0024	11.4 ± 17.7	
D_2^{E0}	0.07 - 0.12	0.1162 ± 0.0008	0.033 ± 0.019	0.1161 ± 0.0008
	0.12 - 0.25	0.1122 ± 0.0059	0.006 ± 0.066	
D_2^{P0}	0.05 - 0.10	0.1210 ± 0.0008	0.117 ± 0.080	0.1209 ± 0.0007
	0.10 - 0.18	0.1207 ± 0.0014	0.095 ± 0.054	
D_2^{P}	0.10 - 0.16	0.1284 ± 0.0037	0.0027 ± 0.0002	0.1173 ± 0.0016
	0.14 - 0.25	0.1149 ± 0.0017	0.0049 ± 0.0007	
D_2^{Jade}	0.06 - 0.12	0.1176 ± 0.0013	0.147 ± 0.088	0.1175 ± 0.0013
	0.11 - 0.28	0.1125 ± 0.0086	0.014 ± 0.185	
D_2^{Durham}	0.015 - 0.070	0.1175 ± 0.0005	0.0113 ± 0.0014	0.1175 ± 0.0005
	0.070 - 0.216	0.1458 ± 0.0143	0.0020 ± 0.0004	
$D_2^{Cambridge}$	0.011 - 0.050	0.1171 ± 0.0006	0.044 ± 0.014	0.1171 ± 0.0006
	0.040 - 0.180	0.1171 ± 0.0054	0.179 ± 0.502	

Table 6.6: Results of $\alpha_s(M_z^2)$ fits to different intervals of oriented shape distributions. The fit range for each observable has been splitted into two (almost) independent intervals. For each observable the two fit ranges and the corresponding results for $\alpha_s(M_z^2)$ and x_μ are shown together with uncertainties as determined from the fits. In the case of asymmetric errors the higher value is given. Also shown is the weighted average $\overline{\alpha_s}(M_z^2)$ for the α_s values from the two fit intervals. The fits for D_2^{Geneva} did not converge.

6.4.6 Scale Setting Methods from Theory

Three different theoretical approaches for the determination of an optimized renormalization scheme are described in Section 2.3. For perturbative predictions in $\mathcal{O}(\alpha_s^2)$, the problem of finding an optimized scheme corresponds to the determination of an optimized renormalization scale value. These optimized scale values are determined as described below.

(*i*) Principle of minimal sensitivity (PMS):

The PMS optimization amounts to the determination of the renormalization scale value, which minimizes the sensitivity of theoretical prediction with respect to its variation. It has been determined by solving the following equation numerically:

$$\frac{\partial}{\partial x_\mu}\left\{\frac{1}{\sigma_{tot}}\frac{d\sigma}{dY}\right\} = 0 \tag{6.6}$$

where the theoretical prediction $1/\sigma_{tot}\ d\sigma/dY$ for the shape observable Y has been integrated over the fit range applied.

(*ii*) Method of effective charges (ECH):

In $\mathcal{O}(\alpha_s^2)$ perturbation theory, the ECH scale value has to be chosen in such a way that the second order term vanishes:

$$B(Y,\cos\vartheta_T) + (2\pi\beta_0 \ln(x_\mu) - 2)A(Y,\cos\vartheta_T) = 0\ . \tag{6.7}$$

For the determination of the ECH scale value the unweighted first and second order coefficients $A(Y,\cos\vartheta_T)$ and $B(Y,\cos\vartheta_T)$ have been integrated over the fit range applied and Eq. 6.7 has been solved numerically.

(*iii*) The method of Brodsky, Lepage and MacKenzie (BLM):

In $\mathcal{O}(\alpha_s^2)$, the BLM scale is fixed by the requirement that x_μ is chosen in such a way that the flavour dependence n_f of the second order term (Eq. 3.28) is removed:

$$\frac{\partial}{\partial n_f}\left\{B(Y,n_f) + (2\pi\beta_0 \ln(x_\mu) - 2)A(Y)\right\}\Big|_{n_f=5} = 0\ . \tag{6.8}$$

Also the above equation has been solved numerically and the perturbative coefficients have been integrated over the fit range applied

The results of the $\alpha_s(M_z^2)$ measurements for the individual observables applying the different scale setting prescriptions are listed in tables 6.7 and 6.8. The weighted averages calculated according to the method described in section 6.4.3 yield the following results for the different methods applied:

(*i*) PMS method :

$$\alpha_s(M_Z^2) = 0.1154 \pm 0.0045 \qquad (\chi^2/n_{df} = 19/17)$$

(*ii*) ECH method :

$$\alpha_s(M_Z^2) = 0.1155 \pm 0.0044 \qquad (\chi^2/n_{df} = 19/17)$$

(*iii*) BLM method :

$$\alpha_s(M_Z^2) = 0.1174 \pm 0.0068 \qquad (\chi^2/n_{df} = 29/13)$$

to be compared with $\alpha_s(M_Z^2) = 0.1168 \pm 0.0026$ ($\chi^2/n_{df} = 6.2/17$) using the experimentally optimized scales.

The weighted averages for the different theoretical methods are in agreement with the average using experimentally optimized scales. The scatter of the individual measurements is lowest for the experimentally optimized scales and highest for the BLM method.

For the ECH and the PMS approaches the $\alpha_s(M_z^2)$ values from the individual measurements are consistent. The results from both methods are very similar, the correlation ρ between ECH and PMS scales is almost 1. It should be noted that the consistency of the $\alpha_s(M_z^2)$ measurements for the PMS and the ECH approaches are of different quality than the consistency obtained by using experimentally optimized renormalization scale values. In the case of PMS and ECH scales the consistency is obtained by assuming an uncertainty due to the variation of the renormalization scale values between $x_\mu^{opt}/2$ and $2x_\mu^{opt}$. whereas for experimentally optimized scale values the individual measurements are perfectly consistent even if no additional uncertainty due to the variation of the renormalization scale is assumed (see Section 6.4.1, page 97).

In the case of the BLM method the χ^2/n_{df} indicates that the individual $\alpha_s(M_z^2)$ measurements are inconsistent. Moreover, the fits using the scales predicted by the BLM method did not converge at all for the observables $JCEF$, O, ρ_D and D_2^{Geneva}.

Figure 6.14 shows the correlation between the logarithms of the experimentally optimized scales and the logarithms of the scales predicted by the ECH, PMS and the BLM methods. For the ECH and the PMS method there are significant correlations of $\rho = 0.75 \pm 0.11$. In the case of BLM there is a slightly negative correlation of $\rho = -0.34 \pm 0.25$, compatible with zero.

The results obtained suggest that the ECH and the PMS methods are useful procedures for obtaining an optimized scale value in those cases where an experimental optimization can not be performed. The BLM method however does not seem to be suitable for the determination of $\alpha_s(M_z^2)$.

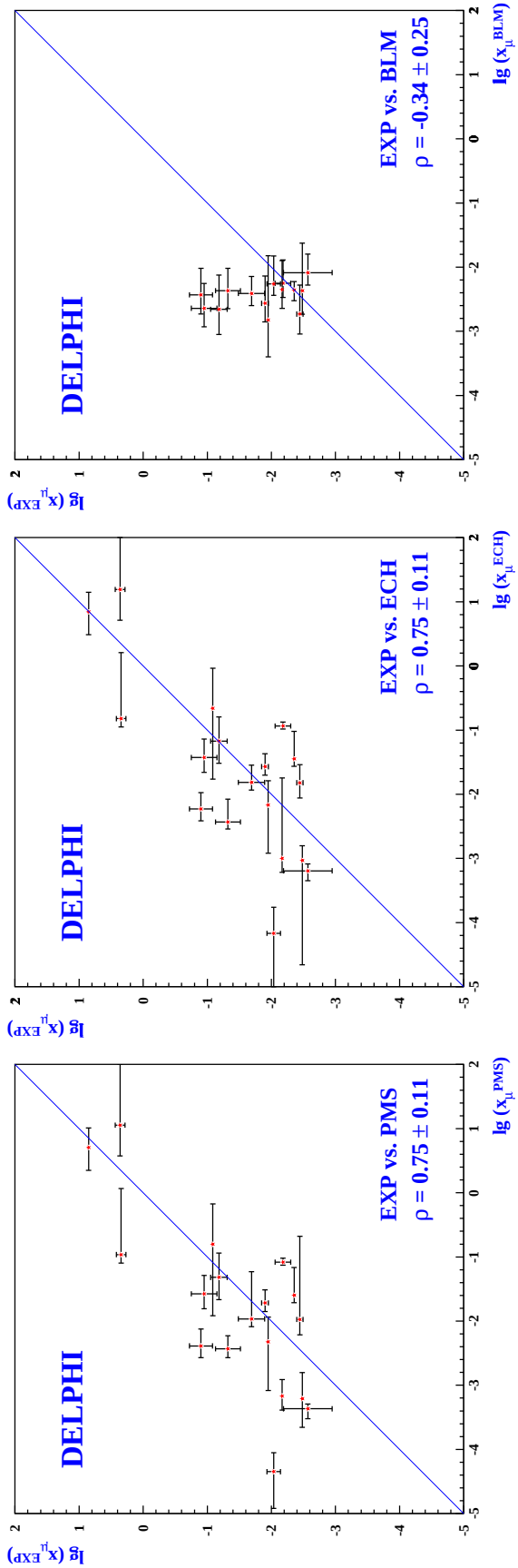

Figure 6.14: Comparison between the logarithms of the experimentally optimized renormalization scales and the logarithms of scales predicted by PMS, ECH and the BLM method. The vertical error bars indicated represent the scale uncertainties from the 2-parameter fits in x_μ and α_s . The horizontal bars represent the range of renormalization scale values for the theoretically motivated scale setting methods evaluated from the individual bins within the fit range of each distribution, whereas the central value has been derived by considering the full theoretical prediction within the fit range.

Observable	$\alpha_s^{EXP}(M_Z^2)$	$\alpha_s^{PMS}(M_Z^2)$	$\alpha_s^{ECH}(M_Z^2)$	$\alpha_s^{BLM}(M_Z^2)$
EEC	0.1142	0.1133	0.1135	0.1142
AEEC	0.1150	0.1063	0.1064	0.1179
JCEF	0.1169	0.1168	0.1169	
$1-\mathrm{T}$	0.1132	0.1101	0.1111	0.1133
O	0.1171	0.1128	0.1124	
C	0.1153	0.1119	0.1124	0.1144
$\mathrm{B_{Max}}$	0.1215	0.1222	0.1217	0.1268
$\mathrm{B_{Sum}}$	0.1138	0.1023	0.1021	0.1118
ρ_{H}	0.1215	0.1197	0.1198	0.1258
ρ_{S}	0.1161	0.1154	0.1149	0.1169
ρ_{D}	0.1172	0.1190	0.1203	
$\mathrm{D_2^{E0}}$	0.1165	0.1145	0.1142	0.1143
$\mathrm{D_2^{P0}}$	0.1210	0.1204	0.1202	0.1232
$\mathrm{D_2^{P}}$	0.1187	0.1110	0.1108	0.1118
$\mathrm{D_2^{Jade}}$	0.1169	0.1137	0.1134	0.1137
$\mathrm{D_2^{Durham}}$	0.1169	0.1162	0.1159	0.1241
$\mathrm{D_2^{Geneva}}$	0.1178	0.1064	0.1171	
$\mathrm{D_2^{Cambridge}}$	0.1164	0.1164	0.1163	0.1124
w. average	0.1168 ± 0.0026	0.1154 ± 0.0045	0.1155 ± 0.0044	0.1174 ± 0.0068
χ^2/n_{df}	6.2 / 17	19 / 17	19 / 17	29 / 13

Table 6.7: Comparison of the $\alpha_s(M_z^2)$ values obtained using the different methods for evaluating the renormalization scale suggested by theory. For each observable the $\alpha_s(M_z^2)$ values using experimentally optimized scales and $\alpha_s(M_z^2)$ values for the scales predicted by the PMS, ECH and BLM methods are shown. The errors for the $\alpha_s(M_z^2)$ measurements are assumed to be identical for all methods (see table 6.2). The weighted averages are calculated using $\rho_{\mathrm{eff}} = 0.635$ and scaling the errors to yield $\chi^2/n_{df} = 1$ in the case of the PMS, ECH and the BLM methods (see text). The χ^2 given for the averaging correspond to the values before adjusting ρ_{eff} and rescaling the measurement uncertainties. The fits using the scales predicted by BLM did not converge for the observables JCEF, O, ρ_D and D_2^{Geneva}.

Observable	x_μ^{EXP}	x_μ^{PMS}	x_μ^{ECH}	x_μ^{BLM}
EEC	0.0112	0.0048	0.0068	0.0015
AEEC	0.0066	0.0830	0.1158	0.0056
JCEF	0.0820	0.1576	0.2189	0.0011
$1-\mathrm{T}$	0.0033	0.0006	0.0009	0.0043
O	2.30	11.33	15.53	0.0015
C	0.0068	0.0007	0.0010	0.0068
$\mathrm{B_{Max}}$	0.0204	0.0108	0.0153	0.0039
$\mathrm{B_{Sum}}$	0.0092	0.00005	0.00007	0.0055
ρ_{H}	0.0036	0.0106	0.0151	0.0019
ρ_{S}	0.0027	0.0004	0.0006	0.0082
ρ_{D}	2.21	0.1086	0.1511	0.0027
$\mathrm{D_2^{E0}}$	0.048	0.0037	0.0037	0.0043
$\mathrm{D_2^{P0}}$	0.112	0.0266	0.0374	0.0023
$\mathrm{D_2^{P}}$	0.0044	0.0253	0.0356	0.0044
$\mathrm{D_2^{Jade}}$	0.126	0.0041	0.0059	0.0037
$\mathrm{D_2^{Durham}}$	0.0126	0.0192	0.0270	0.0027
$\mathrm{D_2^{Geneva}}$	7.10	5.08	6.97	0.0002
$\mathrm{D_2^{Cambridge}}$	0.066	0.048	0.067	0.0022

Table 6.8: Comparison of the scale values obtained using the different methods for evaluating the renormalization scale. For each observable the central scale value as obtained from experimental optimization and the scale values predicted by the PMS, ECH and BLM methods are shown. For the theoretically motivated scale setting methods the values have been derived by considering the full theoretical prediction within the fit range. The variation of these scale values over the fit range is shown in Fig. 6.14.

6.5 Padé Approximation

At present, exact perturbative predictions for most observables are limited to $\mathcal{O}(\alpha_s^2)$. The calculation of the third order QCD matrix elements is yet not complete. So far only the tree level diagram for the production of five partons [100] and the virtual corrections to the four parton production [101] are available. These matrix elements allow the determination of α_s in $\mathcal{O}(\alpha_s^3)$ from 4-jet observables, which is subject of the study in reference [102].

The higher order contributions to a perturbative QCD series can however be estimated by means of Padé Approximations. The Padé Approximant $[N/M]$ to the series

$$S = S_0 + S_1 x + S_2 x^2 + \ldots + S_n x^n \tag{6.9}$$

is defined [103] by

$$[N/M] \equiv \frac{a_0 + a_1 x + a_2 x^2 + \ldots + a_N x^N}{1 + b_1 x + b_2 x^2 + \ldots + b_M x^M} \quad ; \quad N + M = n \tag{6.10}$$

and

$$[N/M] = S + \mathcal{O}(x^{N+M+1}) \ . \tag{6.11}$$

The set of equations (6.11) can be solved, and by considering the terms of $\mathcal{O}(x^{N+M+1})$ one can obtain an estimate of the next order term S_{N+M+1} of the original series. This is called the PA method. Furthermore, for an asymptotic series $[N/M]$ can be taken as an estimate of the sum (PS) of the series to all orders.

The PA method has been used successfully to estimate coefficients in statistical physics [103], and various quantum field theories including QCD [104]. Justifications for some of these successes have been found in mathematical theorems on the convergence and renormalization scale invariance of PAs [104]. The physical interpretation of the renormalization scheme dependence of the approximated predictions implies that in particular the diagonal Padé Approximants $[N/N+1]$ sum up correctly the most important part of higher order QCD contributions, i.e. the contributions related to the running of the strong coupling [105].

In many cases the PAs yield predictions for the higher order coefficients in perturbative series with high accuracy, whereas this accuracy is not expected for

the lower order predictions such as $\mathcal{O}(\alpha_s^3)$. For the application of the $\alpha_s(M_z^2)$ determination from event shapes, the Padé Approximation can serve as a reasonable estimate of the errors due to higher order corrections [106].

For each bin of our observables an estimate for the $\mathcal{O}(\alpha_s^3)$ coefficient $C(y)$ can be derived from [0/1] with $a_0 = A$, $b_1 = -B/A$:

$$C^{Padé}(y) = \frac{B^2(y)}{A(y)}. \tag{6.12}$$

It should be noted that the PA predictions $C^{Padé}(y)$ are positive by construction which will result in large errors for kinematical regions where the $\mathcal{O}(\alpha_s^3)$ contribution is negative. The fit range has therefore been determined in the following way: Starting from the same fit range as in $\mathcal{O}(\alpha_s^2)$, the fit has been accepted if $\chi^2/n_{df} \leq 5$. Otherwise the fit range was reduced bin by bin until the fit yielded $\chi^2/n_{df} \leq 5$.

In addition to the $\mathcal{O}(\alpha_s^3)$ fits in the Padé Approximation, the PS method has been used as an estimate of the sum of the perturbative series and $\alpha_s(M_z^2)$ has been extracted by fitting the [0/1] approximation directly to the data. Here, the fit range has been chosen to be the same as for the fits in the $\mathcal{O}(\alpha_s^3)$ Padé approximation. The χ^2 dependence of the $\alpha_s(M_z^2)$ fits applying the Padé Approximation as a function of the renormalization scale value x_μ is quite small, especially for the PS method. For most of the observables $\alpha_s(M_z^2)$ and x_μ could not be determined in a simultaneous fit. Therefore, the fits have been done choosing a fixed renormalization scale value $x_\mu = 1$. The uncertainty due to the scale dependence of $\alpha_s(M_z^2)$ has been estimated by varying x_μ between 0.5 and 2.

The fit results for the individual observables are listed in tables 6.9 and 6.10. The fit applying PS to the B_{Sum} distribution did not converge for any fit range chosen. For the D_2^{Geneva} distribution, the fits did not converge for either method.

Comparing the fit results of the $\mathcal{O}(\alpha_s^3)$ fits in Padé Approximation with the fit results in $\mathcal{O}(\alpha_s^2)$ applying $x_\mu = 1$, as given in table 6.4, the scale dependence of $\alpha_s(M_z^2)$ is reduced for most of the observables, as one would expect from measurements using exact calculations in $\mathcal{O}(\alpha_s^3)$. For the PS method, the reduction of the scale dependence is even stronger. Here, $\alpha_s(M_z^2)$ is less scale dependent than in the $\mathcal{O}(\alpha_s^2)$ fits for all observables considered. This observation is in very good agreement with the result from the analysis of the Bjorken sum rule [107], where the renormalization scheme dependence of the Padé Sum Prediction is found to be drastically reduced with respect to the original third order prediction.

Observable	Fit Range	$\alpha_s(M_z^2)$	$\Delta\alpha_s$ (Scale.)	$\Delta\alpha_s$ (Tot.)
EEC	$28.8° - 151.2°$	0.1189	± 0.0016	± 0.0026
AEEC	$25.2° - 64.8°$	0.1074	± 0.0030	± 0.0056
JCEF	$104.4° - 169.2°$	0.1169	± 0.0006	± 0.0016
$1 - T$	0.07 - 0.30	0.1207	± 0.0023	± 0.0036
O	0.24 - 0.32	0.1098	± 0.0014	± 0.0044
C	0.32 - 0.72	0.1208	± 0.0023	± 0.0039
B_{Max}	0.10 - 0.24	0.1183	± 0.0016	± 0.0042
B_{Sum}	0.14 - 0.18	0.1127	± 0.0016	± 0.0068
ρ_H	0.03 - 0.14	0.1230	± 0.0015	± 0.0036
ρ_S	0.10 - 0.30	0.1252	± 0.0024	± 0.0038
ρ_D	0.07 - 0.30	0.1045	± 0.0015	± 0.0040
D_2^{E0}	0.05 - 0.18	0.1159	± 0.0014	± 0.0042
D_2^{P0}	0.05 - 0.18	0.1199	± 0.0011	± 0.0034
D_2^{P}	0.10 - 0.20	0.1128	± 0.0008	± 0.0030
D_2^{Jade}	0.06 - 0.25	0.1142	± 0.0014	± 0.0032
D_2^{Durham}	0.015 - 0.16	0.1170	± 0.0009	± 0.0023
$D_2^{Cambridge}$	0.011 - 0.18	0.1164	± 0.0007	± 0.0026
average		0.1168 ± 0.0054	$\chi^2/n_{df} = 30 \ / \ 16$	

Table 6.9: Results on $\alpha_s(M_z^2)$ for QCD-Fits including the $\mathcal{O}(\alpha_s^3)$ Term in the Padé Approximation (PA). For each of the observables the fit range, $\alpha_s(M_z^2)$, the uncertainty due to scale variation between $0.5 \leq x_\mu \leq 2$ and the total uncertainty are shown. The experimental errors and the uncertainties due to the hadronization corrections are assumed to be the same as for the $\mathcal{O}(\alpha_s^2)$ measurements. The weighted average is calculated using $\rho_{\text{eff}} = 0.635$ and scaling the errors to yield $\chi^2/n_{df} = 1$ (see text). The χ^2 given for the averaging corresponds to the value before adjusting ρ_{eff} and rescaling the measurement uncertainties. The fit for D_2^{Geneva} did not converge.

Observable	$\alpha_s(M_z^2)$	$\Delta\alpha_s$ (Scale.)	$\Delta\alpha_s$ (Tot.)
EEC	0.1147	± 0.0003	± 0.0021
AEEC	0.1070	± 0.0002	± 0.0048
JCEF	0.1169	± 0.0003	± 0.0015
$1-\mathrm{T}$	0.1165	± 0.0003	± 0.0028
O	0.1135	± 0.0003	± 0.0042
C	0.1150	± 0.0003	± 0.0032
$\mathrm{B_{Max}}$	0.1196	± 0.0003	± 0.0039
ρ_{H}	0.1219	± 0.0004	± 0.0033
ρ_{S}	0.1161	± 0.0003	± 0.0029
ρ_{D}	0.1098	± 0.0003	± 0.0037
$\mathrm{D_2^{E0}}$	0.1136	± 0.0003	± 0.0040
$\mathrm{D_2^{P0}}$	0.1198	± 0.0003	± 0.0032
$\mathrm{D_2^{P}}$	0.1124	± 0.0003	± 0.0029
$\mathrm{D_2^{Jade}}$	0.1123	± 0.0003	± 0.0029
$\mathrm{D_2^{Durham}}$	0.1164	± 0.0003	± 0.0021
$\mathrm{D_2^{Cambridge}}$	0.1162	± 0.0003	± 0.0025
average	0.1157 ± 0.0037	$\chi^2/n_{df} = 17\ /\ 15$	

Table 6.10: Results on $\alpha_s(M_z^2)$ for QCD-Fits applying the Padé Sum Approximation (PS). For each of the observables $\alpha_s(M_z^2)$, the uncertainty due to scale variation between $0.5 \leq x_\mu \leq 2$ and the total uncertainty are shown. The experimental errors and the uncertainties due to the hadronization corrections are assumed to be the same as for the $\mathcal{O}(\alpha_s^2)$ measurements. The weighted average is calculated using $\rho_{\mathrm{eff}} = 0.635$ and scaling the errors to yield $\chi^2/n_{df} = 1$ (see text). The χ^2 given for the averaging corresponds to the value before adjusting ρ_{eff} and rescaling the measurement uncertainties. The fits for B_{Sum} and D_2^{Geneva} did not converge.

Figure 6.15 shows the scale dependence of $\alpha_s(M_z^2)$ applying the different QCD predictions to the distribution of the Jet Cone Energy Fraction as an example. There is almost no χ^2 dependence of the $\alpha_s(M_z^2)$ fits as a function of the renormalization scale for the PS prediction. For the fits applying $\mathcal{O}(\alpha_s^3)$ in the Padé Approximation, the χ^2 dependence is less than for the $\mathcal{O}(\alpha_s^2)$ prediction. The JCEF is one of the few observables, where a simultaneous fit of $\alpha_s(M_z^2)$ and x_μ is possible.

Assuming the same correlation as in the $\mathcal{O}(\alpha_s^2)$ fits, the weighted averages of $\alpha_s(M_z^2)$ over the observables used have been calculated as:

$$\alpha_s(M_Z^2) = 0.1168 \pm 0.0054$$

for the PA fits and

$$\alpha_s(M_Z^2) = 0.1157 \pm 0.0037$$

for the PS fits. The averages are in excellent agreement with the $\mathcal{O}(\alpha_s^2)$ value of $\alpha_s(M_Z^2) = 0.1168 \pm 0.0026$ using optimized scales. The scatter between the observables, however, is somewhat larger than in the $\mathcal{O}(\alpha_s^2)$ case, in particular for the PA fits. The χ^2/n_{df} for the average values is 30/16 and 17/15 respectively.

It should be noted, that the α_s values derived from the PA prediction are exceptionally small for AEEC, O and ρ_D. The α_s values from the PS prediction to AEEC and ρ_D are again very small, the α_s value from the Oblateness is somewhat increased if the PS prediction is applied. These three observables are however constructed by explicitly subtracting two shape observables from each other. The subtraction results in small or even negative NLO coefficients for these observables. The NLO coefficients of the Oblateness distribution are for example negative over almost the whole kinematical range (see Fig. 3.4). In view of the construction mechanism it might be expected that the NNLO coefficients for these observables have a larger chance for being negative over some kinematical range than for other observables. Thus a sign error of the NLLO Padé Approximants due to the positive definiteness of the prediction (Eq. 6.12) might explain the exceptional values of α_s. Ignoring these observables, the spread of the measurements would be significantly reduced and would be comparable to the result obtained with experimentally optimized scale values.

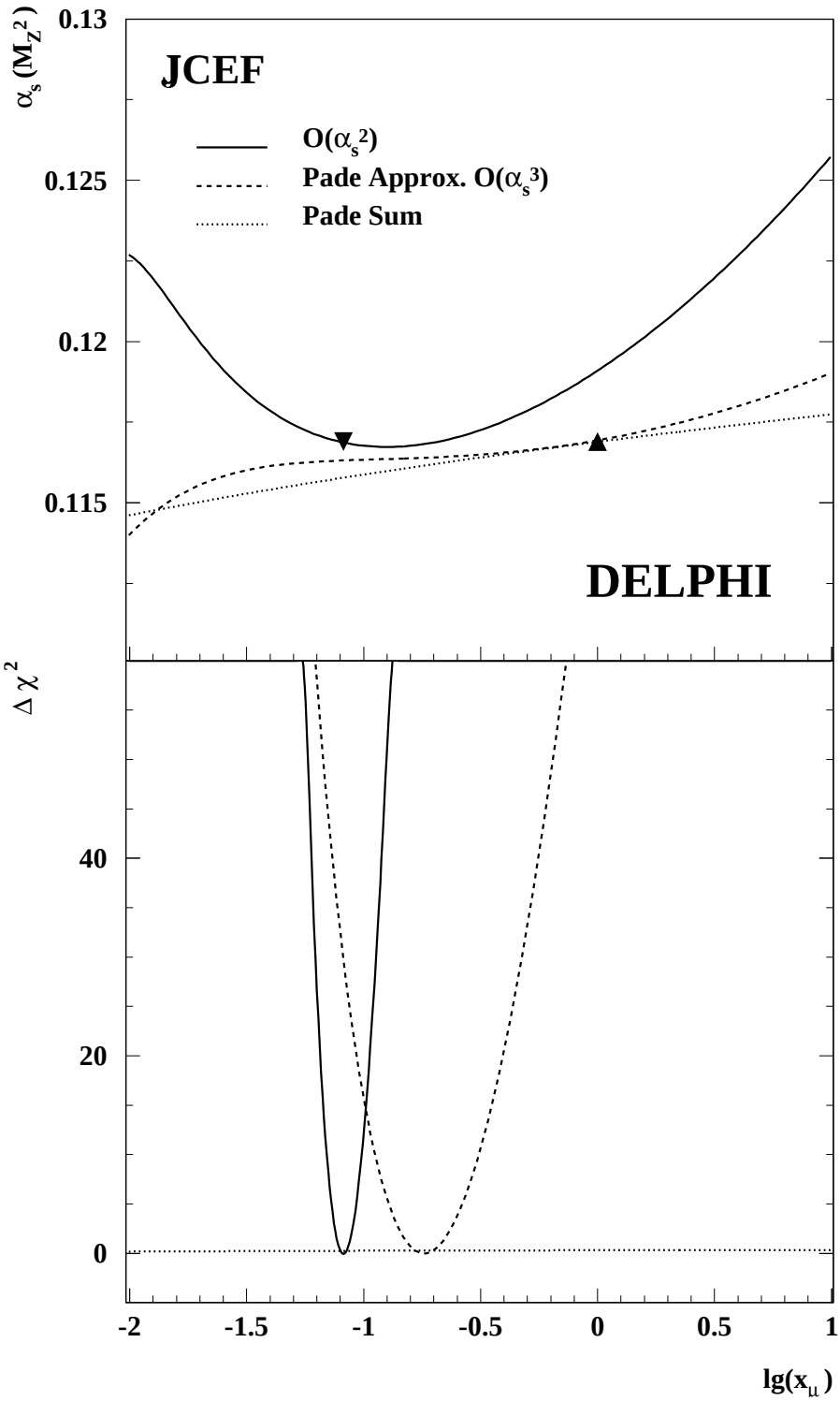

Figure 6.15: $\alpha_s(M_z^2)$ and $\Delta\chi^2 = \chi^2 - \chi^2_{\min}$ for the distribution of the Jet Cone Energy Fraction as a function of x_μ from QCD fits applying $\mathcal{O}(\alpha_s^2)$ prediction, $\mathcal{O}(\alpha_s^3)$ in Padé Approximation and the Padé Sum Approximation. Additionally, the χ^2 minimum for the $\mathcal{O}(\alpha_s^2)$ fit and the renormalization scale value $x_\mu = 1$ have been indicated in the $\alpha_s(M_z^2)$ curves.

6.6 QCD in the Next-to-Leading Log Approximation

All orders resummed QCD calculations in the Next-to-Leading Log Approximation (NLLA) matched with $\mathcal{O}(\alpha_s^2)$ calculations as described in Section 3.4 have been widely used to measure $\alpha_s(M_z^2)$ from event shape observables [9, 84, 108, 109, 110]. Pure NLLA predictions have for example been used in [9] to determine $\alpha_s(M_z^2)$ from the extreme 2-jet region of event shape distributions. In the following, both approaches are used to determine $\alpha_s(M_z^2)$ from angular integrated shape distributions and the results are compared to those obtained from fixed order perturbative predictions.

6.6.1 Measurement of $\alpha_s(M_Z)$ using pure NLLA predictions

To measure $\alpha_s(M_z^2)$ from pure NLLA calculations the fit range has to be restricted to the extreme 2-jet region, where $L = \ln(1/Y)$ becomes large and the resummed logarithms dominate. The ratio ω of the resummed logarithms to the non-exponentiating second order contributions is defined by

$$\omega = \frac{\Sigma(\alpha_s, L)}{H_1(Y)\bar{\alpha}_s + H_2(Y)\bar{\alpha}_s^2} \quad . \tag{6.13}$$

In addition to the fit range criteria listed in Section 6.4 the minimum of the ratio ω is required not to fall below 5 over the whole fit range for the fits in pure NLLA. This leads to the fit ranges listed in table 6.11. For the observable D_2^{Durham} the ratio ω remains small even for small values of y_{cut}. No fit range can be found where the resummed logarithms dominate the prediction. Therefore D_2^{Durham} has not been used for the fits in pure NLLA.

As outlined in Section 2.3 an optimization of the renormalization scale (or more precisely an optimization of the renormalization scheme) can to date not be performed for the resummed NLLA predictions. Therefore the renormalization scale value is fixed to $x_\mu = 1$ for these measurements. The uncertainty due to the scale dependence of $\alpha_s(M_z^2)$ is estimated by varying the scale x_μ between 0.5 and 2.

The fit results for the individual observables are listed in table 6.12. The α_s values measured from the individual observables are consistent within their uncertainties. The experimental and the overall uncertainties of the individual measurements are however larger than for the $\mathcal{O}(\alpha_s^2)$ predictions. This can be explained due to the limited kinematical 2 jet range, where the systematic experimental uncertainties of the data are increased.

Observable	Fit Range (NLLA)	Fit Range (matched)
$1-\mathrm{T}$	0.04 - 0.09	0.04 - 0.30
C	0.08 - 0.16	0.08 - 0.72
$\mathrm{B_{max}}$	0.02 - 0.04	0.02 - 0.24
$\mathrm{B_{sum}}$	0.06 - 0.08	0.06 - 0.24
ρ_{H}	0.03 - 0.06	0.03 - 0.30
$\mathrm{D_2^{Durham}}$		0.015 - 0.16

Table 6.11: Fit range for the observables in pure NLLA and matched NLLA fits. The observable D_2^{Durham} has not been used for pure NLLA fits, since no fit range can be found, where the resummed logarithms dominate the predictions (see text).

The weighted average of $\alpha_s(M_z^2)$ for the 5 observables is

$$\alpha_s(M_z^2) = 0.116 \pm 0.006$$

which is in excellent agreement with the average value for the $\mathcal{O}(\alpha_s^2)$ fits of $\alpha_s(M_z^2) = 0.1168 \pm 0.0026$.

Observable	$\alpha_s(M_z^2)$	$\Delta\alpha_s$(exp.)	$\Delta\alpha_s$(had.)	$\Delta\alpha_s$(scal.)	$\Delta\alpha_s$(tot.)	χ^2/n_{df}
$1-\mathrm{T}$	0.120	± 0.001	± 0.004	± 0.004	± 0.006	0.59
C	0.116	± 0.002	± 0.003	± 0.004	± 0.006	0.53
$\mathrm{B_{max}}$	0.111	± 0.004	± 0.003	± 0.002	± 0.006	2.37
$\mathrm{B_{sum}}$	0.116	± 0.003	± 0.004	± 0.002	± 0.006	1.24
ρ_{H}	0.117	± 0.004	± 0.006	± 0.004	± 0.009	0.43
average	0.116 ± 0.006	$\chi^2/n_{df} = 1.2 \ / \ 4$		$\rho_{\mathrm{eff}} = 0.71$		

Table 6.12: Results for the $\alpha_s(M_z^2)$ fits in pure NLLA for the individual observables together with the individual sources of uncertainties and the χ^2/n_{df} for the NLLA fits. The total error on $\alpha_s(M_z^2)$ listed, is the quadratic sum of the experimental error (statistical and systematic uncertainty), the uncertainty due to the hadronization correction and the uncertainty due to the scale dependence of $\alpha_s(M_z^2)$. Also listed is the weighted average of $\alpha_s(M_z^2)$ for the 5 observables together with the χ^2/n_{df} for the averaging procedure and the correlation parameter ρ_{eff}. The χ^2 corresponds to the value before readjusting according to Eq. 6.4.

6.6.2 Measurement of $\alpha_s(M_Z)$ using NLLA predictions matched with $\mathcal{O}(\alpha_s^2)$

The choice of an appropriate fit range for the matched NLLA and $\mathcal{O}(\alpha_s^2)$ predictions turns out to be nearly as difficult as for the $\mathcal{O}(\alpha_s^2)$ predictions with a fixed renormalization scale value. In general, a stability of $\alpha_s(M_z^2)$ with respect to the variation of the fit range cannot be achieved. Figure 6.16 shows the $\alpha_s(M_z^2)$ values obtained from fits applying the $\ln R$ matching scheme to all three bin intervals of the $1-T$ distribution as introduced in Section 6.4.2 for the α_s measurements in $\mathcal{O}(\alpha_s^2)$. Stability of α_s with respect to a variation of the fit range cannot be observed. The observed change of α_s is large in particular within the two-jet region, where the ratio of contributions from the resummed and the fixed order part of the predictions changes rapidly. The problem of the stability of various theoretical predictions including also power corrections obtained from the energy dependence of shape observables is subject of an ongoing detailed analysis [111].

The matching procedure has originally been designed to obtain improved predictions over the whole kinematical range covered by NLLA and $\mathcal{O}(\alpha_s^2)$ predictions. In order to study the viability of this conjecture, the fit range has been chosen as the combined fit range for the pure NLLA and the $\mathcal{O}(\alpha_s^2)$ fits. The results for the individual observables in the $\ln R$ matching scheme are listed in table 6.13.

The $\alpha_s(M_z^2)$ measurements from the individual observables are consistent with each other within their uncertainties. The additional uncertainty due to the matching ambiguity has been estimated as the maximum difference of $\alpha_s(M_z^2)$ in the $\ln R$ matching scheme and the two alternative matching schemes, R and $R - G_{21}$. The dependence on the choice of Y_{max}, i.e. the value of the upper kinematic limit for the shape observables used for the redefinition of the resummed logarithms according to Eq. 3.57, has been studied by repeating the fits with the value of Y_{max} being reduced by 10 %. The resulting variation in $\alpha_s(M_z^2)$ has been found to be small, the maximum change is about 1 %.

The average value of $\alpha_s(M_z^2)$ in the $\ln R$ matching scheme is

$$\alpha_s(M_z^2) = 0.119 \pm 0.005$$

which is in agreement with the average value for the $\mathcal{O}(\alpha_s^2)$ fits of $\alpha_s(M_z^2) = 0.1168 \pm 0.0026$.

Looking at the individual fit results, one finds from the χ^2/n_{df} that most of the shape distributions cannot be successfully described in a fit range expected to apply

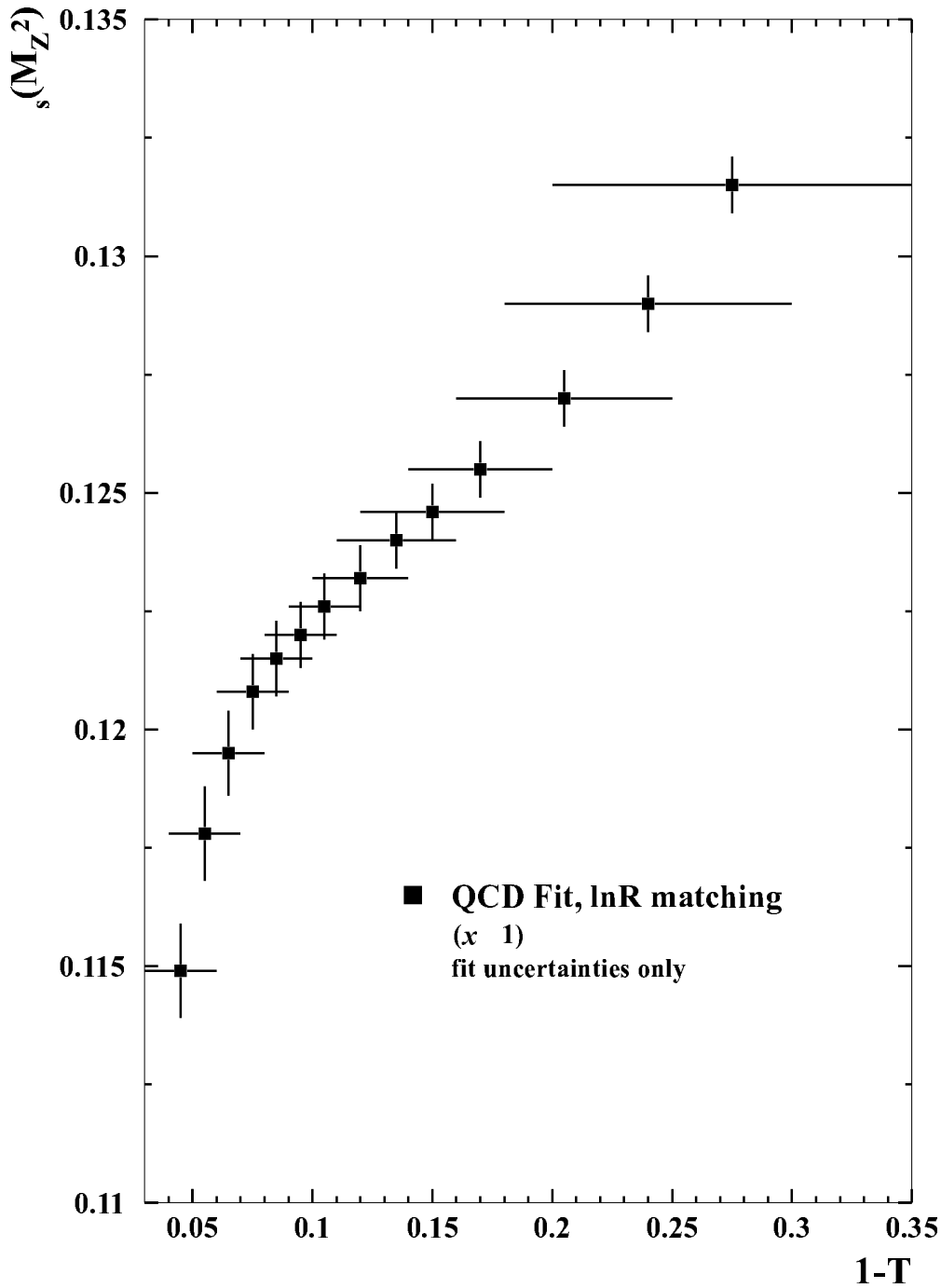

Figure 6.16: $\alpha_s(M_z^2)$ in matched NLLA and $\mathcal{O}(\alpha_s^2)$ precision for the $1-T$ distribution in dependence on the fit range. Fits in the ln R matching scheme have been performed for three bin intervals of the $1-T$ distribution. The symbols show the results of the $\alpha_s(M_z^2)$ measurements, and the horizontal bars indicate the fit ranges applied. The vertical bars represent the uncertainties from the fits.

Observable	$\alpha_s(M_z^2)$	$\Delta\alpha_s$(exp.)	$\Delta\alpha_s$(had.)	$\Delta\alpha_s$(scal.)	$\Delta\alpha_s$mat.)	$\Delta\alpha_s$(tot.)	χ^2/n_{df}
$1-\mathrm{T}$	0.124	± 0.002	± 0.003	± 0.004	± 0.003	± 0.007	9.5
C	0.120	± 0.002	± 0.002	± 0.004	± 0.004	± 0.007	15.2
$\mathrm{B_{max}}$	0.113	± 0.002	± 0.002	± 0.003	± 0.003	± 0.005	8.4
$\mathrm{B_{sum}}$	0.122	± 0.002	± 0.003	± 0.004	± 0.005	± 0.008	11.9
ρ_{H}	0.119	± 0.002	± 0.002	± 0.003	± 0.005	± 0.007	1.33
$\mathrm{D_2^{Durham}}$	0.121	± 0.001	± 0.002	± 0.002	± 0.005	± 0.006	1.70
average	0.119 ± 0.005		$\chi^2/n_{df} = 2.3\ /\ 5$		$\rho_{\mathrm{eff}} = 0.57$		

Table 6.13: Results of the QCD fits in the $\ln R$ matching scheme for the individual observables together with the individual sources of uncertainties and the χ^2/n_{df} for the $\alpha_s(M_z^2)$ fits. The total error is the quadratic sum of the experimental error (statistical and systematic uncertainty), the uncertainty due to the hadronization correction, the uncertainty due to the scale dependence of $\alpha_s(M_z^2)$ and the uncertainty due to the matching ambiguity. Also listed is the weighted average of $\alpha_s(M_z^2)$ for the 6 observables together with the χ^2/n_{df} for the averaging procedure and the correlation parameter ρ_{eff}. The χ^2 corresponds to the value before readjusting according to Eq. 6.4.

for the combined theory. The $\alpha_s(M_z^2)$ values are higher than for the fits in pure NLLA for all observables considered. In the case of $1-T$, C and B_{sum} the measured $\alpha_s(M_z^2)$ values are even above the values for both the pure NLLA fits and the $\mathcal{O}(\alpha_s^2)$ fits using experimentally optimized scales, where one might expect the matched predictions to be a kind of 'average' of the individual theories.

In order to investigate this result further it is instructive to compare the theoretical predictions of the shape distributions for the different methods with the data distributions. Fig. 6.17 shows experimental distributions for $1-T$ and C in comparison with the fitted curves for three different types of QCD fits, namely $\mathcal{O}(\alpha_s^2)$ using experimentally optimized scales, $\mathcal{O}(\alpha_s^2)$ using a fixed renormalization scale $x_\mu = 1$ and the fits in the $\ln R$ matching scheme.

For the fits in $\mathcal{O}(\alpha_s^2)$ using experimentally optimized scales, the data are described well over the whole fit range. For the fits in $\mathcal{O}(\alpha_s^2)$ using a fixed renormalization scale value and for the fits in the $\ln R$ matching scheme, only a poor description of the data is achieved and the slope of both curves show a similar though less distinct systematic distortion with respect to the data. In the case of $\mathcal{O}(\alpha_s^2)$ applying $x_\mu = 1$ the distortion arises from the wrong choice of the renormalization scale. Since the scale value for the matched predictions is also chosen to be $x_\mu = 1$, the similarity of the curves indicates that the subleading and non-logarithmic terms originating

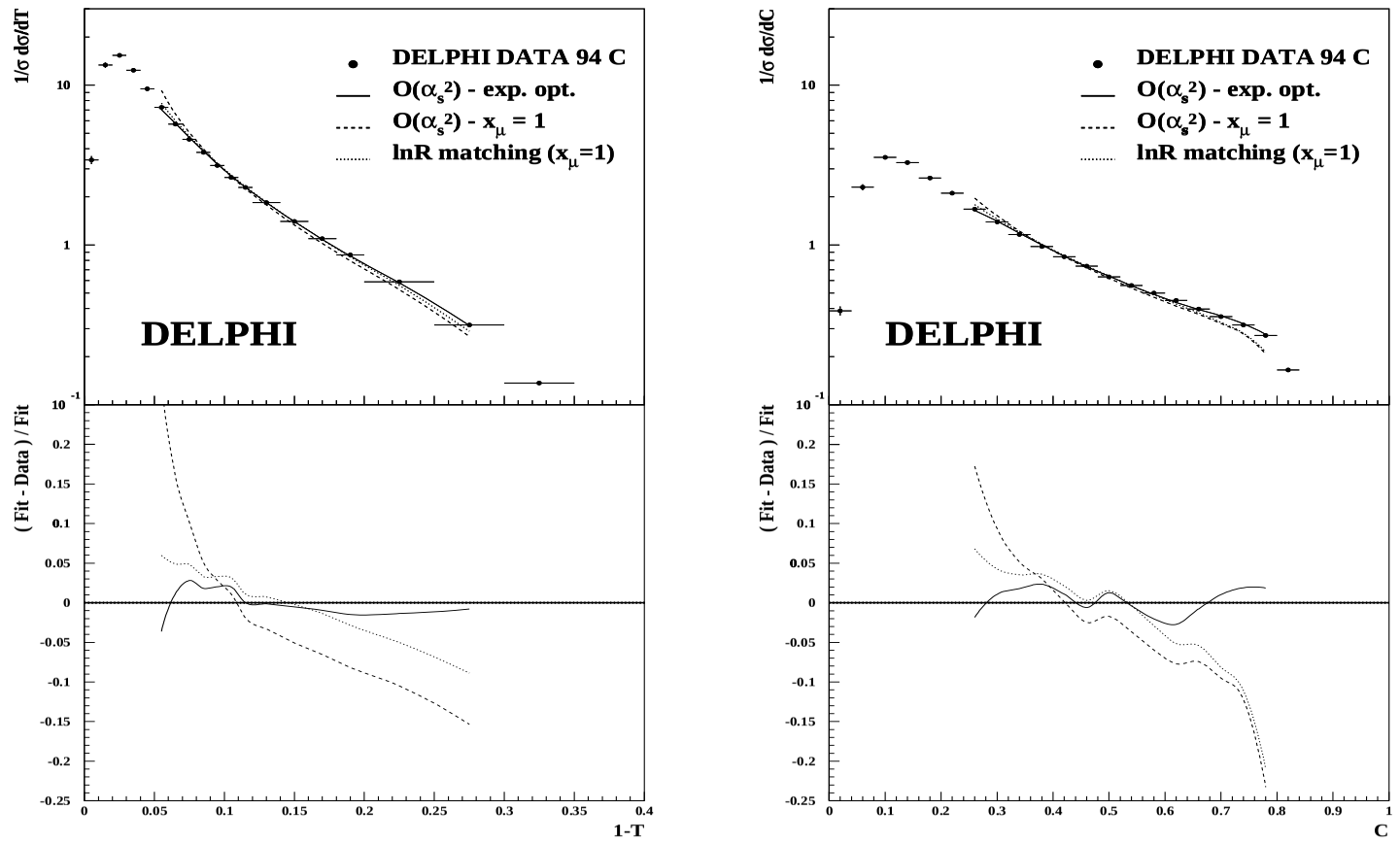

Figure 6.17: *left part:* Comparison of Delphi data with three different QCD Fits: *i*) $\mathcal{O}(\alpha_s^2)$ using an experimentally optimized renormalization scale, *ii*) $\mathcal{O}(\alpha_s^2)$ using a fixed renormalization scale $x_\mu = 1$ and *iii*) $\ln R$ matched NLLA ($x_\mu = 1$) for the thrust Distribution. The lower part shows the relative difference (Fit-Data)/Fit. Whereas the $\mathcal{O}(\alpha_s^2)$ curve describes the data over the whole fit range, the slope of the curves for the fixed scale and $\ln R$ matching show a similar systematic distortion with respect to the data. *right part:* The same for the C-Parameter. Here the distortion is even stronger.

from the $\mathcal{O}(\alpha_s^2)$ part of the matched theory and introduced using the scale value $x_\mu = 1$ distort the $\ln R$ predictions. It should be noted that the matched theory requires a renormalization scale value of $\mathcal{O}(1)$. Unlike the $\mathcal{O}(\alpha_s^2)$ case, 2 parameter fits in $\alpha_s(M_z^2)$ and x_μ do not converge for most of the observables; for such low scale values as in $\mathcal{O}(\alpha_s^2)$ the data can not be described at all in the matched theory.

It seems that the combination of all orders resummed predictions and terms only known in $\mathcal{O}(\alpha_s^2)$ results in a systematic shift in $\alpha_s(M_z^2)$ due to the impossibility of choosing an appropriate renormalization scale value. The comparison of the fit curves in Fig. 6.17 suggests, that the distortion of the fit curves observed the for theoretical predictions in $\mathcal{O}(\alpha_s^2)$ with $x_\mu = 1$ propagates into the matched prediction due to a mismatch of the different renormalization scale values required for NLLA and $\mathcal{O}(\alpha_s^2)$ predictions.

Although the average values for the $\mathcal{O}(\alpha_s^2)$ fits, the fits in pure NLLA and the fits in the $\ln R$ matching scheme agree within the uncertainties, the matched results should be considered to be less reliable than those of the $\mathcal{O}(\alpha_s^2)$ and pure NLLA analyses due to the systematic deviation of the prediction to most of the data distributions (see e.g. Figure 6.17 and Table 6.13) and the inherent dependence of the result on the arbitrary choice of the fit range.

6.7 Correction for Heavy Quark Mass Effects

Studies of the influence of quark mass effects on jet cross-sections [112] have shown that these effects can be important in the study of event shape observables and hence in the measurement of the strong coupling. For a natural mixture of quark flavours, the influence of the quark masses on the measurement of $\alpha_s(M_z^2)$ from event shapes is expected to be $\sim 1\%$ [113].

In order to derive a high precision value of $\alpha_s(M_z^2)$, the $\mathcal{O}(\alpha_s^2)$ measurement with experimentally optimized scales has been refined by considering the influence of b quark mass effects in leading order:

$$\frac{1}{\sigma_{tot}}\frac{d^2\sigma(Y,\cos\vartheta_T)}{dY\,d\cos\vartheta_T} = \bar{\alpha}_s(\mu^2)\cdot A(Y,\cos\vartheta_T)[1+\Delta m]+\bar{\alpha_s}^2(\mu^2)\cdot B(Y,\cos\vartheta_T,x_\mu) \quad (6.14)$$

where

$$\Delta m = \frac{\sum\limits_{q,m_b\neq 0} d^2\sigma_q(Y,\cos\theta_T)/\sum\limits_{q,m_b\neq 0}\sigma_q}{\sum\limits_{q,m_b=0} d^2\sigma_q(Y,\cos\theta_T)/\sum\limits_{q,m_b=0}\sigma_q} - 1 \quad (6.15)$$

The coefficients Δm for the 18 observables studied have been computed numerically [114] for two different definitions of the b–quark mass: The b pole mass of $M_b \approx 4.6\,\mathrm{GeV/c^2}$ and the b running mass at the M_Z, $m_b(M_Z) \approx 2.8\,\mathrm{GeV/c^2}$ [112]. All definitions of the quark mass are equivalent to leading order; differences are entirely due to higher orders in α_s.

Figure 6.18 [115] shows the ratio of theoretical predictions of the 3-jet rate for $b-$ quark events with respect to light quark events

$$R_3^{bl} = \frac{\Gamma_{3jet}^b/\Gamma^b}{\Gamma_{3jet}^l/\Gamma^l} \quad (6.16)$$

for different jet algorithms. Γ_{3jet}^q and Γ^q denote the 3-jet and the total decay width of a Z^0 into a quark pair of flavour q, with $l = u,d,s$ indicating the average over all light flavours. Shown are the LO and the NLO predictions for the pole mass M_b and the running mass $m_b(M_Z)$ definition of the b-quark mass.

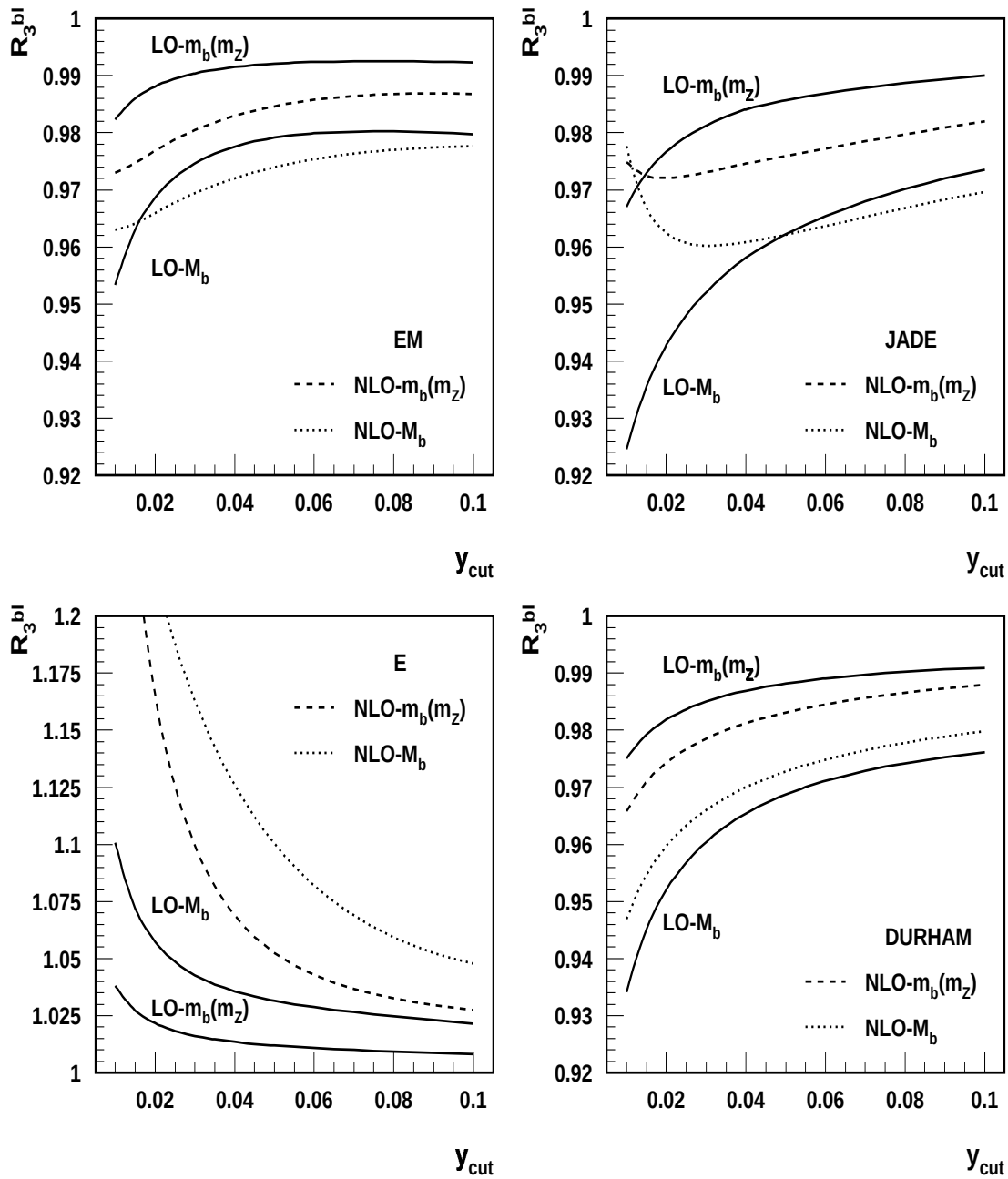

Figure 6.18: Ratio of theoretical predictions for the 3-jet rate for $b-$ quark events with respect to light quark events for the EM, E, Jade and the Durham algorithm [115].

For the Durham and the Jade algorithm, which have both been used within this analysis, the NLO predictions for both definitions of the $b-$ quark mass are in between the LO predictions for almost the whole kinematical range. This behaviour is generally expected for all observables with moderate and small NLO corrections [116]. In combination with the small influence of the quark mass effects on the determination of $\alpha_s(M_z^2)$ for a natural mixture of quark flavours, the LO approximation for the estimation of these influences seems to be appropriate.

For the jet rates determined from the E and the EM algorithm (for a definition of these algorithms see for example [115]) the deviations of the NLO predictions with respect to the LO predictions are larger (see Fig. 6.18). Both algorithms have however not been used within this analysis. In particular the E algorithm is known for the poor reliability of the theoretical predictions. In reference [117] it has been found, that there are very large deviations between the Monte Carlo predictions on the hadron level with respect to the parton level. The NLO correction to the perturbative prediction for example can be as large as 90% of the LO prediction. Also the shift in the resolution parameter y_{cut} produced by the quark mass is positive, whereas from kinematical arguments a negative effect is expected, since massive quarks radiate less gluons than massless quarks [115].

$\alpha_s(M_z^2)$ has been determined applying both the pole and the running mass definition. The average of $\alpha_s(M_z^2)$ derived from both definitions has been taken as the central value, and half the difference has been taken as an estimate of the uncertainty due to higher order mass effects. The results for the individual observables are listed in table 6.14. For a graphical view of the results obtained for $\alpha_s(M_z^2)$ see also Fig. 6.19.

The weighted average of $\alpha_s(M_z^2)$ for $\mathcal{O}(\alpha_s^2)$ predictions including quark mass effects is

$$\alpha_s(M_z^2) = 0.1174 \pm 0.0026$$

corresponding to an average shift of $\Delta\alpha_s(M_Z^2) = +0.0006$ with respect to the result from the massless predictions.

Observable	$\alpha_s(M_z^2)$	$\alpha_s(M_z^2)$ shift	$\Delta\alpha_s$ (Mass)	$\Delta\alpha_s$ (Tot.)
EEC	0.1145	0.0003	$\pm$ 0.0001	$\pm$ 0.0028
AEEC	0.1149	-0.0001	$\pm$ 0.0001	$\pm$ 0.0111
JCEF	0.1180	0.0011	$\pm$ 0.0007	$\pm$ 0.0018
$1-\mathrm{T}$	0.1136	0.0004	$\pm$ 0.0001	$\pm$ 0.0036
O	0.1184	0.0013	$\pm$ 0.0006	$\pm$ 0.0057
C	0.1156	0.0003	$\pm$ 0.0002	$\pm$ 0.0036
$\mathrm{B_{Max}}$	0.1223	0.0008	$\pm$ 0.0002	$\pm$ 0.0041
$\mathrm{B_{Sum}}$	0.1144	0.0006	$\pm$ 0.0003	$\pm$ 0.0053
ρ_{H}	0.1216	0.0001	$\pm$ 0.0001	$\pm$ 0.0060
ρ_{S}	0.1160	-0.0001	$\pm$ 0.0001	$\pm$ 0.0029
ρ_{D}	0.1196	0.0024	$\pm$ 0.0008	$\pm$ 0.0039
$\mathrm{D_2^{E0}}$	0.1165	0.0000	$\pm$ 0.0002	$\pm$ 0.0044
$\mathrm{D_2^{P0}}$	0.1207	-0.0003	$\pm$ 0.0002	$\pm$ 0.0033
$\mathrm{D_2^{P}}$	0.1186	-0.0001	$\pm$ 0.0001	$\pm$ 0.0046
$\mathrm{D_2^{Jade}}$	0.1182	0.0013	$\pm$ 0.0005	$\pm$ 0.0041
$\mathrm{D_2^{Durham}}$	0.1172	0.0003	$\pm$ 0.0003	$\pm$ 0.0026
$\mathrm{D_2^{Geneva}}$	0.1216	0.0038	$\pm$ 0.0013	$\pm$ 0.0310
$\mathrm{D_2^{Cambridge}}$	0.1176	0.0012	$\pm$ 0.0006	$\pm$ 0.0026
average	0.1174 ± 0.0026	$\chi^2/n_{df} = 6.60\ /\ 17$	$\rho_{\mathrm{eff}} = 0.615$	

Table 6.14: Results of the refined $\mathcal{O}(\alpha_s^2)$ measurement of $\alpha_s(M_z^2)$ including b quark mass effects in leading order. The central value of $\alpha_s(M_z^2)$ quoted is the average of α_s derived from applying the b pole mass M_b and the b running mass $m_b(M_Z)$ definition. Also given is the shift of $\alpha_s(M_z^2)$ with respect to the massless prediction. $\Delta\alpha_s(Mass) = |\alpha_s(M_b) - \alpha_s(m_b(M_Z))|\,/2$ has been taken as an estimate of the uncertainty due to quark mass effects of higher orders. The total error displayed is the quadratic sum of the experimental uncertainty, the hadronization uncertainty, the scale uncertainty and the uncertainty due to quark mass effects. The χ^2 given, corresponds to the value before readjusting according to Eq. 6.4.

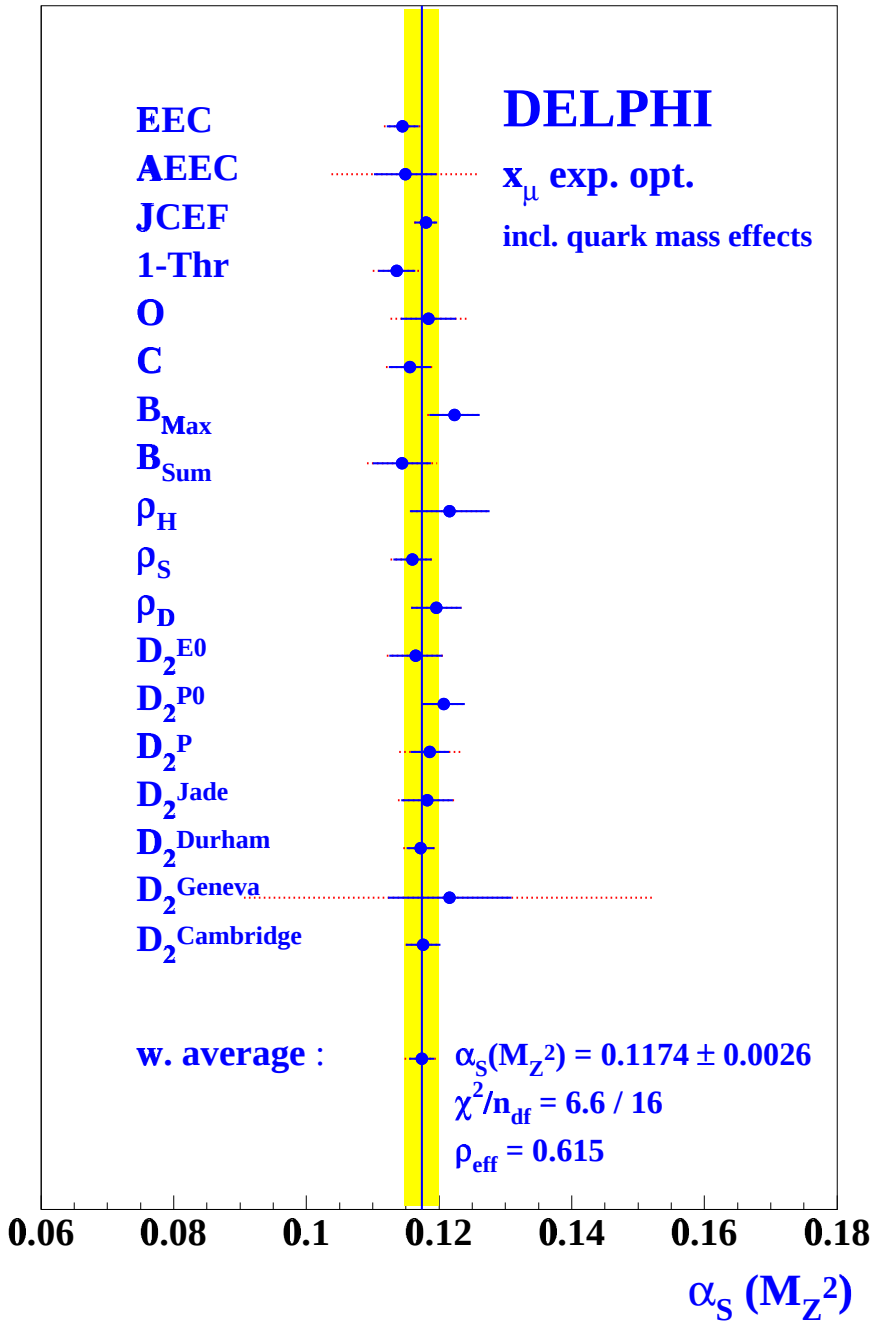

Figure 6.19: $\alpha_s(M_z^2)$ from the refined $\mathcal{O}(\alpha_s^2)$ fits applying experimentally optimized scales including quark mass effects in leading order for 18 oriented event shape distributions. The error bars indicated by the solid lines are the quadratic sum of the experimental and the hadronization uncertainty. The error bars indicated by the dotted lines include also the additional uncertainty due to the variation of the renormalization scale due to scale variation around the central value x_μ^{exp} in the range $0.5 \cdot x_\mu^{exp} \leq x_\mu \leq 2 \cdot x_\mu^{exp}$. Also shown is the correlated weighted average (see text). The χ^2-value is given before readjusting according to Eq. 6.4.

6.8 The Role of the Jet Cone Energy Fraction

Among the observables studied, the Jet Cone Energy Fraction (JCEF) [40] naturally reveals some superior properties. First, the size of the hadronization correction is extremely small, with an average correction within the applied fit range of about 3.5%, the *JCEF* has the smallest hadronization correction from all observables considered.

The scale dependence of $\alpha_s(M_z^2)$ derived from JCEF is very small. Both the experimental and the theoretical uncertainties are smallest for the $\alpha_s(M_z^2)$ measurement from the JCEF distribution.

The second order contributions to the cross-section are also very small. Within the applied fit range, the average ratio of the second to first order contributions is $\langle r_{NLO} \rangle \sim 25\%$ if x_μ is fixed at 1 and only $\langle r_{NLO} \rangle \sim 6\%$ if the experimentally optimized scale value is applied. This indicates a good convergence behavior of the corresponding perturbative series.

Table 6.15 shows a summary of α_s measurements from the JCEF distribution for the different methods studied. The $\alpha_s(M_z^2)$ value determined from the fit applying an experimentally optimized renormalization scale value is in excellent agreement with the result obtained from the fits applying the ECH and the PMS renormalization sale optimization criteria. Also for the Padé Sum estimate and the $\mathcal{O}(\alpha_s^3)$

prediction	$\alpha_s(M_z^2)$	x_μ	χ^2/n_{df}
$\mathcal{O}(\alpha_s^2)$ exp. opt. scale	0.1169 ± 0.0017	0.0820	1.05
ECH/FAC	0.1169 ± 0.0017	0.2189	2.75
PMS	0.1168 ± 0.0017	0.1576	1.91
Padé Sum (fixed scale)	0.1169 ± 0.0015	1.0	3.05
Padé $\mathcal{O}(\alpha_s^3)$ (fixed scale)	0.1169 ± 0.0016	1.0	3.12
Padé Sum (fixed scale)	0.1169 ± 0.0015	1.0	3.05
Padé $\mathcal{O}(\alpha_s^3)$ (exp. opt. scale)	0.1164 ± 0.0015	0.1814	2.45
$\mathcal{O}(\alpha_s^2)$ (fixed scale)	0.1191 ± 0.0024	1.0	7.7
$\mathcal{O}(\alpha_s^2)$ exp. opt. scale + LO quark mass effects	0.1180 ± 0.0018		

Table 6.15: Summary of $\alpha_s(M_z^2)$ measurements from the oriented distribution of the Jet Cone Energy Fraction (JCEF).

prediction in Padé Approximation a perfect agreement is obtained. Due to the reduced renormalization scale dependence of the predictions in Padé Approximation, the difference of $\alpha_s(M_z^2)$ obtained with an experimentally optimized scale value and with $x_\mu = 1$ is only about a few per mille.

It should be noted that the PMS and ECH methods are *a priori* unrelated with the predictions of the Padé Approximation. The PMS and the ECH approach are based on the renormalization group and attempt to minimize the contributions from the higher order perturbative predictions. The Padé Approximation does not use renormalization group ingredients but is considered to resum rapidly growing higher order terms of the perturbative expansion. According to reference [107], a good numerical agreement between these different predictions should be considered as strong evidence that the predictions from both approaches are correct.

Fits applying experimentally optimized renormalization scale values involve no theoretical assumptions at all. They simply try to seek the renormalization scheme which yields an optimal description of the experimental data. The coincidence of $\alpha_s(M_z^2)$ from the two parameter fit to the data with the results from the theoretical approaches supports the conclusion that the theoretical uncertainties of the $\alpha_s(M_z^2)$ measurement from the $JCEF$ distribution due to higher order contributions are indeed very small.

The $\mathcal{O}(\alpha_s^2)$ fit of $\alpha_s(M_z^2)$ applying a fixed renormalization scale value $x_\mu = 1$ clearly fails to describe the data with $\chi^2/n_{df} = 965/125$. However, even for this method, the deviation of $\alpha_s(M_z^2)$ from the value obtained using the experimentally optimized scale value is only about 2 %, wich again demonstrates the remarkable stability of the theoretical prediction with respect to the variation of the renormalization scale.

All other approaches yield nearly identical α_s values within a few per mille. The deviation of the α_s values derived from the different methods, which can serve as an estimate of the theoretical uncertainty due to missing higher order terms [88], is clearly smaller than the uncertainty of ± 0.0008 derived from the variation of the renormalization scale value. Due to the outstanding qualities of this observable, the JCEF is considered as best suited for a precise determination of $\alpha_s(M_z^2)$. After correcting the measured value for heavy quark mass effects, the final result for this observable is

$$\alpha_{\mathrm{s}}(\mathrm{M}_{\mathrm{Z}}^2) = 0.1180 \pm 0.0006(\mathrm{exp.}) \pm 0.0013(\mathrm{hadr.}) \pm 0.0008(\mathrm{scale}) \pm 0.0007(\mathrm{mass}).$$

Chapter 7

Summary

From 1.4 Million hadronic Z^0 decays recorded with the DELPHI detector and reprocessed with improved analysis software, the distributions of 18 infrared and collinear safe event shape observables have been precisely measured at various values of the polar angle ϑ_T of the thrust axis with respect to the beam direction. The ϑ_T dependence of all detector properties has been taken fully into account to achieve an optimal experimental precision. In order to compare with QCD calculations in $\mathcal{O}(\alpha_s^2)$, hadronization corrections are evaluated from precisely tuned fragmentation models.

The precise data are used to measure $\alpha_s(M_z^2)$ applying a number of different methods described in the literature. The most detailed studies have been performed in second order pertubative QCD. Fits taking explicit account of the α_s dependent event orientation as predicted by QCD with experimental acceptance corrections less than $\sim 25\%$ and hadronization corrections less than $\sim 40\%$ yield the result that the data can be surprisingly well described in $\mathcal{O}(\alpha_s^2)$ by using a common value of $\alpha_s(M_z^2)$ with a small uncertainty.

The consistency of the individual $\alpha_s(M_z^2)$ values determined from the 18 oriented event shape distributions is achieved by using the so-called experimentally optimized scales, i.e. the particular values of the renormalization scale x_μ have been determined from the fits to of the individual observables. The significance of the fits is improved due to an improved statistical and systematical accuracy.

The precise experimental data are fully consistent with the expectation from second order QCD. The spread of the $\alpha_s(M_z^2)$ measurements in $\mathcal{O}(\alpha_s^2)$ perturbation theory does not require to introduce any additional theoretical uncertainty like for example due to a variation of the renormalization scale. Thus, the consistency of the indi-

vidual measurements does not rely on controversial assumptions about theoretical uncertainties due to the renormalization scale dependence of the perturbative series.

For most of the investigated observables the scale dependence of α_s is very small in the vicinity of the experimentally optimized scale value. The quoted error of $\alpha_s(M_z^2)$ includes an uncertainty due to a variation of the experimentally optimized scale value in the range between $0.5 \cdot x_\mu^{exp}$ and $2. \cdot x_\mu^{exp}$. Taking account of the correlation among the observables an average value of $\alpha_s(M_Z^2) = 0.1168 \pm 0.0026$ is obtained from the data.

An analysis with a fixed renormalization scale value of $x_\mu = 1$ yields an unacceptable description of the data for many observables and leads to a wide spread of the individual $\alpha_s(M_z^2)$ values. In contrast to fits applying experimentally optimized scales, the stability of the α_s values with respect to the choice of the fit range is in general poor. For many observables the slope of the theoretical predictions does not fit the data neither in the region dominated by 2-jet events nor in the region dominated by 3-jet events. Similar discrepancies of fit curves with respect to the slope of the data can be observed from an examination of figures presented in previous publications (see for example [85]). Due to the improved accuracy of the data, systematic differences between the $\mathcal{O}(\alpha_s^2)$ analysis using experimentally optimized and fixed renormalization scale values $x_\mu = 1$ become significant.

To check the reliability of the α_s results obtained from the experimentally optimized scales three further approaches for choosing an optimized value of the renormalization scale have been investigated: The principle of minimal sensitivity (PMS), the method of effective charges (ECH), and the method of Brodsky, Lepage and MacKenzie (BLM). The weighted averages of α_s from the three methods are in excellent agreement with the weighted average of α_s obtained from the experimental optimization, but their scatter is larger. It is largest for BLM. A significant correlation between the renormalization scale values evaluated with ECH and PMS with the experimentally optimized scale values is observed. No such correlation is observed for the BLM scales.

Further approaches to estimate the influence of higher order contributions to the perturbative QCD series are based on Padé approximants. The [0/1] Padé approximant has been used as an estimate of the sum of the perturbative series as well as for the extrapolation of the unknown $\mathcal{O}(\alpha_s^3)$ coefficients for the 18 distributions. In both studies the renormalization scale has been set to $x_\mu = 1$. The renormalization scale dependence of $\alpha_s(M_z^2)$ obtained from the Padé predictions is largely reduced, in particular for the Padé sum prediction. A similar observation has been made in [107] from an analysis of theoretical predictions for the Bjorken sum rule in deep inelastic scattering. The average values of $\alpha_s(M_z^2)$ obtained from the PA and the PS

predictions are both consistent with the average value from the experimental scale optimization in $\mathcal{O}(\alpha_s^2)$.

Beside the above mentioned determinations of $\alpha_s(M_z^2)$ in fixed order perturbation theory, a further cross check has been performed by applying predictions in all orders resummed next-to-leading logarithmic approximation (NLLA). In a first step, pure NLLA predictions have been confronted with the data in a limited fit range where the ratio of the resummed next-to-leading logarithms to the non-exponentiating $\mathcal{O}(\alpha_s^2)$ contributions is large. Good agreement between the average value of $\alpha_s(M_z^2)$ obtained from the pure NLLA fits with a renormalization scale value $x_\mu = 1$ and the $\mathcal{O}(\alpha_s^2)$ fits using experimentally optimized scales has been obtained.

In a further step NLLA matched to $\mathcal{O}(\alpha_s^2)$ calculations have been applied. The quality of the fits to different observables is in general quite poor. For many observables the χ^2/n_{df} is unacceptable. The stability of the fits with respect to a variation of the fit range is in general poor in comparison with $\mathcal{O}(\alpha_s^2)$ fits with experimentally optimized renormalization scale values. Compared with $\mathcal{O}(\alpha_s^2)$ fits applying $x_\mu = 1$, the stability is somewhat improved. The α_s values from all investigated observables are systematically higher, the average value of $\alpha_s(M_z^2)$ determined in matched NLLA and $\mathcal{O}(\alpha_s^2)$ theory is however still consistent with the $\mathcal{O}(\alpha_s^2)$ result.

For the distributions of $1 - T$ and C a detailed comparison of the matched NLLA predictions with the high precision data has been performed. It has been shown that the trend of the data deviates in a systematic fashion from the predictions of the matched theory. The distortion of the fit curves with respect to the data observed has the same shape as for the $\mathcal{O}(\alpha_s^2)$ fits applying $x_\mu = 1$. The size of the deviations is however somewhat reduced. The observation suggests, that the deviations observed for the $\mathcal{O}(\alpha_s^2)$ predictions applying an improper renormalization scale value propagate also into the matched NLLA predictions. A comparison with the published results from previous analyses [9, 85] shows, that the deviations observed are similar to those observed before. The significance of the fits presented within this analysis is however largely improved. The χ^2/n_{df} for the matched NLLA fits to the thrust distribution increases for example from $\chi^2/n_{df} = 2.3$ in [110] and $\chi^2/n_{df} = 3.4$ in [9] to $\chi^2/n_{df} = 9.5$, corresponding to a probability $P = 3.2 \cdot 10^{-20}$ within the present analysis.

The α_s average values derived from the different approaches considered are in very good agreement. The $\mathcal{O}(\alpha_s^2)$ analysis applying a simultaneous fit of α_s and x_μ to the experimental data yields superior results in all respects.

The influence of heavy quark mass effects on the measurement of $\alpha_s(M_z^2)$ has been studied. The weighted average of $\alpha_s(M_z^2)$ from the $\mathcal{O}(\alpha_s^2)$ measurements using ex-

perimentally optimized renormalization scale values and corrected for the $b-$ mass to leading order yields

$$\alpha_{\mathrm{s}}(\mathrm{M}_{\mathrm{Z}}^2) = 0.1174 \pm 0.0026.$$

Among the observables studied, the Jet Cone Energy Fraction (JCEF) [40] reveals some superior properties. The size of the hadronization correction as well as the second order contribution to the cross-section and the are very small. The latter indicates a good convergence behavior of the corresponding perturbative series. Additionally, the renormalization scale dependence of $\alpha_s(M_z^2)$ derived from JCEF is very small. Fits in $\mathcal{O}(\alpha_s^2)$ applying an experimentally optimized scale value, PMS and ECH scale values as well as fits in $\mathcal{O}(\alpha_s^2)$ Padé approximation with fixed and experimentally optimized renormalization scale values and fits applying the Padé sum prediction yield almost identical values for $\alpha_s(M_z^2)$. In correspondence, both experimental and theoretical uncertainties are smallest for the $\alpha_s(M_z^2)$ measurement from the JCEF distribution.

After correcting the measured $\alpha_s(M_z^2)$ value for heavy quark mass effects, the final result derived from an $\mathcal{O}(\alpha_s^2)$ fit to the $JCEF$ distribution by applying an experimentally optimized renormalization scale value yields

$$\alpha_{\mathrm{s}}(\mathrm{M}_{\mathrm{Z}}^2) = 0.1180 \pm 0.0006(\mathrm{exp.}) \pm 0.0013(\mathrm{hadr.}) \pm 0.0008(\mathrm{scale}) \pm 0.0007(\mathrm{mass}).$$

The result is in very good agreement with the recent PDG world average value of $\alpha_s(M_z^2) = 0.1185 \pm 0.0020$ [118]. Compared with other recent precision measurements of $\alpha_s(M_z^2)$, there is very good agreement with the determination of $\alpha_s(M_z^2) = 0.1174 \pm 0.0024$ from Lattice Gauge Theory [119] and the recent result from an NNLO analysis of ep deep inelastic scattering data of $\alpha_s(M_z^2) = 0.1172 \pm 0.0024$ [120]. The result is also in good agreement with the result from the LEP electroweak working group of $\alpha_s(M_z^2) = 0.119 \pm 0.004$ [1] from the standard model fit to the full set of electroweak precision data. Compared with the most recent result from spectral functions in hadronic tau decays, α_s is smaller than the central value of $\alpha_s(M_z^2) = 0.1219 \pm 0.0020$ quoted in [89], but in very good agreement with the value of $\alpha_s(M_z^2) = 0.1177 \pm 0.0010$ derived in [121] by considering the renormalization scheme invariance of the NNLO prediction and with $\alpha_s(M_z^2) = 0.1169 \pm 0.0017$ derived in [89] by using an alternative analysis method considering renormalon chains.

Chapter 8

Discussion and Outlook

With the present analysis it has been demonstrated for the first time that the spread of the $\alpha_s(M_z^2)$ measurements from a large number of observables in $\mathcal{O}(\alpha_s^2)$ perturbation theory can be understood without assuming theoretical uncertainties due to a variation of the renormalization scale.

For most of the observables and in particular for the jet cone energy fraction a very good agreement of the $\alpha_s(M_z^2)$ values derived by applying experimentally optimized renormalization scale values and by applying the theoretically motivated renormalization scheme optimization approaches is observed. The renormalization scale values obtained by applying the different approaches are strongly correlated. This observation strongly suggests the importance of a renormalization group invariant expansion of perturbative series in QCD.

Diagonal Padé Approximants $[N/N+1]$ have been proven to be exactly renormalization scale invariant in the limit where the $\beta-$function is dominated by the one loop contribution [105]. Beyond the one loop approximation, this invariance is almost completely conserved, since in QCD the one loop running of the coupling is dominant [105]. It should be emphasized that the predictions obtained by Padé Approximants are *a priori* unrelated with the predictions of the PMS and ECH approaches. Therefore the good agreement between the results obtained by the Padé predictions with those obtained by predictions utilizing renormalization group considerations further supports the relevance of a renormalization group invariant perturbative expansion.

In the analysis of event shape observables in matched NLLA and $\mathcal{O}(\alpha_s^2)$ precision within the $\overline{\text{MS}}$ renormalization scheme only a very poor description of the high precision data can be obtained. Another problem arises due to the poor stability of $\alpha_s(M_z^2)$ with respect to the variation of the fit range. The NLLA analysis is however hampered by the fact that with the currently available calculations neither

the renormalization scheme dependence can be parameterized nor a resummation in terms of renormalization group invariants is available.

It should be noted that in NLLA no optimization is achieved by simply performing a combined fit of the strong coupling and the renormalization scale. This has been recognized within the OPAL analysis of event shape observables applying the $\ln R$ matching scheme [110], where fits applying $x_\mu = 1$ have been compared with fits considering x_μ as a free parameter. It has been found, that the description of the data is slightly improved if x_μ is fitted. This is however expected simply do to the additional free parameter. In contrast to measurements in $\mathcal{O}(\alpha_s^2)$ the scatter of the individual measurements is largely increased if x_μ is fitted. A simple mean value calculated from all observables studied yields $\alpha_s(M_z^2) = 0.121 \pm 0.007$ if the scale value is fixed to $x_\mu = 1$ but $\alpha_s(M_z^2) = 0.126 \pm 0.021$ if x_μ is fitted. The main difference between the available predictions in $\mathcal{O}(\alpha_s^2)$ and NLLA predictions is however, that in $\mathcal{O}(\alpha_s^2)$ the renormalization scale completely parameterizes the renormalization scheme dependence, suggesting the major importance of this feature.

Thus, a re-examination of the theoretical predictions in NLLA with respect to the renormalization scheme dependence is strongly suggested. That this is not a principal problem has already been demonstrated in [6] by the resummation of the (during that time incomplete) NLLA prediction of the 2-jet rate in the Durham scheme.

The importance of renormalization group improved perturbative predictions in higher orders perturbation theory has been demonstrated for example with the study of theoretical predictions for the Bjorken sum rule [107]. Within this analysis, it has been found that the $\overline{\text{MS}}$ scheme prediction with $\mu = Q$ yields rather scheme dependent results and is considered as a not well behaved renormalization scheme. In contrast the PMS and ECH schemes turn out to be well behaved as well as the Padé prediction. Using the available data from polarized deep inelastic scattering, $\alpha_s(3GeV^2)$ has been determined by applying the ECH renormalization scheme. Evolving α_s to M_Z yields $\alpha_s(M_z^2) = 0.117^{+0.004}_{-0.007}(exp.) \pm 0.002(theo.)$, which is in perfect agreement with the result obtained in the present analysis. The result that would have been obtained from an α_s determination in the $\overline{\text{MS}}$ scheme is $\alpha_s(M_z^2) = 0.123$ [107], which is outside the theoretical error range quoted by the authors.

In [121] a new approach for an renormalization scheme invariant (RSI) measurement of the strong coupling is introduced. The RSI approach is used to determine α_s from the measured data from the τ hadronic decay. The corresponding effective β function is found to converge reasonably well. The resulting value for the strong coupling is $\alpha_s(m_\tau) = 0.3184 \pm 0.0060(exp.)$. The value is in very good agreement with the value of $\alpha_s(m_\tau) = 0.314 \pm 0.010$ obtained in [122] by applying the Padé Sum prediction. Evolving α_s to M_Z yields $\alpha_s(M_z^2) = 0.1177 \pm 0.0007(exp.) \pm 0.0006(mass.)$ to be

compared with the result obtained by applying the standard $\overline{\rm MS}$ scheme extraction of $\alpha_s(M_z^2) = 0.1202 \pm 0.0008(exp.) \pm 0.0006(mass.)$. Thus, the shift obtained in $\alpha_s(M_z^2)$ by considering the renormalization scheme invariance for the measurement of the strong coupling yields an almost identical value than that obtained within this analysis.

For the application of the RSI method in e^+e^- annihilation the shift in α_s is expected to be smaller due to the better convergence behaviour of the perturbative series at higher energies [123]. Thus, the already very good agreement between the $\alpha_s(M_z^2)$ value determined within this analysis in NLO precision with the value of $\alpha_s(M_z^2) = 0.119 \pm 0.004$ obtained in NNLO precision from from the standard model fit to the electroweak precision data [1] is likely to improve if the RSI method is applied to the NNLO analysis.

The results of the $\alpha_s(M_z^2)$ measurements applying optimized renormalization schemes introduced above including the result of the present analysis agree within 1%, although they involve measurements from different processes at very different energy scales. The agreement is in particular better than the uncertainty of $\Delta\alpha_s(M_Z) = \pm 0.002$ of the current PDG world average [118] which is however derived to a large extent from measurements applying the conventional α_s extraction within an arbitrary renormalization scheme.

The results considered above strongly suggest an improvement of the consistence of the $\alpha_s(M_z^2)$ determination from different processes if renormalization scheme invariant methods are applied. It should be emphasized here that renormalization group invariance is a fundamental property of perturbation theory in quantum field theory which should be respected in any numerical analysis [121].

Appendix A

Figures of the Data Distributions

In the following the figures of the eighteen collinear- and infrared- safe event shape distributions are presented.

The data are based on about 1.5 million events recorded at $\sqrt{s} = M_Z$ with the DELPHI detector in 1994. The distributions are corrected for detector effects, τ background and initial state photon radiation. The corrected cross sections correspond to the charged final state before decays.

For each of the observables the measured distribution is shown integrated over ϑ_T and acceptance corrected to the full solid angle. The central part of the figures show the data distributions in comparison with the prediction from four different hadronization generators: JETSET 7.3 PS D with DELPHI modification of heavy particle decays, JETSET 7.4 PS, ARIADNE 4.8 and HERWIG 5.8 C. For each observable, the fit range applied for the QCD analysis in $\mathcal{O}(\alpha_s^2)$ is indicated. The lower part of the figures shows the ratio (Monte Carlo - Data)/Data for the four hadronization generators. The width of the band indicates the size of the experimental errors. The upper part shows the detector correction including effects due to initial state radiation. The part just below shows the size of the hadronization correction. The width of the band indicates the uncertainty of the correction.

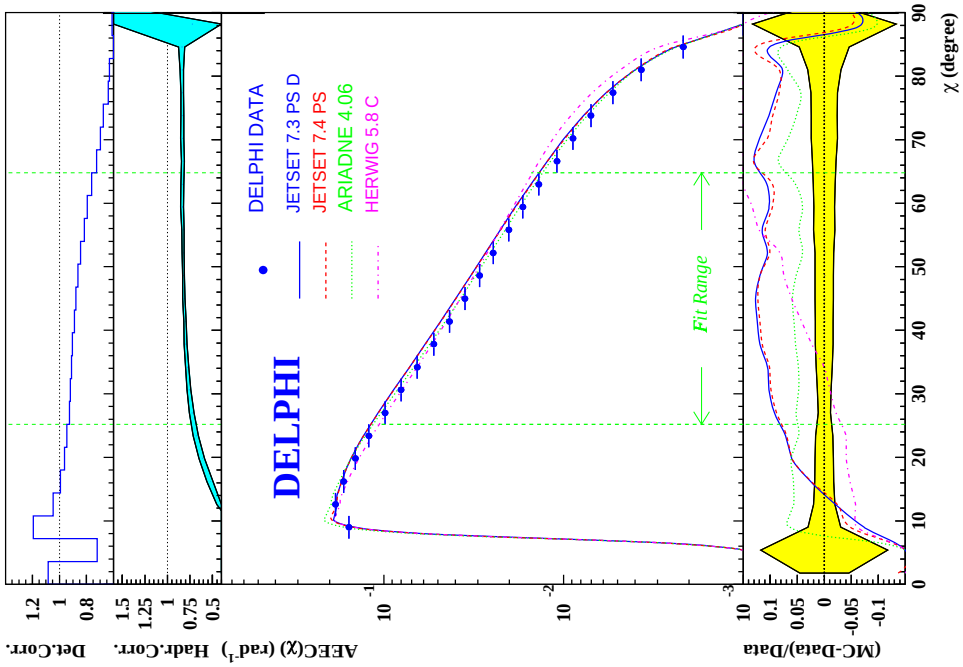

Figure A.2: Asymmetry of the Energy Energy Correlation $AEEC$

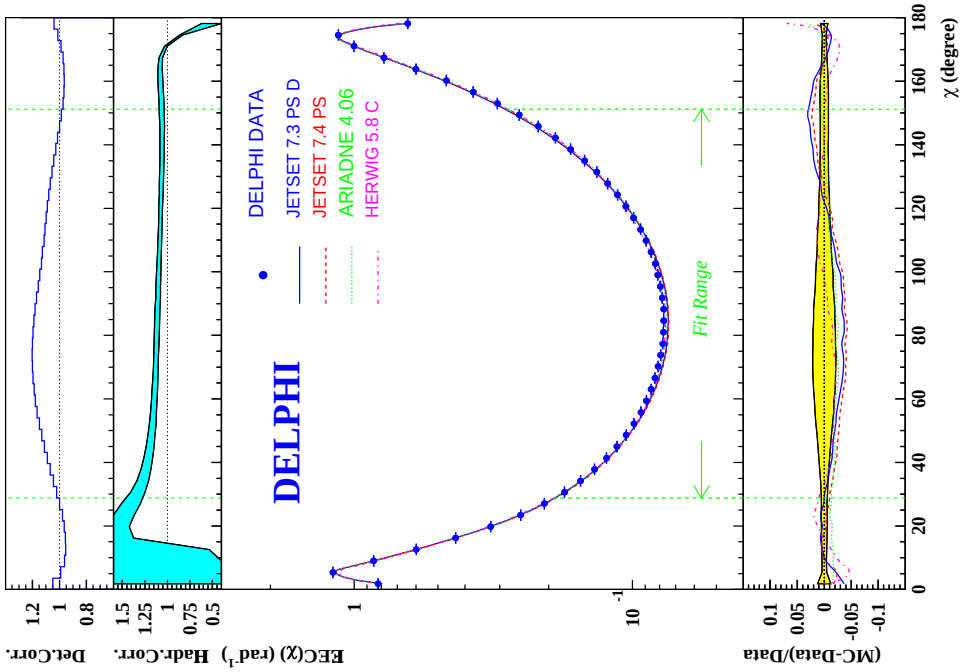

Figure A.1: Energy Energy Correlation EEC

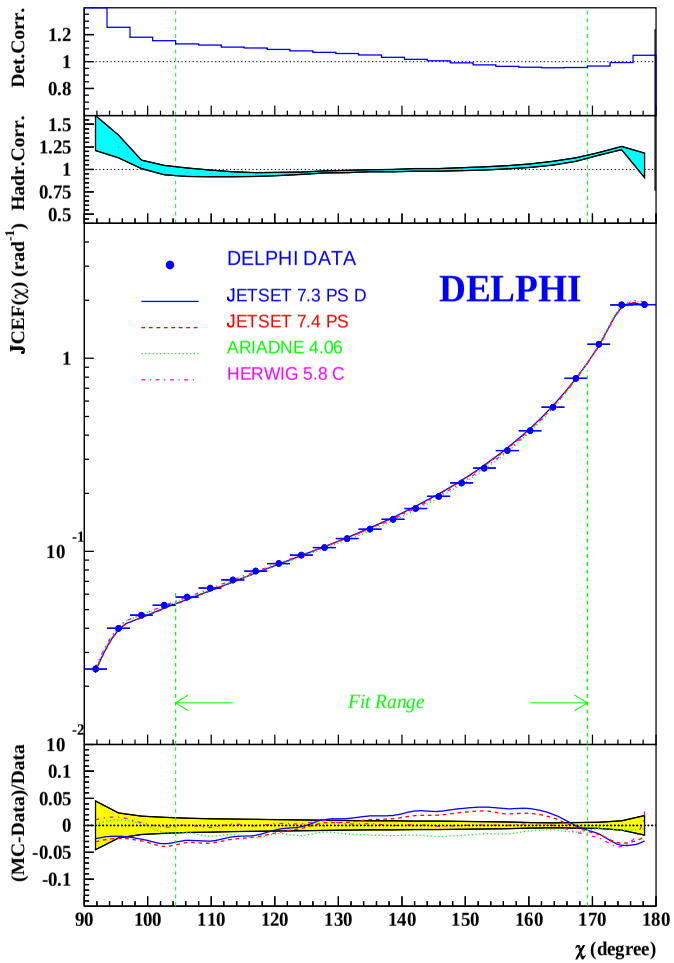

Figure A.3: Jet Cone Energy Fraction $JCEF$

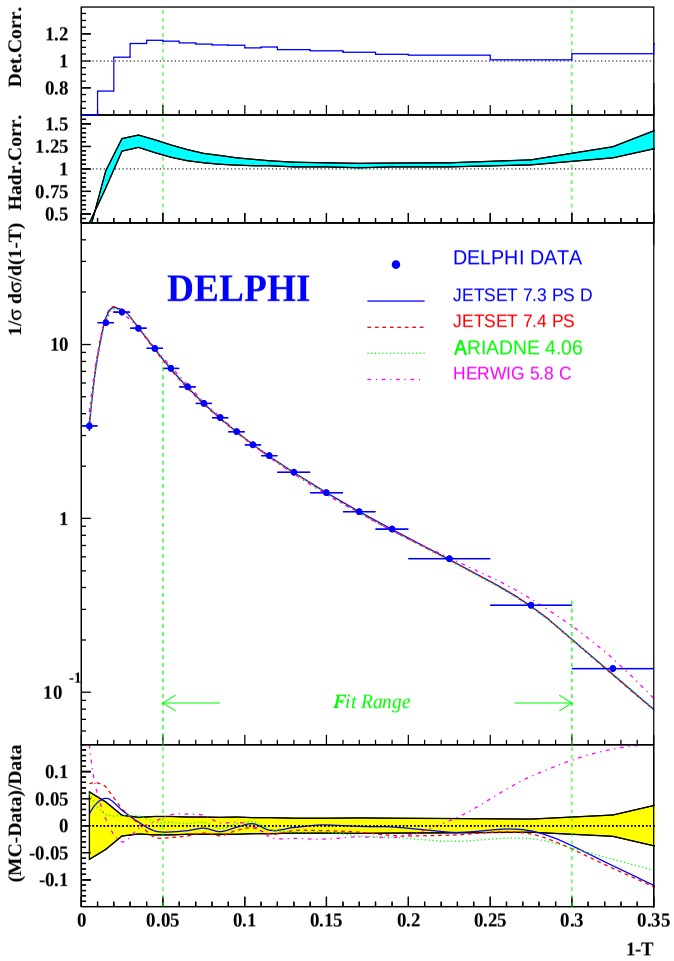

Figure A.4: 1 - Thrust $(1 - T)$

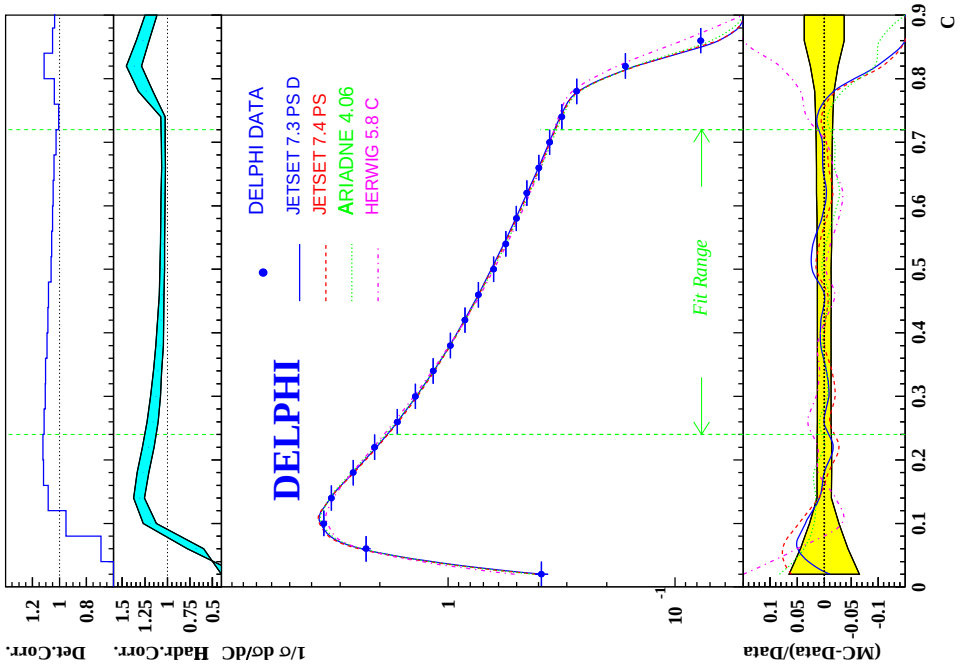

Figure A.6: C-Parameter C

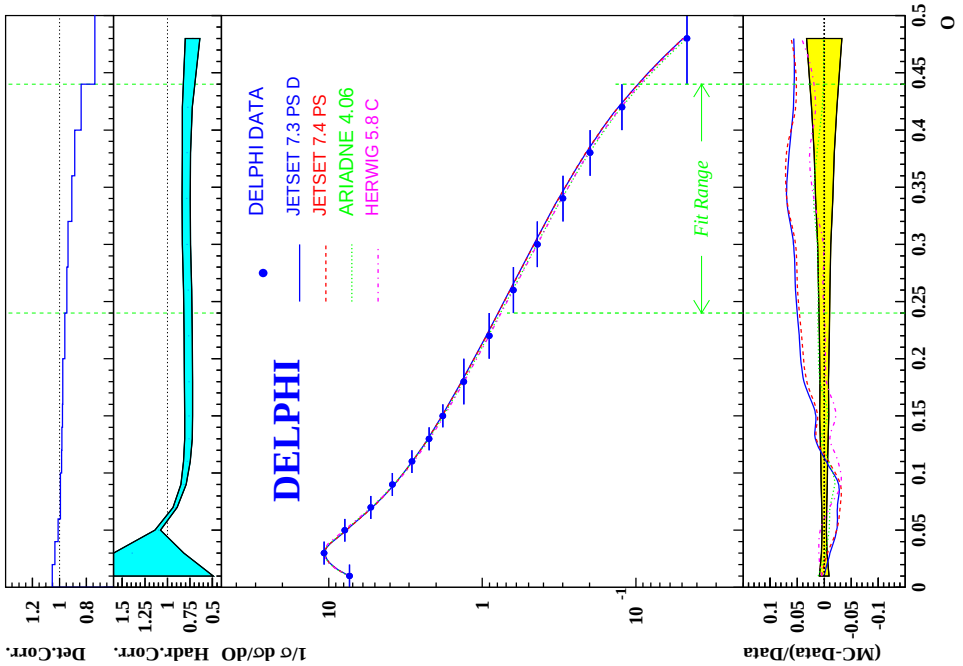

Figure A.5: Oblateness O

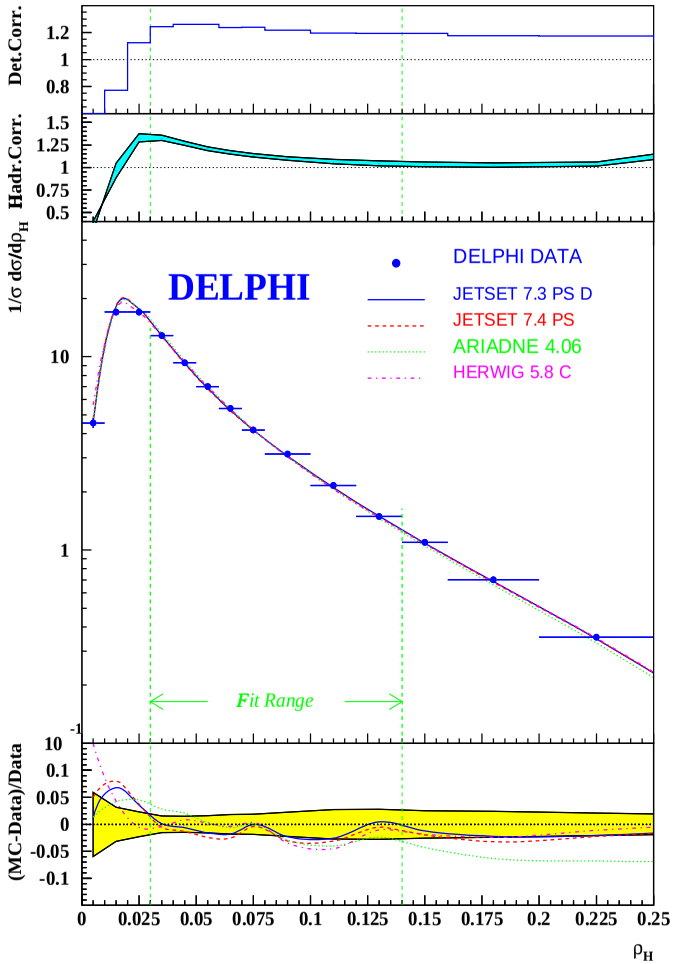

Figure A.7: Heavy Jet Mass ρ_H

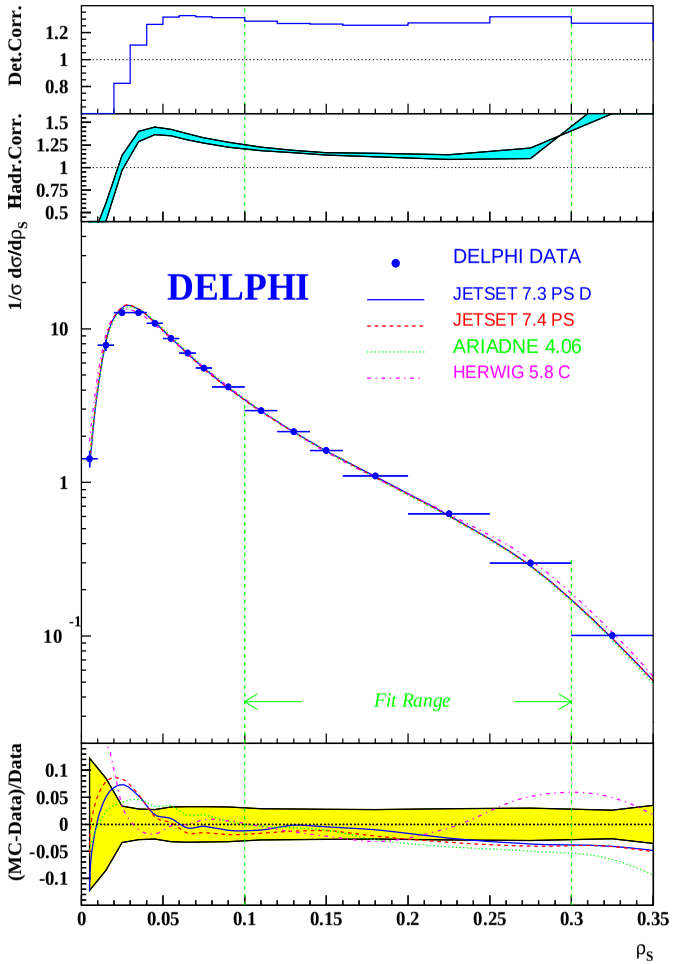

Figure A.8: Sum of the Jet Masses ρ_S

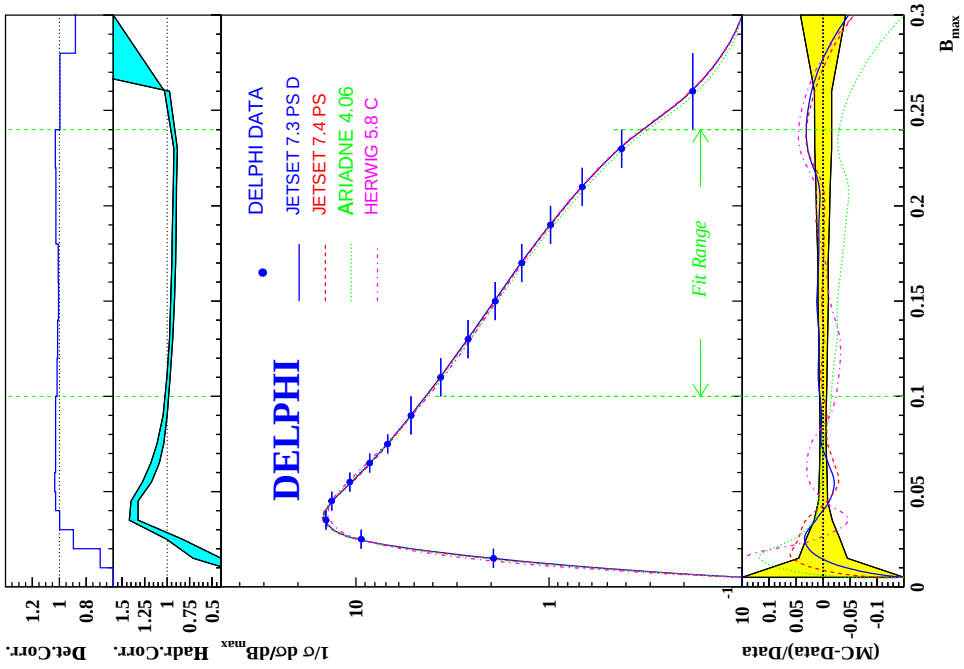

Figure A.10: Wide Jet Broadening B_{Max}

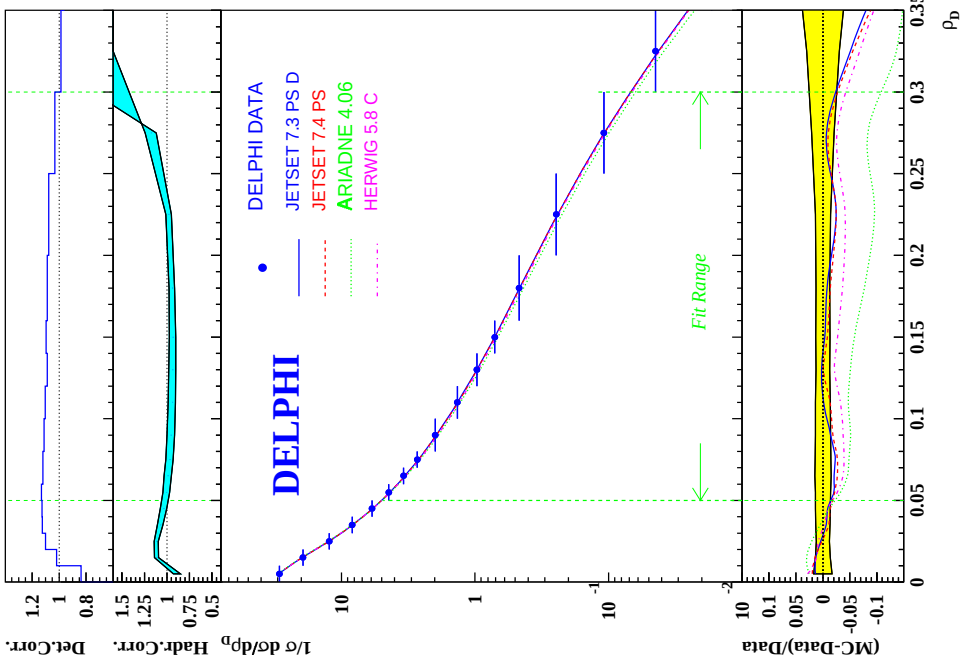

Figure A.9: Difference of the Jet Masses ρ_D

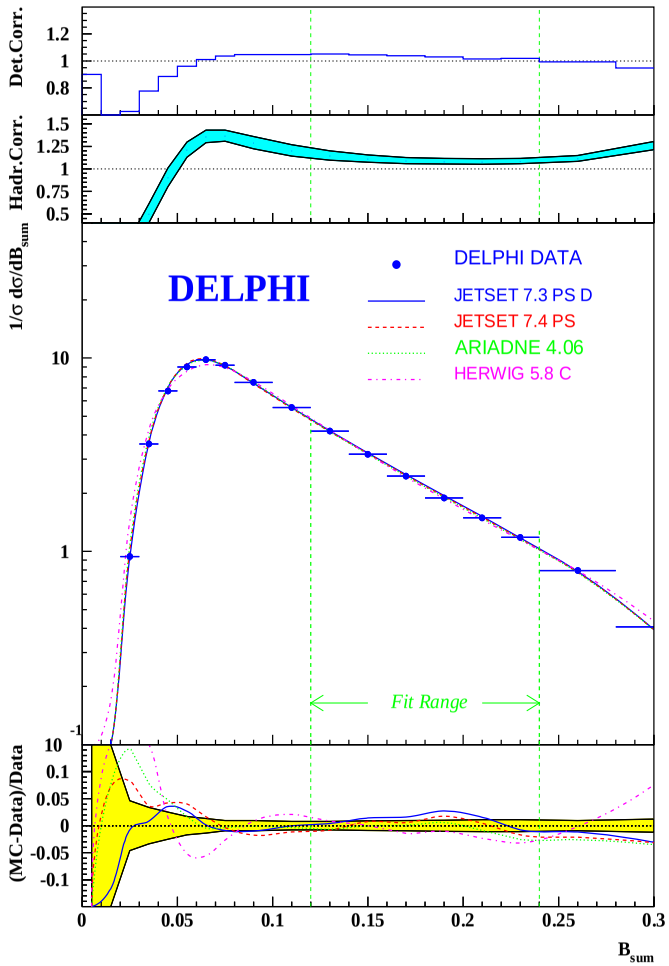

Figure A.11: Total Jet Broadening B_{Sum}

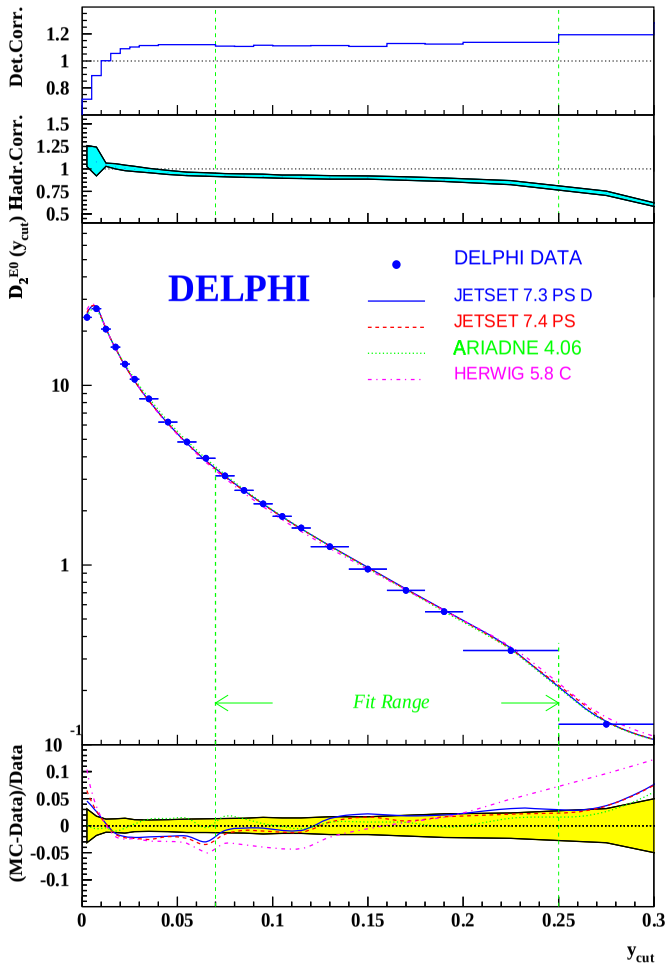

Figure A.12: Differential 2-Jet Rate E_0 Scheme $D_2^{E_0}$

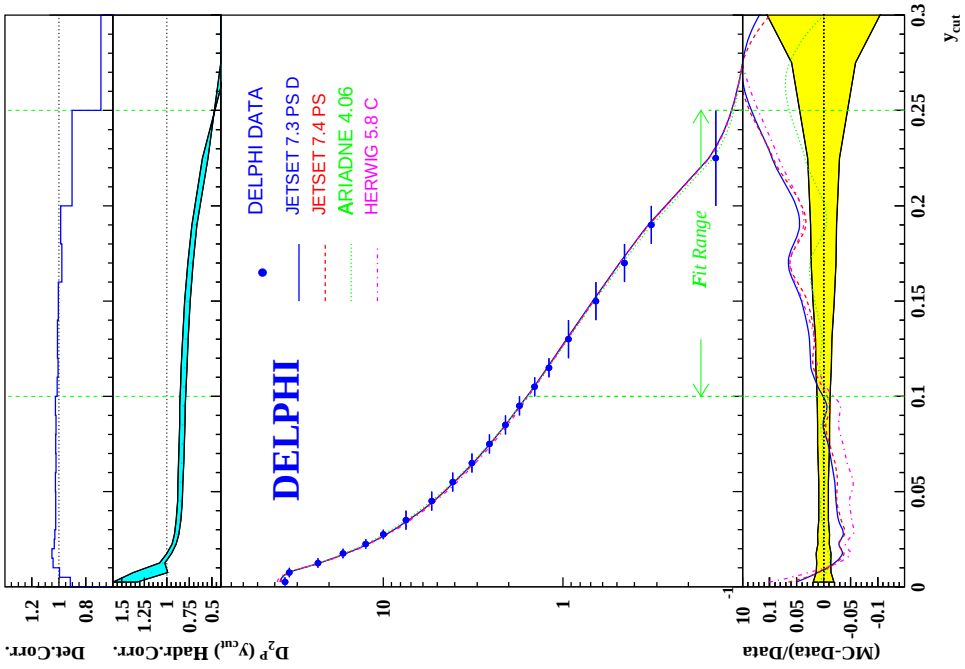

Figure A.14: Differential 2-Jet Rate P Scheme D_2^P

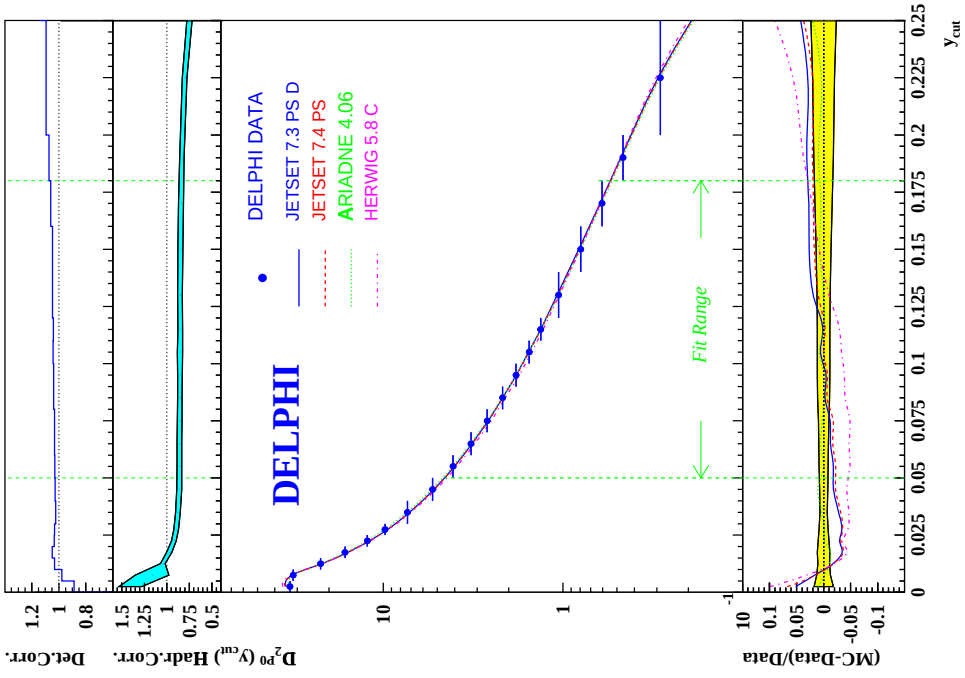

Figure A.13: Differential 2-Jet Rate P_0 Scheme $D_2^{P_0}$

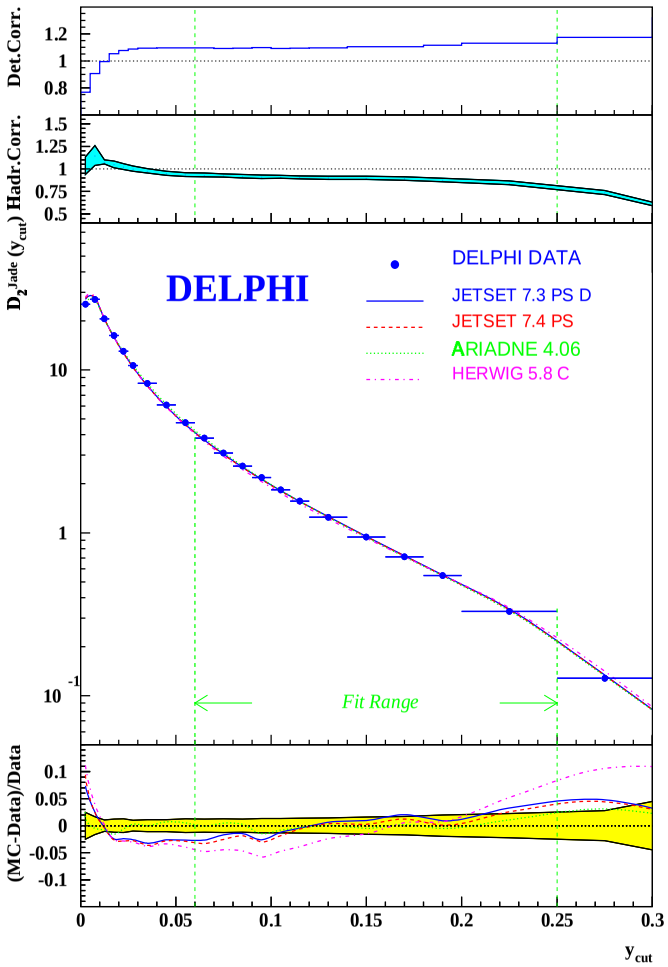

Figure A.15: Differential 2-Jet Rate Jade Algorithm D_2^{Jad}

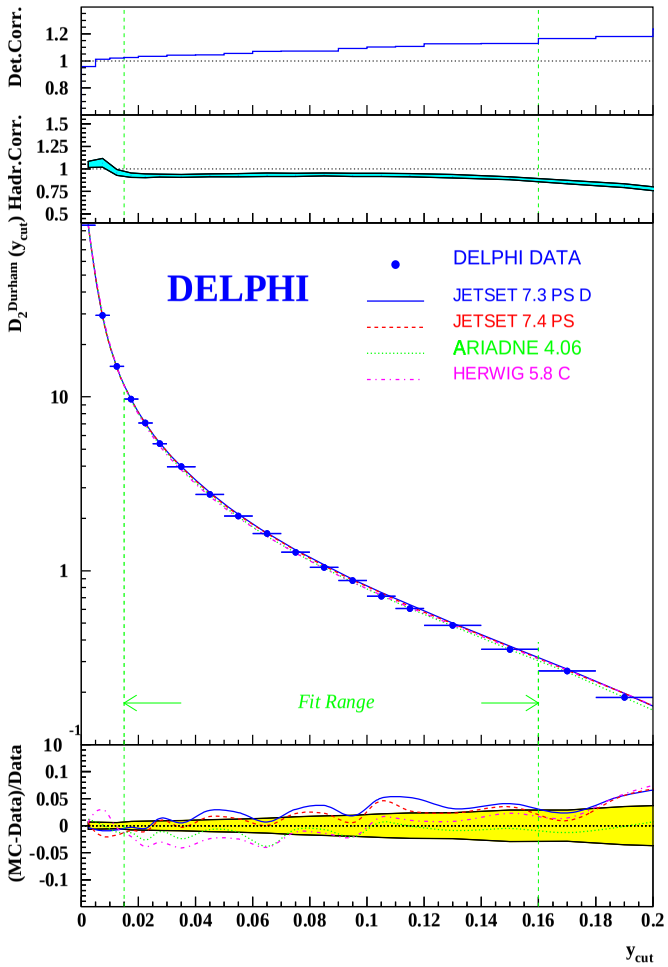

Figure A.16: Differential 2-Jet Rate Durham Algorithm D_2^{Dur}

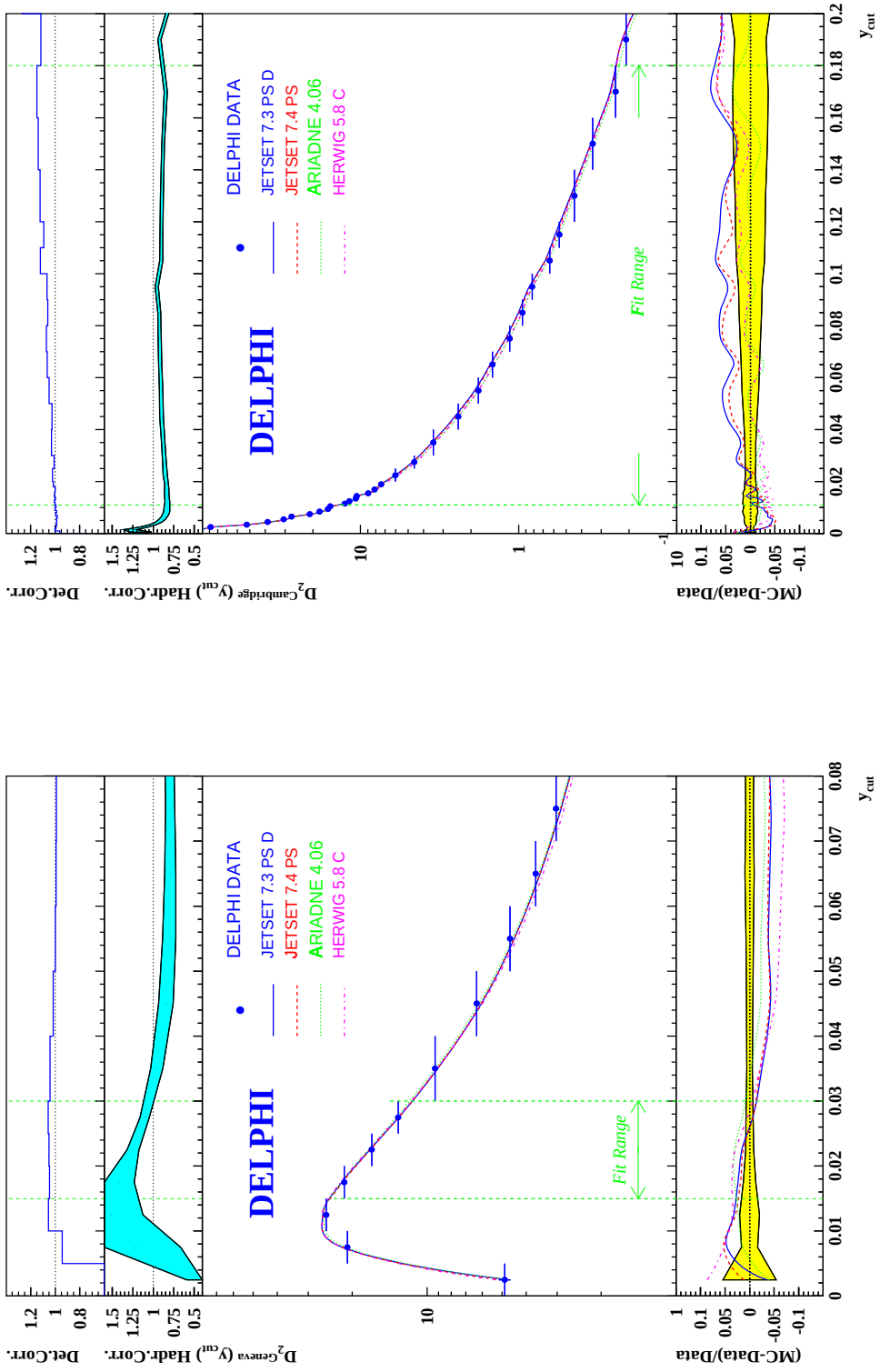

Figure A.17: Differential 2-Jet Rate Geneva Algorithm D_2^{Gen}

Figure A.18: Differential 2-Jet Rate Cambridge Algorithm D_2^{Cam}

Appendix B

Tables of the Data Distributions

In the following the data tables of the collinear- and infrared- safe event shape distributions are presented as a function of the polar angle ϑ_T of the thrust axis with respect to the e^+e^- beam direction as well as integrated and extrapolated to the full solid angle. The data are based on about 1.5 million events recorded at $\sqrt{s} = M_Z$ with the DELPHI detector in 1994.

The double differential cross sections for the shape observables Y in dependence on the event orientation $\cos\vartheta_T$ have been determined from charged particles only within 8 bins of $0.0 < \cos\vartheta_T \leq 0.96$. The data distributions are corrected for detector effects, τ background and initial state photon radiation. The corrected cross sections correspond to the charged final state before decays.

All distributions are normalized to the partial cross section in each $\cos\vartheta_T$ interval:

$$R(Y, \cos\vartheta_T) := \left(\frac{d\sigma}{d\cos\vartheta_T}\right)^{-1} \frac{d^2\sigma(Y, \cos\vartheta_T)}{dY\, d\cos\vartheta_T} \tag{B.1}$$

For each of the observables there is also one column, which contains the data integrated over ϑ_T and acceptance corrected to the full solid angle. The first error displayed is statistical, the second error represents the experimental systematic uncertainty.

Energy Energy Correlation EEC								
$\chi(deg)$	$0.0 < \cos\vartheta_T \leq 0.12$			$0.12 < \cos\vartheta_T \leq 0.24$			$0.24 < \cos\vartheta_T \leq 0.36$	
0.0 - 3.6	0.8101	± 0.0024	± 0.0120	0.8095	± 0.0025	± 0.0081	0.8144	± 0.0032 ± 0.0070
3.6 - 7.2	1.1836	± 0.0029	± 0.0055	1.1845	± 0.0027	± 0.0035	1.1885	± 0.0026 ± 0.0035
7.2 - 10.8	0.8477	± 0.0021	± 0.0041	0.8464	± 0.0013	± 0.0027	0.8478	± 0.0019 ± 0.0031
10.8 - 14.4	0.5997	± 0.0014	± 0.0030	0.5988	± 0.0012	± 0.0025	0.5959	± 0.0014 ± 0.0026
14.4 - 18.0	0.4354	± 0.0013	± 0.0026	0.4317	± 0.0010	± 0.0021	0.4325	± 0.0011 ± 0.0018
18.0 - 21.6	0.3258	± 0.0008	± 0.0020	0.3243	± 0.0009	± 0.0019	0.3241	± 0.0010 ± 0.0015
21.6 - 25.2	0.2538	± 0.0008	± 0.0018	0.2540	± 0.0008	± 0.0014	0.2539	± 0.0008 ± 0.0013
25.2 - 28.8	0.2087	± 0.0008	± 0.0015	0.2083	± 0.0008	± 0.0013	0.2084	± 0.0007 ± 0.0012
28.8 - 32.4	0.1777	± 0.0007	± 0.0012	0.1778	± 0.0006	± 0.0010	0.17728	± 0.00063 ± 0.00078
32.4 - 36.0	0.1559	± 0.0007	± 0.0010	0.15465	± 0.00061	± 0.00091	0.15489	± 0.00061 ± 0.00074
36.0 - 39.6	0.13747	± 0.00062	± 0.00073	0.13755	± 0.00056	± 0.00082	0.13892	± 0.00060 ± 0.00073
39.6 - 43.2	0.12583	± 0.00057	± 0.00065	0.12553	± 0.00055	± 0.00077	0.12411	± 0.00060 ± 0.00087
43.2 - 46.8	0.11522	± 0.00055	± 0.00063	0.11464	± 0.00053	± 0.00077	0.11444	± 0.00050 ± 0.00093
46.8 - 50.4	0.10727	± 0.00053	± 0.00065	0.10676	± 0.00048	± 0.00090	0.1060	± 0.0005 ± 0.0011
50.4 - 54.0	0.10081	± 0.00052	± 0.00079	0.0997	± 0.0005	± 0.0010	0.0996	± 0.0005 ± 0.0012
54.0 - 57.6	0.09475	± 0.00051	± 0.00088	0.0950	± 0.0005	± 0.0011	0.0943	± 0.0005 ± 0.0014
57.6 - 61.2	0.0909	± 0.0005	± 0.0010	0.0904	± 0.0005	± 0.0012	0.0900	± 0.0004 ± 0.0016
61.2 - 64.8	0.0874	± 0.0005	± 0.0012	0.0869	± 0.0005	± 0.0013	0.0869	± 0.0004 ± 0.0016
64.8 - 68.4	0.0839	± 0.0005	± 0.0012	0.0849	± 0.0005	± 0.0014	0.0837	± 0.0005 ± 0.0016
68.4 - 72.0	0.0825	± 0.0005	± 0.0013	0.0828	± 0.0005	± 0.0016	0.0813	± 0.0005 ± 0.0017
72.0 - 75.6	0.0807	± 0.0005	± 0.0014	0.0809	± 0.0005	± 0.0016	0.0794	± 0.0005 ± 0.0017
75.6 - 79.2	0.0792	± 0.0005	± 0.0015	0.0800	± 0.0005	± 0.0016	0.0782	± 0.0005 ± 0.0017
79.2 - 82.8	0.0796	± 0.0005	± 0.0016	0.0790	± 0.0005	± 0.0016	0.0790	± 0.0005 ± 0.0018
82.8 - 86.4	0.0795	± 0.0005	± 0.0016	0.0786	± 0.0005	± 0.0017	0.0781	± 0.0005 ± 0.0017
86.4 - 90.0	0.0792	± 0.0005	± 0.0017	0.0790	± 0.0006	± 0.0017	0.0783	± 0.0004 ± 0.0017
90.0 - 93.6	0.0803	± 0.0007	± 0.0017	0.0798	± 0.0006	± 0.0017	0.0791	± 0.0004 ± 0.0017
93.6 - 97.2	0.0805	± 0.0007	± 0.0017	0.0824	± 0.0006	± 0.0017	0.0809	± 0.0004 ± 0.0016
97.2 - 100.8	0.0840	± 0.0005	± 0.0017	0.0842	± 0.0006	± 0.0016	0.0826	± 0.0004 ± 0.0016
100.8 - 104.4	0.0854	± 0.0007	± 0.0016	0.0853	± 0.0007	± 0.0014	0.0854	± 0.0004 ± 0.0016
104.4 - 108.0	0.0891	± 0.0006	± 0.0013	0.0889	± 0.0007	± 0.0014	0.0875	± 0.0005 ± 0.0015
108.0 - 111.6	0.0927	± 0.0007	± 0.0012	0.0921	± 0.0006	± 0.0012	0.0920	± 0.0005 ± 0.0015
111.6 - 115.2	0.0975	± 0.0007	± 0.0010	0.0974	± 0.0006	± 0.0011	0.0967	± 0.0006 ± 0.0014
115.2 - 118.8	0.1026	± 0.0007	± 0.0010	0.1028	± 0.0006	± 0.0010	0.1018	± 0.0005 ± 0.0013
118.8 - 122.4	0.1093	± 0.0006	± 0.0010	0.10903	± 0.00069	± 0.00080	0.1081	± 0.0006 ± 0.0012
122.4 - 126.0	0.1174	± 0.0006	± 0.0010	0.11747	± 0.00064	± 0.00075	0.1157	± 0.0006 ± 0.0011
126.0 - 129.6	0.1272	± 0.0007	± 0.0010	0.12629	± 0.00065	± 0.00076	0.12592	± 0.00059 ± 0.00090
129.6 - 133.2	0.1382	± 0.0009	± 0.0012	0.13817	± 0.00069	± 0.00091	0.13701	± 0.00077 ± 0.00086
133.2 - 136.8	0.1526	± 0.0009	± 0.0014	0.1523	± 0.0009	± 0.0010	0.1521	± 0.0008 ± 0.0011
136.8 - 140.4	0.1702	± 0.0009	± 0.0018	0.1707	± 0.0009	± 0.0011	0.1694	± 0.0007 ± 0.0014
140.4 - 144.0	0.1924	± 0.0009	± 0.0019	0.1932	± 0.0009	± 0.0014	0.1914	± 0.0009 ± 0.0015
144.0 - 147.6	0.2221	± 0.0010	± 0.0021	0.2201	± 0.0008	± 0.0017	0.2189	± 0.0010 ± 0.0015
147.6 - 151.2	0.2593	± 0.0011	± 0.0023	0.2577	± 0.0011	± 0.0022	0.2566	± 0.0010 ± 0.0017
151.2 - 154.8	0.3098	± 0.0013	± 0.0025	0.3071	± 0.0011	± 0.0023	0.3074	± 0.0011 ± 0.0020
154.8 - 158.4	0.3750	± 0.0014	± 0.0027	0.3757	± 0.0011	± 0.0024	0.3747	± 0.0013 ± 0.0023
158.4 - 162.0	0.4668	± 0.0015	± 0.0029	0.4645	± 0.0013	± 0.0025	0.4662	± 0.0015 ± 0.0026
162.0 - 165.6	0.5979	± 0.0018	± 0.0030	0.5978	± 0.0016	± 0.0025	0.5970	± 0.0016 ± 0.0029
165.6 - 169.2	0.7768	± 0.0024	± 0.0032	0.7771	± 0.0021	± 0.0026	0.7777	± 0.0020 ± 0.0031
169.2 - 172.8	0.9897	± 0.0026	± 0.0039	0.9906	± 0.0024	± 0.0027	0.9960	± 0.0022 ± 0.0032
172.8 - 176.4	1.1131	± 0.0034	± 0.0048	1.1259	± 0.0029	± 0.0036	1.1277	± 0.0024 ± 0.0033
176.4 - 180.0	0.6282	± 0.0038	± 0.0059	0.6291	± 0.0021	± 0.0045	0.63278	± 0.0027 ± 0.0027

Table B.1.a: Energy Energy Correlation EEC

Energy Energy Correlation EEC			
$\chi(deg)$	$0.36 < \cos\vartheta_T \leq 0.48$	$0.48 < \cos\vartheta_T \leq 0.60$	$0.60 < \cos\vartheta_T \leq 0.72$
0.0 - 3.6	0.8157 ± 0.0026 ± 0.0062	0.8184 ± 0.0025 ± 0.0053	0.8238 ± 0.0022 ± 0.0069
3.6 - 7.2	1.1917 ± 0.0024 ± 0.0034	1.1937 ± 0.0020 ± 0.0037	1.1983 ± 0.0020 ± 0.0058
7.2 - 10.8	0.8522 ± 0.0017 ± 0.0032	0.8527 ± 0.0016 ± 0.0035	0.8547 ± 0.0018 ± 0.0042
10.8 - 14.4	0.5960 ± 0.0012 ± 0.0028	0.5986 ± 0.0014 ± 0.0027	0.5971 ± 0.0013 ± 0.0028
14.4 - 18.0	0.4319 ± 0.0010 ± 0.0025	0.4336 ± 0.0012 ± 0.0020	0.4322 ± 0.0010 ± 0.0022
18.0 - 21.6	0.3235 ± 0.0009 ± 0.0018	0.3220 ± 0.0010 ± 0.0016	0.3242 ± 0.0008 ± 0.0018
21.6 - 25.2	0.2525 ± 0.0008 ± 0.0013	0.2537 ± 0.0008 ± 0.0013	0.2512 ± 0.0007 ± 0.0013
25.2 - 28.8	0.2086 ± 0.0007 ± 0.0011	0.2079 ± 0.0007 ± 0.0011	0.2055 ± 0.0007 ± 0.0012
28.8 - 32.4	0.1761 ± 0.0006 ± 0.0010	0.1754 ± 0.0006 ± 0.0010	0.1744 ± 0.0006 ± 0.0011
32.4 - 36.0	0.15434 ± 0.00061 ± 0.00082	0.1534 ± 0.0005 ± 0.0010	0.1523 ± 0.0005 ± 0.0013
36.0 - 39.6	0.13847 ± 0.00056 ± 0.00077	0.1369 ± 0.0005 ± 0.0010	0.1361 ± 0.0005 ± 0.0015
39.6 - 43.2	0.12500 ± 0.00055 ± 0.00091	0.1235 ± 0.0005 ± 0.0012	0.1239 ± 0.0005 ± 0.0018
43.2 - 46.8	0.1141 ± 0.0005 ± 0.0011	0.1128 ± 0.0005 ± 0.0014	0.1132 ± 0.0005 ± 0.0020
46.8 - 50.4	0.1057 ± 0.0005 ± 0.0013	0.1052 ± 0.0004 ± 0.0016	0.1045 ± 0.0005 ± 0.0021
50.4 - 54.0	0.0986 ± 0.0005 ± 0.0014	0.0989 ± 0.0004 ± 0.0018	0.0982 ± 0.0005 ± 0.0021
54.0 - 57.6	0.0931 ± 0.0005 ± 0.0016	0.0930 ± 0.0004 ± 0.0018	0.0929 ± 0.0005 ± 0.0020
57.6 - 61.2	0.0889 ± 0.0005 ± 0.0017	0.0894 ± 0.0004 ± 0.0019	0.0880 ± 0.0004 ± 0.0020
61.2 - 64.8	0.0857 ± 0.0005 ± 0.0018	0.0858 ± 0.0004 ± 0.0020	0.0849 ± 0.0004 ± 0.0020
64.8 - 68.4	0.0830 ± 0.0005 ± 0.0018	0.0837 ± 0.0004 ± 0.0020	0.0824 ± 0.0004 ± 0.0020
68.4 - 72.0	0.0810 ± 0.0005 ± 0.0018	0.0816 ± 0.0004 ± 0.0019	0.0800 ± 0.0004 ± 0.0018
72.0 - 75.6	0.0793 ± 0.0005 ± 0.0018	0.0780 ± 0.0004 ± 0.0019	0.0787 ± 0.0004 ± 0.0017
75.6 - 79.2	0.0784 ± 0.0005 ± 0.0018	0.0782 ± 0.0004 ± 0.0018	0.0775 ± 0.0004 ± 0.0016
79.2 - 82.8	0.0780 ± 0.0005 ± 0.0018	0.0778 ± 0.0004 ± 0.0017	0.0769 ± 0.0004 ± 0.0015
82.8 - 86.4	0.0787 ± 0.0005 ± 0.0017	0.0779 ± 0.0004 ± 0.0016	0.0767 ± 0.0004 ± 0.0014
86.4 - 90.0	0.0789 ± 0.0005 ± 0.0016	0.0781 ± 0.0004 ± 0.0015	0.0769 ± 0.0004 ± 0.0013
90.0 - 93.6	0.0803 ± 0.0004 ± 0.0016	0.0789 ± 0.0005 ± 0.0014	0.0776 ± 0.0004 ± 0.0013
93.6 - 97.2	0.0811 ± 0.0005 ± 0.0016	0.0801 ± 0.0005 ± 0.0014	0.0793 ± 0.0004 ± 0.0012
97.2 - 100.8	0.0825 ± 0.0005 ± 0.0016	0.0818 ± 0.0005 ± 0.0013	0.0802 ± 0.0004 ± 0.0011
100.8 - 104.4	0.0845 ± 0.0006 ± 0.0015	0.0828 ± 0.0005 ± 0.0013	0.0833 ± 0.0004 ± 0.0011
104.4 - 108.0	0.0877 ± 0.0006 ± 0.0015	0.0866 ± 0.0005 ± 0.0013	0.0858 ± 0.0004 ± 0.0011
108.0 - 111.6	0.0909 ± 0.0006 ± 0.0015	0.0898 ± 0.0005 ± 0.0014	0.0892 ± 0.0005 ± 0.0011
111.6 - 115.2	0.0939 ± 0.0007 ± 0.0015	0.0947 ± 0.0005 ± 0.0014	0.0929 ± 0.0005 ± 0.0012
115.2 - 118.8	0.1000 ± 0.0007 ± 0.0015	0.0997 ± 0.0007 ± 0.0015	0.0993 ± 0.0005 ± 0.0013
118.8 - 122.4	0.1072 ± 0.0007 ± 0.0015	0.1060 ± 0.0007 ± 0.0015	0.1053 ± 0.0005 ± 0.0014
122.4 - 126.0	0.1157 ± 0.0007 ± 0.0014	0.1129 ± 0.0007 ± 0.0015	0.1123 ± 0.0006 ± 0.0016
126.0 - 129.6	0.1252 ± 0.0007 ± 0.0012	0.1240 ± 0.0007 ± 0.0015	0.1220 ± 0.0006 ± 0.0016
129.6 - 133.2	0.1362 ± 0.0007 ± 0.0011	0.1342 ± 0.0007 ± 0.0014	0.1334 ± 0.0006 ± 0.0017
133.2 - 136.8	0.1506 ± 0.0008 ± 0.0011	0.1484 ± 0.0007 ± 0.0011	0.1476 ± 0.0007 ± 0.0017
136.8 - 140.4	0.1698 ± 0.0008 ± 0.0011	0.1673 ± 0.0006 ± 0.0010	0.1655 ± 0.0008 ± 0.0017
140.4 - 144.0	0.1913 ± 0.0008 ± 0.0011	0.1899 ± 0.0007 ± 0.0010	0.1879 ± 0.0008 ± 0.0017
144.0 - 147.6	0.2209 ± 0.0009 ± 0.0016	0.2189 ± 0.0008 ± 0.0013	0.2180 ± 0.0009 ± 0.0017
147.6 - 151.2	0.2565 ± 0.0010 ± 0.0018	0.2569 ± 0.0008 ± 0.0014	0.2540 ± 0.0009 ± 0.0017
151.2 - 154.8	0.3056 ± 0.0010 ± 0.0021	0.3067 ± 0.0012 ± 0.0019	0.3041 ± 0.0009 ± 0.0021
154.8 - 158.4	0.3713 ± 0.0011 ± 0.0026	0.3748 ± 0.0013 ± 0.0022	0.3726 ± 0.0010 ± 0.0024
158.4 - 162.0	0.4678 ± 0.0013 ± 0.0028	0.4676 ± 0.0014 ± 0.0027	0.4673 ± 0.0013 ± 0.0030
162.0 - 165.6	0.5980 ± 0.0018 ± 0.0032	0.5978 ± 0.0019 ± 0.0032	0.6011 ± 0.0015 ± 0.0035
165.6 - 169.2	0.7779 ± 0.0023 ± 0.0033	0.7804 ± 0.0023 ± 0.0034	0.7849 ± 0.0022 ± 0.0042
169.2 - 172.8	0.9988 ± 0.0029 ± 0.0035	1.0029 ± 0.0025 ± 0.0035	1.0082 ± 0.0024 ± 0.0047
172.8 - 176.4	1.1310 ± 0.0033 ± 0.0040	1.1382 ± 0.0027 ± 0.0042	1.1457 ± 0.0028 ± 0.0038
176.4 - 180.0	0.6363 ± 0.0024 ± 0.0031	0.6368 ± 0.0028 ± 0.0024	0.6412 ± 0.0029 ± 0.0022

Table B.1.b: Energy Energy Correlation EEC

Energy Energy Correlation EEC			
$\chi(deg)$	$0.72 < \cos\vartheta_T \leq 0.84$	$0.84 < \cos\vartheta_T \leq 0.96$	$0. < \cos\vartheta_T \leq 1.$
0.0 - 3.6	0.8440 ± 0.0023 ± 0.0104	0.8527 ± 0.0033 ± 0.0194	0.8214 ± 0.0009 ± 0.0098
3.6 - 7.2	1.2040 ± 0.0019 ± 0.0079	1.1861 ± 0.0029 ± 0.0091	1.1937 ± 0.0010 ± 0.0051
7.2 - 10.8	0.8545 ± 0.0013 ± 0.0050	0.8350 ± 0.0021 ± 0.0032	0.8513 ± 0.0008 ± 0.0034
10.8 - 14.4	0.5948 ± 0.0010 ± 0.0037	0.5810 ± 0.0018 ± 0.0035	0.5977 ± 0.0005 ± 0.0028
14.4 - 18.0	0.4294 ± 0.0010 ± 0.0020	0.4213 ± 0.0013 ± 0.0042	0.4323 ± 0.0005 ± 0.0022
18.0 - 21.6	0.3192 ± 0.0009 ± 0.0010	0.3139 ± 0.0010 ± 0.0043	0.3234 ± 0.0004 ± 0.0017
21.6 - 25.2	0.2500 ± 0.0007 ± 0.0010	0.2456 ± 0.0008 ± 0.0041	0.2525 ± 0.0003 ± 0.0014
25.2 - 28.8	0.2034 ± 0.0007 ± 0.0012	0.2018 ± 0.0007 ± 0.0038	0.2073 ± 0.0002 ± 0.0010
28.8 - 32.4	0.1728 ± 0.0005 ± 0.0018	0.1717 ± 0.0007 ± 0.0032	0.1758 ± 0.0003 ± 0.0010
32.4 - 36.0	0.1518 ± 0.0005 ± 0.0021	0.1504 ± 0.0007 ± 0.0028	0.1537 ± 0.0003 ± 0.0010
36.0 - 39.6	0.1339 ± 0.0005 ± 0.0022	0.1332 ± 0.0006 ± 0.0023	0.1370 ± 0.0002 ± 0.0011
39.6 - 43.2	0.1218 ± 0.0005 ± 0.0023	0.1209 ± 0.0005 ± 0.0018	0.1242 ± 0.0002 ± 0.0012
43.2 - 46.8	0.1125 ± 0.0005 ± 0.0023	0.1106 ± 0.0005 ± 0.0014	0.1137 ± 0.0002 ± 0.0013
46.8 - 50.4	0.1044 ± 0.0005 ± 0.0023	0.1032 ± 0.0005 ± 0.0010	0.1054 ± 0.0002 ± 0.0014
50.4 - 54.0	0.0979 ± 0.0005 ± 0.0022	0.0979 ± 0.0005 ± 0.0010	0.0988 ± 0.0002 ± 0.0015
54.0 - 57.6	0.0929 ± 0.0004 ± 0.0021	0.09289 ± 0.00051 ± 0.00091	0.0933 ± 0.0002 ± 0.0016
57.6 - 61.2	0.0883 ± 0.0004 ± 0.0019	0.08898 ± 0.00052 ± 0.00074	0.0891 ± 0.0002 ± 0.0016
61.2 - 64.8	0.0853 ± 0.0004 ± 0.0018	0.08521 ± 0.00048 ± 0.00065	0.0857 ± 0.0002 ± 0.0017
64.8 - 68.4	0.0823 ± 0.0004 ± 0.0016	0.08275 ± 0.00045 ± 0.00063	0.0831 ± 0.0002 ± 0.0017
68.4 - 72.0	0.0804 ± 0.0004 ± 0.0015	0.07862 ± 0.00046 ± 0.00057	0.0809 ± 0.0002 ± 0.0017
72.0 - 75.6	0.0787 ± 0.0005 ± 0.0014	0.07824 ± 0.00044 ± 0.00060	0.0792 ± 0.0002 ± 0.0017
75.6 - 79.2	0.0775 ± 0.0005 ± 0.0013	0.07662 ± 0.00046 ± 0.00062	0.0778 ± 0.0002 ± 0.0016
79.2 - 82.8	0.0763 ± 0.0005 ± 0.0012	0.07531 ± 0.00042 ± 0.00067	0.0775 ± 0.0002 ± 0.0016
82.8 - 86.4	0.0757 ± 0.0005 ± 0.0010	0.07433 ± 0.00045 ± 0.00079	0.07727 ± 0.0002 ± 0.0015
86.4 - 90.0	0.0763 ± 0.0005 ± 0.0010	0.07492 ± 0.00044 ± 0.00082	0.07728 ± 0.0002 ± 0.0015
90.0 - 93.6	0.0768 ± 0.0005 ± 0.0010	0.07604 ± 0.00047 ± 0.00085	0.07815 ± 0.0002 ± 0.0014
93.6 - 97.2	0.07734 ± 0.00048 ± 0.00092	0.07643 ± 0.00048 ± 0.00087	0.07929 ± 0.0002 ± 0.0013
97.2 - 100.8	0.07900 ± 0.00053 ± 0.00090	0.07842 ± 0.00045 ± 0.00088	0.08107 ± 0.0002 ± 0.0013
100.8 - 104.4	0.08226 ± 0.00050 ± 0.00091	0.08014 ± 0.00049 ± 0.00087	0.08295 ± 0.0002 ± 0.0012
104.4 - 108.0	0.08417 ± 0.00053 ± 0.00091	0.08186 ± 0.00046 ± 0.00090	0.08583 ± 0.0002 ± 0.0011
108.0 - 111.6	0.0875 ± 0.0005 ± 0.0010	0.08607 ± 0.00051 ± 0.00091	0.08932 ± 0.0002 ± 0.0011
111.6 - 115.2	0.0907 ± 0.0005 ± 0.0010	0.09038 ± 0.00051 ± 0.00092	0.09350 ± 0.0002 ± 0.0011
115.2 - 118.8	0.0969 ± 0.0005 ± 0.0010	0.0954 ± 0.0005 ± 0.0010	0.09911 ± 0.0003 ± 0.0010
118.8 - 122.4	0.1030 ± 0.0005 ± 0.0010	0.1024 ± 0.0005 ± 0.0010	0.10558 ± 0.0003 ± 0.0010
122.4 - 126.0	0.1095 ± 0.0005 ± 0.0012	0.1107 ± 0.0006 ± 0.0011	0.11311 ± 0.0003 ± 0.0010
126.0 - 129.6	0.1200 ± 0.0005 ± 0.0014	0.1195 ± 0.0006 ± 0.0012	0.12298 ± 0.0003 ± 0.0010
129.6 - 133.2	0.1317 ± 0.0006 ± 0.0016	0.1305 ± 0.0006 ± 0.0012	0.13427 ± 0.0003 ± 0.0010
133.2 - 136.8	0.1456 ± 0.0006 ± 0.0018	0.1448 ± 0.0008 ± 0.0015	0.14855 ± 0.0003 ± 0.0011
136.8 - 140.4	0.1628 ± 0.0007 ± 0.0021	0.1605 ± 0.0009 ± 0.0018	0.16680 ± 0.0003 ± 0.0012
140.4 - 144.0	0.1854 ± 0.0007 ± 0.0022	0.1815 ± 0.0010 ± 0.0025	0.18934 ± 0.0003 ± 0.0014
144.0 - 147.6	0.2143 ± 0.0007 ± 0.0023	0.2095 ± 0.0010 ± 0.0032	0.21842 ± 0.0004 ± 0.0016
147.6 - 151.2	0.2513 ± 0.0009 ± 0.0023	0.2459 ± 0.0012 ± 0.0044	0.25555 ± 0.0004 ± 0.0019
151.2 - 154.8	0.3006 ± 0.0010 ± 0.0025	0.2960 ± 0.0012 ± 0.0051	0.30565 ± 0.0004 ± 0.0024
154.8 - 158.4	0.3692 ± 0.0011 ± 0.0026	0.3643 ± 0.0013 ± 0.0061	0.37366 ± 0.0005 ± 0.0028
158.4 - 162.0	0.4643 ± 0.0013 ± 0.0033	0.4559 ± 0.0014 ± 0.0070	0.46704 ± 0.0005 ± 0.0033
162.0 - 165.6	0.5970 ± 0.0015 ± 0.0043	0.5843 ± 0.0019 ± 0.0073	0.59937 ± 0.0007 ± 0.0035
165.6 - 169.2	0.7832 ± 0.0018 ± 0.0056	0.7665 ± 0.0022 ± 0.0076	0.78214 ± 0.0009 ± 0.0037
169.2 - 172.8	1.0172 ± 0.0019 ± 0.0061	0.9923 ± 0.0024 ± 0.0080	1.00379 ± 0.0009 ± 0.0038
172.8 - 176.4	1.1532 ± 0.0028 ± 0.0047	1.1510 ± 0.0043 ± 0.0082	1.13862 ± 0.0016 ± 0.0039
176.4 - 180.0	0.6553 ± 0.0031 ± 0.0035	0.7031 ± 0.0030 ± 0.0147	0.6419 ± 0.0010 ± 0.0041

Table B.1.c: Energy Energy Correlation EEC

Asymmetry of the Energy Energy Correlation $AEEC$			
$\chi(deg)$	$0.0 < \cos\vartheta_T \leq 0.12$	$0.12 < \cos\vartheta_T \leq 0.24$	$0.24 < \cos\vartheta_T \leq 0.36$
0.0 - 3.6	-0.1827 ± 0.0039 ± 0.0073	-0.1807 ± 0.0017 ± 0.0068	-0.1826 ± 0.0019 ± 0.0063
3.6 - 7.2	-0.0702 ± 0.0028 ± 0.0069	-0.0595 ± 0.0015 ± 0.0048	-0.0613 ± 0.0016 ± 0.0042
7.2 - 10.8	0.1483 ± 0.0024 ± 0.0049	0.1473 ± 0.0014 ± 0.0042	0.1508 ± 0.0014 ± 0.0035
10.8 - 14.4	0.1790 ± 0.0015 ± 0.0040	0.1792 ± 0.0011 ± 0.0030	0.1826 ± 0.0013 ± 0.0028
14.4 - 18.0	0.1627 ± 0.0012 ± 0.0032	0.1666 ± 0.0009 ± 0.0024	0.1647 ± 0.0010 ± 0.0024
18.0 - 21.6	0.1410 ± 0.0008 ± 0.0030	0.1402 ± 0.0008 ± 0.0021	0.1422 ± 0.0008 ± 0.0020
21.6 - 25.2	0.1212 ± 0.0007 ± 0.0025	0.1218 ± 0.0007 ± 0.0018	0.1208 ± 0.0007 ± 0.0017
25.2 - 28.8	0.1011 ± 0.0006 ± 0.0021	0.0989 ± 0.0006 ± 0.0015	0.0990 ± 0.0006 ± 0.0015
28.8 - 32.4	0.0817 ± 0.0005 ± 0.0019	0.0801 ± 0.0005 ± 0.0013	0.0796 ± 0.0005 ± 0.0012
32.4 - 36.0	0.0664 ± 0.0005 ± 0.0017	0.0658 ± 0.0005 ± 0.0012	0.0644 ± 0.0005 ± 0.0010
36.0 - 39.6	0.0551 ± 0.0004 ± 0.0016	0.0559 ± 0.0004 ± 0.0011	0.0530 ± 0.0004 ± 0.00092
39.6 - 43.2	0.0448 ± 0.0004 ± 0.0013	0.0455 ± 0.0004 ± 0.00087	0.0456 ± 0.0004 ± 0.00087
43.2 - 46.8	0.0377 ± 0.0004 ± 0.0010	0.0380 ± 0.0003 ± 0.00085	0.0379 ± 0.0003 ± 0.00072
46.8 - 50.4	0.0314 ± 0.0003 ± 0.0009	0.0318 ± 0.0003 ± 0.00064	0.0314 ± 0.0003 ± 0.00056
50.4 - 54.0	0.0267 ± 0.0003 ± 0.0007	0.0268 ± 0.0002 ± 0.00052	0.0265 ± 0.0003 ± 0.00051
54.0 - 57.6	0.0230 ± 0.0003 ± 0.0006	0.0227 ± 0.0002 ± 0.00041	0.0217 ± 0.0003 ± 0.0004
57.6 - 61.2	0.0187 ± 0.0003 ± 0.0005	0.0188 ± 0.0002 ± 0.00037	0.0183 ± 0.0002 ± 0.0003
61.2 - 64.8	0.0156 ± 0.0003 ± 0.0003	0.0161 ± 0.0002 ± 0.00031	0.0150 ± 0.0002 ± 0.00027
64.8 - 68.4	0.0137 ± 0.0003 ± 0.0003	0.0127 ± 0.0003 ± 0.00029	0.0131 ± 0.0002 ± 0.00025
68.4 - 72.0	0.0104 ± 0.0003 ± 0.0002	0.0097 ± 0.0003 ± 0.00025	0.0108 ± 0.0002 ± 0.00024
72.0 - 75.6	0.0085 ± 0.0002 ± 0.0002	0.0084 ± 0.0003 ± 0.00017	0.0083 ± 0.0002 ± 0.00022
75.6 - 79.2	0.0066 ± 0.0002 ± 0.0002	0.0057 ± 0.0003 ± 0.00019	0.0071 ± 0.0002 ± 0.00019
79.2 - 82.8	0.0047 ± 0.0002 ± 0.0003	0.0053 ± 0.0003 ± 0.00021	0.0038 ± 0.0002 ± 0.00017
82.8 - 86.4	0.0008 ± 0.0002 ± 0.0003	0.0029 ± 0.0004 ± 0.00036	0.0027 ± 0.0002 ± 0.00015
86.4 - 90.0	0.0017 ± 0.0005 ± 0.0001	0.0016 ± 0.0006 ± 0.00031	0.0005 ± 0.0003 ± 0.00017

Table B.2.a: Asymmetry of the Energy Energy Correlation $AEEC$

Asymmetry of the Energy Energy Correlation $AEEC$			
$\chi(deg)$	$0.36 < \cos\vartheta_T \leq 0.48$	$0.48 < \cos\vartheta_T \leq 0.60$	$0.60 < \cos\vartheta_T \leq 0.72$
0.0 - 3.6	-0.1796 ± 0.0019 ± 0.0059	-0.1815 ± 0.0018 ± 0.0059	-0.1817 ± 0.0016 ± 0.0082
3.6 - 7.2	-0.0611 ± 0.0017 ± 0.0041	-0.0567 ± 0.0016 ± 0.0048	-0.0529 ± 0.0015 ± 0.0071
7.2 - 10.8	0.1489 ± 0.0015 ± 0.0037	0.1523 ± 0.0015 ± 0.0041	0.1558 ± 0.0012 ± 0.0051
10.8 - 14.4	0.1826 ± 0.0012 ± 0.0033	0.1823 ± 0.0013 ± 0.0029	0.1882 ± 0.0011 ± 0.0035
14.4 - 18.0	0.1662 ± 0.0010 ± 0.0024	0.1643 ± 0.0011 ± 0.0024	0.1688 ± 0.0009 ± 0.0029
18.0 - 21.6	0.1443 ± 0.0008 ± 0.0021	0.1456 ± 0.0008 ± 0.0020	0.1432 ± 0.0007 ± 0.0027
21.6 - 25.2	0.1190 ± 0.0006 ± 0.0017	0.1212 ± 0.0007 ± 0.0017	0.1215 ± 0.0005 ± 0.0019
25.2 - 28.8	0.0973 ± 0.0005 ± 0.0015	0.0991 ± 0.0006 ± 0.0014	0.0987 ± 0.0004 ± 0.0016
28.8 - 32.4	0.0807 ± 0.0004 ± 0.0013	0.0817 ± 0.0005 ± 0.0011	0.0799 ± 0.0004 ± 0.0011
32.4 - 36.0	0.0668 ± 0.0004 ± 0.0011	0.0657 ± 0.0004 ± 0.00091	0.0658 ± 0.0004 ± 0.00091
36.0 - 39.6	0.0533 ± 0.0003 ± 0.0008	0.0533 ± 0.0004 ± 0.00070	0.0521 ± 0.0003 ± 0.00066
39.6 - 43.2	0.0452 ± 0.0003 ± 0.0007	0.0441 ± 0.0004 ± 0.00057	0.0420 ± 0.0003 ± 0.00051
43.2 - 46.8	0.0368 ± 0.0003 ± 0.0006	0.0358 ± 0.0003 ± 0.00046	0.0349 ± 0.0003 ± 0.00046
46.8 - 50.4	0.0307 ± 0.0003 ± 0.0005	0.0293 ± 0.0003 ± 0.00042	0.0292 ± 0.0003 ± 0.00043
50.4 - 54.0	0.0267 ± 0.0003 ± 0.0004	0.0253 ± 0.0003 ± 0.00039	0.0241 ± 0.0003 ± 0.00040
54.0 - 57.6	0.0226 ± 0.0003 ± 0.0003	0.0202 ± 0.0003 ± 0.00036	0.0197 ± 0.0002 ± 0.00039
57.6 - 61.2	0.0184 ± 0.0003 ± 0.0003	0.0170 ± 0.0002 ± 0.00034	0.0171 ± 0.0002 ± 0.00037
61.2 - 64.8	0.0146 ± 0.0003 ± 0.0003	0.0141 ± 0.0002 ± 0.00032	0.0143 ± 0.0002 ± 0.00035
64.8 - 68.4	0.0113 ± 0.0002 ± 0.0002	0.0113 ± 0.0002 ± 0.00029	0.0108 ± 0.0001 ± 0.00033
68.4 - 72.0	0.0101 ± 0.0002 ± 0.0002	0.0088 ± 0.0001 ± 0.00027	0.0090 ± 0.0001 ± 0.00031
72.0 - 75.6	0.0085 ± 0.0002 ± 0.0002	0.0071 ± 0.0001 ± 0.00024	0.0071 ± 0.0001 ± 0.00028
75.6 - 79.2	0.0060 ± 0.0002 ± 0.0002	0.0050 ± 0.0001 ± 0.00021	0.0057 ± 0.0001 ± 0.00024
79.2 - 82.8	0.0043 ± 0.0001 ± 0.0001	0.0039 ± 0.0001 ± 0.00018	0.0034 ± 0.0001 ± 0.00022
82.8 - 86.4	0.0025 ± 0.0001 ± 0.0001	0.0025 ± 0.0001 ± 0.00014	0.0023 ± 0.0001 ± 0.00013
86.4 - 90.0	0.0039 ± 0.0022 ± 0.0013	0.0009 ± 0.0001 ± 0.00011	0.0011 ± 0.0004 ± 0.00019

Table B.2.b: Asymmetry of the Energy Energy Correlation $AEEC$

Asymmetry of the Energy Energy Correlation $AEEC$			
$\chi(deg)$	$0.72 < \cos\vartheta_T \leq 0.84$	$0.84 < \cos\vartheta_T \leq 0.96$	$0. < \cos\vartheta_T \leq 1.$
0.0 - 3.6	-0.1866 ± 0.0015 ± 0.0146	-0.1563 ± 0.0009 ± 0.0194	-0.1792 ± 0.000 ± 0.0081
3.6 - 7.2	-0.0529 ± 0.0010 ± 0.0116	-0.0336 ± 0.0027 ± 0.0626	-0.0565 ± 0.000 ± 0.0066
7.2 - 10.8	0.1664 ± 0.0014 ± 0.0082	0.1567 ± 0.0018 ± 0.0085	0.1564 ± 0.000 ± 0.0047
10.8 - 14.4	0.1889 ± 0.0013 ± 0.0051	0.1855 ± 0.0013 ± 0.0056	0.1856 ± 0.000 ± 0.0036
14.4 - 18.0	0.1676 ± 0.0008 ± 0.0036	0.1630 ± 0.0011 ± 0.0036	0.1673 ± 0.000 ± 0.0029
18.0 - 21.6	0.1450 ± 0.0007 ± 0.0030	0.1420 ± 0.0008 ± 0.0029	0.1437 ± 0.000 ± 0.0024
21.6 - 25.2	0.1193 ± 0.0006 ± 0.0023	0.1188 ± 0.0007 ± 0.0024	0.1212 ± 0.000 ± 0.0019
25.2 - 28.8	0.0974 ± 0.0005 ± 0.0019	0.0944 ± 0.0006 ± 0.0017	0.0985 ± 0.000 ± 0.0011
28.8 - 32.4	0.0787 ± 0.0005 ± 0.0012	0.0745 ± 0.0005 ± 0.0014	0.0800 ± 0.000 ± 0.0010
32.4 - 36.0	0.0629 ± 0.0004 ± 0.0010	0.0594 ± 0.0004 ± 0.00125	0.0651 ± 0.000 ± 0.00094
36.0 - 39.6	0.0517 ± 0.0004 ± 0.0008	0.0486 ± 0.0004 ± 0.00088	0.0527 ± 0.000 ± 0.00085
39.6 - 43.2	0.0413 ± 0.0004 ± 0.0008	0.0398 ± 0.0004 ± 0.00078	0.0430 ± 0.000 ± 0.00069
43.2 - 46.8	0.0335 ± 0.0003 ± 0.0007	0.0342 ± 0.0003 ± 0.00074	0.0353 ± 0.000 ± 0.00059
46.8 - 50.4	0.0278 ± 0.0003 ± 0.0006	0.0273 ± 0.0003 ± 0.00070	0.0293 ± 0.000 ± 0.00049
50.4 - 54.0	0.0226 ± 0.0002 ± 0.0006	0.0217 ± 0.0003 ± 0.00065	0.0245 ± 0.000 ± 0.00041
54.0 - 57.6	0.0176 ± 0.0002 ± 0.0005	0.0178 ± 0.0003 ± 0.00064	0.0201 ± 0.000 ± 0.00038
57.6 - 61.2	0.0150 ± 0.0002 ± 0.0005	0.0133 ± 0.0003 ± 0.00068	0.0168 ± 0.000 ± 0.00031
61.2 - 64.8	0.0120 ± 0.0002 ± 0.0005	0.0102 ± 0.0003 ± 0.00070	0.0137 ± 0.000 ± 0.00026
64.8 - 68.4	0.0091 ± 0.0001 ± 0.0004	0.0072 ± 0.0004 ± 0.00083	0.0109 ± 0.000 ± 0.00022
68.4 - 72.0	0.0075 ± 0.0001 ± 0.0003	0.0078 ± 0.0004 ± 0.0010	0.0088 ± 0.000 ± 0.00020
72.0 - 75.6	0.0057 ± 0.0001 ± 0.0003	0.0012 ± 0.0006 ± 0.0014	0.0070 ± 0.000 ± 0.00015
75.6 - 79.2	0.0046 ± 0.0001 ± 0.0002	0.0017 ± 0.0009 ± 0.0019	0.0053 ± 0.000 ± 0.00011
79.2 - 82.8	0.0029 ± 0.0001 ± 0.0001	0.0007 ± 0.0015 ± 0.0021	0.0037 ± 0.000 ± 0.00009
82.8 - 86.4	0.0016 ± 0.0001 ± 0.0001	0.0000 ± 0.0026 ± 0.0044	0.0021 ± 0.000 ± 0.00008
86.4 - 90.0	0.0019 ± 0.0008 ± 0.0001	0.0121 ± 0.0104 ± 0.0384	0.0008 ± 0.000 ± 0.00007

Table B.2.c: Asymmetry of the Energy Energy Correlation $AEEC$

Jet Cone Energy Fraction $JCEF$			
$\chi(deg)$	$0.0 < \cos\vartheta_T \leq 0.12$	$0.12 < \cos\vartheta_T \leq 0.24$	$0.24 < \cos\vartheta_T \leq 0.36$
90.0 - 93.6	0.0244 ± 0.0005 ± 0.0019	0.0248 ± 0.0005 ± 0.0017	0.0244 ± 0.0004 ± 0.0014
93.6 - 97.2	0.0410 ± 0.0006 ± 0.0018	0.0408 ± 0.0006 ± 0.0016	0.0404 ± 0.0005 ± 0.0013
97.2 - 100.8	0.0472 ± 0.0007 ± 0.0016	0.0471 ± 0.0007 ± 0.0013	0.0480 ± 0.0006 ± 0.0012
100.8 - 104.4	0.0530 ± 0.0008 ± 0.0012	0.0540 ± 0.0008 ± 0.0012	0.0544 ± 0.0007 ± 0.0012
104.4 - 108.0	0.05863 ± 0.00082 ± 0.00093	0.0592 ± 0.0009 ± 0.0011	0.0591 ± 0.0007 ± 0.0012
108.0 - 111.6	0.06727 ± 0.00089 ± 0.00086	0.0666 ± 0.0009 ± 0.0010	0.0668 ± 0.0008 ± 0.0011
111.6 - 115.2	0.07337 ± 0.00093 ± 0.00082	0.0747 ± 0.0010 ± 0.0010	0.0737 ± 0.0009 ± 0.0011
115.2 - 118.8	0.0821 ± 0.0010 ± 0.0008	0.0824 ± 0.0011 ± 0.0009	0.0788 ± 0.0009 ± 0.0010
118.8 - 122.4	0.0916 ± 0.0010 ± 0.0009	0.0893 ± 0.0011 ± 0.0007	0.0892 ± 0.0010 ± 0.0009
122.4 - 126.0	0.1000 ± 0.0011 ± 0.0009	0.1002 ± 0.0012 ± 0.0008	0.0978 ± 0.0011 ± 0.0007
126.0 - 129.6	0.1103 ± 0.0012 ± 0.0010	0.1104 ± 0.0012 ± 0.0009	0.1057 ± 0.0011 ± 0.0007
129.6 - 133.2	0.1229 ± 0.0013 ± 0.0012	0.1224 ± 0.0013 ± 0.0010	0.1193 ± 0.0012 ± 0.0008
133.2 - 136.8	0.1354 ± 0.0014 ± 0.0013	0.1358 ± 0.0013 ± 0.0011	0.1352 ± 0.0013 ± 0.0009
136.8 - 140.4	0.1514 ± 0.0014 ± 0.0014	0.1509 ± 0.0014 ± 0.0012	0.1518 ± 0.0013 ± 0.0009
140.4 - 144.0	0.1726 ± 0.0016 ± 0.0016	0.1736 ± 0.0015 ± 0.0013	0.1713 ± 0.0015 ± 0.0010
144.0 - 147.6	0.1985 ± 0.0018 ± 0.0017	0.1958 ± 0.0018 ± 0.0015	0.1963 ± 0.0016 ± 0.0012
147.6 - 151.2	0.2317 ± 0.0019 ± 0.0020	0.2306 ± 0.0020 ± 0.0016	0.2296 ± 0.0017 ± 0.0015
151.2 - 154.8	0.2755 ± 0.0023 ± 0.0023	0.2749 ± 0.0022 ± 0.0018	0.2740 ± 0.0018 ± 0.0016
154.8 - 158.4	0.3387 ± 0.0026 ± 0.0026	0.3372 ± 0.0026 ± 0.0020	0.3358 ± 0.0020 ± 0.0017
158.4 - 162.0	0.4261 ± 0.0031 ± 0.0035	0.4237 ± 0.0029 ± 0.0023	0.4241 ± 0.0023 ± 0.0018
162.0 - 165.6	0.5643 ± 0.0040 ± 0.0041	0.5589 ± 0.0034 ± 0.0027	0.5592 ± 0.0027 ± 0.0025
165.6 - 169.2	0.7896 ± 0.0044 ± 0.0047	0.7894 ± 0.0037 ± 0.0034	0.7845 ± 0.0041 ± 0.0032
169.2 - 172.8	1.1848 ± 0.0052 ± 0.0063	1.1750 ± 0.0046 ± 0.0056	1.1859 ± 0.0055 ± 0.0043
172.8 - 176.4	1.8620 ± 0.0083 ± 0.0202	1.8765 ± 0.0073 ± 0.0136	1.8823 ± 0.0087 ± 0.0127
176.4 - 180.0	1.8626 ± 0.0102 ± 0.0383	1.8540 ± 0.0062 ± 0.0291	1.8648 ± 0.0094 ± 0.0272

Table B.3.a: Jet Cone Energy Fraction $JCEF$

Jet Cone Energy Fraction $JCEF$			
$\chi(deg)$	$0.36 < \cos\vartheta_T \leq 0.48$	$0.48 < \cos\vartheta_T \leq 0.60$	$0.60 < \cos\vartheta_T \leq 0.72$
90.0 - 93.6	0.02514 ± 0.00050 ± 0.00094	0.02510 ± 0.00023 ± 0.00100	0.02443 ± 0.00035 ± 0.00083
93.6 - 97.2	0.04060 ± 0.00054 ± 0.00091	0.04064 ± 0.00048 ± 0.00077	0.04000 ± 0.00038 ± 0.00072
97.2 - 100.8	0.04763 ± 0.00058 ± 0.00090	0.04686 ± 0.00053 ± 0.00075	0.04690 ± 0.00042 ± 0.00058
100.8 - 104.4	0.0532 ± 0.0006 ± 0.0010	0.05230 ± 0.00060 ± 0.00074	0.05284 ± 0.00056 ± 0.00052
104.4 - 108.0	0.0590 ± 0.0007 ± 0.0011	0.05800 ± 0.00071 ± 0.00078	0.05770 ± 0.00060 ± 0.00059
108.0 - 111.6	0.0656 ± 0.0009 ± 0.0012	0.06433 ± 0.00078 ± 0.00095	0.06397 ± 0.00069 ± 0.00068
111.6 - 115.2	0.0720 ± 0.0010 ± 0.0013	0.0716 ± 0.0008 ± 0.0012	0.07004 ± 0.00075 ± 0.00071
115.2 - 118.8	0.0792 ± 0.0010 ± 0.0016	0.0800 ± 0.0009 ± 0.0014	0.0790 ± 0.0008 ± 0.0010
118.8 - 122.4	0.0877 ± 0.0011 ± 0.0015	0.0869 ± 0.0010 ± 0.0016	0.0869 ± 0.0009 ± 0.0013
122.4 - 126.0	0.0970 ± 0.0012 ± 0.0014	0.0969 ± 0.0011 ± 0.0019	0.0935 ± 0.0009 ± 0.0017
126.0 - 129.6	0.1059 ± 0.0013 ± 0.0013	0.1047 ± 0.0011 ± 0.0018	0.1036 ± 0.0010 ± 0.0019
129.6 - 133.2	0.1193 ± 0.0013 ± 0.0009	0.1167 ± 0.0012 ± 0.0016	0.1145 ± 0.0011 ± 0.0023
133.2 - 136.8	0.1338 ± 0.0014 ± 0.0007	0.1290 ± 0.0012 ± 0.0013	0.1292 ± 0.0012 ± 0.0025
136.8 - 140.4	0.1516 ± 0.0015 ± 0.0008	0.1475 ± 0.0013 ± 0.0011	0.1449 ± 0.0013 ± 0.0025
140.4 - 144.0	0.1707 ± 0.0017 ± 0.0009	0.1674 ± 0.0014 ± 0.0009	0.1626 ± 0.0014 ± 0.0023
144.0 - 147.6	0.1973 ± 0.0018 ± 0.0009	0.1965 ± 0.0015 ± 0.0010	0.1896 ± 0.0015 ± 0.0017
147.6 - 151.2	0.2295 ± 0.0019 ± 0.0011	0.2299 ± 0.0017 ± 0.0013	0.2236 ± 0.0016 ± 0.0013
151.2 - 154.8	0.2698 ± 0.0021 ± 0.0014	0.2728 ± 0.0019 ± 0.0016	0.2712 ± 0.0018 ± 0.0014
154.8 - 158.4	0.3341 ± 0.0025 ± 0.0018	0.3367 ± 0.0022 ± 0.0018	0.3331 ± 0.0022 ± 0.0018
158.4 - 162.0	0.4236 ± 0.0027 ± 0.0025	0.4234 ± 0.0025 ± 0.0025	0.4213 ± 0.0027 ± 0.0025
162.0 - 165.6	0.5524 ± 0.0030 ± 0.0029	0.5591 ± 0.0029 ± 0.0030	0.5633 ± 0.0029 ± 0.0031
165.6 - 169.2	0.7885 ± 0.0048 ± 0.0036	0.7861 ± 0.0034 ± 0.0039	0.7877 ± 0.0034 ± 0.0046
169.2 - 172.8	1.1790 ± 0.0053 ± 0.0048	1.1822 ± 0.0047 ± 0.0047	1.1917 ± 0.0051 ± 0.0049
172.8 - 176.4	1.8890 ± 0.0078 ± 0.0127	1.8930 ± 0.0062 ± 0.0107	1.9072 ± 0.0059 ± 0.0123
176.4 - 180.0	1.8735 ± 0.0100 ± 0.0268	1.8775 ± 0.0082 ± 0.0224	1.8656 ± 0.0077 ± 0.0263

Table B.3.b: Jet Cone Energy Fraction $JCEF$

Jet Cone Energy Fraction $JCEF$			
$\chi(deg)$	$0.72 < \cos\vartheta_T \leq 0.84$	$0.84 < \cos\vartheta_T \leq 0.96$	$0. < \cos\vartheta_T \leq 1.$
90.0 - 93.6	0.02451 ± 0.00031 ± 0.00090	0.02426 ± 0.00031 ± 0.00089	0.0246 ± 0.0001 ± 0.0011
93.6 - 97.2	0.03969 ± 0.00035 ± 0.00067	0.03867 ± 0.00040 ± 0.00063	0.04001 ± 0.00012 ± 0.00092
97.2 - 100.8	0.04668 ± 0.00049 ± 0.00065	0.04507 ± 0.00053 ± 0.00050	0.04671 ± 0.00020 ± 0.00077
100.8 - 104.4	0.05262 ± 0.00058 ± 0.00061	0.05019 ± 0.00061 ± 0.00051	0.05256 ± 0.00023 ± 0.00075
104.4 - 108.0	0.05764 ± 0.00063 ± 0.00058	0.05680 ± 0.00073 ± 0.00062	0.05800 ± 0.00026 ± 0.00073
108.0 - 111.6	0.06292 ± 0.00069 ± 0.00060	0.06230 ± 0.00077 ± 0.00069	0.06448 ± 0.00028 ± 0.00075
111.6 - 115.2	0.06874 ± 0.00076 ± 0.00062	0.06925 ± 0.00082 ± 0.00077	0.07110 ± 0.00033 ± 0.00077
115.2 - 118.8	0.07700 ± 0.00080 ± 0.00071	0.07708 ± 0.00089 ± 0.00081	0.07889 ± 0.00034 ± 0.00079
118.8 - 122.4	0.08334 ± 0.00086 ± 0.00087	0.08356 ± 0.00095 ± 0.00088	0.08655 ± 0.00035 ± 0.00083
122.4 - 126.0	0.0923 ± 0.0009 ± 0.0010	0.09339 ± 0.00098 ± 0.00092	0.09555 ± 0.00036 ± 0.00087
126.0 - 129.6	0.1027 ± 0.0010 ± 0.0014	0.10197 ± 0.0010 ± 0.0010	0.10478 ± 0.00038 ± 0.00091
129.6 - 133.2	0.1122 ± 0.0011 ± 0.0017	0.11250 ± 0.0011 ± 0.0011	0.11652 ± 0.00042 ± 0.00095
133.2 - 136.8	0.1252 ± 0.0012 ± 0.0022	0.1253 ± 0.0012 ± 0.0014	0.1301 ± 0.0004 ± 0.0010
136.8 - 140.4	0.1425 ± 0.0013 ± 0.0026	0.1412 ± 0.0013 ± 0.0017	0.1468 ± 0.0005 ± 0.0011
140.4 - 144.0	0.1615 ± 0.0014 ± 0.0029	0.1636 ± 0.0014 ± 0.0020	0.1668 ± 0.0006 ± 0.0012
144.0 - 147.6	0.1903 ± 0.0015 ± 0.0033	0.1865 ± 0.0016 ± 0.0027	0.1931 ± 0.0007 ± 0.0013
147.6 - 151.2	0.2217 ± 0.0016 ± 0.0036	0.2201 ± 0.0018 ± 0.0040	0.2263 ± 0.0007 ± 0.0015
151.2 - 154.8	0.2649 ± 0.0018 ± 0.0031	0.2641 ± 0.0021 ± 0.0049	0.2705 ± 0.0008 ± 0.0016
154.8 - 158.4	0.3280 ± 0.0019 ± 0.0026	0.3248 ± 0.0025 ± 0.0054	0.3331 ± 0.0009 ± 0.0018
158.4 - 162.0	0.4139 ± 0.0022 ± 0.0022	0.4110 ± 0.0030 ± 0.0059	0.4208 ± 0.0010 ± 0.0020
162.0 - 165.6	0.5530 ± 0.0028 ± 0.0039	0.5500 ± 0.0034 ± 0.0065	0.5578 ± 0.0012 ± 0.0023
165.6 - 169.2	0.7886 ± 0.0035 ± 0.0064	0.7777 ± 0.0039 ± 0.0073	0.7870 ± 0.0014 ± 0.0037
169.2 - 172.8	1.1911 ± 0.0042 ± 0.0099	1.1639 ± 0.0051 ± 0.0079	1.1821 ± 0.0019 ± 0.0062
172.8 - 176.4	1.9128 ± 0.0058 ± 0.0178	1.8781 ± 0.0075 ± 0.0289	1.8895 ± 0.0031 ± 0.0161
176.4 - 180.0	1.9184 ± 0.0084 ± 0.0411	2.0028 ± 0.0087 ± 0.0650	1.8978 ± 0.0025 ± 0.0345

Table B.3.c: Jet Cone Energy Fraction $JCEF$

1 - Thrust $(1-T)$									
$1-T$	$0.0 < \cos\vartheta_T \leq 0.12$			$0.12 < \cos\vartheta_T \leq 0.24$			$0.24 < \cos\vartheta_T \leq 0.36$		
0.00 - 0.01	3.305	± 0.043	± 0.186	3.340	± 0.041	± 0.190	3.330	± 0.046	± 0.193
0.01 - 0.02	13.031	± 0.104	± 0.527	13.219	± 0.105	± 0.542	13.315	± 0.098	± 0.572
0.02 - 0.03	15.170	± 0.132	± 0.235	15.038	± 0.122	± 0.339	15.224	± 0.127	± 0.222
0.03 - 0.04	12.262	± 0.126	± 0.173	12.395	± 0.119	± 0.180	12.207	± 0.119	± 0.147
0.04 - 0.05	9.555	± 0.114	± 0.151	9.376	± 0.106	± 0.152	9.392	± 0.102	± 0.135
0.05 - 0.06	7.214	± 0.096	± 0.135	7.122	± 0.088	± 0.117	7.304	± 0.091	± 0.114
0.06 - 0.07	5.717	± 0.080	± 0.076	5.743	± 0.080	± 0.101	5.762	± 0.078	± 0.099
0.07 - 0.08	4.577	± 0.076	± 0.069	4.555	± 0.076	± 0.072	4.627	± 0.069	± 0.066
0.08 - 0.09	3.886	± 0.067	± 0.066	3.868	± 0.066	± 0.061	3.723	± 0.065	± 0.056
0.09 - 0.10	3.156	± 0.065	± 0.051	3.106	± 0.063	± 0.053	3.180	± 0.061	± 0.048
0.10 - 0.11	2.713	± 0.060	± 0.046	2.670	± 0.060	± 0.045	2.730	± 0.056	± 0.044
0.11 - 0.12	2.320	± 0.053	± 0.036	2.384	± 0.052	± 0.038	2.168	± 0.053	± 0.041
0.12 - 0.14	1.885	± 0.040	± 0.027	1.852	± 0.033	± 0.027	1.832	± 0.039	± 0.035
0.14 - 0.16	1.413	± 0.032	± 0.026	1.409	± 0.028	± 0.022	1.405	± 0.028	± 0.030
0.16 - 0.18	1.111	± 0.028	± 0.024	1.185	± 0.026	± 0.018	1.158	± 0.025	± 0.019
0.18 - 0.20	0.900	± 0.024	± 0.013	0.893	± 0.022	± 0.015	0.891	± 0.022	± 0.009
0.20 - 0.25	0.642	± 0.012	± 0.009	0.626	± 0.012	± 0.007	0.617	± 0.012	± 0.006
0.25 - 0.30	0.3419	± 0.0081	± 0.0047	0.3540	± 0.0083	± 0.0054	0.3498	± 0.0085	± 0.0042
0.30 - 0.35	0.1643	± 0.0061	± 0.0018	0.1602	± 0.0059	± 0.0033	0.1538	± 0.0060	± 0.0035
0.35 - 0.40	0.0293	± 0.0033	± 0.0012	0.0272	± 0.0029	± 0.0024	0.0251	± 0.0033	± 0.0031
0.40 - 0.50	0.00043	± 0.00025	± 0.00029	0.00028	± 0.00016	± 0.00010	0.00031	± 0.00015	± 0.00019

Table B.4.a: 1 - Thrust $(1-T)$

1 - Thrust $(1-T)$									
$1-T$	$0.36 < \cos\vartheta_T \leq 0.48$			$0.48 < \cos\vartheta_T \leq 0.60$			$0.60 < \cos\vartheta_T \leq 0.72$		
0.00 - 0.01	3.365	± 0.040	± 0.195	3.391	± 0.040	± 0.198	3.434	± 0.037	± 0.208
0.01 - 0.02	13.288	± 0.097	± 0.589	13.383	± 0.095	± 0.557	13.484	± 0.093	± 0.585
0.02 - 0.03	15.278	± 0.114	± 0.266	15.445	± 0.113	± 0.382	15.414	± 0.120	± 0.189
0.03 - 0.04	12.330	± 0.109	± 0.154	12.293	± 0.108	± 0.153	12.391	± 0.109	± 0.173
0.04 - 0.05	9.563	± 0.102	± 0.145	9.447	± 0.097	± 0.134	9.269	± 0.097	± 0.136
0.05 - 0.06	7.216	± 0.087	± 0.098	7.210	± 0.085	± 0.105	7.379	± 0.089	± 0.116
0.06 - 0.07	5.635	± 0.075	± 0.077	5.658	± 0.075	± 0.084	5.732	± 0.072	± 0.091
0.07 - 0.08	4.576	± 0.072	± 0.061	4.486	± 0.066	± 0.058	4.621	± 0.065	± 0.075
0.08 - 0.09	3.760	± 0.063	± 0.056	3.720	± 0.061	± 0.052	3.822	± 0.061	± 0.059
0.09 - 0.10	3.112	± 0.059	± 0.050	3.204	± 0.056	± 0.048	3.104	± 0.056	± 0.052
0.10 - 0.11	2.730	± 0.056	± 0.041	2.643	± 0.053	± 0.041	2.595	± 0.048	± 0.047
0.11 - 0.12	2.313	± 0.048	± 0.037	2.340	± 0.049	± 0.035	2.365	± 0.043	± 0.042
0.12 - 0.14	1.820	± 0.031	± 0.030	1.878	± 0.034	± 0.027	1.827	± 0.031	± 0.020
0.14 - 0.16	1.470	± 0.027	± 0.025	1.404	± 0.027	± 0.021	1.396	± 0.024	± 0.016
0.16 - 0.18	1.104	± 0.025	± 0.021	1.119	± 0.025	± 0.016	1.056	± 0.021	± 0.014
0.18 - 0.20	0.904	± 0.023	± 0.015	0.902	± 0.019	± 0.013	0.883	± 0.019	± 0.010
0.20 - 0.25	0.609	± 0.012	± 0.009	0.600	± 0.011	± 0.008	0.589	± 0.010	± 0.009
0.25 - 0.30	0.3354	± 0.0083	± 0.0051	0.3081	± 0.0081	± 0.0093	0.3190	± 0.0074	± 0.0057
0.30 - 0.35	0.1416	± 0.0060	± 0.0039	0.1488	± 0.0060	± 0.0048	0.1211	± 0.0048	± 0.0032
0.35 - 0.40	0.0248	± 0.0031	± 0.0018	0.0216	± 0.0024	± 0.0020	0.0199	± 0.0022	± 0.0013
0.40 - 0.50	0.00019	± 0.00011	± 0.00006	0.00046	± 0.00021	± 0.00008	0.00016	± 0.00010	± 0.00012

Table B.4.b: 1 - Thrust $(1-T)$

1 - Thrust $(1-T)$									
$1-T$	$0.72 < \cos\vartheta_T \leq 0.84$			$0.84 < \cos\vartheta_T \leq 0.96$			$0. < \cos\vartheta_T \leq 1.$		
0.00 - 0.01	3.523	± 0.036	± 0.219	3.982	± 0.034	± 0.342	3.402	± 0.015	± 0.212
0.01 - 0.02	13.549	± 0.084	± 0.575	13.227	± 0.088	± 0.543	13.367	± 0.038	± 0.585
0.02 - 0.03	15.349	± 0.100	± 0.253	15.164	± 0.111	± 0.432	15.337	± 0.048	± 0.292
0.03 - 0.04	12.600	± 0.098	± 0.231	12.337	± 0.106	± 0.232	12.403	± 0.044	± 0.183
0.04 - 0.05	9.335	± 0.085	± 0.154	9.338	± 0.087	± 0.172	9.493	± 0.041	± 0.158
0.05 - 0.06	7.227	± 0.075	± 0.117	7.127	± 0.080	± 0.124	7.272	± 0.034	± 0.118
0.06 - 0.07	5.683	± 0.065	± 0.088	5.575	± 0.066	± 0.089	5.708	± 0.030	± 0.086
0.07 - 0.08	4.595	± 0.059	± 0.071	4.506	± 0.060	± 0.080	4.582	± 0.027	± 0.067
0.08 - 0.09	3.780	± 0.054	± 0.056	3.839	± 0.057	± 0.072	3.798	± 0.025	± 0.054
0.09 - 0.10	3.131	± 0.051	± 0.048	3.045	± 0.052	± 0.051	3.144	± 0.023	± 0.045
0.10 - 0.11	2.631	± 0.047	± 0.040	2.647	± 0.045	± 0.043	2.649	± 0.020	± 0.034
0.11 - 0.12	2.311	± 0.041	± 0.037	2.203	± 0.042	± 0.033	2.294	± 0.017	± 0.030
0.12 - 0.14	1.858	± 0.027	± 0.024	1.855	± 0.027	± 0.023	1.843	± 0.013	± 0.022
0.14 - 0.16	1.415	± 0.023	± 0.019	1.392	± 0.024	± 0.019	1.405	± 0.011	± 0.016
0.16 - 0.18	1.069	± 0.020	± 0.012	1.060	± 0.021	± 0.017	1.095	± 0.010	± 0.012
0.18 - 0.20	0.817	± 0.018	± 0.009	0.820	± 0.018	± 0.014	0.8676	± 0.0085	± 0.0086
0.20 - 0.25	0.5482	± 0.0091	± 0.0074	0.551	± 0.009	± 0.011	0.5881	± 0.0044	± 0.0063
0.25 - 0.30	0.3082	± 0.0073	± 0.0055	0.2990	± 0.0066	± 0.0042	0.3163	± 0.0029	± 0.0026
0.30 - 0.35	0.1199	± 0.0047	± 0.0026	0.1178	± 0.0042	± 0.0025	0.1368	± 0.0021	± 0.0017
0.35 - 0.40	0.0165	± 0.0016	± 0.0008	0.0160	± 0.0016	± 0.0009	0.01964	± 0.00083	± 0.00069
0.40 - 0.50	0.00007	± 0.00009	± 0.00011	0.00021	± 0.00010	± 0.00025	0.00096	± 0.00022	± 0.00014

Table B.4.c: 1 - Thrust $(1-T)$

Oblateness O									
O	$0.0 < \cos\vartheta_T \leq 0.12$			$0.12 < \cos\vartheta_T \leq 0.24$			$0.24 < \cos\vartheta_T \leq 0.36$		
0.00 - 0.02	7.194	± 0.062	± 0.090	7.159	± 0.058	± 0.049	7.329	± 0.060	± 0.053
0.02 - 0.04	10.582	± 0.073	± 0.097	10.684	± 0.074	± 0.079	10.579	± 0.069	± 0.048
0.04 - 0.06	7.840	± 0.062	± 0.031	7.756	± 0.060	± 0.059	7.792	± 0.057	± 0.052
0.06 - 0.08	5.278	± 0.055	± 0.027	5.291	± 0.050	± 0.043	5.283	± 0.049	± 0.049
0.08 - 0.10	3.862	± 0.044	± 0.025	3.835	± 0.044	± 0.037	3.834	± 0.041	± 0.042
0.10 - 0.12	2.906	± 0.037	± 0.022	2.849	± 0.039	± 0.031	2.941	± 0.037	± 0.033
0.12 - 0.14	2.204	± 0.033	± 0.021	2.244	± 0.034	± 0.026	2.215	± 0.033	± 0.021
0.14 - 0.16	1.817	± 0.029	± 0.017	1.829	± 0.029	± 0.020	1.844	± 0.029	± 0.011
0.16 - 0.20	1.335	± 0.017	± 0.014	1.347	± 0.018	± 0.014	1.339	± 0.017	± 0.010
0.20 - 0.24	0.919	± 0.015	± 0.011	0.940	± 0.015	± 0.008	0.910	± 0.014	± 0.008
0.24 - 0.28	0.681	± 0.013	± 0.009	0.652	± 0.012	± 0.006	0.637	± 0.012	± 0.006
0.28 - 0.32	0.470	± 0.010	± 0.007	0.465	± 0.010	± 0.005	0.449	± 0.010	± 0.005
0.32 - 0.36	0.3191	± 0.0081	± 0.0071	0.3150	± 0.0080	± 0.0045	0.3147	± 0.0080	± 0.0049
0.36 - 0.40	0.2199	± 0.0071	± 0.0053	0.2231	± 0.0066	± 0.0037	0.2140	± 0.0066	± 0.0039
0.40 - 0.44	0.1498	± 0.0055	± 0.0039	0.1334	± 0.0052	± 0.0031	0.1401	± 0.0051	± 0.0027
0.44 - 0.52	0.0538	± 0.0021	± 0.0018	0.0573	± 0.0023	± 0.0023	0.0487	± 0.0021	± 0.0014
0.52 - 0.56	0.0083	± 0.0011	± 0.0009	0.0100	± 0.0013	± 0.0007	0.0090	± 0.0013	± 0.0005
0.56 - 0.64	0.00146	± 0.00040	± 0.00022	0.00099	± 0.00027	± 0.00009	0.00107	± 0.00036	± 0.00013

Table B.5.a: Oblateness O

Oblateness O									
O	$0.36 < \cos\vartheta_T \leq 0.48$			$0.48 < \cos\vartheta_T \leq 0.60$			$0.60 < \cos\vartheta_T \leq 0.72$		
0.00 - 0.02	7.245	± 0.056	± 0.044	7.373	± 0.053	± 0.033	7.284	± 0.050	± 0.042
0.02 - 0.04	10.712	± 0.067	± 0.049	10.670	± 0.064	± 0.039	10.790	± 0.060	± 0.043
0.04 - 0.06	7.820	± 0.058	± 0.042	7.884	± 0.054	± 0.037	7.884	± 0.054	± 0.029
0.06 - 0.08	5.294	± 0.047	± 0.035	5.325	± 0.044	± 0.034	5.315	± 0.045	± 0.026
0.08 - 0.10	3.848	± 0.040	± 0.030	3.813	± 0.038	± 0.029	3.823	± 0.037	± 0.023
0.10 - 0.12	2.874	± 0.036	± 0.026	2.801	± 0.034	± 0.021	2.876	± 0.033	± 0.020
0.12 - 0.14	2.217	± 0.031	± 0.021	2.254	± 0.030	± 0.012	2.243	± 0.028	± 0.016
0.14 - 0.16	1.825	± 0.028	± 0.013	1.772	± 0.026	± 0.010	1.804	± 0.024	± 0.013
0.16 - 0.20	1.338	± 0.017	± 0.010	1.336	± 0.018	± 0.009	1.324	± 0.016	± 0.008
0.20 - 0.24	0.915	± 0.014	± 0.008	0.919	± 0.013	± 0.007	0.903	± 0.013	± 0.006
0.24 - 0.28	0.636	± 0.012	± 0.005	0.627	± 0.010	± 0.006	0.614	± 0.010	± 0.004
0.28 - 0.32	0.447	± 0.010	± 0.004	0.4428	± 0.0093	± 0.0051	0.4372	± 0.0085	± 0.0033
0.32 - 0.36	0.3147	± 0.0094	± 0.0039	0.3001	± 0.0079	± 0.0038	0.2992	± 0.0070	± 0.0024
0.36 - 0.40	0.2087	± 0.0074	± 0.0033	0.2070	± 0.0064	± 0.0021	0.1935	± 0.0058	± 0.0015
0.40 - 0.44	0.1215	± 0.0049	± 0.0029	0.1276	± 0.0049	± 0.0017	0.1185	± 0.0046	± 0.0012
0.44 - 0.52	0.0517	± 0.0022	± 0.0013	0.0479	± 0.0020	± 0.0014	0.0476	± 0.0022	± 0.0008
0.52 - 0.56	0.0102	± 0.0014	± 0.0006	0.0105	± 0.0015	± 0.0006	0.0069	± 0.0010	± 0.0006
0.56 - 0.64	0.00098	± 0.00032	± 0.00011	0.00104	± 0.00028	± 0.00011	0.00107	± 0.00036	± 0.00006

Table B.5.b: Oblateness O

Oblateness O									
O	$0.72 < \cos\vartheta_T \leq 0.84$			$0.84 < \cos\vartheta_T \leq 0.96$			$0. < \cos\vartheta_T \leq 1.$		
0.00 - 0.02	7.456	± 0.048	± 0.069	7.868	± 0.057	± 0.184	7.328	± 0.022	± 0.060
0.02 - 0.04	10.866	± 0.056	± 0.055	10.769	± 0.062	± 0.086	10.737	± 0.027	± 0.049
0.04 - 0.06	7.858	± 0.048	± 0.043	7.847	± 0.054	± 0.056	7.869	± 0.023	± 0.022
0.06 - 0.08	5.360	± 0.041	± 0.031	5.284	± 0.044	± 0.052	5.333	± 0.018	± 0.018
0.08 - 0.10	3.854	± 0.035	± 0.023	3.782	± 0.034	± 0.037	3.848	± 0.016	± 0.014
0.10 - 0.12	2.854	± 0.030	± 0.020	2.796	± 0.031	± 0.032	2.876	± 0.014	± 0.012
0.12 - 0.14	2.258	± 0.027	± 0.017	2.259	± 0.025	± 0.027	2.223	± 0.012	± 0.011
0.14 - 0.16	1.777	± 0.024	± 0.014	1.791	± 0.021	± 0.021	1.805	± 0.011	± 0.010
0.16 - 0.20	1.302	± 0.016	± 0.011	1.299	± 0.015	± 0.016	1.3200	± 0.0065	± 0.0079
0.20 - 0.24	0.872	± 0.013	± 0.007	0.881	± 0.012	± 0.010	0.9021	± 0.0050	± 0.0066
0.24 - 0.28	0.615	± 0.010	± 0.004	0.611	± 0.010	± 0.007	0.6283	± 0.0043	± 0.0049
0.28 - 0.32	0.4102	± 0.0083	± 0.0034	0.4233	± 0.0088	± 0.0053	0.4376	± 0.0036	± 0.0040
0.32 - 0.36	0.2813	± 0.0067	± 0.0026	0.2865	± 0.0068	± 0.0046	0.2984	± 0.0031	± 0.0036
0.36 - 0.40	0.1865	± 0.0054	± 0.0023	0.1925	± 0.0058	± 0.0039	0.1983	± 0.0025	± 0.0027
0.40 - 0.44	0.1134	± 0.0042	± 0.0020	0.1081	± 0.0038	± 0.0028	0.1232	± 0.0019	± 0.0022
0.44 - 0.52	0.0414	± 0.0017	± 0.0013	0.0419	± 0.0017	± 0.0014	0.0466	± 0.0008	± 0.0013
0.52 - 0.56	0.0099	± 0.0014	± 0.0006	0.0077	± 0.0010	± 0.0004	0.00796	± 0.00038	± 0.00045
0.56 - 0.64	0.00086	± 0.00022	± 0.00006	0.00068	± 0.00017	± 0.00010	0.00079	± 0.00008	± 0.00008

Table B.5.c: Oblateness O

C-Parameter C			
C	$0.0 < \cos\vartheta_T \leq 0.12$	$0.12 < \cos\vartheta_T \leq 0.24$	$0.24 < \cos\vartheta_T \leq 0.36$
0.00 - 0.04	0.363 ± 0.007 ± 0.021	0.382 ± 0.007 ± 0.022	0.378 ± 0.007 ± 0.022
0.04 - 0.08	2.252 ± 0.021 ± 0.096	2.266 ± 0.020 ± 0.089	2.282 ± 0.019 ± 0.100
0.08 - 0.12	3.469 ± 0.030 ± 0.085	3.479 ± 0.029 ± 0.111	3.532 ± 0.032 ± 0.089
0.12 - 0.16	3.242 ± 0.029 ± 0.039	3.264 ± 0.029 ± 0.060	3.215 ± 0.029 ± 0.032
0.16 - 0.20	2.606 ± 0.026 ± 0.030	2.589 ± 0.027 ± 0.029	2.612 ± 0.027 ± 0.030
0.20 - 0.24	2.111 ± 0.023 ± 0.028	2.072 ± 0.023 ± 0.024	2.111 ± 0.024 ± 0.028
0.24 - 0.28	1.669 ± 0.022 ± 0.019	1.666 ± 0.021 ± 0.020	1.658 ± 0.021 ± 0.026
0.28 - 0.32	1.409 ± 0.021 ± 0.016	1.364 ± 0.019 ± 0.015	1.391 ± 0.020 ± 0.023
0.32 - 0.36	1.183 ± 0.020 ± 0.012	1.174 ± 0.019 ± 0.013	1.176 ± 0.018 ± 0.016
0.36 - 0.40	0.987 ± 0.017 ± 0.011	0.993 ± 0.016 ± 0.012	0.989 ± 0.017 ± 0.014
0.40 - 0.44	0.867 ± 0.016 ± 0.010	0.844 ± 0.016 ± 0.012	0.852 ± 0.016 ± 0.013
0.44 - 0.48	0.728 ± 0.015 ± 0.010	0.755 ± 0.015 ± 0.011	0.733 ± 0.015 ± 0.012
0.48 - 0.52	0.648 ± 0.014 ± 0.009	0.649 ± 0.013 ± 0.010	0.593 ± 0.013 ± 0.011
0.52 - 0.56	0.574 ± 0.013 ± 0.008	0.556 ± 0.013 ± 0.009	0.566 ± 0.012 ± 0.010
0.56 - 0.60	0.502 ± 0.012 ± 0.008	0.534 ± 0.012 ± 0.008	0.514 ± 0.012 ± 0.008
0.60 - 0.64	0.465 ± 0.012 ± 0.007	0.458 ± 0.011 ± 0.007	0.481 ± 0.011 ± 0.007
0.64 - 0.68	0.425 ± 0.011 ± 0.006	0.413 ± 0.011 ± 0.007	0.416 ± 0.010 ± 0.006
0.68 - 0.72	0.383 ± 0.010 ± 0.006	0.395 ± 0.010 ± 0.006	0.3721 ± 0.0095 ± 0.0053
0.72 - 0.76	0.3419 ± 0.0092 ± 0.0059	0.3400 ± 0.0090 ± 0.0049	0.3359 ± 0.0091 ± 0.0042
0.76 - 0.80	0.3025 ± 0.0089 ± 0.0055	0.3115 ± 0.0087 ± 0.0041	0.2927 ± 0.0086 ± 0.0037
0.80 - 0.84	0.1807 ± 0.0070 ± 0.0053	0.1964 ± 0.0073 ± 0.0032	0.1877 ± 0.0077 ± 0.0033
0.84 - 0.88	0.0943 ± 0.0052 ± 0.0051	0.0777 ± 0.0045 ± 0.0024	0.0859 ± 0.0058 ± 0.0026
0.88 - 0.92	0.0466 ± 0.0039 ± 0.0023	0.0389 ± 0.0033 ± 0.0014	0.0472 ± 0.0046 ± 0.0021
0.92 - 1.00	0.0086 ± 0.0013 ± 0.0002	0.0097 ± 0.0014 ± 0.0009	0.0086 ± 0.0012 ± 0.0006

Table B.6.a: C-Parameter C

C-Parameter C			
C	$0.36 < \cos\vartheta_T \leq 0.48$	$0.48 < \cos\vartheta_T \leq 0.60$	$0.60 < \cos\vartheta_T \leq 0.72$
0.00 - 0.04	0.382 ± 0.007 ± 0.022	0.374 ± 0.007 ± 0.022	0.392 ± 0.006 ± 0.024
0.04 - 0.08	2.288 ± 0.018 ± 0.099	2.319 ± 0.018 ± 0.099	2.318 ± 0.017 ± 0.107
0.08 - 0.12	3.527 ± 0.027 ± 0.105	3.524 ± 0.025 ± 0.112	3.557 ± 0.024 ± 0.081
0.12 - 0.16	3.221 ± 0.026 ± 0.029	3.310 ± 0.027 ± 0.050	3.262 ± 0.025 ± 0.034
0.16 - 0.20	2.627 ± 0.025 ± 0.028	2.584 ± 0.024 ± 0.047	2.620 ± 0.024 ± 0.030
0.20 - 0.24	2.107 ± 0.023 ± 0.026	2.121 ± 0.022 ± 0.045	2.092 ± 0.021 ± 0.026
0.24 - 0.28	1.703 ± 0.020 ± 0.024	1.655 ± 0.020 ± 0.023	1.676 ± 0.019 ± 0.020
0.28 - 0.32	1.377 ± 0.018 ± 0.016	1.376 ± 0.017 ± 0.017	1.410 ± 0.017 ± 0.016
0.32 - 0.36	1.150 ± 0.018 ± 0.015	1.134 ± 0.016 ± 0.015	1.170 ± 0.016 ± 0.014
0.36 - 0.40	0.965 ± 0.017 ± 0.014	0.978 ± 0.016 ± 0.012	0.977 ± 0.015 ± 0.012
0.40 - 0.44	0.843 ± 0.016 ± 0.013	0.837 ± 0.015 ± 0.009	0.848 ± 0.014 ± 0.011
0.44 - 0.48	0.726 ± 0.015 ± 0.012	0.744 ± 0.013 ± 0.008	0.739 ± 0.013 ± 0.010
0.48 - 0.52	0.649 ± 0.013 ± 0.010	0.648 ± 0.012 ± 0.008	0.624 ± 0.012 ± 0.009
0.52 - 0.56	0.571 ± 0.012 ± 0.009	0.574 ± 0.012 ± 0.007	0.546 ± 0.011 ± 0.008
0.56 - 0.60	0.518 ± 0.011 ± 0.008	0.501 ± 0.011 ± 0.007	0.499 ± 0.011 ± 0.007
0.60 - 0.64	0.456 ± 0.011 ± 0.007	0.467 ± 0.010 ± 0.006	0.438 ± 0.010 ± 0.006
0.64 - 0.68	0.418 ± 0.010 ± 0.007	0.408 ± 0.010 ± 0.006	0.3960 ± 0.0091 ± 0.006
0.68 - 0.72	0.366 ± 0.010 ± 0.006	0.3558 ± 0.0092 ± 0.0062	0.3553 ± 0.0087 ± 0.0058
0.72 - 0.76	0.3301 ± 0.0091 ± 0.0062	0.3194 ± 0.0085 ± 0.0057	0.3135 ± 0.0084 ± 0.0052
0.76 - 0.80	0.2877 ± 0.0086 ± 0.0050	0.2809 ± 0.0083 ± 0.0048	0.2880 ± 0.0080 ± 0.0045
0.80 - 0.84	0.1796 ± 0.0082 ± 0.0041	0.1715 ± 0.0074 ± 0.0043	0.1562 ± 0.0056 ± 0.0036
0.84 - 0.88	0.0866 ± 0.0054 ± 0.0032	0.0822 ± 0.0047 ± 0.0031	0.0750 ± 0.0045 ± 0.0027
0.88 - 0.92	0.0338 ± 0.0033 ± 0.0013	0.0363 ± 0.0034 ± 0.0017	0.0323 ± 0.0031 ± 0.0016
0.92 - 1.00	0.0098 ± 0.0015 ± 0.0006	0.0082 ± 0.0010 ± 0.0009	0.0050 ± 0.0010 ± 0.0002

Table B.6.b: C-Parameter C

C-Parameter C								
C	$0.72 < \cos\vartheta_T \leq 0.84$			$0.84 < \cos\vartheta_T \leq 0.96$			$0. < \cos\vartheta_T \leq 1.$	
0.00 - 0.04	0.417	± 0.006	± 0.026	0.518	± 0.007	± 0.057	0.388	± 0.003	± 0.025
0.04 - 0.08	2.330	± 0.016	± 0.107	2.271	± 0.017	± 0.102	2.300	± 0.008	± 0.101
0.08 - 0.12	3.559	± 0.020	± 0.083	3.470	± 0.025	± 0.108	3.533	± 0.011	± 0.096
0.12 - 0.16	3.299	± 0.023	± 0.052	3.229	± 0.027	± 0.063	3.274	± 0.011	± 0.042
0.16 - 0.20	2.622	± 0.021	± 0.037	2.604	± 0.023	± 0.037	2.622	± 0.010	± 0.034
0.20 - 0.24	2.078	± 0.019	± 0.028	2.053	± 0.020	± 0.029	2.112	± 0.009	± 0.027
0.24 - 0.28	1.671	± 0.017	± 0.022	1.666	± 0.018	± 0.026	1.675	± 0.008	± 0.020
0.28 - 0.32	1.395	± 0.016	± 0.019	1.358	± 0.016	± 0.018	1.395	± 0.007	± 0.016
0.32 - 0.36	1.176	± 0.015	± 0.017	1.143	± 0.015	± 0.014	1.164	± 0.007	± 0.013
0.36 - 0.40	0.952	± 0.013	± 0.013	0.970	± 0.014	± 0.017	0.978	± 0.006	± 0.011
0.40 - 0.44	0.845	± 0.012	± 0.012	0.837	± 0.013	± 0.010	0.8432	± 0.0055	± 0.0091
0.44 - 0.48	0.746	± 0.011	± 0.011	0.740	± 0.013	± 0.009	0.7356	± 0.0053	± 0.0079
0.48 - 0.52	0.635	± 0.011	± 0.011	0.633	± 0.012	± 0.008	0.6310	± 0.0047	± 0.0066
0.52 - 0.56	0.572	± 0.010	± 0.010	0.553	± 0.010	± 0.008	0.5578	± 0.0044	± 0.0061
0.56 - 0.60	0.481	± 0.010	± 0.008	0.486	± 0.010	± 0.007	0.5014	± 0.0043	± 0.0052
0.60 - 0.64	0.4289	± 0.0095	± 0.0081	0.4318	± 0.0090	± 0.0073	0.4505	± 0.0042	± 0.0048
0.64 - 0.68	0.3761	± 0.0084	± 0.0072	0.3738	± 0.0081	± 0.0068	0.3982	± 0.0038	± 0.0043
0.68 - 0.72	0.3431	± 0.0082	± 0.0064	0.3365	± 0.0074	± 0.0066	0.3569	± 0.0035	± 0.0039
0.72 - 0.76	0.3006	± 0.0079	± 0.0054	0.2985	± 0.0072	± 0.0063	0.3156	± 0.0032	± 0.0038
0.76 - 0.80	0.2458	± 0.0069	± 0.0050	0.2399	± 0.0064	± 0.0057	0.2716	± 0.0031	± 0.0037
0.80 - 0.84	0.1570	± 0.0058	± 0.0044	0.1532	± 0.0052	± 0.0048	0.1656	± 0.0026	± 0.0034
0.84 - 0.88	0.0695	± 0.0039	± 0.0018	0.0699	± 0.0035	± 0.0028	0.0771	± 0.0018	± 0.0022
0.88 - 0.92	0.0317	± 0.0028	± 0.0013	0.0291	± 0.0022	± 0.0006	0.0343	± 0.0012	± 0.0004
0.92 - 1.00	0.0055	± 0.0010	± 0.0004	0.0064	± 0.0010	± 0.0003	0.00653	± 0.00034	± 0.00016

Table B.6.c: C-Parameter C

Heavy Jet Mass ρ_H								
ρ_H	$0.0 < \cos\vartheta_T \leq 0.12$			$0.12 < \cos\vartheta_T \leq 0.24$			$0.24 < \cos\vartheta_T \leq 0.36$	
0.00 - 0.01	4.358	± 0.107	± 0.357	4.435	± 0.117	± 0.348	4.456	± 0.090	± 0.363
0.01 - 0.02	16.681	± 0.182	± 0.538	16.932	± 0.204	± 0.519	16.928	± 0.182	± 0.508
0.02 - 0.03	17.076	± 0.147	± 0.289	16.823	± 0.143	± 0.294	16.802	± 0.142	± 0.273
0.03 - 0.04	12.843	± 0.127	± 0.193	12.607	± 0.127	± 0.201	12.781	± 0.129	± 0.178
0.04 - 0.05	9.226	± 0.119	± 0.154	9.249	± 0.112	± 0.175	9.288	± 0.110	± 0.159
0.05 - 0.06	6.945	± 0.102	± 0.116	6.958	± 0.092	± 0.158	7.200	± 0.098	± 0.136
0.06 - 0.07	5.426	± 0.099	± 0.097	5.456	± 0.083	± 0.138	5.264	± 0.079	± 0.127
0.07 - 0.08	4.202	± 0.073	± 0.084	4.338	± 0.075	± 0.103	4.399	± 0.072	± 0.105
0.08 - 0.10	3.238	± 0.048	± 0.058	3.198	± 0.048	± 0.069	3.106	± 0.044	± 0.070
0.10 - 0.12	2.198	± 0.039	± 0.031	2.139	± 0.037	± 0.045	2.092	± 0.039	± 0.037
0.12 - 0.14	1.559	± 0.031	± 0.026	1.566	± 0.029	± 0.020	1.591	± 0.035	± 0.031
0.14 - 0.16	1.114	± 0.024	± 0.016	1.149	± 0.025	± 0.013	1.113	± 0.027	± 0.017
0.16 - 0.20	0.745	± 0.014	± 0.012	0.742	± 0.015	± 0.011	0.739	± 0.017	± 0.014
0.20 - 0.25	0.3809	± 0.0092	± 0.0042	0.3853	± 0.0086	± 0.0062	0.3753	± 0.0096	± 0.0060
0.25 - 0.30	0.1748	± 0.0069	± 0.0023	0.1615	± 0.0058	± 0.0028	0.1575	± 0.0057	± 0.0031
0.30 - 0.35	0.0651	± 0.0037	± 0.0017	0.0620	± 0.0037	± 0.0006	0.0691	± 0.0039	± 0.0011
0.35 - 0.40	0.0194	± 0.0019	± 0.0018	0.0229	± 0.0024	± 0.0006	0.0205	± 0.0019	± 0.0002

Table B.7.a: Heavy Jet Mass ρ_H

Heavy Jet Mass ρ_H			
ρ_H	$0.36 < \cos\vartheta_T \leq 0.48$	$0.48 < \cos\vartheta_T \leq 0.60$	$0.60 < \cos\vartheta_T \leq 0.72$
0.00 - 0.01	4.522 ± 0.111 ± 0.340	4.540 ± 0.102 ± 0.360	4.566 ± 0.096 ± 0.327
0.01 - 0.02	16.826 ± 0.179 ± 0.487	16.999 ± 0.156 ± 0.472	17.257 ± 0.160 ± 0.566
0.02 - 0.03	16.899 ± 0.148 ± 0.253	17.161 ± 0.121 ± 0.291	16.860 ± 0.120 ± 0.272
0.03 - 0.04	12.946 ± 0.131 ± 0.184	12.738 ± 0.118 ± 0.251	13.017 ± 0.111 ± 0.183
0.04 - 0.05	9.322 ± 0.102 ± 0.152	9.266 ± 0.098 ± 0.169	9.468 ± 0.101 ± 0.161
0.05 - 0.06	7.011 ± 0.094 ± 0.129	7.013 ± 0.092 ± 0.133	6.934 ± 0.082 ± 0.134
0.06 - 0.07	5.355 ± 0.083 ± 0.116	5.330 ± 0.085 ± 0.117	5.346 ± 0.071 ± 0.110
0.07 - 0.08	4.234 ± 0.075 ± 0.103	4.244 ± 0.073 ± 0.094	4.245 ± 0.065 ± 0.107
0.08 - 0.10	3.177 ± 0.055 ± 0.064	3.168 ± 0.038 ± 0.065	3.083 ± 0.040 ± 0.070
0.10 - 0.12	2.201 ± 0.040 ± 0.049	2.175 ± 0.034 ± 0.049	2.123 ± 0.030 ± 0.051
0.12 - 0.14	1.539 ± 0.026 ± 0.031	1.483 ± 0.030 ± 0.041	1.500 ± 0.028 ± 0.042
0.14 - 0.16	1.119 ± 0.025 ± 0.023	1.107 ± 0.025 ± 0.025	1.105 ± 0.025 ± 0.034
0.16 - 0.20	0.729 ± 0.015 ± 0.016	0.713 ± 0.013 ± 0.018	0.682 ± 0.012 ± 0.020
0.20 - 0.25	0.3482 ± 0.0079 ± 0.0082	0.3606 ± 0.0094 ± 0.0107	0.3422 ± 0.0082 ± 0.0107
0.25 - 0.30	0.1522 ± 0.0054 ± 0.0066	0.1423 ± 0.0055 ± 0.0043	0.1563 ± 0.0053 ± 0.0054
0.30 - 0.35	0.0612 ± 0.0041 ± 0.0018	0.0674 ± 0.0039 ± 0.0023	0.0549 ± 0.0031 ± 0.0026
0.35 - 0.40	0.0224 ± 0.0021 ± 0.0013	0.0229 ± 0.0023 ± 0.0010	0.0204 ± 0.0020 ± 0.0013

Table B.7.b: Heavy Jet Mass ρ_H

Heavy Jet Mass ρ_H			
ρ_H	$0.72 < \cos\vartheta_T \leq 0.84$	$0.84 < \cos\vartheta_T \leq 0.96$	$0. < \cos\vartheta_T \leq 1.$
0.00 - 0.01	4.635 ± 0.102 ± 0.373	4.628 ± 0.094 ± 0.406	4.537 ± 0.095 ± 0.252
0.01 - 0.02	17.190 ± 0.164 ± 0.582	17.134 ± 0.156 ± 0.582	17.046 ± 0.134 ± 0.525
0.02 - 0.03	17.196 ± 0.115 ± 0.291	17.067 ± 0.110 ± 0.363	17.024 ± 0.062 ± 0.386
0.03 - 0.04	12.802 ± 0.104 ± 0.163	12.841 ± 0.107 ± 0.316	12.838 ± 0.051 ± 0.188
0.04 - 0.05	9.295 ± 0.092 ± 0.132	9.287 ± 0.095 ± 0.217	9.303 ± 0.047 ± 0.131
0.05 - 0.06	6.971 ± 0.078 ± 0.118	6.921 ± 0.085 ± 0.158	6.990 ± 0.040 ± 0.103
0.06 - 0.07	5.483 ± 0.065 ± 0.104	5.305 ± 0.071 ± 0.129	5.385 ± 0.037 ± 0.089
0.07 - 0.08	4.281 ± 0.061 ± 0.095	4.270 ± 0.065 ± 0.109	4.177 ± 0.029 ± 0.073
0.08 - 0.10	3.124 ± 0.038 ± 0.078	3.112 ± 0.037 ± 0.072	3.137 ± 0.018 ± 0.068
0.10 - 0.12	2.074 ± 0.029 ± 0.058	2.085 ± 0.029 ± 0.049	2.156 ± 0.013 ± 0.057
0.12 - 0.14	1.516 ± 0.026 ± 0.051	1.503 ± 0.026 ± 0.032	1.491 ± 0.011 ± 0.040
0.14 - 0.16	1.050 ± 0.021 ± 0.029	1.066 ± 0.020 ± 0.023	1.096 ± 0.010 ± 0.026
0.16 - 0.20	0.665 ± 0.011 ± 0.019	0.687 ± 0.014 ± 0.009	0.703 ± 0.005 ± 0.016
0.20 - 0.25	0.3227 ± 0.0076 ± 0.0089	0.3626 ± 0.0066 ± 0.0048	0.3546 ± 0.0032 ± 0.0067
0.25 - 0.30	0.1566 ± 0.0053 ± 0.0044	0.1415 ± 0.0044 ± 0.0040	0.1528 ± 0.0018 ± 0.0020
0.30 - 0.35	0.0537 ± 0.0027 ± 0.0023	0.0599 ± 0.0027 ± 0.0025	0.0616 ± 0.0011 ± 0.0010
0.35 - 0.40	0.0206 ± 0.0018 ± 0.0009	0.0213 ± 0.0018 ± 0.0013	0.02065 ± 0.00064 ± 0.00091

Table B.7.c: Heavy Jet Mass ρ_H

Sum of the Jet Masses ρ_S									
ρ_S	$0.0 < \cos\vartheta_T \leq 0.12$			$0.12 < \cos\vartheta_T \leq 0.24$			$0.24 < \cos\vartheta_T \leq 0.36$		
0.00 - 0.01	1.34	± 0.05	± 0.15	1.36	± 0.04	± 0.14	1.37	± 0.05	± 0.15
0.01 - 0.02	7.68	± 0.15	± 0.62	7.71	± 0.15	± 0.65	7.79	± 0.14	± 0.68
0.02 - 0.03	12.53	± 0.17	± 0.41	12.83	± 0.14	± 0.48	12.64	± 0.15	± 0.37
0.03 - 0.04	12.77	± 0.14	± 0.33	12.57	± 0.13	± 0.36	12.92	± 0.14	± 0.32
0.04 - 0.05	10.90	± 0.12	± 0.28	10.73	± 0.12	± 0.29	10.70	± 0.13	± 0.28
0.05 - 0.06	8.540	± 0.117	± 0.254	8.618	± 0.114	± 0.274	8.726	± 0.115	± 0.271
0.06 - 0.07	7.036	± 0.107	± 0.202	6.856	± 0.098	± 0.229	7.036	± 0.105	± 0.247
0.07 - 0.08	5.511	± 0.089	± 0.168	5.692	± 0.088	± 0.181	5.560	± 0.083	± 0.176
0.08 - 0.10	4.258	± 0.059	± 0.128	4.217	± 0.057	± 0.137	4.135	± 0.053	± 0.124
0.10 - 0.12	2.994	± 0.043	± 0.075	3.009	± 0.044	± 0.084	2.956	± 0.050	± 0.091
0.12 - 0.14	2.183	± 0.037	± 0.055	2.162	± 0.037	± 0.053	2.095	± 0.037	± 0.054
0.14 - 0.16	1.629	± 0.031	± 0.040	1.629	± 0.030	± 0.037	1.634	± 0.032	± 0.045
0.16 - 0.20	1.131	± 0.019	± 0.019	1.163	± 0.019	± 0.024	1.144	± 0.018	± 0.029
0.20 - 0.25	0.6671	± 0.0144	± 0.0143	0.6555	± 0.0119	± 0.0162	0.6593	± 0.0127	± 0.0175
0.25 - 0.30	0.3422	± 0.0127	± 0.0072	0.3347	± 0.0092	± 0.0088	0.3232	± 0.0098	± 0.0120
0.30 - 0.35	0.1104	± 0.0055	± 0.0027	0.1118	± 0.0050	± 0.0024	0.1139	± 0.0052	± 0.0035
0.35 - 0.40	0.0293	± 0.0025	± 0.0015	0.0299	± 0.0026	± 0.0007	0.0285	± 0.0027	± 0.0004

Table B.8.a: Sum of the Jet Masses ρ_S

Sum of the Jet Masses ρ_S									
ρ_S	$0.36 < \cos\vartheta_T \leq 0.48$			$0.48 < \cos\vartheta_T \leq 0.60$			$0.60 < \cos\vartheta_T \leq 0.72$		
0.00 - 0.01	1.39	± 0.04	± 0.15	1.38	± 0.05	± 0.15	1.43	± 0.05	± 0.16
0.01 - 0.02	7.79	± 0.15	± 0.68	7.91	± 0.15	± 0.66	7.91	± 0.15	± 0.65
0.02 - 0.03	12.80	± 0.14	± 0.43	12.87	± 0.13	± 0.46	12.90	± 0.13	± 0.39
0.03 - 0.04	12.61	± 0.13	± 0.35	12.87	± 0.12	± 0.35	12.83	± 0.12	± 0.35
0.04 - 0.05	10.92	± 0.12	± 0.29	10.90	± 0.11	± 0.28	10.95	± 0.11	± 0.31
0.05 - 0.06	8.647	± 0.112	± 0.279	8.572	± 0.103	± 0.265	8.662	± 0.098	± 0.265
0.06 - 0.07	7.002	± 0.108	± 0.230	6.792	± 0.095	± 0.219	7.111	± 0.096	± 0.232
0.07 - 0.08	5.643	± 0.098	± 0.183	5.601	± 0.084	± 0.185	5.460	± 0.082	± 0.183
0.08 - 0.10	4.181	± 0.051	± 0.129	4.132	± 0.049	± 0.127	4.195	± 0.047	± 0.132
0.10 - 0.12	2.935	± 0.042	± 0.085	3.010	± 0.047	± 0.087	2.924	± 0.040	± 0.088
0.12 - 0.14	2.232	± 0.037	± 0.065	2.135	± 0.033	± 0.063	2.134	± 0.034	± 0.062
0.14 - 0.16	1.643	± 0.030	± 0.044	1.636	± 0.030	± 0.047	1.587	± 0.028	± 0.049
0.16 - 0.20	1.122	± 0.020	± 0.030	1.121	± 0.019	± 0.036	1.119	± 0.020	± 0.040
0.20 - 0.25	0.6574	± 0.016	± 0.0253	0.6344	± 0.014	± 0.025	0.6095	± 0.0112	± 0.0236
0.25 - 0.30	0.2960	± 0.008	± 0.0140	0.2903	± 0.0079	± 0.0137	0.2877	± 0.0074	± 0.0151
0.30 - 0.35	0.0982	± 0.005	± 0.0047	0.1069	± 0.0051	± 0.0059	0.1031	± 0.0049	± 0.0059
0.35 - 0.40	0.0309	± 0.002	± 0.0015	0.0301	± 0.0029	± 0.0015	0.0257	± 0.0024	± 0.0013

Table B.8.b: Sum of the Jet Masses ρ_S

Sum of the Jet Masses ρ_S									
ρ_S	$0.72 < \cos\vartheta_T \leq 0.84$			$0.84 < \cos\vartheta_T \leq 0.96$			$0. < \cos\vartheta_T \leq 1.$		
0.00 - 0.01	1.44	± 0.04	± 0.17	1.59	± 0.05	± 0.28	1.43	± 0.04	± 0.17
0.01 - 0.02	7.97	± 0.13	± 0.67	7.79	± 0.14	± 0.69	7.84	± 0.13	± 0.66
0.02 - 0.03	12.91	± 0.12	± 0.43	12.67	± 0.13	± 0.43	12.79	± 0.09	± 0.42
0.03 - 0.04	12.94	± 0.11	± 0.36	12.67	± 0.12	± 0.39	12.80	± 0.06	± 0.36
0.04 - 0.05	10.87	± 0.10	± 0.28	10.90	± 0.11	± 0.34	10.87	± 0.05	± 0.29
0.05 - 0.06	8.682	± 0.091	± 0.264	8.614	± 0.092	± 0.302	8.640	± 0.045	± 0.275
0.06 - 0.07	6.951	± 0.095	± 0.229	6.814	± 0.093	± 0.235	6.944	± 0.041	± 0.225
0.07 - 0.08	5.576	± 0.079	± 0.181	5.523	± 0.081	± 0.193	5.562	± 0.036	± 0.178
0.08 - 0.10	4.271	± 0.045	± 0.146	4.071	± 0.049	± 0.146	4.180	± 0.025	± 0.132
0.10 - 0.12	2.900	± 0.037	± 0.091	2.903	± 0.040	± 0.085	2.942	± 0.019	± 0.083
0.12 - 0.14	2.132	± 0.031	± 0.068	2.123	± 0.031	± 0.065	2.143	± 0.014	± 0.059
0.14 - 0.16	1.598	± 0.028	± 0.054	1.586	± 0.026	± 0.044	1.611	± 0.012	± 0.043
0.16 - 0.20	1.050	± 0.014	± 0.037	1.063	± 0.018	± 0.030	1.103	± 0.008	± 0.029
0.20 - 0.25	0.5839	± 0.010	± 0.0229	0.6116	± 0.0102	± 0.0133	0.6250	± 0.0049	± 0.0173
0.25 - 0.30	0.2862	± 0.007	± 0.0129	0.2759	± 0.0063	± 0.0033	0.2979	± 0.0032	± 0.0084
0.30 - 0.35	0.0920	± 0.004	± 0.0033	0.0918	± 0.0037	± 0.0027	0.1007	± 0.0015	± 0.0022
0.35 - 0.40	0.0241	± 0.002	± 0.0010	0.0276	± 0.0018	± 0.0016	0.0274	± 0.0008	± 0.0009

Table B.8.c: Sum of the Jet Masses ρ_S

Difference of the Jet Masses ρ_D									
ρ_D	$0.0 < \cos\vartheta_T \leq 0.12$			$0.12 < \cos\vartheta_T \leq 0.24$			$0.24 < \cos\vartheta_T \leq 0.36$		
0.00 - 0.01	28.63	± 0.19	± 0.40	28.69	± 0.18	± 0.47	28.83	± 0.20	± 0.48
0.01 - 0.02	19.34	± 0.15	± 0.25	19.30	± 0.14	± 0.25	19.30	± 0.15	± 0.19
0.02 - 0.03	12.37	± 0.13	± 0.16	12.47	± 0.12	± 0.17	12.45	± 0.12	± 0.16
0.03 - 0.04	8.252	± 0.12	± 0.11	8.320	± 0.108	± 0.129	8.270	± 0.095	± 0.127
0.04 - 0.05	5.931	± 0.087	± 0.062	5.810	± 0.090	± 0.088	6.096	± 0.089	± 0.112
0.05 - 0.06	4.465	± 0.075	± 0.055	4.493	± 0.071	± 0.076	4.538	± 0.081	± 0.093
0.06 - 0.07	3.410	± 0.064	± 0.046	3.445	± 0.064	± 0.045	3.318	± 0.064	± 0.074
0.07 - 0.08	2.841	± 0.052	± 0.033	2.738	± 0.058	± 0.035	2.665	± 0.051	± 0.052
0.08 - 0.10	2.075	± 0.039	± 0.016	1.999	± 0.036	± 0.023	2.009	± 0.038	± 0.025
0.10 - 0.12	1.407	± 0.031	± 0.013	1.449	± 0.032	± 0.021	1.350	± 0.028	± 0.019
0.12 - 0.14	1.013	± 0.022	± 0.010	0.9785	± 0.0251	± 0.0171	1.017	± 0.023	± 0.010
0.14 - 0.16	0.7215	± 0.0206	± 0.0092	0.7404	± 0.0201	± 0.0082	0.7241	± 0.0207	± 0.0071
0.16 - 0.20	0.4937	± 0.0116	± 0.0058	0.5062	± 0.0129	± 0.0059	0.4845	± 0.0128	± 0.0060
0.20 - 0.25	0.2644	± 0.0095	± 0.0047	0.2672	± 0.0073	± 0.0042	0.2601	± 0.0070	± 0.0038
0.25 - 0.30	0.1274	± 0.0050	± 0.0024	0.1121	± 0.0046	± 0.0030	0.1145	± 0.0047	± 0.0015
0.30 - 0.35	0.0433	± 0.0028	± 0.0020	0.0463	± 0.0030	± 0.0011	0.0517	± 0.0037	± 0.0009
0.35 - 0.40	0.0161	± 0.0016	± 0.0017	0.0183	± 0.0021	± 0.0004	0.0170	± 0.0019	± 0.0004

Table B.9.a: Difference of the Jet Masses ρ_D

Difference of the Jet Masses ρ_D									
ρ_D	$0.36 < \cos\vartheta_T \leq 0.48$			$0.48 < \cos\vartheta_T \leq 0.60$			$0.60 < \cos\vartheta_T \leq 0.72$		
0.00 - 0.01	28.76	± 0.21	± 0.49	29.11	± 0.17	± 0.51	29.24	± 0.18	± 0.52
0.01 - 0.02	19.63	± 0.16	± 0.25	19.37	± 0.14	± 0.24	19.55	± 0.13	± 0.26
0.02 - 0.03	12.30	± 0.14	± 0.13	12.29	± 0.11	± 0.13	12.49	± 0.11	± 0.11
0.03 - 0.04	8.248	± 0.101	± 0.103	8.511	± 0.104	± 0.11	8.369	± 0.084	± 0.101
0.04 - 0.05	5.991	± 0.082	± 0.082	5.803	± 0.081	± 0.071	5.816	± 0.075	± 0.085
0.05 - 0.06	4.388	± 0.068	± 0.076	4.517	± 0.074	± 0.062	4.419	± 0.064	± 0.064
0.06 - 0.07	3.555	± 0.063	± 0.063	3.387	± 0.058	± 0.053	3.448	± 0.053	± 0.051
0.07 - 0.08	2.729	± 0.058	± 0.045	2.697	± 0.051	± 0.035	2.641	± 0.047	± 0.042
0.08 - 0.10	2.079	± 0.043	± 0.038	2.006	± 0.033	± 0.027	1.932	± 0.034	± 0.029
0.10 - 0.12	1.341	± 0.027	± 0.024	1.338	± 0.027	± 0.018	1.327	± 0.023	± 0.021
0.12 - 0.14	0.9749	± 0.0238	± 0.0131	0.9705	± 0.0231	± 0.0137	0.9642	± 0.0212	± 0.0198
0.14 - 0.16	0.7207	± 0.0189	± 0.0100	0.7565	± 0.0181	± 0.0121	0.7141	± 0.0181	± 0.0149
0.16 - 0.20	0.4927	± 0.0111	± 0.0071	0.4667	± 0.0115	± 0.0108	0.4529	± 0.0098	± 0.0106
0.20 - 0.25	0.2362	± 0.0069	± 0.0046	0.2408	± 0.0066	± 0.0051	0.2471	± 0.0081	± 0.0068
0.25 - 0.30	0.1067	± 0.0046	± 0.0035	0.1037	± 0.0042	± 0.0025	0.1100	± 0.0041	± 0.0021
0.30 - 0.35	0.0472	± 0.0034	± 0.0013	0.0472	± 0.0031	± 0.0011	0.0419	± 0.0029	± 0.0017
0.35 - 0.40	0.0183	± 0.0018	± 0.0009	0.0205	± 0.0025	± 0.0009	0.0154	± 0.0017	± 0.0007

Table B.9.b: Difference of the Jet Masses ρ_D

Difference of the Jet Masses ρ_D									
ρ_D	$0.72 < \cos\vartheta_T \leq 0.84$			$0.84 < \cos\vartheta_T \leq 0.96$			$0. < \cos\vartheta_T \leq 1.$		
0.00 - 0.01	29.39	± 0.17	± 0.51	29.97	± 0.19	± 0.54	29.18	± 0.14	± 0.48
0.01 - 0.02	19.61	± 0.11	± 0.31	19.28	± 0.12	± 0.32	19.44	± 0.06	± 0.26
0.02 - 0.03	12.30	± 0.09	± 0.11	12.17	± 0.10	± 0.17	12.35	± 0.05	± 0.14
0.03 - 0.04	8.315	± 0.082	± 0.099	8.180	± 0.092	± 0.106	8.303	± 0.035	± 0.105
0.04 - 0.05	5.936	± 0.072	± 0.080	5.884	± 0.074	± 0.089	5.899	± 0.032	± 0.076
0.05 - 0.06	4.430	± 0.065	± 0.064	4.315	± 0.060	± 0.065	4.432	± 0.025	± 0.057
0.06 - 0.07	3.460	± 0.057	± 0.058	3.394	± 0.056	± 0.059	3.424	± 0.022	± 0.047
0.07 - 0.08	2.747	± 0.049	± 0.049	2.704	± 0.047	± 0.053	2.709	± 0.020	± 0.034
0.08 - 0.10	1.956	± 0.030	± 0.035	1.894	± 0.029	± 0.024	1.980	± 0.014	± 0.024
0.10 - 0.12	1.3276	± 0.0233	± 0.0251	1.354	± 0.024	± 0.017	1.353	± 0.011	± 0.015
0.12 - 0.14	0.9452	± 0.0215	± 0.0164	0.9316	± 0.0189	± 0.0146	0.9660	± 0.0073	± 0.0101
0.14 - 0.16	0.6831	± 0.0197	± 0.0135	0.7093	± 0.0152	± 0.0112	0.7133	± 0.0065	± 0.0069
0.16 - 0.20	0.4320	± 0.0096	± 0.0083	0.4666	± 0.0102	± 0.0062	0.4676	± 0.0039	± 0.0046
0.20 - 0.25	0.2318	± 0.0063	± 0.0042	0.2518	± 0.0059	± 0.0056	0.2467	± 0.0026	± 0.0023
0.25 - 0.30	0.1097	± 0.0042	± 0.0020	0.0963	± 0.0038	± 0.0047	0.1082	± 0.0015	± 0.0017
0.30 - 0.35	0.0406	± 0.0024	± 0.0012	0.0457	± 0.0020	± 0.0024	0.04446	± 0.0009	± 0.0010
0.35 - 0.40	0.0160	± 0.0015	± 0.0008	0.0178	± 0.0016	± 0.0012	0.01682	± 0.00056	± 0.00053

Table B.9.c: Difference of the Jet Masses ρ_D

Wide Jet Broadening B_{Max}			
B_{Max}	$0.0 < \cos\vartheta_T \leq 0.12$	$0.12 < \cos\vartheta_T \leq 0.24$	$0.24 < \cos\vartheta_T \leq 0.36$
0.00 - 0.01	0.027 ± 0.007 ± 0.012	0.020 ± 0.007 ± 0.010	0.015 ± 0.006 ± 0.009
0.01 - 0.02	1.895 ± 0.038 ± 0.056	1.887 ± 0.036 ± 0.055	1.883 ± 0.037 ± 0.055
0.02 - 0.03	9.222 ± 0.093 ± 0.225	9.260 ± 0.084 ± 0.172	9.326 ± 0.082 ± 0.179
0.03 - 0.04	14.040 ± 0.120 ± 0.188	14.256 ± 0.111 ± 0.196	14.295 ± 0.110 ± 0.196
0.04 - 0.05	13.180 ± 0.116 ± 0.121	13.153 ± 0.113 ± 0.095	13.156 ± 0.107 ± 0.090
0.05 - 0.06	10.699 ± 0.098 ± 0.082	10.646 ± 0.102 ± 0.084	10.699 ± 0.095 ± 0.077
0.06 - 0.07	8.618 ± 0.094 ± 0.050	8.339 ± 0.089 ± 0.069	8.498 ± 0.084 ± 0.051
0.07 - 0.08	6.803 ± 0.081 ± 0.045	6.813 ± 0.081 ± 0.056	6.802 ± 0.079 ± 0.033
0.08 - 0.10	5.191 ± 0.049 ± 0.038	5.230 ± 0.054 ± 0.039	5.195 ± 0.050 ± 0.025
0.10 - 0.12	3.689 ± 0.041 ± 0.026	3.650 ± 0.042 ± 0.034	3.651 ± 0.037 ± 0.023
0.12 - 0.14	2.686 ± 0.035 ± 0.024	2.614 ± 0.039 ± 0.029	2.688 ± 0.035 ± 0.021
0.14 - 0.16	1.968 ± 0.032 ± 0.022	2.052 ± 0.032 ± 0.021	1.881 ± 0.029 ± 0.017
0.16 - 0.18	1.441 ± 0.025 ± 0.019	1.433 ± 0.026 ± 0.013	1.452 ± 0.026 ± 0.014
0.18 - 0.20	1.077 ± 0.023 ± 0.015	1.047 ± 0.023 ± 0.009	1.021 ± 0.021 ± 0.009
0.20 - 0.22	0.715 ± 0.019 ± 0.012	0.742 ± 0.019 ± 0.007	0.737 ± 0.019 ± 0.005
0.22 - 0.24	0.472 ± 0.014 ± 0.007	0.466 ± 0.015 ± 0.005	0.450 ± 0.015 ± 0.004
0.24 - 0.28	0.2069 ± 0.0067 ± 0.0048	0.1997 ± 0.0064 ± 0.00331	0.1970 ± 0.0066 ± 0.0004
0.28 - 0.32	0.0284 ± 0.0024 ± 0.0015	0.0295 ± 0.0024 ± 0.00205	0.0302 ± 0.0026 ± 0.0006

Table B.10.a: Wide Jet Broadening B_{Max}

Wide Jet Broadening B_{Max}			
B_{Max}	$0.36 < \cos\vartheta_T \leq 0.48$	$0.48 < \cos\vartheta_T \leq 0.60$	$0.60 < \cos\vartheta_T \leq 0.72$
0.00 - 0.01	0.027 ± 0.007 ± 0.008	0.020 ± 0.007 ± 0.009	0.027 ± 0.006 ± 0.009
0.01 - 0.02	1.924 ± 0.034 ± 0.055	1.852 ± 0.032 ± 0.055	1.994 ± 0.031 ± 0.063
0.02 - 0.03	9.324 ± 0.082 ± 0.197	9.494 ± 0.078 ± 0.195	9.404 ± 0.072 ± 0.185
0.03 - 0.04	14.241 ± 0.104 ± 0.159	14.354 ± 0.099 ± 0.184	14.312 ± 0.096 ± 0.155
0.04 - 0.05	13.442 ± 0.108 ± 0.113	13.332 ± 0.096 ± 0.084	13.517 ± 0.091 ± 0.089
0.05 - 0.06	10.568 ± 0.093 ± 0.090	10.702 ± 0.089 ± 0.068	10.737 ± 0.084 ± 0.070
0.06 - 0.07	8.380 ± 0.085 ± 0.056	8.436 ± 0.084 ± 0.036	8.558 ± 0.075 ± 0.041
0.07 - 0.08	6.928 ± 0.076 ± 0.042	6.881 ± 0.078 ± 0.024	6.763 ± 0.071 ± 0.037
0.08 - 0.10	5.215 ± 0.048 ± 0.037	5.139 ± 0.044 ± 0.021	5.203 ± 0.041 ± 0.030
0.10 - 0.12	3.599 ± 0.037 ± 0.030	3.660 ± 0.037 ± 0.018	3.675 ± 0.036 ± 0.027
0.12 - 0.14	2.691 ± 0.033 ± 0.027	2.669 ± 0.031 ± 0.014	2.574 ± 0.029 ± 0.022
0.14 - 0.16	1.924 ± 0.031 ± 0.022	1.903 ± 0.028 ± 0.012	1.875 ± 0.026 ± 0.018
0.16 - 0.18	1.417 ± 0.025 ± 0.012	1.404 ± 0.025 ± 0.010	1.362 ± 0.023 ± 0.015
0.18 - 0.20	1.008 ± 0.021 ± 0.010	1.015 ± 0.021 ± 0.009	0.967 ± 0.019 ± 0.014
0.20 - 0.22	0.713 ± 0.017 ± 0.009	0.682 ± 0.017 ± 0.008	0.653 ± 0.016 ± 0.012
0.22 - 0.24	0.427 ± 0.014 ± 0.008	0.400 ± 0.014 ± 0.006	0.427 ± 0.013 ± 0.011
0.24 - 0.28	0.1807 ± 0.0062 ± 0.0024	0.1857 ± 0.0066 ± 0.0034	0.1729 ± 0.0059 ± 0.0063
0.28 - 0.32	0.0343 ± 0.0028 ± 0.0010	0.0315 ± 0.0027 ± 0.0007	0.0297 ± 0.0026 ± 0.0016

Table B.10.b: Wide Jet Broadening B_{Max}

Wide Jet Broadening B_{Max}									
B_{Max}	$0.72 < \cos\vartheta_T \leq 0.84$			$0.84 < \cos\vartheta_T \leq 0.96$			$0. < \cos\vartheta_T \leq 1.$		
0.00 - 0.01	0.083	± 0.010	± 0.017	0.296	± 0.017	± 0.088	0.041	± 0.003	± 0.036
0.01 - 0.02	2.094	± 0.029	± 0.073	2.267	± 0.031	± 0.138	1.945	± 0.014	± 0.087
0.02 - 0.03	9.625	± 0.071	± 0.227	9.413	± 0.071	± 0.246	9.412	± 0.039	± 0.295
0.03 - 0.04	14.380	± 0.092	± 0.185	14.152	± 0.097	± 0.203	14.307	± 0.045	± 0.235
0.04 - 0.05	13.299	± 0.087	± 0.093	12.932	± 0.089	± 0.136	13.367	± 0.039	± 0.105
0.05 - 0.06	10.859	± 0.083	± 0.061	10.459	± 0.084	± 0.094	10.755	± 0.035	± 0.073
0.06 - 0.07	8.510	± 0.070	± 0.049	8.393	± 0.076	± 0.073	8.510	± 0.032	± 0.045
0.07 - 0.08	6.816	± 0.064	± 0.039	6.843	± 0.069	± 0.060	6.849	± 0.030	± 0.025
0.08 - 0.10	5.185	± 0.040	± 0.031	5.119	± 0.043	± 0.057	5.193	± 0.017	± 0.023
0.10 - 0.12	3.621	± 0.034	± 0.028	3.599	± 0.035	± 0.052	3.639	± 0.015	± 0.022
0.12 - 0.14	2.577	± 0.031	± 0.026	2.563	± 0.031	± 0.040	2.625	± 0.014	± 0.016
0.14 - 0.16	1.849	± 0.026	± 0.024	1.801	± 0.025	± 0.031	1.900	± 0.012	± 0.014
0.16 - 0.18	1.361	± 0.022	± 0.021	1.331	± 0.022	± 0.022	1.3878	± 0.0094	± 0.0091
0.18 - 0.20	0.909	± 0.017	± 0.017	0.929	± 0.017	± 0.010	0.9828	± 0.0082	± 0.0082
0.20 - 0.22	0.610	± 0.015	± 0.012	0.657	± 0.014	± 0.008	0.6722	± 0.0065	± 0.0062
0.22 - 0.24	0.387	± 0.011	± 0.010	0.407	± 0.011	± 0.006	0.4212	± 0.0050	± 0.0043
0.24 - 0.28	0.1722	± 0.0056	± 0.0028	0.1654	± 0.0048	± 0.0052	0.1802	± 0.0024	± 0.0016
0.28 - 0.32	0.0303	± 0.0024	± 0.0007	0.0293	± 0.0020	± 0.0017	0.0292	± 0.0010	± 0.0007

Table B.10.c: Wide Jet Broadening B_{Max}

Total Jet Broadening B_{Sum}									
B_{Sum}	$0.0 < \cos\vartheta_T \leq 0.12$			$0.12 < \cos\vartheta_T \leq 0.24$			$0.24 < \cos\vartheta_T \leq 0.36$		
0.00 - 0.01	0.003	± 0.002	± 0.009	0.001	± 0.001	± 0.002	0.004	± 0.003	± 0.004
0.01 - 0.02	0.089	± 0.010	± 0.012	0.089	± 0.010	± 0.015	0.091	± 0.009	± 0.011
0.02 - 0.03	0.949	± 0.027	± 0.043	0.942	± 0.026	± 0.041	0.924	± 0.024	± 0.042
0.03 - 0.04	3.517	± 0.055	± 0.145	3.594	± 0.051	± 0.114	3.489	± 0.051	± 0.107
0.04 - 0.05	6.571	± 0.079	± 0.159	6.522	± 0.073	± 0.128	6.739	± 0.070	± 0.165
0.05 - 0.06	8.726	± 0.097	± 0.144	8.959	± 0.091	± 0.161	9.042	± 0.093	± 0.185
0.06 - 0.07	9.705	± 0.099	± 0.126	9.709	± 0.097	± 0.122	9.613	± 0.095	± 0.135
0.07 - 0.08	9.047	± 0.097	± 0.103	9.043	± 0.099	± 0.083	9.148	± 0.089	± 0.041
0.08 - 0.10	7.453	± 0.062	± 0.059	7.394	± 0.060	± 0.072	7.399	± 0.055	± 0.038
0.10 - 0.12	5.580	± 0.051	± 0.030	5.439	± 0.051	± 0.043	5.538	± 0.049	± 0.036
0.12 - 0.14	4.196	± 0.047	± 0.028	4.222	± 0.044	± 0.037	4.192	± 0.044	± 0.026
0.14 - 0.16	3.259	± 0.040	± 0.027	3.210	± 0.039	± 0.026	3.168	± 0.039	± 0.024
0.16 - 0.18	2.442	± 0.034	± 0.026	2.499	± 0.036	± 0.021	2.446	± 0.032	± 0.022
0.18 - 0.20	1.957	± 0.030	± 0.025	1.925	± 0.030	± 0.019	1.913	± 0.030	± 0.020
0.20 - 0.22	1.509	± 0.026	± 0.023	1.547	± 0.026	± 0.018	1.472	± 0.027	± 0.018
0.22 - 0.24	1.226	± 0.024	± 0.017	1.215	± 0.023	± 0.016	1.269	± 0.023	± 0.016
0.24 - 0.28	0.870	± 0.014	± 0.013	0.848	± 0.014	± 0.007	0.849	± 0.014	± 0.006
0.28 - 0.32	0.443	± 0.010	± 0.007	0.452	± 0.010	± 0.005	0.441	± 0.010	± 0.003
0.32 - 0.36	0.1537	± 0.0058	± 0.0042	0.1506	± 0.0061	± 0.0020	0.1368	± 0.0057	± 0.0030
0.36 - 0.40	0.0133	± 0.0032	± 0.0009	0.0143	± 0.0028	± 0.0011	0.0117	± 0.0025	± 0.0007

Table B.11.a: Total Jet Broadening B_{Sum}

Total Jet Broadening B_{Sum}			
B_{Sum}	$0.36 < \cos\vartheta_T \leq 0.48$	$0.48 < \cos\vartheta_T \leq 0.60$	$0.60 < \cos\vartheta_T \leq 0.72$
0.00 - 0.01	0.002 ± 0.002 ± 0.003	0.002 ± 0.001 ± 0.004	0.004 ± 0.002 ± 0.003
0.01 - 0.02	0.097 ± 0.010 ± 0.007	0.085 ± 0.008 ± 0.010	0.089 ± 0.008 ± 0.013
0.02 - 0.03	0.898 ± 0.023 ± 0.044	0.903 ± 0.024 ± 0.042	0.972 ± 0.022 ± 0.043
0.03 - 0.04	3.614 ± 0.050 ± 0.120	3.545 ± 0.045 ± 0.103	3.603 ± 0.046 ± 0.108
0.04 - 0.05	6.693 ± 0.068 ± 0.141	6.911 ± 0.071 ± 0.216	6.843 ± 0.069 ± 0.202
0.05 - 0.06	9.010 ± 0.085 ± 0.143	8.974 ± 0.080 ± 0.169	8.978 ± 0.077 ± 0.121
0.06 - 0.07	9.750 ± 0.091 ± 0.140	9.901 ± 0.094 ± 0.123	9.764 ± 0.091 ± 0.100
0.07 - 0.08	9.016 ± 0.087 ± 0.079	9.256 ± 0.091 ± 0.102	9.212 ± 0.085 ± 0.059
0.08 - 0.10	7.452 ± 0.057 ± 0.071	7.351 ± 0.054 ± 0.039	7.507 ± 0.050 ± 0.052
0.10 - 0.12	5.591 ± 0.047 ± 0.044	5.571 ± 0.046 ± 0.034	5.509 ± 0.044 ± 0.037
0.12 - 0.14	4.158 ± 0.042 ± 0.038	4.086 ± 0.041 ± 0.030	4.231 ± 0.036 ± 0.033
0.14 - 0.16	3.117 ± 0.038 ± 0.030	3.129 ± 0.034 ± 0.027	3.189 ± 0.033 ± 0.031
0.16 - 0.18	2.470 ± 0.034 ± 0.016	2.499 ± 0.031 ± 0.024	2.430 ± 0.030 ± 0.028
0.18 - 0.20	1.889 ± 0.027 ± 0.015	1.902 ± 0.029 ± 0.021	1.843 ± 0.026 ± 0.022
0.20 - 0.22	1.538 ± 0.024 ± 0.014	1.532 ± 0.026 ± 0.017	1.501 ± 0.024 ± 0.020
0.22 - 0.24	1.250 ± 0.022 ± 0.012	1.184 ± 0.024 ± 0.010	1.161 ± 0.021 ± 0.017
0.24 - 0.28	0.817 ± 0.013 ± 0.007	0.806 ± 0.013 ± 0.009	0.769 ± 0.013 ± 0.014
0.28 - 0.32	0.430 ± 0.010 ± 0.005	0.430 ± 0.010 ± 0.005	0.426 ± 0.010 ± 0.013
0.32 - 0.36	0.1346 ± 0.0060 ± 0.0034	0.1259 ± 0.0054 ± 0.0032	0.1168 ± 0.0059 ± 0.0055
0.36 - 0.40	0.0163 ± 0.0037 ± 0.0021	0.0077 ± 0.0019 ± 0.0007	0.0063 ± 0.0013 ± 0.0008

Table B.11.b: Total Jet Broadening B_{Sum}

Total Jet Broadening B_{Sum}			
B_{Sum}	$0.72 < \cos\vartheta_T \leq 0.84$	$0.84 < \cos\vartheta_T \leq 0.96$	$0. < \cos\vartheta_T \leq 1.$
0.00 - 0.01	0.001 ± 0.001 ± 0.014	0.153 ± 0.052 ± 0.088	0.010 ± 0.003 ± 0.025
0.01 - 0.02	0.120 ± 0.012 ± 0.022	0.300 ± 0.012 ± 0.069	0.091 ± 0.004 ± 0.015
0.02 - 0.03	0.973 ± 0.034 ± 0.045	1.138 ± 0.020 ± 0.086	0.939 ± 0.010 ± 0.042
0.03 - 0.04	3.714 ± 0.066 ± 0.142	3.585 ± 0.040 ± 0.167	3.590 ± 0.019 ± 0.119
0.04 - 0.05	6.856 ± 0.095 ± 0.188	6.704 ± 0.061 ± 0.185	6.772 ± 0.027 ± 0.169
0.05 - 0.06	9.041 ± 0.115 ± 0.116	8.957 ± 0.075 ± 0.173	9.003 ± 0.033 ± 0.151
0.06 - 0.07	9.803 ± 0.123 ± 0.102	9.510 ± 0.081 ± 0.166	9.788 ± 0.035 ± 0.127
0.07 - 0.08	9.298 ± 0.127 ± 0.085	8.883 ± 0.076 ± 0.125	9.167 ± 0.036 ± 0.079
0.08 - 0.10	7.667 ± 0.078 ± 0.079	7.351 ± 0.048 ± 0.087	7.485 ± 0.022 ± 0.066
0.10 - 0.12	5.541 ± 0.068 ± 0.041	5.401 ± 0.040 ± 0.066	5.554 ± 0.019 ± 0.039
0.12 - 0.14	4.173 ± 0.059 ± 0.034	4.121 ± 0.035 ± 0.058	4.188 ± 0.017 ± 0.028
0.14 - 0.16	3.135 ± 0.048 ± 0.032	3.170 ± 0.033 ± 0.051	3.178 ± 0.014 ± 0.024
0.16 - 0.18	2.422 ± 0.044 ± 0.031	2.438 ± 0.029 ± 0.032	2.454 ± 0.013 ± 0.019
0.18 - 0.20	1.892 ± 0.037 ± 0.015	1.867 ± 0.025 ± 0.025	1.891 ± 0.011 ± 0.016
0.20 - 0.22	1.421 ± 0.034 ± 0.013	1.437 ± 0.023 ± 0.022	1.493 ± 0.010 ± 0.013
0.22 - 0.24	1.123 ± 0.030 ± 0.009	1.113 ± 0.021 ± 0.020	1.1823 ± 0.0092 ± 0.0093
0.24 - 0.28	0.762 ± 0.017 ± 0.007	0.759 ± 0.012 ± 0.013	0.7968 ± 0.0047 ± 0.0059
0.28 - 0.32	0.358 ± 0.012 ± 0.005	0.372 ± 0.010 ± 0.004	0.4062 ± 0.0035 ± 0.0035
0.32 - 0.36	0.1127 ± 0.0064 ± 0.0024	0.1065 ± 0.0043 ± 0.0027	0.1229 ± 0.0019 ± 0.0016
0.36 - 0.40	0.0058 ± 0.0014 ± 0.0010	0.0065 ± 0.0012 ± 0.0002	0.00758 ± 0.00054 ± 0.00011

Table B.11.c: Total Jet Broadening B_{Sum}

Differential 2-Jet Rate E_0 Scheme $D_2^{E_0}$								
y_{23}	$0.0 < \cos\vartheta_T \leq 0.12$			$0.12 < \cos\vartheta_T \leq 0.24$			$0.24 < \cos\vartheta_T \leq 0.36$	
0.000 - 0.005	23.43	± 0.25	± 0.65	23.04	± 0.19	± 0.77	23.43	± 0.22	± 0.72
0.005 - 0.010	26.19	± 0.23	± 0.47	26.55	± 0.22	± 0.45	26.62	± 0.21	± 0.48
0.010 - 0.015	20.55	± 0.21	± 0.21	20.49	± 0.20	± 0.26	20.35	± 0.20	± 0.25
0.015 - 0.020	15.98	± 0.19	± 0.16	16.26	± 0.19	± 0.22	16.25	± 0.19	± 0.19
0.020 - 0.025	13.08	± 0.17	± 0.13	12.84	± 0.17	± 0.17	13.11	± 0.17	± 0.15
0.025 - 0.030	10.78	± 0.15	± 0.12	10.77	± 0.15	± 0.12	10.83	± 0.16	± 0.13
0.030 - 0.040	8.264	± 0.106	± 0.111	8.603	± 0.116	± 0.108	8.414	± 0.096	± 0.116
0.040 - 0.050	6.366	± 0.091	± 0.089	6.180	± 0.095	± 0.073	6.171	± 0.084	± 0.076
0.050 - 0.060	4.883	± 0.073	± 0.063	4.824	± 0.072	± 0.061	4.741	± 0.070	± 0.065
0.060 - 0.070	4.009	± 0.067	± 0.052	3.825	± 0.064	± 0.053	3.937	± 0.062	± 0.054
0.070 - 0.080	3.151	± 0.063	± 0.044	3.178	± 0.060	± 0.048	3.053	± 0.057	± 0.046
0.080 - 0.090	2.569	± 0.058	± 0.040	2.749	± 0.057	± 0.045	2.658	± 0.054	± 0.042
0.090 - 0.100	2.204	± 0.053	± 0.035	2.203	± 0.053	± 0.040	2.280	± 0.052	± 0.037
0.100 - 0.110	1.940	± 0.049	± 0.028	1.911	± 0.042	± 0.035	1.913	± 0.047	± 0.031
0.110 - 0.120	1.630	± 0.046	± 0.014	1.588	± 0.039	± 0.029	1.660	± 0.040	± 0.027
0.120 - 0.140	1.327	± 0.030	± 0.022	1.316	± 0.028	± 0.017	1.256	± 0.027	± 0.021
0.140 - 0.160	0.9687	± 0.0248	± 0.0209	0.9940	± 0.0237	± 0.012	0.9813	± 0.0244	± 0.0205
0.160 - 0.180	0.7907	± 0.0213	± 0.0110	0.7829	± 0.0209	± 0.0114	0.7487	± 0.0200	± 0.0123
0.180 - 0.200	0.5526	± 0.0182	± 0.0095	0.5892	± 0.0177	± 0.0108	0.6101	± 0.0149	± 0.0111
0.200 - 0.250	0.3669	± 0.0088	± 0.0061	0.3602	± 0.0086	± 0.0092	0.3557	± 0.0082	± 0.0085
0.250 - 0.300	0.1474	± 0.0058	± 0.0031	0.1479	± 0.0064	± 0.0047	0.1363	± 0.0059	± 0.0038
0.300 - 0.350	0.0212	± 0.0042	± 0.0016	0.0146	± 0.0019	± 0.0011	0.0187	± 0.0028	± 0.0012

Table B.12.a: Differential 2-Jet Rate E_0 Scheme $D_2^{E_0}$

Differential 2-Jet Rate E_0 Scheme $D_2^{E_0}$								
y_{23}	$0.36 < \cos\vartheta_T \leq 0.48$			$0.48 < \cos\vartheta_T \leq 0.60$			$0.60 < \cos\vartheta_T \leq 0.72$	
0.000 - 0.005	23.31	± 0.20	± 0.76	23.65	± 0.18	± 0.76	23.64	± 0.17	± 0.78
0.005 - 0.010	26.57	± 0.21	± 0.48	26.75	± 0.21	± 0.48	26.77	± 0.19	± 0.47
0.010 - 0.015	20.55	± 0.19	± 0.25	20.66	± 0.20	± 0.32	20.64	± 0.18	± 0.24
0.015 - 0.020	16.26	± 0.17	± 0.19	16.35	± 0.18	± 0.31	16.61	± 0.17	± 0.17
0.020 - 0.025	12.98	± 0.16	± 0.17	13.05	± 0.16	± 0.15	13.20	± 0.16	± 0.14
0.025 - 0.030	10.98	± 0.13	± 0.15	10.83	± 0.13	± 0.11	10.68	± 0.12	± 0.11
0.030 - 0.040	8.442	± 0.112	± 0.121	8.371	± 0.089	± 0.097	8.481	± 0.105	± 0.101
0.040 - 0.050	6.199	± 0.094	± 0.077	6.219	± 0.070	± 0.082	6.243	± 0.075	± 0.081
0.050 - 0.060	4.840	± 0.077	± 0.062	4.803	± 0.066	± 0.070	4.909	± 0.069	± 0.067
0.060 - 0.070	4.034	± 0.068	± 0.057	3.924	± 0.062	± 0.063	3.907	± 0.065	± 0.056
0.070 - 0.080	3.214	± 0.059	± 0.054	3.216	± 0.057	± 0.055	3.153	± 0.060	± 0.050
0.080 - 0.090	2.636	± 0.053	± 0.049	2.504	± 0.050	± 0.042	2.529	± 0.054	± 0.039
0.090 - 0.100	2.248	± 0.049	± 0.045	2.263	± 0.048	± 0.037	2.112	± 0.049	± 0.032
0.100 - 0.110	1.890	± 0.045	± 0.036	1.850	± 0.046	± 0.031	1.939	± 0.041	± 0.029
0.110 - 0.120	1.586	± 0.038	± 0.027	1.647	± 0.042	± 0.025	1.594	± 0.037	± 0.026
0.120 - 0.140	1.287	± 0.024	± 0.018	1.282	± 0.025	± 0.024	1.235	± 0.023	± 0.022
0.140 - 0.160	0.9625	± 0.0221	± 0.0165	0.9538	± 0.0226	± 0.0232	0.9602	± 0.0217	± 0.0203
0.160 - 0.180	0.7255	± 0.0205	± 0.0149	0.7362	± 0.0218	± 0.0215	0.7282	± 0.0181	± 0.0175
0.180 - 0.200	0.6095	± 0.0173	± 0.0115	0.5599	± 0.0189	± 0.0175	0.5452	± 0.0143	± 0.0141
0.200 - 0.250	0.3341	± 0.0079	± 0.0095	0.3403	± 0.0094	± 0.0107	0.3297	± 0.0079	± 0.0103
0.250 - 0.300	0.1347	± 0.0056	± 0.0069	0.1293	± 0.0054	± 0.0061	0.1356	± 0.0055	± 0.0070
0.300 - 0.350	0.0129	± 0.0019	± 0.0008	0.0146	± 0.0021	± 0.0032	0.0152	± 0.0020	± 0.0014

Table B.12.b: Differential 2-Jet Rate E_0 Scheme $D_2^{E_0}$

Differential 2-Jet Rate E_0 Scheme $D_2^{E_0}$									
y_{23}	$0.72 < \cos\vartheta_T \leq 0.84$			$0.84 < \cos\vartheta_T \leq 0.96$			$0. < \cos\vartheta_T \leq 1.$		
0.000 - 0.005	24.18	± 0.17	± 0.79	25.51	± 0.19	± 0.91	23.88	± 0.11	± 0.74
0.005 - 0.010	27.02	± 0.20	± 0.51	26.48	± 0.19	± 0.44	26.68	± 0.08	± 0.47
0.010 - 0.015	20.73	± 0.17	± 0.29	20.26	± 0.17	± 0.31	20.54	± 0.07	± 0.24
0.015 - 0.020	16.26	± 0.15	± 0.18	16.12	± 0.15	± 0.27	16.28	± 0.06	± 0.20
0.020 - 0.025	13.24	± 0.13	± 0.14	13.23	± 0.14	± 0.23	13.11	± 0.06	± 0.17
0.025 - 0.030	10.81	± 0.11	± 0.12	10.75	± 0.13	± 0.11	10.80	± 0.05	± 0.11
0.030 - 0.040	8.358	± 0.088	± 0.103	8.316	± 0.081	± 0.093	8.401	± 0.035	± 0.081
0.040 - 0.050	6.352	± 0.074	± 0.075	6.170	± 0.068	± 0.081	6.242	± 0.029	± 0.063
0.050 - 0.060	4.965	± 0.065	± 0.063	4.779	± 0.063	± 0.065	4.842	± 0.026	± 0.054
0.060 - 0.070	3.793	± 0.056	± 0.058	3.968	± 0.058	± 0.055	3.919	± 0.023	± 0.045
0.070 - 0.080	3.104	± 0.052	± 0.053	3.072	± 0.051	± 0.046	3.133	± 0.019	± 0.037
0.080 - 0.090	2.673	± 0.046	± 0.049	2.561	± 0.046	± 0.042	2.599	± 0.017	± 0.032
0.090 - 0.100	2.127	± 0.041	± 0.044	2.212	± 0.043	± 0.035	2.193	± 0.018	± 0.028
0.100 - 0.110	1.797	± 0.037	± 0.040	1.828	± 0.040	± 0.028	1.866	± 0.014	± 0.023
0.110 - 0.120	1.639	± 0.034	± 0.033	1.564	± 0.031	± 0.023	1.603	± 0.013	± 0.019
0.120 - 0.140	1.267	± 0.021	± 0.030	1.227	± 0.024	± 0.019	1.264	± 0.010	± 0.018
0.140 - 0.160	0.8996	± 0.0191	± 0.0181	0.9240	± 0.0200	± 0.0157	0.9492	± 0.0079	± 0.0136
0.160 - 0.180	0.6517	± 0.0168	± 0.0159	0.7035	± 0.0178	± 0.0116	0.7223	± 0.0067	± 0.0122
0.180 - 0.200	0.5146	± 0.0134	± 0.0135	0.5080	± 0.0137	± 0.0108	0.5503	± 0.0060	± 0.0103
0.200 - 0.250	0.3228	± 0.0070	± 0.0101	0.3162	± 0.0069	± 0.0096	0.3347	± 0.0027	± 0.0074
0.250 - 0.300	0.1140	± 0.0043	± 0.0041	0.1250	± 0.0047	± 0.0047	0.1298	± 0.0017	± 0.0037
0.300 - 0.350	0.0126	± 0.0016	± 0.0009	0.0094	± 0.0013	± 0.0007	0.01310	± 0.00064	± 0.00062

Table B.12.c: Differential 2-Jet Rate E_0 Scheme $D_2^{E_0}$

Differential 2-Jet Rate P_0 Scheme $D_2^{P_0}$									
y_{23}	$0.0 < \cos\vartheta_T \leq 0.12$			$0.12 < \cos\vartheta_T \leq 0.24$			$0.24 < \cos\vartheta_T \leq 0.36$		
0.000 - 0.005	32.26	± 0.24	± 0.49	31.79	± 0.22	± 0.62	32.36	± 0.23	± 0.54
0.005 - 0.010	31.19	± 0.24	± 0.36	31.75	± 0.24	± 0.36	31.51	± 0.22	± 0.42
0.010 - 0.015	22.22	± 0.20	± 0.24	22.28	± 0.22	± 0.25	22.31	± 0.19	± 0.14
0.015 - 0.020	16.19	± 0.18	± 0.19	16.34	± 0.21	± 0.18	16.18	± 0.18	± 0.22
0.020 - 0.025	12.23	± 0.16	± 0.07	11.97	± 0.15	± 0.08	11.99	± 0.15	± 0.13
0.025 - 0.030	9.674	± 0.140	± 0.056	9.719	± 0.121	± 0.074	10.09	± 0.13	± 0.09
0.030 - 0.040	7.304	± 0.095	± 0.048	7.335	± 0.088	± 0.065	7.329	± 0.086	± 0.071
0.040 - 0.050	5.445	± 0.077	± 0.042	5.401	± 0.076	± 0.049	5.187	± 0.074	± 0.055
0.050 - 0.060	4.085	± 0.069	± 0.038	3.906	± 0.058	± 0.038	4.141	± 0.069	± 0.044
0.060 - 0.070	3.267	± 0.055	± 0.035	3.328	± 0.055	± 0.033	3.241	± 0.058	± 0.033
0.070 - 0.080	2.612	± 0.050	± 0.029	2.743	± 0.051	± 0.028	2.599	± 0.054	± 0.025
0.080 - 0.090	2.180	± 0.047	± 0.025	2.164	± 0.047	± 0.021	2.182	± 0.048	± 0.019
0.090 - 0.100	1.866	± 0.044	± 0.023	1.877	± 0.044	± 0.016	1.892	± 0.042	± 0.016
0.100 - 0.110	1.600	± 0.042	± 0.020	1.619	± 0.041	± 0.013	1.556	± 0.037	± 0.013
0.110 - 0.120	1.403	± 0.040	± 0.017	1.301	± 0.035	± 0.011	1.342	± 0.033	± 0.012
0.120 - 0.140	1.103	± 0.023	± 0.014	1.079	± 0.022	± 0.010	1.070	± 0.024	± 0.010
0.140 - 0.160	0.8011	± 0.0201	± 0.0129	0.8577	± 0.0198	± 0.0091	0.8468	± 0.0215	± 0.0091
0.160 - 0.180	0.6568	± 0.0182	± 0.0098	0.6716	± 0.0185	± 0.0083	0.6317	± 0.0161	± 0.0083
0.180 - 0.200	0.4816	± 0.0134	± 0.0081	0.5072	± 0.0143	± 0.0078	0.5020	± 0.0118	± 0.0071
0.200 - 0.250	0.3227	± 0.0074	± 0.0078	0.3065	± 0.0076	± 0.0052	0.3085	± 0.0058	± 0.0057
0.250 - 0.300	0.1349	± 0.0046	± 0.0048	0.1243	± 0.0052	± 0.0028	0.1162	± 0.0046	± 0.0046
0.300 - 0.350	0.0128	± 0.0016	± 0.0019	0.0181	± 0.0022	± 0.0009	0.0194	± 0.0026	± 0.0014

Table B.13.a: Differential 2-Jet Rate P_0 Scheme $D_2^{P_0}$

Differential 2-Jet Rate P_0 Scheme $D_2^{P_0}$									
y_{23}	$0.36 < \cos\vartheta_T \leq 0.48$			$0.48 < \cos\vartheta_T \leq 0.60$			$0.60 < \cos\vartheta_T \leq 0.72$		
0.000 - 0.005	32.36	± 0.21	± 0.62	32.60	± 0.20	± 0.60	32.71	± 0.19	± 0.64
0.005 - 0.010	31.52	± 0.21	± 0.39	31.89	± 0.21	± 0.40	31.84	± 0.22	± 0.42
0.010 - 0.015	22.30	± 0.19	± 0.24	22.22	± 0.20	± 0.35	22.42	± 0.16	± 0.15
0.015 - 0.020	16.08	± 0.16	± 0.16	16.33	± 0.17	± 0.22	16.41	± 0.14	± 0.13
0.020 - 0.025	12.29	± 0.14	± 0.13	12.39	± 0.14	± 0.15	12.28	± 0.13	± 0.11
0.025 - 0.030	9.975	± 0.126	± 0.089	9.662	± 0.110	± 0.058	9.616	± 0.110	± 0.101
0.030 - 0.040	7.324	± 0.070	± 0.074	7.294	± 0.071	± 0.049	7.476	± 0.076	± 0.085
0.040 - 0.050	5.201	± 0.067	± 0.063	5.215	± 0.062	± 0.036	5.311	± 0.062	± 0.062
0.050 - 0.060	4.196	± 0.064	± 0.048	4.069	± 0.069	± 0.029	4.149	± 0.057	± 0.051
0.060 - 0.070	3.293	± 0.055	± 0.039	3.281	± 0.054	± 0.024	3.155	± 0.050	± 0.043
0.070 - 0.080	2.636	± 0.047	± 0.028	2.667	± 0.049	± 0.019	2.692	± 0.046	± 0.035
0.080 - 0.090	2.238	± 0.044	± 0.023	2.216	± 0.043	± 0.017	2.047	± 0.038	± 0.026
0.090 - 0.100	1.897	± 0.040	± 0.019	1.855	± 0.039	± 0.016	1.813	± 0.035	± 0.022
0.100 - 0.110	1.533	± 0.037	± 0.016	1.542	± 0.034	± 0.015	1.555	± 0.032	± 0.017
0.110 - 0.120	1.310	± 0.034	± 0.013	1.325	± 0.030	± 0.012	1.318	± 0.028	± 0.013
0.120 - 0.140	1.097	± 0.023	± 0.011	1.060	± 0.023	± 0.011	1.057	± 0.020	± 0.011
0.140 - 0.160	0.8179	± 0.0196	± 0.0095	0.8104	± 0.0182	± 0.0093	0.7859	± 0.0185	± 0.0093
0.160 - 0.180	0.6263	± 0.0188	± 0.0087	0.6164	± 0.0178	± 0.0088	0.5845	± 0.0149	± 0.0083
0.180 - 0.200	0.4771	± 0.0161	± 0.0071	0.4610	± 0.0144	± 0.0171	0.4624	± 0.0123	± 0.0071
0.200 - 0.250	0.2897	± 0.0065	± 0.0048	0.2937	± 0.0072	± 0.0059	0.2908	± 0.0070	± 0.0062
0.250 - 0.300	0.1182	± 0.0051	± 0.0039	0.1087	± 0.0048	± 0.0041	0.1114	± 0.0043	± 0.0051
0.300 - 0.350	0.0109	± 0.0016	± 0.0009	0.0162	± 0.0023	± 0.0013	0.0106	± 0.0015	± 0.0009

Table B.13.b: Differential 2-Jet Rate P_0 Scheme $D_2^{P_0}$

Differential 2-Jet Rate P_0 Scheme $D_2^{P_0}$									
y_{23}	$0.72 < \cos\vartheta_T \leq 0.84$			$0.84 < \cos\vartheta_T \leq 0.96$			$0. < \cos\vartheta_T \leq 1.$		
0.000 - 0.005	33.34	± 0.17	± 0.63	34.92	± 0.21	± 0.88	32.94	± 0.09	± 0.58
0.005 - 0.010	32.07	± 0.18	± 0.39	31.22	± 0.19	± 0.38	31.69	± 0.08	± 0.39
0.010 - 0.015	22.30	± 0.16	± 0.25	21.98	± 0.16	± 0.33	22.25	± 0.07	± 0.23
0.015 - 0.020	16.29	± 0.14	± 0.15	16.35	± 0.15	± 0.24	16.29	± 0.06	± 0.18
0.020 - 0.025	12.39	± 0.12	± 0.12	12.23	± 0.13	± 0.12	12.24	± 0.05	± 0.11
0.025 - 0.030	9.737	± 0.112	± 0.108	9.752	± 0.117	± 0.118	9.765	± 0.043	± 0.068
0.030 - 0.040	7.275	± 0.069	± 0.074	7.269	± 0.067	± 0.085	7.330	± 0.026	± 0.042
0.040 - 0.050	5.418	± 0.064	± 0.061	5.265	± 0.060	± 0.074	5.304	± 0.021	± 0.034
0.050 - 0.060	4.114	± 0.054	± 0.057	4.083	± 0.051	± 0.058	4.089	± 0.019	± 0.028
0.060 - 0.070	3.213	± 0.047	± 0.048	3.222	± 0.042	± 0.049	3.241	± 0.017	± 0.023
0.070 - 0.080	2.659	± 0.045	± 0.039	2.544	± 0.039	± 0.044	2.635	± 0.016	± 0.020
0.080 - 0.090	2.238	± 0.042	± 0.032	2.146	± 0.037	± 0.033	2.169	± 0.015	± 0.019
0.090 - 0.100	1.780	± 0.035	± 0.025	1.724	± 0.036	± 0.025	1.823	± 0.014	± 0.016
0.100 - 0.110	1.471	± 0.033	± 0.022	1.562	± 0.032	± 0.020	1.541	± 0.012	± 0.013
0.110 - 0.120	1.321	± 0.031	± 0.016	1.353	± 0.030	± 0.018	1.326	± 0.010	± 0.012
0.120 - 0.140	1.030	± 0.019	± 0.013	1.031	± 0.018	± 0.016	1.056	± 0.007	± 0.011
0.140 - 0.160	0.7503	± 0.0170	± 0.0111	0.7693	± 0.0171	± 0.0131	0.7942	± 0.0062	± 0.0092
0.160 - 0.180	0.5379	± 0.0149	± 0.0098	0.5888	± 0.0159	± 0.0104	0.6047	± 0.0053	± 0.0080
0.180 - 0.200	0.4477	± 0.0117	± 0.0088	0.4460	± 0.0143	± 0.0093	0.4632	± 0.0041	± 0.0072
0.200 - 0.250	0.2677	± 0.0060	± 0.0064	0.2622	± 0.0066	± 0.0082	0.2868	± 0.0023	± 0.0053
0.250 - 0.300	0.0964	± 0.0036	± 0.0032	0.0951	± 0.0035	± 0.0045	0.1091	± 0.0015	± 0.0025
0.300 - 0.350	0.0113	± 0.0015	± 0.0006	0.0114	± 0.0016	± 0.0006	0.01253	± 0.00054	± 0.00053

Table B.13.c: Differential 2-Jet Rate P_0 Scheme $D_2^{P_0}$

Differential 2-Jet Rate P Scheme D_2^P									
y_{23}	$0.0 < \cos\vartheta_T \leq 0.12$			$0.12 < \cos\vartheta_T \leq 0.24$			$0.24 < \cos\vartheta_T \leq 0.36$		
0.000 - 0.005	34.40	± 0.26	± 0.56	33.94	± 0.24	± 0.72	34.59	± 0.25	± 0.60
0.005 - 0.010	32.71	± 0.28	± 0.39	33.31	± 0.25	± 0.44	33.12	± 0.24	± 0.52
0.010 - 0.015	23.21	± 0.22	± 0.36	23.26	± 0.23	± 0.30	22.93	± 0.22	± 0.19
0.015 - 0.020	16.62	± 0.19	± 0.16	16.51	± 0.20	± 0.27	16.55	± 0.18	± 0.16
0.020 - 0.025	12.43	± 0.17	± 0.08	12.35	± 0.16	± 0.12	12.46	± 0.16	± 0.101
0.025 - 0.030	9.932	± 0.139	± 0.082	9.878	± 0.140	± 0.077	10.31	± 0.14	± 0.090
0.030 - 0.040	7.469	± 0.092	± 0.078	7.571	± 0.095	± 0.069	7.402	± 0.080	± 0.079
0.040 - 0.050	5.501	± 0.081	± 0.066	5.311	± 0.076	± 0.057	5.273	± 0.072	± 0.055
0.050 - 0.060	4.019	± 0.062	± 0.058	4.049	± 0.067	± 0.049	4.157	± 0.066	± 0.048
0.060 - 0.070	3.180	± 0.059	± 0.053	3.323	± 0.058	± 0.045	3.154	± 0.060	± 0.035
0.070 - 0.080	2.607	± 0.054	± 0.048	2.545	± 0.049	± 0.040	2.659	± 0.055	± 0.031
0.080 - 0.090	2.116	± 0.041	± 0.041	2.181	± 0.045	± 0.033	2.067	± 0.052	± 0.027
0.090 - 0.100	1.805	± 0.049	± 0.034	1.782	± 0.041	± 0.027	1.814	± 0.047	± 0.022
0.100 - 0.110	1.564	± 0.046	± 0.029	1.404	± 0.039	± 0.019	1.418	± 0.039	± 0.016
0.110 - 0.120	1.227	± 0.040	± 0.025	1.308	± 0.037	± 0.016	1.247	± 0.033	± 0.013
0.120 - 0.140	0.9518	± 0.0238	± 0.0237	0.9890	± 0.0234	± 0.0149	0.9617	± 0.0220	± 0.0123
0.140 - 0.160	0.7157	± 0.0193	± 0.0149	0.7017	± 0.0196	± 0.0128	0.6840	± 0.0185	± 0.0114
0.160 - 0.180	0.4932	± 0.0158	± 0.0122	0.5078	± 0.0164	± 0.0102	0.4994	± 0.0165	± 0.0096
0.180 - 0.200	0.3673	± 0.0136	± 0.0093	0.3406	± 0.0129	± 0.0079	0.3554	± 0.0127	± 0.0067
0.200 - 0.250	0.1622	± 0.0059	± 0.0049	0.1614	± 0.0054	± 0.0058	0.1473	± 0.0055	± 0.0039
0.250 - 0.300	0.0239	± 0.0023	± 0.0016	0.0216	± 0.0019	± 0.0018	0.0246	± 0.0020	± 0.0015
0.300 - 0.350	0.00005	± 0.00005	± 0.00007	0.00000	± 0.00000	± 0.00003	0.00000	± 0.00000	± 0.00002

Table B.14.a: Differential 2-Jet Rate P Scheme D_2^P

Differential 2-Jet Rate P Scheme D_2^P									
y_{23}	$0.36 < \cos\vartheta_T \leq 0.48$			$0.48 < \cos\vartheta_T \leq 0.60$			$0.60 < \cos\vartheta_T \leq 0.72$		
0.000 - 0.005	34.59	± 0.23	± 0.70	34.66	± 0.21	± 0.68	34.84	± 0.21	± 0.74
0.005 - 0.010	32.95	± 0.22	± 0.46	33.54	± 0.23	± 0.44	33.38	± 0.25	± 0.50
0.010 - 0.015	23.03	± 0.20	± 0.25	23.01	± 0.21	± 0.39	23.83	± 0.18	± 0.21
0.015 - 0.020	16.64	± 0.18	± 0.23	16.93	± 0.18	± 0.32	16.83	± 0.16	± 0.17
0.020 - 0.025	12.71	± 0.16	± 0.20	12.48	± 0.15	± 0.08	12.42	± 0.14	± 0.13
0.025 - 0.030	10.02	± 0.13	± 0.11	9.930	± 0.134	± 0.057	10.01	± 0.12	± 0.10
0.030 - 0.040	7.404	± 0.083	± 0.056	7.365	± 0.083	± 0.046	7.580	± 0.081	± 0.091
0.040 - 0.050	5.370	± 0.071	± 0.045	5.277	± 0.069	± 0.037	5.392	± 0.069	± 0.062
0.050 - 0.060	4.196	± 0.062	± 0.041	4.169	± 0.062	± 0.032	4.058	± 0.057	± 0.050
0.060 - 0.070	3.198	± 0.056	± 0.039	3.242	± 0.058	± 0.026	3.189	± 0.052	± 0.042
0.070 - 0.080	2.648	± 0.047	± 0.036	2.538	± 0.053	± 0.023	2.509	± 0.049	± 0.035
0.080 - 0.090	2.164	± 0.045	± 0.032	2.128	± 0.048	± 0.021	2.059	± 0.046	± 0.027
0.090 - 0.100	1.721	± 0.043	± 0.027	1.807	± 0.042	± 0.019	1.764	± 0.043	± 0.021
0.100 - 0.110	1.488	± 0.038	± 0.025	1.458	± 0.038	± 0.018	1.419	± 0.037	± 0.018
0.110 - 0.120	1.202	± 0.035	± 0.023	1.167	± 0.034	± 0.016	1.171	± 0.031	± 0.016
0.120 - 0.140	0.9610	± 0.0223	± 0.0214	0.9324	± 0.0207	± 0.0145	0.9355	± 0.0199	± 0.0150
0.140 - 0.160	0.6842	± 0.0209	± 0.0155	0.6937	± 0.0183	± 0.0117	0.6361	± 0.0172	± 0.0123
0.160 - 0.180	0.4628	± 0.0152	± 0.0106	0.4575	± 0.0164	± 0.0097	0.4480	± 0.0154	± 0.0109
0.180 - 0.200	0.3126	± 0.0122	± 0.0077	0.3219	± 0.0117	± 0.0085	0.3332	± 0.0131	± 0.0093
0.200 - 0.250	0.1482	± 0.0052	± 0.0042	0.1388	± 0.0049	± 0.0027	0.1453	± 0.0044	± 0.0053
0.250 - 0.300	0.0207	± 0.0017	± 0.0009	0.0208	± 0.0020	± 0.0011	0.0186	± 0.0015	± 0.0018
0.300 - 0.350	0.00003	± 0.00003	± 0.00010	0.00002	± 0.00002	± 0.00009	0.00000	± 0.00000	± 0.00007

Table B.14.b: Differential 2-Jet Rate P Scheme D_2^P

Differential 2-Jet Rate P Scheme D_2^P									
y_{23}	$0.72 < \cos\vartheta_T \leq 0.84$			$0.84 < \cos\vartheta_T \leq 0.96$			$0. < \cos\vartheta_T \leq 1.$		
0.000 - 0.005	35.58	± 0.19	± 0.72	37.15	± 0.23	± 0.97	35.13	± 0.087	± 0.66
0.005 - 0.010	33.61	± 0.20	± 0.43	32.64	± 0.22	± 0.45	33.21	± 0.082	± 0.45
0.010 - 0.015	23.08	± 0.17	± 0.27	22.92	± 0.18	± 0.39	23.08	± 0.074	± 0.29
0.015 - 0.020	16.68	± 0.15	± 0.21	16.83	± 0.16	± 0.23	16.73	± 0.061	± 0.22
0.020 - 0.025	12.67	± 0.13	± 0.18	12.39	± 0.14	± 0.15	12.50	± 0.058	± 0.12
0.025 - 0.030	9.916	± 0.108	± 0.159	9.928	± 0.11	± 0.12	9.979	± 0.055	± 0.094
0.030 - 0.040	7.423	± 0.078	± 0.070	7.344	± 0.079	± 0.082	7.445	± 0.029	± 0.058
0.040 - 0.050	5.475	± 0.068	± 0.049	5.334	± 0.066	± 0.054	5.363	± 0.023	± 0.041
0.050 - 0.060	4.071	± 0.055	± 0.039	4.126	± 0.057	± 0.052	4.104	± 0.021	± 0.031
0.060 - 0.070	3.226	± 0.049	± 0.035	3.152	± 0.053	± 0.049	3.202	± 0.019	± 0.026
0.070 - 0.080	2.614	± 0.046	± 0.031	2.480	± 0.044	± 0.043	2.563	± 0.017	± 0.023
0.080 - 0.090	2.033	± 0.041	± 0.027	2.043	± 0.040	± 0.032	2.084	± 0.016	± 0.017
0.090 - 0.100	1.668	± 0.037	± 0.024	1.747	± 0.037	± 0.027	1.746	± 0.014	± 0.015
0.100 - 0.110	1.386	± 0.035	± 0.021	1.440	± 0.034	± 0.024	1.434	± 0.012	± 0.014
0.110 - 0.120	1.200	± 0.033	± 0.018	1.152	± 0.031	± 0.019	1.195	± 0.011	± 0.013
0.120 - 0.140	0.8925	± 0.0201	± 0.0151	0.9003	± 0.0179	± 0.0171	0.9306	± 0.0074	± 0.012
0.140 - 0.160	0.5913	± 0.0151	± 0.0135	0.6327	± 0.0153	± 0.0152	0.6555	± 0.0060	± 0.0113
0.160 - 0.180	0.4165	± 0.0127	± 0.0097	0.4267	± 0.0132	± 0.0121	0.4544	± 0.0056	± 0.0087
0.180 - 0.200	0.3075	± 0.0078	± 0.0078	0.2889	± 0.0102	± 0.0099	0.3216	± 0.0043	± 0.0064
0.200 - 0.250	0.1215	± 0.0037	± 0.0033	0.1331	± 0.0040	± 0.0042	0.1408	± 0.0017	± 0.0038
0.250 - 0.300	0.0194	± 0.0016	± 0.0011	0.0139	± 0.0011	± 0.0011	0.01920	± 0.00058	± 0.00098
0.300 - 0.350	0.00001	± 0.00001	± 0.00004	0.00002	± 0.00002	± 0.00005	0.00011	± 0.00004	± 0.00012

Table B.14.c: Differential 2-Jet Rate P Scheme D_2^P

Differential 2-Jet Rate Jade Algorithm D_2^{Jad}									
y_{23}	$0.0 < \cos\vartheta_T \leq 0.12$			$0.12 < \cos\vartheta_T \leq 0.24$			$0.24 < \cos\vartheta_T \leq 0.36$		
0.000 - 0.005	25.041	± 0.202	± 0.532	25.038	± 0.179	± 0.636	25.267	± 0.185	± 0.610
0.005 - 0.010	26.901	± 0.239	± 0.433	26.883	± 0.215	± 0.382	27.288	± 0.220	± 0.470
0.010 - 0.015	20.539	± 0.204	± 0.195	20.456	± 0.183	± 0.272	20.316	± 0.192	± 0.201
0.015 - 0.020	16.128	± 0.183	± 0.143	16.440	± 0.168	± 0.233	16.054	± 0.167	± 0.157
0.020 - 0.025	12.933	± 0.172	± 0.138	12.722	± 0.159	± 0.132	12.978	± 0.166	± 0.147
0.025 - 0.030	10.565	± 0.143	± 0.125	10.555	± 0.151	± 0.111	10.601	± 0.143	± 0.097
0.030 - 0.040	8.148	± 0.109	± 0.105	8.314	± 0.105	± 0.093	8.287	± 0.096	± 0.091
0.040 - 0.050	6.110	± 0.087	± 0.085	5.989	± 0.078	± 0.062	6.031	± 0.083	± 0.083
0.050 - 0.060	4.787	± 0.075	± 0.072	4.760	± 0.071	± 0.059	4.654	± 0.077	± 0.069
0.060 - 0.070	3.791	± 0.068	± 0.059	3.738	± 0.068	± 0.055	3.830	± 0.065	± 0.058
0.070 - 0.080	3.106	± 0.058	± 0.047	3.085	± 0.055	± 0.046	2.960	± 0.054	± 0.046
0.080 - 0.090	2.523	± 0.050	± 0.034	2.622	± 0.049	± 0.038	2.676	± 0.050	± 0.042
0.090 - 0.100	2.210	± 0.048	± 0.023	2.237	± 0.046	± 0.029	2.147	± 0.047	± 0.037
0.100 - 0.110	1.909	± 0.046	± 0.021	1.821	± 0.042	± 0.021	1.910	± 0.045	± 0.028
0.110 - 0.120	1.571	± 0.039	± 0.018	1.594	± 0.039	± 0.018	1.593	± 0.039	± 0.023
0.120 - 0.140	1.273	± 0.028	± 0.016	1.275	± 0.028	± 0.014	1.238	± 0.032	± 0.019
0.140 - 0.160	0.994	± 0.025	± 0.014	0.991	± 0.024	± 0.011	0.989	± 0.028	± 0.016
0.160 - 0.180	0.759	± 0.019	± 0.011	0.770	± 0.019	± 0.010	0.737	± 0.025	± 0.011
0.180 - 0.200	0.545	± 0.016	± 0.009	0.566	± 0.017	± 0.009	0.598	± 0.018	± 0.010
0.200 - 0.250	0.3653	± 0.0081	± 0.0057	0.3587	± 0.0081	± 0.0078	0.3487	± 0.0079	± 0.0083
0.250 - 0.300	0.1452	± 0.0053	± 0.0029	0.1469	± 0.0056	± 0.0047	0.1366	± 0.0055	± 0.0033
0.300 - 0.350	0.0200	± 0.0029	± 0.0012	0.0140	± 0.0018	± 0.0007	0.0197	± 0.0023	± 0.0013

Table B.15.a: Differential 2-Jet Rate Jade Algorithm D_2^{Jad}

Differential 2-Jet Rate Jade Algorithm D_2^{Jad}									
y_{23}	$0.36 < \cos\vartheta_T \leq 0.48$			$0.48 < \cos\vartheta_T \leq 0.60$			$0.60 < \cos\vartheta_T \leq 0.72$		
0.000 - 0.005	25.281	± 0.186	± 0.645	25.426	± 0.167	± 0.642	25.552	± 0.160	± 0.670
0.005 - 0.010	27.223	± 0.181	± 0.443	27.440	± 0.180	± 0.438	27.359	± 0.177	± 0.452
0.010 - 0.015	20.336	± 0.177	± 0.194	20.719	± 0.168	± 0.274	20.561	± 0.160	± 0.196
0.015 - 0.020	16.308	± 0.159	± 0.177	16.163	± 0.156	± 0.190	16.583	± 0.148	± 0.170
0.020 - 0.025	12.861	± 0.149	± 0.165	12.930	± 0.152	± 0.098	13.172	± 0.134	± 0.154
0.025 - 0.030	10.931	± 0.136	± 0.122	10.683	± 0.143	± 0.091	10.343	± 0.115	± 0.083
0.030 - 0.040	8.274	± 0.091	± 0.108	8.190	± 0.080	± 0.078	8.261	± 0.089	± 0.072
0.040 - 0.050	5.928	± 0.075	± 0.069	6.001	± 0.066	± 0.064	6.133	± 0.074	± 0.068
0.050 - 0.060	4.700	± 0.068	± 0.048	4.694	± 0.062	± 0.049	4.793	± 0.069	± 0.062
0.060 - 0.070	3.901	± 0.064	± 0.043	3.860	± 0.058	± 0.046	3.753	± 0.058	± 0.055
0.070 - 0.080	3.068	± 0.055	± 0.035	3.153	± 0.053	± 0.040	3.074	± 0.047	± 0.035
0.080 - 0.090	2.602	± 0.052	± 0.031	2.466	± 0.049	± 0.035	2.494	± 0.043	± 0.027
0.090 - 0.100	2.227	± 0.047	± 0.029	2.171	± 0.047	± 0.031	2.113	± 0.041	± 0.025
0.100 - 0.110	1.812	± 0.042	± 0.026	1.892	± 0.045	± 0.028	1.838	± 0.039	± 0.023
0.110 - 0.120	1.565	± 0.039	± 0.019	1.515	± 0.039	± 0.025	1.517	± 0.037	± 0.021
0.120 - 0.140	1.267	± 0.027	± 0.017	1.262	± 0.025	± 0.022	1.245	± 0.025	± 0.018
0.140 - 0.160	0.971	± 0.024	± 0.015	0.928	± 0.023	± 0.020	0.955	± 0.020	± 0.016
0.160 - 0.180	0.699	± 0.022	± 0.014	0.717	± 0.018	± 0.017	0.685	± 0.018	± 0.014
0.180 - 0.200	0.586	± 0.017	± 0.012	0.573	± 0.016	± 0.014	0.541	± 0.016	± 0.012
0.200 - 0.250	0.3394	± 0.0078	± 0.0091	0.3320	± 0.0091	± 0.0090	0.3284	± 0.0071	± 0.0095
0.250 - 0.300	0.1288	± 0.0056	± 0.0060	0.1279	± 0.0052	± 0.0047	0.1347	± 0.0058	± 0.0064
0.300 - 0.350	0.0150	± 0.0019	± 0.0010	0.0149	± 0.0018	± 0.0014	0.0129	± 0.0015	± 0.0006

Table B.15.b: Differential 2-Jet Rate Jade Algorithm D_2^{Jad}

Differential 2-Jet Rate Jade Algorithm D_2^{Jad}									
y_{23}	$0.72 < \cos\vartheta_T \leq 0.84$			$0.84 < \cos\vartheta_T \leq 0.96$			$0. < \cos\vartheta_T \leq 1.$		
0.000 - 0.005	26.088	± 0.161	± 0.655	27.460	± 0.177	± 0.882	25.268	± 0.066	± 0.624
0.005 - 0.010	27.609	± 0.179	± 0.454	27.048	± 0.187	± 0.368	27.173	± 0.070	± 0.439
0.010 - 0.015	20.789	± 0.156	± 0.247	20.302	± 0.165	± 0.293	20.591	± 0.065	± 0.207
0.015 - 0.020	16.184	± 0.139	± 0.144	16.172	± 0.147	± 0.225	16.298	± 0.063	± 0.189
0.020 - 0.025	13.028	± 0.145	± 0.123	12.908	± 0.127	± 0.178	13.010	± 0.060	± 0.153
0.025 - 0.030	10.619	± 0.118	± 0.116	10.529	± 0.118	± 0.090	10.648	± 0.053	± 0.090
0.030 - 0.040	8.203	± 0.077	± 0.069	8.153	± 0.073	± 0.079	8.285	± 0.034	± 0.085
0.040 - 0.050	6.103	± 0.061	± 0.061	6.025	± 0.064	± 0.065	6.106	± 0.029	± 0.062
0.050 - 0.060	4.762	± 0.058	± 0.059	4.745	± 0.058	± 0.059	4.739	± 0.027	± 0.053
0.060 - 0.070	3.811	± 0.054	± 0.057	3.823	± 0.055	± 0.053	3.810	± 0.024	± 0.039
0.070 - 0.080	3.014	± 0.045	± 0.047	2.913	± 0.047	± 0.042	3.091	± 0.021	± 0.033
0.080 - 0.090	2.620	± 0.041	± 0.043	2.563	± 0.044	± 0.040	2.564	± 0.018	± 0.026
0.090 - 0.100	2.093	± 0.036	± 0.037	2.137	± 0.042	± 0.026	2.186	± 0.017	± 0.023
0.100 - 0.110	1.735	± 0.032	± 0.031	1.800	± 0.036	± 0.023	1.838	± 0.015	± 0.019
0.110 - 0.120	1.574	± 0.032	± 0.028	1.525	± 0.033	± 0.021	1.564	± 0.013	± 0.017
0.120 - 0.140	1.270	± 0.020	± 0.024	1.199	± 0.023	± 0.019	1.247	± 0.010	± 0.015
0.140 - 0.160	0.876	± 0.018	± 0.017	0.912	± 0.019	± 0.015	0.943	± 0.009	± 0.012
0.160 - 0.180	0.643	± 0.015	± 0.014	0.700	± 0.015	± 0.013	0.7105	± 0.0070	± 0.0097
0.180 - 0.200	0.496	± 0.012	± 0.012	0.499	± 0.012	± 0.011	0.5474	± 0.0063	± 0.0089
0.200 - 0.250	0.3199	± 0.0070	± 0.0093	0.3064	± 0.0062	± 0.0087	0.3295	± 0.0027	± 0.0069
0.250 - 0.300	0.1131	± 0.0040	± 0.0035	0.1236	± 0.0044	± 0.0038	0.1279	± 0.0018	± 0.0031
0.300 - 0.350	0.0106	± 0.0014	± 0.0006	0.0096	± 0.0012	± 0.0004	0.01482	± 0.00069	± 0.00060

Table B.15.c: Differential 2-Jet Rate Jade Algorithm D_2^{Jad}

Differential 2-Jet Rate Durham Algorithm D_2^{Dur}									
y_{23}	$0.0 < \cos\vartheta_T \leq 0.12$			$0.12 < \cos\vartheta_T \leq 0.24$			$0.24 < \cos\vartheta_T \leq 0.36$		
0.000 - 0.005	95.620	± 0.374	± 0.667	95.693	± 0.354	± 0.552	96.188	± 0.363	± 0.570
0.005 - 0.010	29.162	± 0.235	± 0.126	29.357	± 0.218	± 0.131	29.123	± 0.217	± 0.092
0.010 - 0.015	15.164	± 0.179	± 0.073	15.008	± 0.163	± 0.101	14.928	± 0.162	± 0.073
0.015 - 0.020	9.539	± 0.139	± 0.053	9.618	± 0.130	± 0.090	9.696	± 0.132	± 0.071
0.020 - 0.025	7.200	± 0.115	± 0.046	7.089	± 0.107	± 0.057	7.125	± 0.116	± 0.066
0.025 - 0.030	5.533	± 0.109	± 0.042	5.302	± 0.098	± 0.046	5.527	± 0.106	± 0.049
0.030 - 0.040	4.045	± 0.066	± 0.032	3.980	± 0.056	± 0.034	3.973	± 0.057	± 0.027
0.040 - 0.050	2.856	± 0.051	± 0.028	2.779	± 0.051	± 0.025	2.734	± 0.049	± 0.023
0.050 - 0.060	2.069	± 0.046	± 0.026	2.152	± 0.045	± 0.022	2.136	± 0.046	± 0.020
0.060 - 0.070	1.693	± 0.043	± 0.024	1.722	± 0.041	± 0.020	1.714	± 0.040	± 0.018
0.070 - 0.080	1.334	± 0.036	± 0.022	1.361	± 0.035	± 0.018	1.284	± 0.035	± 0.017
0.080 - 0.090	1.105	± 0.035	± 0.019	1.101	± 0.033	± 0.017	1.076	± 0.032	± 0.015
0.090 - 0.100	0.933	± 0.029	± 0.017	0.955	± 0.030	± 0.016	0.910	± 0.029	± 0.014
0.100 - 0.110	0.758	± 0.026	± 0.015	0.773	± 0.028	± 0.013	0.749	± 0.026	± 0.013
0.110 - 0.120	0.629	± 0.023	± 0.010	0.648	± 0.025	± 0.011	0.634	± 0.022	± 0.012
0.120 - 0.140	0.510	± 0.016	± 0.009	0.523	± 0.016	± 0.009	0.510	± 0.015	± 0.010
0.140 - 0.160	0.398	± 0.014	± 0.008	0.372	± 0.013	± 0.008	0.360	± 0.013	± 0.009
0.160 - 0.180	0.280	± 0.012	± 0.007	0.284	± 0.012	± 0.006	0.295	± 0.012	± 0.007
0.180 - 0.200	0.217	± 0.011	± 0.006	0.202	± 0.010	± 0.005	0.207	± 0.010	± 0.005
0.200 - 0.250	0.1169	± 0.0054	± 0.0027	0.1143	± 0.0053	± 0.0037	0.1121	± 0.0046	± 0.0034
0.250 - 0.300	0.0275	± 0.0026	± 0.0023	0.0285	± 0.0027	± 0.0013	0.0262	± 0.0023	± 0.0011
0.300 - 0.350	0.00032	± 0.00018	± 0.00016	0.00051	± 0.00023	± 0.00032	0.00010	± 0.00008	± 0.00064

Table B.16.a: Differential 2-Jet Rate Durham Algorithm D_2^{Dur}

Differential 2-Jet Rate Durham Algorithm D_2^{Dur}									
y_{23}	$0.36 < \cos\vartheta_T \leq 0.48$			$0.48 < \cos\vartheta_T \leq 0.60$			$0.60 < \cos\vartheta_T \leq 0.72$		
0.000 - 0.005	96.619	± 0.342	± 0.565	96.976	± 0.329	± 0.617	97.122	± 0.310	± 0.650
0.005 - 0.010	29.141	± 0.205	± 0.176	29.227	± 0.209	± 0.093	29.688	± 0.199	± 0.120
0.010 - 0.015	15.061	± 0.159	± 0.066	14.740	± 0.153	± 0.088	14.919	± 0.146	± 0.063
0.015 - 0.020	9.779	± 0.126	± 0.046	9.724	± 0.116	± 0.077	9.811	± 0.124	± 0.058
0.020 - 0.025	7.002	± 0.112	± 0.038	7.093	± 0.100	± 0.053	6.972	± 0.097	± 0.049
0.025 - 0.030	5.422	± 0.098	± 0.036	5.377	± 0.088	± 0.036	5.331	± 0.082	± 0.041
0.030 - 0.040	3.945	± 0.058	± 0.032	3.895	± 0.056	± 0.030	3.950	± 0.057	± 0.035
0.040 - 0.050	2.776	± 0.048	± 0.025	2.839	± 0.046	± 0.026	2.719	± 0.043	± 0.029
0.050 - 0.060	2.052	± 0.045	± 0.023	2.147	± 0.041	± 0.021	2.054	± 0.038	± 0.026
0.060 - 0.070	1.689	± 0.037	± 0.021	1.669	± 0.037	± 0.020	1.528	± 0.034	± 0.024
0.070 - 0.080	1.251	± 0.034	± 0.019	1.310	± 0.032	± 0.019	1.251	± 0.032	± 0.023
0.080 - 0.090	1.025	± 0.032	± 0.018	1.066	± 0.030	± 0.017	1.056	± 0.030	± 0.021
0.090 - 0.100	0.899	± 0.029	± 0.017	0.871	± 0.028	± 0.015	0.892	± 0.025	± 0.020
0.100 - 0.110	0.771	± 0.027	± 0.016	0.729	± 0.026	± 0.014	0.680	± 0.023	± 0.018
0.110 - 0.120	0.652	± 0.025	± 0.015	0.582	± 0.022	± 0.013	0.612	± 0.022	± 0.014
0.120 - 0.140	0.514	± 0.016	± 0.013	0.503	± 0.015	± 0.012	0.471	± 0.014	± 0.013
0.140 - 0.160	0.369	± 0.014	± 0.011	0.346	± 0.012	± 0.010	0.357	± 0.012	± 0.012
0.160 - 0.180	0.298	± 0.012	± 0.010	0.264	± 0.011	± 0.009	0.261	± 0.011	± 0.011
0.180 - 0.200	0.188	± 0.010	± 0.006	0.182	± 0.010	± 0.008	0.197	± 0.010	± 0.009
0.200 - 0.250	0.0948	± 0.0045	± 0.0058	0.10320	± 0.0043	± 0.0049	0.1056	± 0.0046	± 0.0055
0.250 - 0.300	0.0256	± 0.0025	± 0.0015	0.02305	± 0.0022	± 0.0015	0.0235	± 0.0021	± 0.0017
0.300 - 0.350	0.00043	± 0.00021	± 0.00039	0.0001	± 0.0001	± 0.0006	0.00010	± 0.00007	± 0.00011

Table B.16.b: Differential 2-Jet Rate Durham Algorithm D_2^{Dur}

Differential 2-Jet Rate Durham Algorithm D_2^{Dur}									
y_{23}	$0.72 < \cos\vartheta_T \leq 0.84$			$0.84 < \cos\vartheta_T \leq 0.96$			$0. < \cos\vartheta_T \leq 1.$		
0.000 - 0.005	97.718	± 0.292	± 0.679	98.223	± 0.301	± 0.937	96.947	± 0.139	± 0.660
0.005 - 0.010	29.759	± 0.179	± 0.215	29.467	± 0.174	± 0.313	29.417	± 0.086	± 0.154
0.010 - 0.015	15.058	± 0.126	± 0.098	14.813	± 0.132	± 0.152	14.978	± 0.061	± 0.062
0.015 - 0.020	9.721	± 0.106	± 0.086	9.807	± 0.114	± 0.115	9.704	± 0.051	± 0.055
0.020 - 0.025	7.119	± 0.090	± 0.065	6.797	± 0.099	± 0.076	7.077	± 0.042	± 0.040
0.025 - 0.030	5.330	± 0.085	± 0.053	5.500	± 0.084	± 0.070	5.370	± 0.036	± 0.032
0.030 - 0.040	3.946	± 0.049	± 0.045	3.884	± 0.050	± 0.049	3.960	± 0.025	± 0.027
0.040 - 0.050	2.669	± 0.044	± 0.041	2.746	± 0.041	± 0.033	2.743	± 0.018	± 0.025
0.050 - 0.060	2.032	± 0.039	± 0.032	2.020	± 0.034	± 0.030	2.065	± 0.017	± 0.019
0.060 - 0.070	1.572	± 0.036	± 0.029	1.599	± 0.031	± 0.028	1.639	± 0.015	± 0.017
0.070 - 0.080	1.251	± 0.030	± 0.026	1.215	± 0.029	± 0.025	1.280	± 0.014	± 0.016
0.080 - 0.090	1.007	± 0.028	± 0.023	1.036	± 0.027	± 0.021	1.044	± 0.013	± 0.014
0.090 - 0.100	0.835	± 0.026	± 0.019	0.786	± 0.024	± 0.017	0.878	± 0.011	± 0.013
0.100 - 0.110	0.693	± 0.023	± 0.017	0.668	± 0.023	± 0.014	0.714	± 0.010	± 0.012
0.110 - 0.120	0.604	± 0.020	± 0.015	0.622	± 0.021	± 0.012	0.607	± 0.009	± 0.011
0.120 - 0.140	0.448	± 0.014	± 0.011	0.489	± 0.013	± 0.009	0.485	± 0.006	± 0.010
0.140 - 0.160	0.317	± 0.010	± 0.009	0.330	± 0.010	± 0.007	0.3537	± 0.0050	± 0.0090
0.160 - 0.180	0.2285	± 0.0094	± 0.0071	0.2233	± 0.0087	± 0.0062	0.2653	± 0.0044	± 0.0063
0.180 - 0.200	0.1651	± 0.0079	± 0.0059	0.1633	± 0.0074	± 0.0079	0.1871	± 0.0037	± 0.0055
0.200 - 0.250	0.0918	± 0.0036	± 0.0038	0.0878	± 0.0034	± 0.0033	0.1004	± 0.0019	± 0.0037
0.250 - 0.300	0.0220	± 0.0025	± 0.0019	0.0247	± 0.0019	± 0.0014	0.0242	± 0.0009	± 0.0011
0.300 - 0.350	0.00025	± 0.00013	± 0.00044	0.00006	± 0.00005	± 0.00005	0.00101	± 0.00020	± 0.00011

Table B.16.c: Differential 2-Jet Rate Durham Algorithm D_2^{Dur}

Differential 2-Jet Rate Geneva Algorithm D_2^{Gen}									
y_{23}	$0.0 < \cos\vartheta_T \leq 0.12$			$0.12 < \cos\vartheta_T \leq 0.24$			$0.24 < \cos\vartheta_T \leq 0.36$		
0.000 - 0.005	4.52	± 0.08	± 0.21	4.60	± 0.08	± 0.24	4.53	± 0.08	± 0.23
0.005 - 0.010	20.66	± 0.22	± 0.52	20.84	± 0.20	± 0.44	20.92	± 0.19	± 0.30
0.010 - 0.015	24.56	± 0.24	± 0.39	25.26	± 0.24	± 0.56	25.27	± 0.22	± 0.41
0.015 - 0.020	21.58	± 0.22	± 0.19	21.52	± 0.22	± 0.20	21.30	± 0.20	± 0.17
0.020 - 0.025	16.61	± 0.20	± 0.16	16.41	± 0.20	± 0.16	16.54	± 0.19	± 0.13
0.025 - 0.030	13.17	± 0.18	± 0.14	13.01	± 0.17	± 0.13	13.11	± 0.15	± 0.11
0.030 - 0.040	9.191	± 0.101	± 0.061	9.257	± 0.098	± 0.081	9.323	± 0.095	± 0.072
0.040 - 0.050	6.351	± 0.079	± 0.037	6.307	± 0.081	± 0.052	6.297	± 0.078	± 0.061
0.050 - 0.060	4.694	± 0.069	± 0.034	4.696	± 0.077	± 0.045	4.688	± 0.066	± 0.050
0.060 - 0.070	3.722	± 0.067	± 0.033	3.747	± 0.059	± 0.039	3.636	± 0.064	± 0.040
0.070 - 0.080	3.051	± 0.063	± 0.030	3.010	± 0.054	± 0.032	3.135	± 0.060	± 0.022
0.080 - 0.090	2.691	± 0.055	± 0.027	2.606	± 0.052	± 0.028	2.524	± 0.049	± 0.019
0.090 - 0.100	2.169	± 0.050	± 0.024	2.213	± 0.048	± 0.022	2.219	± 0.046	± 0.017
0.100 - 0.110	1.897	± 0.046	± 0.021	1.939	± 0.045	± 0.019	1.954	± 0.041	± 0.016
0.110 - 0.120	1.758	± 0.042	± 0.019	1.857	± 0.040	± 0.018	1.644	± 0.038	± 0.015
0.120 - 0.140	1.469	± 0.028	± 0.017	1.490	± 0.028	± 0.015	1.409	± 0.027	± 0.013
0.140 - 0.160	1.229	± 0.025	± 0.014	1.203	± 0.026	± 0.012	1.225	± 0.025	± 0.011
0.160 - 0.180	1.001	± 0.021	± 0.012	0.990	± 0.021	± 0.011	1.031	± 0.023	± 0.009
0.180 - 0.200	0.814	± 0.019	± 0.011	0.808	± 0.018	± 0.010	0.793	± 0.021	± 0.008
0.200 - 0.250	0.596	± 0.011	± 0.010	0.594	± 0.013	± 0.008	0.591	± 0.011	± 0.007
0.250 - 0.300	0.2818	± 0.0073	± 0.0068	0.2863	± 0.0072	± 0.0073	0.2728	± 0.0076	± 0.0059
0.300 - 0.350	0.0348	± 0.0029	± 0.0018	0.0374	± 0.0029	± 0.0014	0.0417	± 0.0038	± 0.0029

Table B.17.a: Differential 2-Jet Rate Geneva Algorithm D_2^{Gen}

Differential 2-Jet Rate Geneva Algorithm D_2^{Gen}									
y_{23}	$0.36 < \cos\vartheta_T \leq 0.48$			$0.48 < \cos\vartheta_T \leq 0.60$			$0.60 < \cos\vartheta_T \leq 0.72$		
0.000 - 0.005	4.68	± 0.07	± 0.24	4.63	± 0.08	± 0.24	4.73	± 0.07	± 0.20
0.005 - 0.010	20.65	± 0.22	± 0.34	21.10	± 0.20	± 0.33	21.04	± 0.19	± 0.28
0.010 - 0.015	25.29	± 0.20	± 0.40	25.55	± 0.20	± 0.42	25.65	± 0.21	± 0.35
0.015 - 0.020	21.41	± 0.19	± 0.22	21.44	± 0.18	± 0.17	21.68	± 0.16	± 0.17
0.020 - 0.025	16.74	± 0.17	± 0.14	16.75	± 0.17	± 0.12	16.79	± 0.15	± 0.11
0.025 - 0.030	12.93	± 0.16	± 0.12	13.04	± 0.15	± 0.10	13.00	± 0.13	± 0.10
0.030 - 0.040	9.285	± 0.091	± 0.057	9.361	± 0.088	± 0.055	9.196	± 0.085	± 0.053
0.040 - 0.050	6.447	± 0.080	± 0.046	6.229	± 0.074	± 0.044	6.309	± 0.070	± 0.047
0.050 - 0.060	4.694	± 0.063	± 0.041	4.624	± 0.063	± 0.037	4.705	± 0.058	± 0.034
0.060 - 0.070	3.621	± 0.056	± 0.038	3.701	± 0.058	± 0.032	3.759	± 0.055	± 0.029
0.070 - 0.080	3.071	± 0.052	± 0.034	2.940	± 0.051	± 0.029	3.087	± 0.046	± 0.024
0.080 - 0.090	2.476	± 0.046	± 0.029	2.615	± 0.047	± 0.026	2.507	± 0.044	± 0.021
0.090 - 0.100	2.242	± 0.044	± 0.024	2.182	± 0.045	± 0.022	2.209	± 0.041	± 0.019
0.100 - 0.110	2.032	± 0.042	± 0.016	1.995	± 0.039	± 0.018	1.872	± 0.036	± 0.017
0.110 - 0.120	1.737	± 0.039	± 0.014	1.718	± 0.036	± 0.015	1.720	± 0.033	± 0.016
0.120 - 0.140	1.466	± 0.033	± 0.013	1.458	± 0.025	± 0.014	1.441	± 0.023	± 0.015
0.140 - 0.160	1.198	± 0.027	± 0.012	1.174	± 0.023	± 0.013	1.201	± 0.021	± 0.013
0.160 - 0.180	0.970	± 0.024	± 0.011	0.986	± 0.021	± 0.012	0.927	± 0.019	± 0.011
0.180 - 0.200	0.819	± 0.018	± 0.010	0.848	± 0.017	± 0.010	0.796	± 0.015	± 0.009
0.200 - 0.250	0.570	± 0.010	± 0.008	0.544	± 0.010	± 0.007	0.539	± 0.009	± 0.008
0.250 - 0.300	0.2613	± 0.0069	± 0.0087	0.249	± 0.0069	± 0.0077	0.2464	± 0.0065	± 0.0082
0.300 - 0.350	0.0321	± 0.0032	± 0.0023	0.028	± 0.0025	± 0.0023	0.0342	± 0.0031	± 0.0035

Table B.17.b: Differential 2-Jet Rate Geneva Algorithm D_2^{Gen}

Differential 2-Jet Rate Geneva Algorithm D_2^{Gen}									
y_{23}	$0.72 < \cos\vartheta_T \leq 0.84$			$0.84 < \cos\vartheta_T \leq 0.96$			$0. < \cos\vartheta_T \leq 1.$		
0.000 - 0.005	4.88	± 0.07	± 0.20	6.05	± 0.08	± 0.52	4.883	± 0.052	± 0.259
0.005 - 0.010	21.15	± 0.18	± 0.28	20.41	± 0.18	± 0.66	20.905	± 0.095	± 0.329
0.010 - 0.015	25.53	± 0.20	± 0.39	25.67	± 0.22	± 0.73	25.442	± 0.092	± 0.508
0.015 - 0.020	21.96	± 0.18	± 0.17	21.30	± 0.18	± 0.33	21.501	± 0.067	± 0.263
0.020 - 0.025	16.85	± 0.14	± 0.12	16.75	± 0.17	± 0.21	16.698	± 0.062	± 0.121
0.025 - 0.030	13.21	± 0.13	± 0.09	13.11	± 0.14	± 0.13	13.071	± 0.060	± 0.071
0.030 - 0.040	9.445	± 0.087	± 0.054	9.324	± 0.081	± 0.116	9.297	± 0.036	± 0.040
0.040 - 0.050	6.377	± 0.064	± 0.047	6.289	± 0.060	± 0.089	6.322	± 0.029	± 0.029
0.050 - 0.060	4.549	± 0.054	± 0.043	4.614	± 0.053	± 0.082	4.645	± 0.021	± 0.028
0.060 - 0.070	3.595	± 0.048	± 0.038	3.628	± 0.050	± 0.063	3.663	± 0.020	± 0.028
0.070 - 0.080	3.059	± 0.045	± 0.034	2.945	± 0.048	± 0.055	3.030	± 0.017	± 0.017
0.080 - 0.090	2.578	± 0.043	± 0.029	2.596	± 0.043	± 0.041	2.565	± 0.016	± 0.017
0.090 - 0.100	2.171	± 0.039	± 0.024	2.199	± 0.041	± 0.025	2.192	± 0.015	± 0.013
0.100 - 0.110	1.944	± 0.037	± 0.022	1.955	± 0.035	± 0.020	1.942	± 0.014	± 0.008
0.110 - 0.120	1.702	± 0.033	± 0.019	1.687	± 0.029	± 0.019	1.723	± 0.013	± 0.011
0.120 - 0.140	1.475	± 0.026	± 0.016	1.406	± 0.024	± 0.017	1.4460	± 0.0081	± 0.0071
0.140 - 0.160	1.160	± 0.019	± 0.014	1.160	± 0.021	± 0.016	1.1863	± 0.0074	± 0.0063
0.160 - 0.180	0.961	± 0.017	± 0.012	0.896	± 0.018	± 0.015	0.9581	± 0.0081	± 0.0071
0.180 - 0.200	0.722	± 0.015	± 0.010	0.756	± 0.015	± 0.013	0.7867	± 0.0064	± 0.0078
0.200 - 0.250	0.509	± 0.008	± 0.009	0.525	± 0.009	± 0.011	0.5504	± 0.0035	± 0.0078
0.250 - 0.300	0.2227	± 0.0055	± 0.0076	0.2281	± 0.0055	± 0.0099	0.2493	± 0.0022	± 0.0069
0.300 - 0.350	0.0243	± 0.0021	± 0.0019	0.0261	± 0.0024	± 0.0018	0.0301	± 0.0008	± 0.0014

Table B.17.c: Differential 2-Jet Rate Geneva Algorithm D_2^{Gen}

Differential 2-Jet Rate Cambridge Algorithm D_2^{Cam}									
y_{23}	$0.0 < \cos\vartheta_T \leq 0.12$			$0.12 < \cos\vartheta_T \leq 0.24$			$0.24 < \cos\vartheta_T \leq 0.36$		
0.000 - 0.001	235.3	± 1.6	± 2.9	235.9	± 1.6	± 2.6	236.4	± 1.6	± 2.4
0.001 - 0.002	145.4	± 1.4	± 1.8	144.9	± 1.3	± 1.2	146.8	± 1.3	± 1.0
0.002 - 0.003	88.25	± 1.10	± 0.49	89.96	± 1.07	± 0.84	90.34	± 0.98	± 0.74
0.003 - 0.004	53.64	± 0.85	± 0.45	51.89	± 0.79	± 0.75	52.07	± 0.75	± 0.31
0.004 - 0.005	39.58	± 0.76	± 0.43	38.72	± 0.68	± 0.71	37.80	± 0.72	± 0.29
0.005 - 0.006	30.81	± 0.67	± 0.31	30.34	± 0.61	± 0.65	30.23	± 0.60	± 0.27
0.006 - 0.007	26.68	± 0.58	± 0.28	26.94	± 0.58	± 0.63	26.94	± 0.57	± 0.26
0.007 - 0.008	20.61	± 0.57	± 0.27	20.74	± 0.56	± 0.58	20.42	± 0.51	± 0.25
0.008 - 0.009	18.24	± 0.56	± 0.25	17.68	± 0.54	± 0.53	18.58	± 0.47	± 0.24
0.009 - 0.010	16.12	± 0.55	± 0.24	16.51	± 0.52	± 0.47	16.51	± 0.46	± 0.24
0.010 - 0.011	16.01	± 0.54	± 0.23	15.45	± 0.50	± 0.43	15.98	± 0.45	± 0.23
0.011 - 0.012	12.19	± 0.52	± 0.22	13.15	± 0.48	± 0.40	12.19	± 0.45	± 0.22
0.012 - 0.013	12.02	± 0.47	± 0.20	12.03	± 0.45	± 0.25	11.22	± 0.43	± 0.16
0.013 - 0.014	10.87	± 0.44	± 0.17	11.14	± 0.43	± 0.22	11.06	± 0.42	± 0.14
0.014 - 0.015	10.56	± 0.41	± 0.14	10.39	± 0.37	± 0.16	10.84	± 0.41	± 0.12
0.015 - 0.016	8.807	± 0.334	± 0.108	9.046	± 0.328	± 0.112	9.398	± 0.401	± 0.105
0.016 - 0.018	8.168	± 0.236	± 0.095	8.195	± 0.231	± 0.074	8.086	± 0.272	± 0.089
0.018 - 0.020	7.240	± 0.186	± 0.084	7.378	± 0.168	± 0.053	7.447	± 0.233	± 0.081
0.020 - 0.025	6.181	± 0.125	± 0.064	5.868	± 0.129	± 0.045	6.140	± 0.141	± 0.075
0.025 - 0.030	4.716	± 0.102	± 0.057	4.561	± 0.101	± 0.038	4.474	± 0.109	± 0.063
0.030 - 0.040	3.554	± 0.067	± 0.055	3.540	± 0.075	± 0.034	3.521	± 0.073	± 0.052
0.040 - 0.050	2.503	± 0.052	± 0.052	2.392	± 0.061	± 0.029	2.408	± 0.057	± 0.040
0.050 - 0.060	1.793	± 0.047	± 0.048	1.911	± 0.055	± 0.027	1.846	± 0.047	± 0.030
0.060 - 0.070	1.475	± 0.044	± 0.042	1.575	± 0.045	± 0.025	1.527	± 0.043	± 0.026
0.070 - 0.080	1.213	± 0.042	± 0.031	1.227	± 0.040	± 0.024	1.172	± 0.039	± 0.023
0.080 - 0.090	1.023	± 0.038	± 0.024	0.9860	± 0.0388	± 0.0231	0.9985	± 0.0378	± 0.0203
0.090 - 0.100	0.8332	± 0.0341	± 0.0222	0.8906	± 0.0353	± 0.0213	0.8459	± 0.0353	± 0.0183
0.100 - 0.110	0.6835	± 0.0296	± 0.0201	0.7347	± 0.0307	± 0.0190	0.6747	± 0.0335	± 0.0151
0.110 - 0.120	0.5679	± 0.0270	± 0.0169	0.5592	± 0.0273	± 0.0165	0.5732	± 0.0255	± 0.0143
0.120 - 0.140	0.4666	± 0.0244	± 0.0128	0.4798	± 0.0194	± 0.0151	0.4484	± 0.0162	± 0.0125
0.140 - 0.160	0.3833	± 0.0189	± 0.0110	0.3629	± 0.0158	± 0.0131	0.3576	± 0.0142	± 0.0104
0.160 - 0.180	0.2548	± 0.0147	± 0.0093	0.2796	± 0.0141	± 0.0102	0.2839	± 0.0131	± 0.0088
0.180 - 0.200	0.2546	± 0.0130	± 0.0074	0.2303	± 0.0122	± 0.0061	0.2219	± 0.0115	± 0.0061
0.200 - 0.250	0.0949	± 0.0053	± 0.0038	0.0932	± 0.0051	± 0.0038	0.0967	± 0.0053	± 0.0050
0.250 - 0.300	0.0344	± 0.0030	± 0.0022	0.0331	± 0.0032	± 0.0022	0.0327	± 0.0044	± 0.0023
0.300 - 0.350	0.00109	± 0.00051	± 0.00055	0.00125	± 0.00052	± 0.00046	0.00090	± 0.00049	± 0.00016

Table B.18.a: Differential 2-Jet Rate Cambridge Algorithm D_2^{Cam}

Differential 2-Jet Rate Cambridge Algorithm D_2^{Cam}									
y_{23}	$0.36 < \cos\vartheta_T \leq 0.48$			$0.48 < \cos\vartheta_T \leq 0.60$			$0.60 < \cos\vartheta_T \leq 0.72$		
0.000 - 0.001	237.5	± 1.5	± 2.3	240.6	± 1.5	± 2.0	240.9	± 1.4	± 2.7
0.001 - 0.002	147.2	± 1.2	± 1.2	146.5	± 1.2	± 0.9	147.9	± 1.2	± 1.0
0.002 - 0.003	87.71	± 0.98	± 1.05	88.83	± 0.96	± 0.62	88.28	± 0.93	± 0.77
0.003 - 0.004	53.60	± 0.75	± 0.49	51.93	± 0.78	± 0.37	53.10	± 0.75	± 0.62
0.004 - 0.005	38.81	± 0.66	± 0.37	39.43	± 0.74	± 0.33	38.73	± 0.58	± 0.44
0.005 - 0.006	30.17	± 0.62	± 0.33	30.66	± 0.58	± 0.26	30.92	± 0.55	± 0.37
0.006 - 0.007	28.14	± 0.57	± 0.31	28.22	± 0.55	± 0.23	27.27	± 0.55	± 0.35
0.007 - 0.008	20.75	± 0.54	± 0.29	20.57	± 0.47	± 0.21	21.50	± 0.48	± 0.33
0.008 - 0.009	18.17	± 0.49	± 0.28	18.41	± 0.46	± 0.20	18.43	± 0.46	± 0.32
0.009 - 0.010	16.21	± 0.47	± 0.28	15.22	± 0.44	± 0.19	15.40	± 0.44	± 0.31
0.010 - 0.011	16.17	± 0.46	± 0.27	15.14	± 0.43	± 0.18	15.46	± 0.42	± 0.30
0.011 - 0.012	12.53	± 0.45	± 0.26	12.22	± 0.42	± 0.16	13.18	± 0.38	± 0.29
0.012 - 0.013	12.11	± 0.43	± 0.24	11.49	± 0.37	± 0.13	12.28	± 0.33	± 0.27
0.013 - 0.014	10.74	± 0.41	± 0.23	11.06	± 0.36	± 0.12	11.26	± 0.32	± 0.25
0.014 - 0.015	10.21	± 0.39	± 0.21	10.30	± 0.35	± 0.10	10.19	± 0.31	± 0.23
0.015 - 0.016	9.087	± 0.341	± 0.203	8.919	± 0.304	± 0.085	8.909	± 0.184	± 0.178
0.016 - 0.018	8.413	± 0.258	± 0.158	8.165	± 0.221	± 0.074	8.154	± 0.205	± 0.116
0.018 - 0.020	7.479	± 0.228	± 0.120	7.457	± 0.185	± 0.066	7.637	± 0.185	± 0.087
0.020 - 0.025	5.982	± 0.119	± 0.085	6.123	± 0.124	± 0.059	5.860	± 0.108	± 0.075
0.025 - 0.030	4.644	± 0.099	± 0.064	4.583	± 0.091	± 0.052	4.499	± 0.091	± 0.055
0.030 - 0.040	3.417	± 0.066	± 0.048	3.409	± 0.062	± 0.044	3.414	± 0.056	± 0.043
0.040 - 0.050	2.460	± 0.054	± 0.034	2.489	± 0.051	± 0.041	2.390	± 0.046	± 0.041
0.050 - 0.060	1.803	± 0.045	± 0.032	1.818	± 0.048	± 0.036	1.866	± 0.044	± 0.039
0.060 - 0.070	1.492	± 0.041	± 0.029	1.500	± 0.043	± 0.032	1.395	± 0.039	± 0.035
0.070 - 0.080	1.057	± 0.037	± 0.026	1.260	± 0.041	± 0.028	1.062	± 0.032	± 0.033
0.080 - 0.090	0.9302	± 0.0351	± 0.0247	0.9597	± 0.0363	± 0.0232	0.9315	± 0.0318	± 0.0310
0.090 - 0.100	0.8609	± 0.0337	± 0.0234	0.8166	± 0.0324	± 0.0204	0.8366	± 0.0304	± 0.0299
0.100 - 0.110	0.6649	± 0.0314	± 0.0223	0.6345	± 0.0303	± 0.0192	0.6381	± 0.0291	± 0.0279
0.110 - 0.120	0.6097	± 0.0296	± 0.0211	0.5375	± 0.0245	± 0.0187	0.5849	± 0.0274	± 0.0255
0.120 - 0.140	0.4815	± 0.0167	± 0.0169	0.4462	± 0.0175	± 0.0166	0.4221	± 0.0165	± 0.0225
0.140 - 0.160	0.3597	± 0.0154	± 0.0155	0.3524	± 0.0158	± 0.0156	0.3318	± 0.0137	± 0.0202
0.160 - 0.180	0.2637	± 0.0141	± 0.0137	0.2225	± 0.0126	± 0.0134	0.2499	± 0.0131	± 0.0144
0.180 - 0.200	0.2084	± 0.0122	± 0.0103	0.2112	± 0.0107	± 0.0118	0.2176	± 0.0127	± 0.0115
0.200 - 0.250	0.0861	± 0.0053	± 0.0066	0.0862	± 0.0050	± 0.0073	0.0902	± 0.0049	± 0.0076
0.250 - 0.300	0.0281	± 0.0032	± 0.0022	0.0302	± 0.0046	± 0.0039	0.0274	± 0.0027	± 0.0037
0.300 - 0.350	0.00089	± 0.00048	± 0.00027	0.00053	± 0.00028	± 0.00086	0.00067	± 0.00035	± 0.00008

Table B.18.b: Differential 2-Jet Rate Cambridge Algorithm D_2^{Cam}

Differential 2-Jet Rate Cambridge Algorithm D_2^{Cam}									
y_{23}	$0.72 < \cos\vartheta_T \leq 0.84$			$0.84 < \cos\vartheta_T \leq 0.96$			$0. < \cos\vartheta_T \leq 1.$		
0.000 - 0.001	245.9	± 1.3	± 3.1	253.9	± 1.4	± 5.8	241.95	± 0.62	± 2.61
0.001 - 0.002	146.4	± 1.1	± 1.3	143.7	± 1.0	± 1.3	146.21	± 0.43	± 0.96
0.002 - 0.003	89.48	± 0.82	± 0.63	87.25	± 0.91	± 0.96	88.75	± 0.32	± 0.50
0.003 - 0.004	52.13	± 0.67	± 0.50	51.76	± 0.66	± 0.79	52.46	± 0.28	± 0.47
0.004 - 0.005	38.55	± 0.62	± 0.42	38.63	± 0.64	± 0.67	38.71	± 0.27	± 0.38
0.005 - 0.006	31.31	± 0.53	± 0.37	30.13	± 0.54	± 0.51	30.55	± 0.24	± 0.31
0.006 - 0.007	27.75	± 0.45	± 0.35	26.78	± 0.52	± 0.48	27.35	± 0.20	± 0.27
0.007 - 0.008	21.63	± 0.43	± 0.33	20.97	± 0.47	± 0.43	20.93	± 0.18	± 0.24
0.008 - 0.009	18.56	± 0.42	± 0.32	17.56	± 0.44	± 0.39	18.17	± 0.17	± 0.22
0.009 - 0.010	16.28	± 0.41	± 0.31	16.76	± 0.42	± 0.34	16.05	± 0.16	± 0.16
0.010 - 0.011	14.80	± 0.40	± 0.29	15.71	± 0.40	± 0.31	15.53	± 0.15	± 0.14
0.011 - 0.012	12.63	± 0.39	± 0.27	12.24	± 0.38	± 0.27	12.55	± 0.14	± 0.13
0.012 - 0.013	11.25	± 0.35	± 0.23	12.04	± 0.35	± 0.23	11.76	± 0.14	± 0.11
0.013 - 0.014	11.06	± 0.34	± 0.20	10.53	± 0.33	± 0.19	10.75	± 0.14	± 0.08
0.014 - 0.015	10.63	± 0.31	± 0.16	10.44	± 0.31	± 0.15	10.58	± 0.13	± 0.07
0.015 - 0.016	8.439	± 0.288	± 0.126	9.461	± 0.291	± 0.142	8.960	± 0.122	± 0.061
0.016 - 0.018	8.191	± 0.193	± 0.088	8.033	± 0.229	± 0.129	8.163	± 0.077	± 0.053
0.018 - 0.020	7.540	± 0.175	± 0.081	7.209	± 0.181	± 0.121	7.412	± 0.071	± 0.051
0.020 - 0.025	6.102	± 0.116	± 0.072	5.901	± 0.102	± 0.109	6.010	± 0.039	± 0.044
0.025 - 0.030	4.594	± 0.099	± 0.060	4.599	± 0.090	± 0.094	4.576	± 0.034	± 0.036
0.030 - 0.040	3.380	± 0.057	± 0.053	3.560	± 0.064	± 0.076	3.465	± 0.021	± 0.032
0.040 - 0.050	2.439	± 0.049	± 0.050	2.334	± 0.052	± 0.044	2.413	± 0.020	± 0.027
0.050 - 0.060	1.710	± 0.041	± 0.046	1.742	± 0.042	± 0.035	1.797	± 0.017	± 0.025
0.060 - 0.070	1.402	± 0.037	± 0.042	1.457	± 0.037	± 0.032	1.464	± 0.015	± 0.023
0.070 - 0.080	1.109	± 0.034	± 0.034	1.098	± 0.035	± 0.029	1.138	± 0.013	± 0.020
0.080 - 0.090	0.9142	± 0.0327	± 0.0302	0.9389	± 0.0331	± 0.0265	0.9459	± 0.0125	± 0.0178
0.090 - 0.100	0.8244	± 0.0316	± 0.0257	0.7551	± 0.0272	± 0.0242	0.8188	± 0.0108	± 0.0163
0.100 - 0.110	0.5863	± 0.0256	± 0.0219	0.5884	± 0.0220	± 0.0226	0.6350	± 0.0096	± 0.0154
0.110 - 0.120	0.5265	± 0.0229	± 0.0191	0.5418	± 0.0211	± 0.0195	0.5534	± 0.0081	± 0.0145
0.120 - 0.140	0.4228	± 0.0186	± 0.0177	0.4513	± 0.0156	± 0.0135	0.4433	± 0.0069	± 0.0118
0.140 - 0.160	0.3043	± 0.0126	± 0.0122	0.3253	± 0.0131	± 0.0108	0.3398	± 0.0057	± 0.0103
0.160 - 0.180	0.2267	± 0.0104	± 0.0110	0.2189	± 0.0116	± 0.0085	0.2439	± 0.0045	± 0.0076
0.180 - 0.200	0.1972	± 0.0094	± 0.0095	0.1889	± 0.0093	± 0.0067	0.2093	± 0.0036	± 0.0057
0.200 - 0.250	0.0741	± 0.0039	± 0.0051	0.0778	± 0.0040	± 0.0044	0.0848	± 0.0017	± 0.0046
0.250 - 0.300	0.0293	± 0.0033	± 0.0034	0.0271	± 0.0024	± 0.0019	0.0290	± 0.0012	± 0.0018
0.300 - 0.350	0.00055	± 0.00026	± 0.00018	0.00027	± 0.00016	± 0.00008	0.00133	± 0.00026	± 0.00021

Table B.18.c: Differential 2-Jet Rate Cambridge Algorithm D_2^{Cam}

List of Figures

List of Tables

References

[1] The LEP Collaborations ALEPH, DELPHI, L3, OPAL,
the LEP Electroweak Working Group and the SLD Heavy Flavour
and Electroweak Groups, D. Abbanneo et al., CERN-EP/99-15 (1999).

[2] P. M. Stevenson, Nucl. Phys. B231 (1984) 65.

[3] P. M. Stevenson, Phys. Rev. D23 (1981), 2916.

[4] G. Grunberg, Phys. Lett. B95 (1980) 70,
G. Grunberg, Phys. Rev. D29 (1984) 2315.

[5] S. Brodsky, G. Lepage, P. MacKenzie, Phys. Rev. D28 (1983) 228.

[6] D. T. Barclay, C. J. Maxwell, M. T. Reader, Phys. Rev. D49 (1994) 3480.

[7] N. Magnussen, Thesis, Universität Wuppertal, WUB-DIS 88-04 (1988),
DESY F22-89-01.
S. Bethke, Z. Phys. C43 (1989) 331.
DELPHI Collab., P. Abreu et al., Phys. Lett. B247 (1990) 167.
DELPHI Collab., P. Abreu et al., Phys. Lett. B252 (1990) 149.
JADE Collab., N. Magnussen et al., Z. Phys. C49 (1991) 29.
OPAL Collab., M.Z: Akrawy et al., Z. Phys C49 (1991) 384.
P.N. Burrows, H. Masuda, D. Muller, Phys. Lett. B382 (1996) 157.

[8] DELPHI Collab., P. Abreu et al., Z. Phys. C 54 (1992) 55.

[9] DELPHI Collab., P. Abreu et al., Z. Phys. C 59 (1993) 21.

[10] E. Leader, E. Predazzi, *An introduction to gauge theories and modern particle physics, volume 1 and 2*, Cambridge University Press (1996)

[11] J. Chýla and A. L. Kataev, in CERN Report 95-03 (1995) 313.

[12] Super-Kamiokande Collab., Y. Fukuda et al., Phys. Rev. Lett. 81 (1998) 1562.

[13] E. Fermie, Z. Phys. 88 (1934) 161.

[14] S.L. Glashow, Nucl. Phys. 22 (1967) 567,
S. Weinberg, Phys. Rev. Lett. 19 (1967) 1264,
S. Salam in *Elementary Particle Theory*, 367 Stockholm (1968).

[15] C. S. Wu et al, Phys. Rev. 105 (1957) 1413.

[16] M. Gell-Mann, Phys. Lett. 8 (1994) 214.

[17] G. Zweig, CERN-TH-401 (1964),
G. Zweig, CERN-TH-412 (1964).

[18] H. Fritzsch, M. Gell-Mann and H. Leutwyler, Phys. Lett. B47 (1973) 365.

[19] N.V. Krasnikov and A.A. Pivovarov, Mod. Phys. Lett. A11 (1996) 335.

[20] J. Fischer, Int. J. Mod. Phys. A12 (1997) 3625.

[21] A. Pich, *Quantum Chromodynamics*, in CERN-Report 95-04 (1995) 157.

[22] G. 't Hooft and M. Veltman, Nucl. Phys. B44 (1972) 189,
G. 't Hooft, Nucl. Phys. B61 (1973) 455.

[23] W.J. Marciano, Phys. Rev. D29 (1984) 580.

[24] M.L. Mangano, in CERN-Report 99-04 (1999) 53.

[25] C. J. Maxwell, hep-ph/9908463 (1999).

[26] W. Celmaster and P.M. Stevenson, Phys. Lett. B125 (1983), 493.

[27] J. Chýla, Phys. Lett. B356 (1995) 341.

[28] MARK II Collab. S. Komamiya et al., Phys. Rev. Lett. 64 (1990) 987.

[29] Y.L. Dokshitzer and B.R. Webber, Phys. Lett. B404 (1997) 321.

[30] E. Braaten, Talk given at the TAU 96, Colorado, 16-19 Sep 1996, Nucl. Phys. Proc. Suppl. 55C (1997) 369.

[31] S. Brandt et al., Phys. Lett. 12 (1964) 57,
E. Fahri, Phys. Rev. Lett. 39 (1977) 1587.

[32] Mark J Collab., D. P. Barber et al., Phys. Rev. Lett. 43 (1979) 830,
Mark J Collab., D. P. Barber et al., Phys. Lett. 89b (1979) 139.

[33] R.K. Ellis, D.A. Ross, A.E. Terrano: Nucl. Phys. B178 (1981) 421,
G. Parisi: Phys. Lett. B74 (1978) 65,
J.F. Donohue, F.E. Low, S.Y. Pi: Phys. Rev. D20 (1979) 2759.

[34] S. Catani, G. Turnock and B. R. Webber, Phys. Lett. B295 (1992) 269.

[35] S. Bethke et al., Nucl. Phys. B370 (1992) 310.

[36] JADE collab., W. Bartel et al., Z. Phys. C33 (1986) 23,
JADE collab., S. Bethke et al., Phys. Lett. B213 (1988) 235,
S. Catani and M. Seymour, Nucl. Phys. B485(1997) 291-419.

[37] N. Brown and W. J. Stirling, Phys. Lett. B252 (1990) 657,
S. Bethke et al., Nucl. Phys. B370 (1992) 310.

[38] Yu. L. Dokshitzer et al., JHEP 08 (1998) 001.

[39] C. L. Basham et al., Phys. Rev. Lett. 41 (1978) 1585,
C. L. Basham et al., Phys. Rev. D17 (1978) 2298

[40] Y. Ohnishi and H. Masuda, SLAC-PUB-6560 (1994);
see also [84].

[41] J. Ellis, M.K. Gaillard and G.G. Ross, Nucl. Phys. B111 (1976) 253.

[42] T. Kinoshita, J. Math. Phys. 3 (1962) 659,
T. D. Lee, M. Nauenberg, Phys. Rev. 133B (1964) 1549.

[43] E.B. Zijlstra and W.L. van Neerven, Nucl. Phys. B383 (1992) 525.

[44] R. K. Ellis, D.A. Ross and A.E. Terrano, Nucl. Phys. B178 (1981) 421.

[45] L.G. Nnowles et al., *QCD Event Generators*, in CERN-Report 96-02 Vol. 2 (1996) 103.

[46] program EVENT2, M. Seymour,
URL: http://hepwww.rl.ac.uk/theory/seymour/nlo.

[47] S. Catani and M. Seymour, Nucl. Phys. B485 (1997) 291-419.

[48] W. Celmaster and R. J. Gonsalves, Phys. Rev. D21 (1980) 3112.

[49] B. Lampe, Phys. Lett. B301 (1993) 435.

[50] ALEPH Collab., R. Barate et al, Phys. Rept. 294 (1998), 1.

[51] S. Catani, CERN-TH 6281/91, Invited talk given at 17th Workshop of INFN Eloisatron Project, QCD at 200-TeV, Erice, Italy, Jun 11-17, 1991.

[52] S. Catani et al., Phys. Lett. B263 (1991) 491.

[53] S. Catani and B. R. Webber, CERN-TH-98-31 (1998).

[54] S. Catani et al., Phys. Lett. B295 (1992) 269.

[55] S. Catani et al., Phys. Lett. B272 (1991) 368.

[56] G. Dissertori and M. Schmelling, Phys. Lett. B361 (1995) 167.

[57] Yu. L. Dokshitzer et al., JHEP 01 (1998) 011.

[58] S. Catani et al., Nucl. Phys. B407 (1993) 3.

[59] B. R. Webber, in Proceedings of the Workshop "QCD - 20 years later", Aachen, Germany, 1992 (Word Scientific, Singapore, 1993) p 73.

[60] T. Sjöstrand, Comp. Phys. Comm. 39 (1986) 347.
T. Sjöstrand and M. Bengtsson, Comp. Phys. Comm. 46 (1987) 367.

[61] DELPHI Collab., P. Abreu et al., Z. Phys. C 73 (1996) 11.

[62] OPAL Collab., M.Z. Akrawy et al., Phys. Lett. B252 (1990), 159.

[63] G. Altarelli and G. Parisi, Nucl. Phys. B126 (1977) 298.

[64] G. Marchesini et al., Comp. Phys. Comm. 67 (1992) 465.

[65] L. Lönnblad, Comp. Phys. Comm. 71 (1992) 15.

[66] B. Anderson et al., Phys. Rep. 97 (1983) 31.

[67] G. Marchesini and B. Webber, Nucl. Phys. B238 (1984) 1.
G. Marchesini and B. Webber, Nucl. Phys. B310 (1988) 461.

[68] DELPHI Collab., P. Aarnio et al., Nucl Instr. Meth. A303 (1991) 233.

[69] DELPHI Collab., P. Abreu et al., Nucl. Intr. Meth. A378 (1996) 57.

[70] ALEPH Collab., D. Decamp et al., Nucl Instr. Meth. A294 (1990) 121.

[71] L3 Collab., B. Adeva et al., Nucl Instr. Meth. A289 (1990) 35.

[72] ALEPH Collab., K. Ahmet et al., Nucl Instr. Meth. A305 (1991) 275.

[73] CERN, Geneva, *LEP design report*:
Vol.1 - The LEP injector chain, CERN LEP TH 83-29 (1983).
Vol.2 - The LEP main ring, CERN LEP 84-01 (1984).
Vol.3 - LEP 2, CERN AC 96-01 (1996).

[74] DELPHI collab., DELPHI 89-44 PROG 137 (1989).

[75] DELPHI collab., DELPHI 89-67 PROG 142 (1989).
DELPHI collab., DELPHI 89-68 PROG 143 (1989).

[76] F. Jadach, B.F.L. Ward, Z. Was, Comp. Phys. Comm. 40 (1986) 285.
Nucl. Phys. B253 (1985) 441.

[77] V. Blobel in CERN-REPORT 85-09 (1985) 88.

[78] G. D'Agostini, Nucl. Instr. Meth. A362 (1995) 487.

[79] M. Weierstall, Thesis, University of Wuppertal, WUB-DIS 95-11 (1995).

[80] J.E. Campagne and R. Zitoun, Z. Phys. C 43 (1989) 469.

[81] ALEPH collab., D. Decamp et al., Z. Phys. C55 (1992) 209.

[82] L3 collab., B. Adeva et al., Z. Phys. C55 (1992) 39.

[83] Opal collab., M.Z. Akrawy et al., Z. Phys. C47 (1990) 505.

[84] SLD Collab., K. Abe et al., Phys. Rev. D 51 (1995) 962.

[85] OPAL Collab., P.D. Acton et al., Z. Phys. C55 (1992) 1.

[86] ALEPH Collab., D. Decamp et al., Phys. Lett. B 284 (1992) 1.

[87] W. de Boer, H. Fürstenau and J.H. Köhne, Z. Phys. C49 (1991) 141.

[88] Particle Data Group, C. Caso et al., Europ. Phys. Jour. C3 (1998), 1.

[89] Opal Collab., K. Ackerstaff et al., Eur. Phys. J. C7 (1999) 571.

[90] P. Nason et al., *QCD*, in CERN-Report 96-01 Vol. 1 (1996) 250.

[91] L3 Collab., O. Adriani et al., Phys. Lett. B284 (1992) 471.

[92] A. Wehr, Thesis, University of Wuppertal, WUB-DIS 94-2 (1994).

[93] ALEPH Collab., Contribution to the International Conference on High Energy Physics, Warsaw, Poland, 25. - 31. July 1996.

[94] M. Schmelling, Phys. Scripta 51 (1995) 676.

[95] M. Schmelling, Phys. Scripta 51 (1995) 683.

[96] S. Hahn, DELPHI 98-174 PHYS 813, hep-ex/9812021, Plenary talk presented at the Hadron Structure'98, Stara Lesna, Sept. 1998.

[97] S. Bethke, hep-ex/9812026.

[98] K. Hamacher, private communication.

[99] G. Kramer and B. Lampe, Z. Phys. C39 (1988) 101.

[100] K. Hagiwara and D. Zeppenfeld, Nucl. Phys. B313 (1989) 56.

[101] Z. Bern et al, Nucl Phys B489 (1997) 3. E.W.N. Glover and D.J. Miller, Phys. Lett B396 (1997) 257.

[102] U. Flagmeyer, Thesis, University of Wuppertal, in preparation.

[103] M. A. Samuel, G. Li, E. Steinfels, Phys. Rev. D48 (1993) 228.
M. A. Samuel, G. Li, E. Steinfels, Phys. Rev. E51 (1995) 3911.

[104] J. Ellis et al., Phys. Rev. D57 (1998) 2665 and references therein.

[105] E. Gardi, Acta Phys. Polon. B28 (1997) 3067.
E. Gardi, Phys. Rev. D56 (1997) 68.

[106] J. Ellis, private communication.

[107] J. Ellis et al, Phys. Rev. D54 (1996) 6986.

[108] ALEPH Collab., D. Decamp et al., Phys. Lett. B284 (1992) 1.

[109] L3 Collab., O. Adriani et al., Phys. Lett. B284 (1992) 471.

[110] OPAL Collab., P. Acton et al., Z. Phys. C59 (1993) 1.

[111] R. Reinhardt, Thesis, University of Wuppertal, in preparation.

[112] G. Rodrigo, A. Santamaria and M. Bilenky, hep-ph/9812433.

[113] S. Hahn, J. Drees, DELPHI 98-84 CONF 152, ICHEP'98 #142

[114] Program provided by G. Rodrigo.

[115] G. Rodrigo, M. Bilenky and A. Santamaria, Nucl. Phys. B554 (1999) 257.

[116] G. Rodrigo, private communication.

[117] H. Staeck, Thesis, University of Wuppertal, WUB-DIS 93-4.

[118] Particle Data Group, C. Caso et al., Europ. Phys. Jour. C3 (1998), 1;
1999 partial update of the WEB edition - URL: http://pdg.lbl/gov/

[119] C.T.H. Davies et al., Phys. Rev. D56, (1997) 2755.

[120] J. Santiago and F. J. Ynduráin, Nucl. Phys. B563 (1999) 45.

[121] J. G. Körner, F. Krajewski, A.A. Pivovarow, hep-ph/0002166.

[122] T.G. Steele and V. Elias, Mod. Phys. Lett. A13 (1998) 3151.

[123] F. Krajewski, private communication.

Acknowledgements

First and foremost, I wish to express my utmost gratitude to Prof. Dr. J. Drees, who inspired these studies and accompanied them with great interest. He gave me the opportunity to participate and to contribute to an extraordinarily exiting topic of High Energy Physics research. He enabled my numerous stays at CERN and my participation in various international conferences, where I had the chance to present my studies and to discuss various aspects of the analysis with approved experts of the particular fields.

Modern large scale experiments like the LEP storage ring and the DELPHI experiment require the engagement and the team work of several hundred specialists. I want to thank all collaborators for their great support, for their corporation and for their work in building and operating the DELPHI detector, in software development and maintenance and for their enormous efforts in providing the precise data, which are the foundation of this dissertation.

Particularly I want to express my gratitude to Dr. Juan Fuster and Dr. German Rodrigo from València for their extraordinary corporation in evaluating the effects of massive b-quarks. I also want to thank Dr. Wilbur Venus, Dr. Klaus Moenig and Dr. Dave Crennel for the kind and encouraging attention to my work and for the proof reading of publications, which helped to improve my work both in the physical content and in English language.

Many thanks to my colleagues from the Wuppertal working group for their friendly support and corporation during the work on my diploma and doctoral thesis. I am especially grateful to Dr. Klaus Hamacher. I appreciated very much the fruitful and stimulating discussions with him and I benefited a lot from his comments and suggestions and from the proof reading of this thesis and other manuscripts. In particular I want to thank Oliver Passon, Ralf Reinhardt, Uwe Flagmeyer and Dr. Daniel Wicke for numerous discussions and suggestions and for the great teamwork and engagement in verifying some of the most important aspects of the outcome of this thesis.

Finally, I want to express my gratitude to my dearest Heike for her love, her continuous support and her incredible patience during the analysis and the writing down of this thesis.